Multiscale Investigation of the Earth's Internal Structure and Processes Using Seismic Arrays

by

Jingchuan Wang

A thesis submitted in partial fulfillment of the requirements for the degree of

Doctor of Philosophy

in

Geophysics

Department of Physics

University of Alberta

Abstract

The fast expansion of seismic arrays has improved our ability to understand the Earth's internal structure and dynamics at various spatial scales. This thesis applies both conventional and novel approaches to dense array recordings to address major questions in (1) earthquake location and source mechanisms, (2) upper-crustal seismic structure, (3) subduction zone dynamics, and (4) variations in the elastic properties of upper mantle transition zone discontinuities.

We present the first example of a quick-response nodal experiment in western Canada to investigate the spatiotemporal characteristics of a hydraulic fracturing-induced earthquake swarm in central Alberta at a local scale. A high-precision earthquake catalog is constructed using a machine-learning phase picker and a sequential earthquake association and location method. The outcomes capture the geometry of the reactivated faults and highlight the significance of trailing seismicity in hazard assessment. In Chapter 3, a regional background survey of southwestern Canada based on ambient noise tomography reveals lateral variations in both velocity and anisotropy with spatial affinities to major geological domains. We observe strong radial anisotropy in the southern Canadian Cordillera due to crustal extension similar to that observed in the western United States, while the anisotropic anomaly in the Cordilleran foreland may have resulted from horizontal compression during the plate convergence at the western margin of the North American craton. In the third component of the thesis, a self-consistent model of subduction dynamics at transition zone depths beneath South America is presented, through a combined analysis of travel times and amplitudes of underside shear wave reflections. Our updated topography model of transition zone discontinuities suggests contrasting styles of slab-transition zone interaction. A joint analysis of seismic data and mineral physics modeling provides observational evidence for thermo-chemical anomalies within the mantle. Finally, we expand the underside reflection data set for global coverage, and a novel amplitude-versus-offset inversion is applied to map lateral variations in density jump across the 660-km discontinuity. Major subduction zones are generally featured by low density jumps; this implies a compositional difference with excess basalt relative to the global average.

Preface

Chapter 2 of this thesis has been published as Wang, J., Li, T., Gu, Y. J., Schultz, R., Yusifbayov, J., & Zhang, M. (2020). Sequential fault reactivation and secondary triggering in the March 2019 Red Deer induced earthquake swarm. *Geophysical Research Letters, 47*(22), e2020GL090219. I was responsible for seismic data collection and analysis as well as manuscript composition. T. Li conducted focal mechanism determination and contributed to manuscript edits. Y. J. Gu was the supervisory author and was involved with manuscript revision. R. Schultz contributed to result interpretation and assisted with manuscript review. J. Yusifbayov and M. Zhang contributed to manuscript review and editing.

Chapter 3 of this thesis has been published as Wang, J., Gu, Y. J., & Chen, Y. (2020). Shear velocity and radial anisotropy beneath southwestern Canada: Evidence for crustal extension and thick-skinned tectonics. *Journal of Geophysical Research: Solid Earth, 125*(2), e2019JB018310. I was responsible for data collection and analysis as well as manuscript preparation. Y. J. Gu was the supervisory author and was involved with concept formation and assisted with manuscript preparation. Y. Chen assisted with data collection and contributed to manuscript review.

Chapter 4 of this thesis has been revised for *Earth and Planetary Science Letters* as Wang. J. & Gu Y. J. Slab stagnation vs. penetration of Nazca subduction inferred from shear wave reflectivity. I was responsible for data collection, programming, formal analysis, and manuscript composition. Y. J. Gu was the supervisory author and assisted with manuscript editing. Both authors contributed to conceptualization and manuscript revision.

Chapter 5 of this thesis has been submitted to *Geophysical Research Letters*. I was responsible for data curation and formal analysis as well as manuscript composition. Y. J. Gu was the supervisory author and was involved with manuscript preparation.

This thesis is dedicated to my parents
for their endless love and encouragement.

Acknowledgments

First and foremost, I am very fortunate and honored to have had a great seismologist, Yu Jeffrey Gu, as my Ph.D. supervisor. Jeff has been extremely supportive, open, and patient whenever I encounter questions about my research projects. I sincerely appreciate the freedom he has granted to me to work on diverse research topics. His continued support and guidance always direct me toward the right path and inspire me to think critically and scientifically.

I would like to thank my supervisory committee members Mauricio Sacchi and Vadim Kravchinsky for their generous support and helpful discussions. I am grateful to my examination committee members Maureen Long and Elena Konstantinovskaya for their broad and insightful inputs. I would also like to thank other professors who taught me at the University of Alberta: Claire Currie from whom I learned global geodynamics, Doug Schmitt who introduced me to rock physics, David Potter from whom I learned well log analysis, and Mirko van der Baan from whom I learned seismic data processing.

Special thanks go to Jan Dettmer who brought me into the field of seismology and encouraged me to pursue academic goals.

Being a member of the Global Seismology Group has been one of the luckiest things in my life. I wish to thank all of my past and current group members which include Yunfeng Chen, Ruijia Wang, Tianyang Li, Lei Wu, Wenhan Sun, Cheng Zhang, Songyun Huang, Weiqing Fan, Farhanah Mohammed, Camryn Undershute, Hang Wang, Weiheng Geng, and Haixia Sun. In particular, Yunfeng “shixiong” and Ruijia “shijie” has offered me technical and emotional support throughout the years. My thanks also go to my collaborators Ryan Schultz, Javad Yusifbayov, and Miao Zhang for their technical assistance.

There are others within the department who made my study at U of A a happy experience: Yiru Zhou, Haojie Ni, Xiaowen Liu, Zhihong Pan, Tai-Chieh Yu, Rongzhi Lin, Yi Guo, Guanhua Li, Dawei Liu, Hongling Chen, Jieyu Zhang, Benjamin Lysak, Breno Bahia, Ke Chen, and Ji Li. I also want to thank Ruoxi Peng, Ziguang Su, and Bowen Li for their long-time friendship.

I also want to express my gratitude to my wonderful friends with whom I have enjoyed playing badminton: Mingfei Li, Weiliang Yu, Dongxiao Hou, Haoyang Li, Enze Zhou, Yiwenkai Ren, Owen Wang, Richard Lee, and many others.

Finally, I would not be finishing this dissertation without the understanding and sacrifice of my families. My lovely nephew, Miduo, brings me a lot of joy. Thank you, mom and dad. I can always feel your love though we are 9,000 km apart.

Contents

1 Introduction 1
1.1 Overview 1
1.2 Thesis Outline 4

2 Rapid Characterization of the March 2019 Red Deer Induced Earthquake Swarm Using a Near-Source Nodal Array 7
2.1 Introduction 7
2.2 Regional Setting 8
2.3 Data and Methods 9
  2.3.1 Seismic Data 9
  2.3.2 Local Earthquake Catalog Development 9
  2.3.3 Focal Mechanism Solutions 12
2.4 Spatiotemporal Evolution of the Swarm 13
2.5 Discussion 17
  2.5.1 Event Triggering 17
  2.5.2 Geological Implications 21
2.6 Conclusions 22

3 Crustal Shear Structure of Southwestern Canada Using Ambient Noise Tomography on Regional Broadband Arrays 24
3.1 Introduction 24
3.2 Tectonic Setting and Previous Geophysical Surveys 26
3.3 Data and Methods 29
  3.3.1 Ambient Seismic Noise and Data Processing 29
  3.3.2 Dispersion Measurements and Tomographic Inversion 31
  3.3.3 Inversion for Shear Velocity and Radial Anisotropy 34
3.4 Results 35
  3.4.1 Group Velocity Maps 35
  3.4.2 Shear Velocity Models 37
  3.4.3 Radial Anisotropy 40
  3.4.4 Model Robustness Test 42
  3.4.5 Uncertainty in Radial Anisotropy 44
3.5 Discussion 46
  3.5.1 General Assessment 46
  3.5.2 The Foreland Belt 50
  3.5.3 The Omineca Belt 52
3.6 Conclusions 55

4 Shear Wave Reflectivity Imaging of Upper Mantle Discontinuity Structure Beneath South America 57
4.1 Introduction 57
4.2 Seismic Stacking Method 59

4.2.1 Data Preprocessing 59
4.2.2 Common Midpoint Stacking 61
4.3 Mineral Physics Modeling 63
4.4 Inverse Problem 65
4.4.1 Inversion for Mantle Temperature and Composition 65
4.4.2 Amplitude-Versus-Offset Inversion 66
4.5 Results 71
4.5.1 Overview of Transition Zone Observations 71
4.5.2 Variations in Seismic Reflectivity and Composition 72
4.5.3 Validation 76
4.6 Discussion 78
4.6.1 An Integrate Model of MTZ Slab Dynamics 78
4.6.2 Structural Analogy to Northeast Asia 79
4.7 Conclusions 83

5 Global Variability of Density Jump Across the 660-km Discontinuity From SS Precursors 84
5.1 Introduction 84
5.2 Data Processing 86
5.2.1 Data Preprocessing 86
5.2.2 Waveform Stacking 88
5.3 Results 88
5.3.1 Topography of the 660 88
5.3.2 Variations of Density Jump 91
5.4 Discussion 94
5.4.1 General Assessment 94
5.4.2 Comparison With Seismic Tomography 95
5.4.3 Physical Implications 96
5.5 Conclusions 99

6 Conclusions and Outlook 101
6.1 Conclusions 101
6.2 Future Directions 103

References 106

Appendix A Supplementary Materials for Chapter 2 130
A.1 Modeling Coulomb Stress Changes 130

Appendix B Supplementary Materials for Chapter 3 137
B.1 Azimuthal Anisotropy 137

Appendix C Supplementary Materials for Chapter 4 141
C.1 The Effect of Low-Velocity Layers on S410S Reflectivity 141

Appendix D Supplementary Materials for Chapter 5 153

Appendix E List of Software 157

List of Tables

A.1 A Local Velocity Model 131
A.2 Focal Mechanism Solutions of Selected Earthquakes 136

E.1 List of Software 157

List of Figures

1.1 Examples of Seismic Arrays 3

2.1 Map of Seismicity and Seismic Stations in Central Alberta 10
2.2 Map and Cross-Sectional Views of Relocated Events 14
2.3 Frequency-Magnitude Distribution of the Nodal Group 15
2.4 Event Space-Time Evolution 16
2.5 Focal Mechanisam Solutions 18
2.6 3-D View of the Earthquakes and Temporal Change of Strike Orientation 20

3.1 Tectonic Setting of the Cordillera–Craton Transition Region in Southwestern Canada 27
3.2 Noise Cross-Correlation Functions 29
3.3 Group Velocity Maps 36
3.4 Group Velocity Profile Along A-A$'$ 38
3.5 Group Velocity Uncertainty 39
3.6 Shear Velocity Maps 40
3.7 Maps of Radial Anisotropy 42
3.8 Cross-Sections of Shear Velocity and Anisotropy 43
3.9 Variance Reduction 45
3.10 Sensitivity Test of the Starting Model 47
3.11 Radial Anisotropy Uncertainty 47
3.12 Checkerboard Test 49
3.13 Monte Carlo Simulation 54
3.14 Schematic Diagram Showing the Origins of the Anisotropy 56

4.1 Tectonic Setting of South America 61
4.2 SS Precursor Data Coverage 62
4.3 Mineral Physics Modeling: EA and MM Models 64
4.4 Mineral Physics Modeling: Hydrous MM Model 65
4.5 Sensitivity Analysis 69
4.6 AVO Synthetic Inversion 70
4.7 Transition Zone Observations 73
4.8 SS Precursor Amplitudes 74
4.9 Inversion for Temperature and Composition: MM Model 75
4.10 AVO Inversion of Real Data 77
4.11 Schematic Diagram of Compositional Heterogeneity 80
4.12 Comparison of Subduction Systems 82

5.1 Global Data Set of SS Precursors 87
5.2 Record Section 89
5.3 Map of the 660 Topography and S660S Amplitudes 90
5.4 Spherical Harmonic Expansion 91

5.5 AVO Inversions of the Global Data Set and a Cap Data Subset . . . 92
5.6 Global Variations of Velocity and Density Jumps 93
5.7 Tectonic Regionalization 94
5.8 Map of Density Jump From Constrained Inversion 95
5.9 Correlation Analysis 97
5.10 Mineral Physics Modeling of the 660 Density Jump 99

A.1 Match&Locate Detection Using Broadband Waveforms 132
A.2 Match&Locate Detection Using Nodal Waveforms 133
A.3 Modeling of Coulomb Stress Changes 134

B.1 Azimuthal Dependence of Noise Correlation Functions 138
B.2 Trade-Off Curves 139
B.3 Inversion for Azimuthal Anisotropy 140

C.1 MTZ Topography 143
C.2 Correlation Between MTZ Thickness and Velocity Anomalies . . . 144
C.3 MTZ Topography Uncertainty 145
C.4 Effect of Temperature, Composition, and Water Content on SS Precursors 146
C.5 Geometric Spreading and Attenuation Correction 147
C.6 Comparison of Approximated and Exact Zoeppritz Equation 148
C.7 Inversion for Temperature and Composition: EA Model 149
C.8 Inversion for Temperature and Composition: Hydrous MM Model . 150
C.9 Forward Modeling 151
C.10 Reflectivity Modeling of Low-Velocity Layers 152

D.1 Comparison of Topography Model 154
D.2 Correlation Between S660S Amplitudes and Velocity Anomalies . . 155
D.3 Frequency Dependence 155
D.4 Mineral Physics Modeling of Density Jump in a Hydrous MTZ . . . 156

Chapter 1

Introduction

1.1 Overview

A seismic array is typically composed of a set of seismic sensors arranged in a well-defined geometry that involves the following criteria (Rost & Garnero, 2004; Rost & Thomas, 2002): (1) more than three identical seismometers, (2) an aperture ranging from a few to hundreds of kilometers, (3) processing of the data as an ensemble instead of individual components, and (4) centralized data acquisition. This definition applies to both a classical seismic array and a network of seismic stations, although a seismic network usually provides a regional- or continental-scale spatial sampling but exhibits lower signal coherency. In this thesis, the term "array" refers to both seismic arrays and seismic networks.

Seismic arrays were originally built to improve the capability to monitor nuclear explosions in compliance with the Nuclear Test Ban Treaty in the 1950–60 decade. In addition to their political incentives, arrays have opened a new chapter in mapping the Earth's structure and characterizing earthquake sources. An important step was taken when the U.S. Coast and Geodetic Survey created the World-Wide Standardized Seismograph Network (WWSSN) in the 1960s. The analog records contributed to the construction of the first maps of global seismicity and focal mechanisms that established the foundation for the plate tectonic theory (Isacks et al., 1968; Oliver & Murphy, 1971). The success of WWSSN then facilitated the installation of permanent digital networks in the 1970s and 80s, most notably the GEOSCOPE program (Romanowicz et al., 1984) and the Global Seismographic

Network (GSN; Figure 1.1a). The digital seismic data have revolutionized the seismic imaging of the Earth's deep interior, including the first models of mantle 3-D heterogeneity (Woodhouse & Dziewonski, 1984) and transition zone topography (Flanagan & Shearer, 1998). More recently, the densification of regional broadband arrays has formed the backbone for real-time seismicity monitoring and significantly refined our understanding of the structure and evolution of the continental lithosphere. For instance, the USArray Transportable Array (Figure 1.1b) has revealed 3-D variations of velocity and anisotropy in the crust and upper mantle beneath the North American continent in great detail (Long et al., 2014; Moschetti et al., 2010; W. Shen & Ritzwoller, 2016). Similar projects were also developed in Japan with an ultimate goal of better understanding the generation mechanisms of strong ground motions (Okada et al., 2004). Their success inspired the deployment of other national-level passive seismic networks such as AusArray in Australia (Haynes et al., 2020), ChinArray in China (Xiao et al., 2020), and AlpArray for the European Alps (Hetényi et al., 2018). In the past decade, the use of spatially dense arrays, also called "large-N" arrays, has become prevalent in passive seismology thanks to advances in geophone instrumentation (Karplus & Schmandt, 2018). Notable examples include the Long Beach Array (Figure 1.1c; Lin et al., 2013) and the IRIS Community Wavefield Demonstration Experiment in Oklahoma (Sweet et al., 2018). Data from dense arrays, which provide a nominal resolution that could rival that of exploration seismology, have enabled imaging near-surface structures and monitoring microseismic activities at an unprecedented scale.

Compared to a single seismic sensor, seismic arrays have their unique advantages: (1) vastly improved signal-to-noise ratio (SNR) by suppressing random noise through waveform stacking that helps to extract weak seismic signals from background noise and (2) dense spatial sampling that provides estimates of both the direction (back azimuth) and apparent velocity (slowness) of incoming wavefronts. Based on the plane wave assumption and time-shifted signal coherency, several array methods have commonly been adopted in global seismology, including (1) vespagram (slant stacking) which stacks seismic energy along different slownesses, (2) frequency-wavenumber analysis that measures the slowness and back azimuth

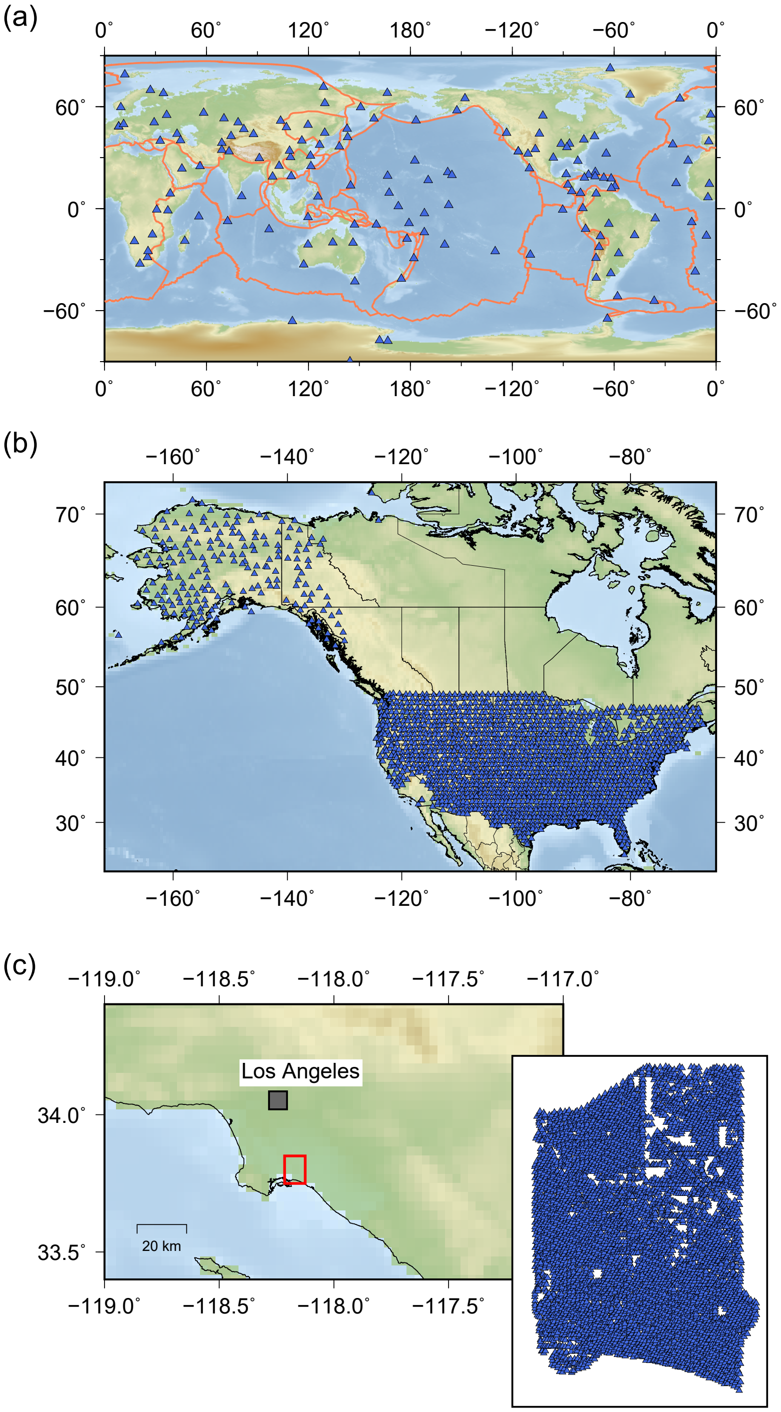

Figure 1.1: (a) Map showing the distribution of GSN stations (blue triangles). The plate boundaries (orange lines) are plotted after Bird (2003). (b) USArray Transportable Array stations (blue triangles). (c) Regional map of southern California. The red box marks the location of the Long Beach Array, and the inset map (bottom right) shows the distribution of the nodal sensors (blue triangles).

simultaneously by performing a grid search over all combinations and finding the maximum energy of the summed signal, and (3) migration (backprojection) to locate the source that generates the signal that maximizes the amplitudes of the shifted and stacked traces. Rost and Thomas (2002) provided an in-depth review of conventional techniques applied to array data. In response to increased data volume and improved computational power, machine learning-based techniques have emerged as an powerful tool to identify weak signals from dense array data sets with the potential to detect earthquakes (Zhu & Beroza, 2019) and resolve fine-scale structure in the deep mantle (D. Kim et al., 2020).

1.2 Thesis Outline

There are two principal themes that have guided this dissertation: (1) improved source characterization and (2) high-resolution seismic imaging of the crustal and mantle structure, by analyzing recordings from different types of arrays. The lines of research are as follows:

1. Local scale: earthquake location and focal mechanism determination of a hydraulic fracturing-induced earthquake sequence based on continuous recordings of a temporary nodal geophone array (**Chapter 2**).
2. Regional scale: upper-crustal shear velocity and radial anisotropy in the Canadian Cordillera-Craton transition region using cross correlation of ambient noise recordings on several regional broadband arrays (**Chapter 3**).
3. Continental scale: transition zone discontinuity topography and subduction-transition zone interactions beneath South America using array processing of SS precursors recorded by global seismic networks (**Chapter 4**).
4. Global scale: global mapping of density jumps across the 660-km discontinuity from amplitudes of a global data set of SS precursors (**Chapter 5**).

In **Chapter 2**, we characterize the seismicity near Red Deer, Alberta, a region with increasing cases of hydraulic fracturing-induced earthquakes, using data from nodal geophones and nearby broadband seismometers. A cluster of 417 events is detected, and their spatial distribution and focal mechanisms reveal a NE trending rupture area with two strike-slip fault planes. Reactivation of pre-existing faults by pore pressure diffusion is likely responsible for the occurrence of the earthquake sequence following the M_L 4.18 mainshock. The temporal sequence of reactivated fault orientations suggests apparent changes in the local stress field following the mainshock, which is also responsible for a remotely triggered cluster observed one month after the mainshock. This secondary triggering process enhances our understanding of the trailing effect of hydraulic fracturing-induced seismicity.

In **Chapter 3**, we present a new analysis of the crustal shear velocity and anisotropy by analyzing fundamental mode Rayleigh and Love waves from cross correlations of ambient seismic noise. Continuous recordings from 118 regional broadband stations reveal lateral variations in both velocity and anisotropy with strong spatial affinities to major geological domains. Strong variations in radial anisotropy, which dips westward and extends to at least mid-crustal depths, suggest a "thick-skinned" foreland thrust-and-fold belt beneath the Canadian Rocky Mountains. Our regional data also suggest increased horizontal shear velocities beneath the southern Canadian Cordillera, particularly near the Omineca Belt, which may have resulted from strong zonal deformation within the Cordilleran crust. This anisotropic anomaly migrates southward, and its spatial extent agrees well with the normal fault distribution to the west of the Rocky Mountain Trench. Our observations offer new evidence for the Eocene extension of the orogenic hinterland during the trans-tensional motion of the Cordillera to the North American craton.

In **Chapter 4**, we investigate the seismic reflectivity structure at transition zone depths beneath South America by combining the arrival times and amplitudes of an updated data set of SS precursors. We observe broad regions with up to 20 km depressed 410- and 660-km discontinuities and diminished precursor amplitudes beneath the back-arc region of Nazca subduction, incompatible with temperature-dominated mineral phase boundary perturbations. A probabilistic inversion is applied to simultaneously determine mantle temperature and composition, and the outcomes suggest a mechanically mixed transition zone with basalt enrichment beneath the Amazon basin. This is corroborated by a novel amplitude-versus-offset inversion that measures changes in density and shear velocity across the discontinuities. Our observations offer direct evidence for thermochemical anomalies within the mantle, which are largely associated with temporary slab stagnation. The slab-transition zone interactions suggest that the Nazca-South American convergence may represent a later-stage analog to the Pacific plate subduction in northeast Asia.

In **Chapter 5**, we introduce a novel method to simultaneously retrieve the topography, velocity and density contrasts of the 660-km discontinuity based on inversions of amplitude variations with offset (see Chapter 4). Our observations reveal a global average velocity jump of 4.2% and density jump of 5.3%, favoring a pyrolitic bulk composition. Near major subduction zones, most notably the western Pacific and South America, we identify decreased density jumps in regions of depressed 660-km discontinuity, consistent with basalt fractions greater than 30% in a non-equilibrated mantle. The causal association between density jump and compositional changes is further supported by a moderate correlation between lateral variations in density jump and those of water content anomalies.

Chapter 6 summarizes the results and interpretations obtained in this thesis, and recommendations for future work will be discussed.

This dissertation preferentially uses the pronoun “we” instead of “I” to acknowledge and honor the contributions from Yu J. Gu to most of the work presented in this thesis, Tianyang Li to the work on focal mechanism determination, and Yunfeng Chen to the discussion of seismic imaging and regional tectonics.

Chapter 2

Rapid Characterization of the March 2019 Red Deer Induced Earthquake Swarm Using a Near-Source Nodal Array

2.1 Introduction

Over the past decade, the notable increase of seismicity rate in western Canada, especially in the vicinity of Fox Creek, Alberta, has been attributed to hydraulic fracturing (HF) within the low-permeability Duvernay Shale Formation (e.g., Atkinson et al., 2016; Schultz et al., 2017). Recently, emerging cases of seismicity in the East Shale Basin portion of the Duvernay raised major public concern and scientific interest (Schultz et al., 2019; Schultz & Wang, 2020), largely in response to two moderate ($M_L > 3$) and a series of smaller (M_L 1–3) earthquakes. These events show high spatiotemporal correlations with adjacent HF operations (Schultz & Wang, 2020), despite the low susceptibility of this area to induced earthquakes (Pawley et al., 2018). The largest event (M_L 4.18, hereafter ML4) occurred on 4 March 2019, near an HF site in the Red Deer area, Alberta, which catalyzed a new traffic light protocol (Alberta Energy Regulator, 2019). A thorough understanding of surrounding earthquakes on potentially hazardous faults is therefore critical.

Compared with the well-studied Fox Creek area, low station density in central Alberta has posed a key challenge for event detection and monitoring. This limitation has contributed to notable discrepancies in hypocenter location or constraint on the source characteristics of earthquakes potentially induced by anthropogenic activities. A practical solution is the use of nodal instruments, where smaller, cable-free geophones offer new opportunities for quick-reaction seismic deployments for both seismicity monitoring and subsurface imaging (e.g., Hansen & Schmandt, 2015; Lin et al., 2013; Y. Wang et al., 2019).

In this chapter, we investigate the space-time evolution and dynamics of the March 2019 Red Deer induced earthquake swarm. Our analysis is facilitated by a temporary nodal geophone array, deployed approximately two weeks after ML4. Based on a large number of recordings and the distribution of the detected events, we are able to (1) characterize the faults activated during the swarm and (2) explore spatiotemporal variations of the regional seismic activity in central Alberta.

2.2 Regional Setting

Previously, most of the HF-induced earthquakes were reported in the Duvernay West Shale Basin (near the municipality of Fox Creek). The epicenter of ML4 lies within a separate geological play of the Upper Devonian Duvernay Formation, the Duvernay East Shale Basin (Figure 2.1; Schultz & Wang, 2020). The Duvernay Formation, which is largely composed of organic-rich mudstone in an overpressured regime, was deposited in a marine basin environment (Fox & Soltanzadeh, 2015) and is bisected by the Leduc Reef (Schultz et al., 2016). Compared with the West Shale Basin where extensive shale deposition occurred, the carbonate platform beneath the East Shale Basin resulted in a higher overall carbonate concentration (Knapp et al., 2017; Preston et al., 2016; Switzer et al., 1994).

The state of stress within the basin was first studied by Bell and Gough (1979) and frequently updated in the following 30 years (Bell & Grasby, 2012; Bell et al., 1994; Fordjor et al., 1983) based on borehole breakouts. These in situ measurements were later included in the World Stress Map (Heidbach et al., 2018) and reviewed by Reiter et al. (2014). The compilations of stress data consistently show NE-SW compressive stress across the basin, indicating that the present-day maximum horizontal stress (S_{Hmax}) orients in the northeast direction at an angle of 45–47°, approximately perpendicular to the northwest striking Canadian Rocky Mountains. One exceptional cluster resides in the Peace River Arch region in northern Alberta, where a 10–20° departure from the main regional trend is observed possibly due to the presence of upper-crustal intruded sills or subsurface structural heterogeneities (Bell & Grasby, 2012; Reiter et al., 2014).

2.3 Data and Methods

2.3.1 Seismic Data

Previous seismic monitoring in central Alberta relied on regional seismograph networks. To densify the data coverage, and as a part of a collaborative project between the University of Alberta and the Alberta Geological Survey, a temporary array of 16 three-component (5 Hz) Fairfield Nodal geophones (Ringler et al., 2018) was deployed within a 5-km radius of the two HF wells and recorded continuous data from 20 March to 10 April 2019 at a sampling rate of 250 Hz (Figure 2.1). To improve the constraints on the events occurred during the two-week-long gap after ML4 (and before the nodal deployment), we also incorporated broadband recordings from the Canadian Rockies and Alberta Network (CRANE; Gu et al., 2011), the Regional Alberta Observatory for Earthquake Studies Network (RAVEN; Schultz & Stern, 2015), and the TransAlta Dam Monitoring Network (TD).

2.3.2 Local Earthquake Catalog Development

First, we used broadband data from six regional stations to refine the regional earthquake catalog from Schultz and Wang (2020) using GrowClust, a hierarchical clustering relocation algorithm that uses waveform cross-correlation (CC)-based differential times (Trugman & Shearer, 2017). For reliable relocation, we (1) adopted a modified 16-layer crustal model (Table A.1) from recent regional receiver function inversions (Y. Chen et al., 2015; C. Zhang et al., 2019) beneath two nearby stations JOF and RDR of the CRANE network and (2) set the minimum CC coefficient to 0.6 and the maximum root-mean-square time residual for a proposed cluster to 0.2 s for GrowClust parameterization. This data set contains 19 relocated earthquakes

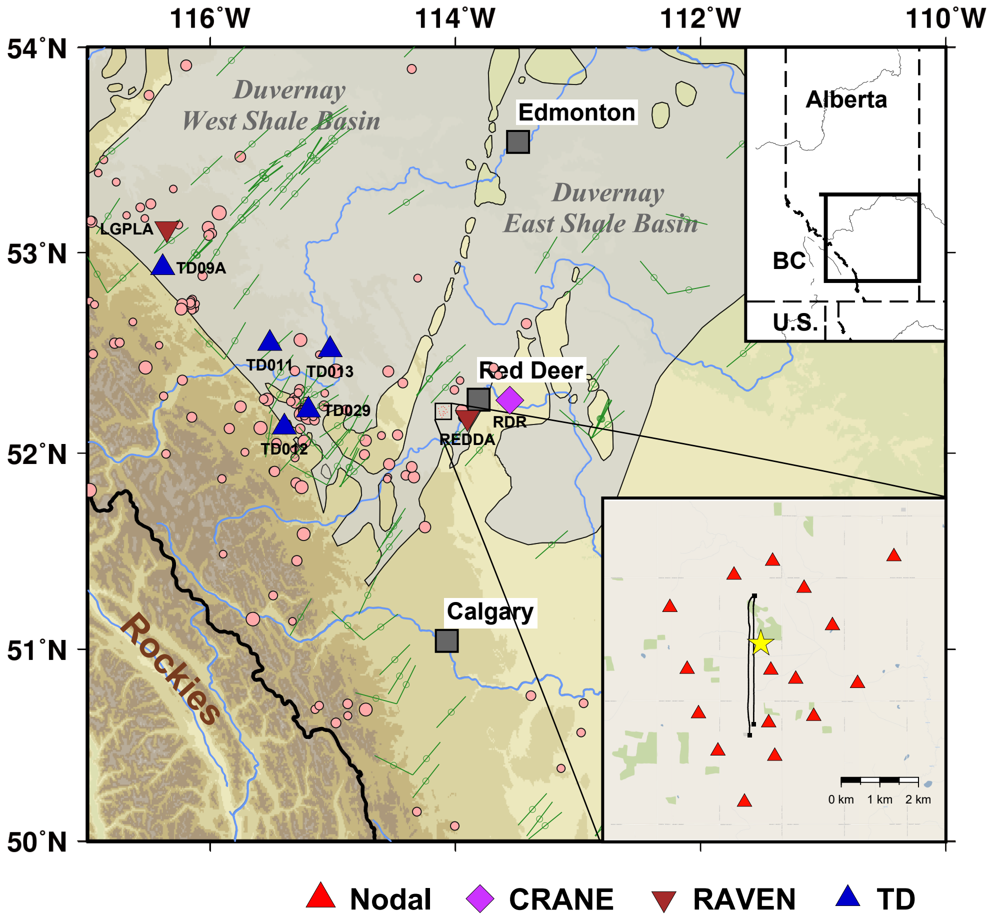

Figure 2.1: Spatial distributions of seismic stations (colored by network) and earthquakes recorded before 2019 (pink circles) with magnitudes greater than 2.0. The earthquake data were retrieved from the Alberta Geological Survey Seismicity Dashboard (`https://ags-aer.shinyapps.io/Seismicity_waveform_app`, last accessed 23 July 2020). Crustal stress orientations from the World Stress Map (Heidbach et al., 2018) are represented by green lines. The gray shaded area shows the geographic extent of the Duvernay Formation. The inset map in the lower right corner shows the spatial distribution of our nodal array (red triangles), the HF well trajectory (black lines), and the relocated ML4 (yellow star).

before ML4, during which 1,440 (608 P and 832 S) differential times from six regional stations were measured based on epicentral distance and data quality. After performing a 100-trial bootstrap resampling test, we determined the mean horizontal and vertical location errors to be 21 m and 26 m, respectively.

We then extended the regional catalog by applying the Match&Locate method (M&L; M. Zhang & Wen, 2015) to the continuous broadband data for the two weeks between 5 March and 19 March 2019 (Figure A.1). The M&L detects and locates small-magnitude events simultaneously by maximizing the stacked CC coefficients between the template and the continuous waveforms based on a delay-and-sum approach. To reduce the computational cost, the waveforms were downsampled to 20 Hz and bandpass filtered between 2 and 8 Hz. We searched for potential earthquakes within a mesh (0.01° in latitude, 0.015° in longitude, and 0.5 km in depth) centered at each template location with spacings of 0.001° and 0.1 km in epicentral location and depth; S phases were used because of their high amplitudes, and the template window length was set to 4.0 s (1.0 s before and 3.0 s after S arrivals). We detected 31 earthquakes with M_L 0.5–1.9 via pre-set thresholds (i.e., a CC coefficient of 0.3 and 12 times median-absolute-deviation of the daily stacked CC function) and visual inspection. This refined regional earthquake catalog contains 51 earthquakes before 20 March 2019 (which we refer to as the 'AGS group'), of which only five events following ML4 have been reported (Schultz & Wang, 2020; Stern et al., 2013). The updated number of detected events represents a major improvement over those of earlier reports, though the actual number of events with similar magnitudes is likely underestimated due to the lack of near-field stations.

For the subsequent three weeks where nodal data were available, we adopted a modified workflow proposed by M. Zhang et al. (2019) to process the continuous data from the nodal array. The standard short-term average/long-term average (STA/LTA) detection algorithm was first applied to the envelopes of bandpass (5–35 Hz) filtered traces. Among these STA/LTA picks, we picked 964 P arrivals and 1,062 S arrivals from the raw waveforms using a machine-learning phase picker (Zhu & Beroza, 2019). Events were associated and preliminarily located using a grid search-based earthquake association and location method (M. Liu et al., 2020;

M. Zhang et al., 2019). The search space (0.2° in horizontal dimension and down to 20 km depth) is discretized into uniform grids with a constant size of 0.01° × 0.01° × 2 km, and a minimum of 5 P picks and 10 P+S picks is required for each event. To determine more accurate event locations, we utilized the least squares location program VELEST (Kissling et al., 1994) while fixing the velocity model (Table A.1) and rejecting events with a travel time residual >0.6 s. This preliminary aftershock catalog was then improved by the double-difference relocation algorithm hypoDD (Waldhauser & Ellsworth, 2000), yielding 80 detected events from 20 March 2019 to 7 April 2019. The magnitudes of these events were estimated based on a regional coda magnitude (M_d) scale (Rodríguez-Pradilla & Eaton, 2019), where the coda duration was measured in seconds between the P onset and the time when the coda amplitude dropped to 110% of the noise level.

We then applied the M&L to identify weak microseismic events within the nodal array operation period (Figure A.2). The waveforms were downsampled to 25 Hz, and subsequently bandpass filtered between 2 and 8 Hz. We pre-selected 19 template events with $M_d > 0$ and searched for potential earthquakes within cells (0.01° × 0.015° × 0.5 km) with a spatial (i.e., both latitude and longitude) interval of 0.0005° and a depth interval of 0.1 km. In total, we identifed 366 events (including 19 templates) with magnitudes between -1.5 and 1.2 from the nodal data (referred to as the 'nodal group') within 1 km of the injection field.

2.3.3 Focal Mechanism Solutions

Recent studies have shown that induced seismicity in central Alberta is dominated by strike-slip or thrust faulting mechanisms, whereas non-double-couple components have only limited contributions (Eaton et al., 2018; Schultz & Wang, 2020; R. Wang et al., 2018). The double-couple component has been suggested to directly reflect the architecture of the reactivated basement-rooted faults (R. Wang et al., 2017). Here we determined all possible fault-plane solutions based on double-couple components using P, SH, and SV first-motion polarities and amplitude ratios (Snoke, 1984) in a frequency band of 1–10 Hz. For earthquakes prior to the nodal deployment (i.e., the AGS group), the polarities were determined from the rotated (vertical, radial, and transverse) three-component seismograms. The amplitudes were measured at the first peak or trough following the first-motion onset on the integrated traces. For each event, we required at least 10 polarities and 5 amplitude ratios. The maximum differences between observed and calculated S/P amplitude ratios were less than 0.5 after the free-surface correction. We pre-set the maximum numbers allowed for polarity and ratio errors to zero, and the final solution was obtained by a grid search over the focal sphere with an increment of 5°. We rejected solutions for events with $M_L < 1$ in the AGS group due to the poor SNR resulting from the limited azimuthal coverage of regional broadband seismic data. In comparison, the nodal instruments offer far superior azimuthal distribution and signal quality. The focal mechanisms of the events in the nodal group with magnitudes of $M_d > 0.4$ were robustly constrained using the 16 P wave polarity information alone.

2.4 Spatiotemporal Evolution of the Swarm

Including the foreshocks (loosely defined as small earthquakes before ML4) and mainshock (i.e., ML4), we identified 417 earthquakes in total between 4 March and 10 April 2019 (Figure 2.2). The timing of the events ranges from $\sim$9 hours before to 37 days after ML4. The earthquake magnitudes decreased after the shutdown of the HF wells (immediately following ML4), and the occurrence frequencies within both the AGS and nodal groups tapered off during the shut-in phase (Figure 2.2e). Based on the nodal group, we estimated a magnitude of completeness of -0.89 and a b value of the Gutenberg-Richter relation of 1.15 (Figure 2.3). A typical b value of 1 is adopted for seismicity in Alberta (Cui & Atkinson, 2016). Our estimated value is slightly higher than the regional average of 1.02 (Schultz et al., 2015) and the previous reports in the Fox Creek area (0.73–0.90; Schultz et al., 2018) since our catalog is dominated by small-magnitude earthquakes.

The foreshocks and mainshock are located immediately to the east of the wells with an average distance of $\sim$150 m (Figure 2.2b). Their relocated hypocenters appear to follow a north-south trending fault line. The majority of the aftershocks are populated in close proximity to the well pads, all within 2 km of the HF wells.

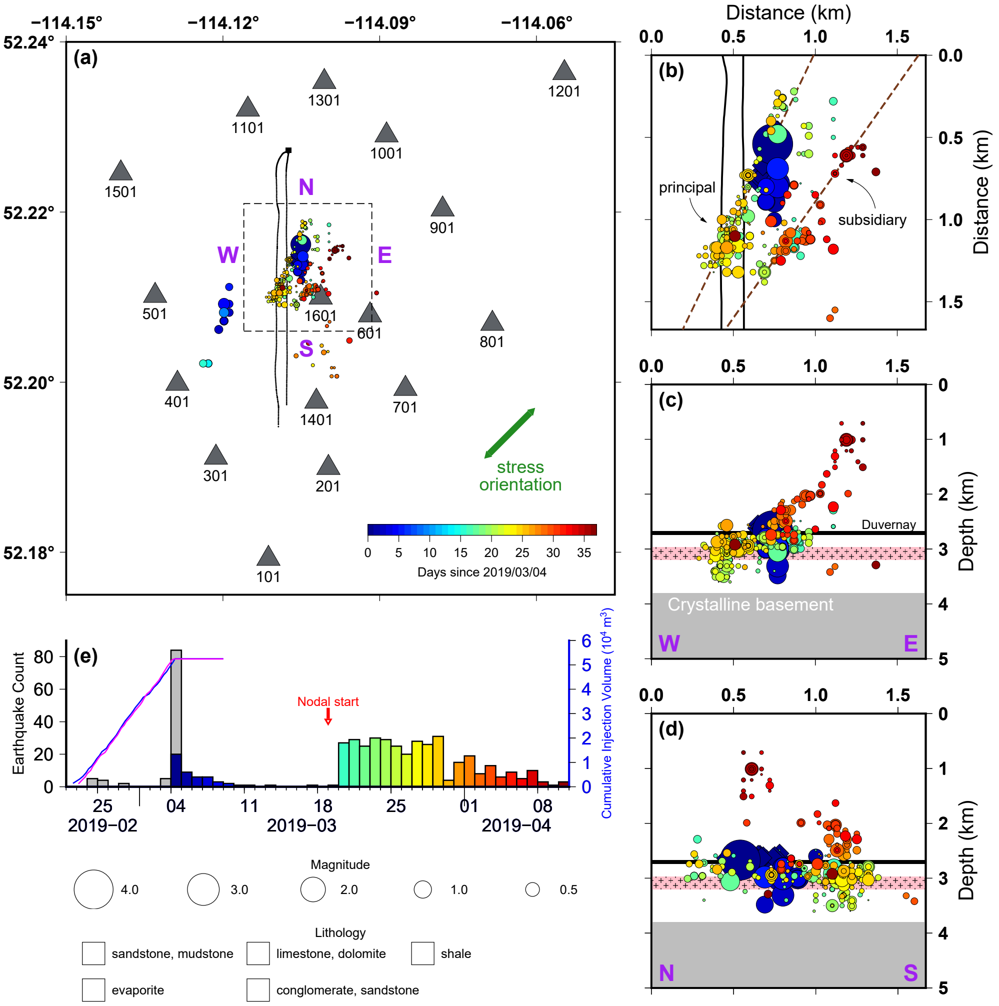

Figure 2.2: (a) Map view of the nodal geophones (gray triangles) and all the relocated earthquakes (diamonds: foreshocks; circles: ML4 and its aftershocks). The two HF wells are shown by the black lines. (b) Zoom-in and (c-d) cross-sectional views of the event distribution within the dashed box in (a). The earthquakes are scaled based on their magnitudes and colored by the day of occurrence. The dashed brown lines show our preferred fault orientations. (e) Daily seismicity rate and HF stimulation at the two wells (blue and magenta curves). The earthquake catalog from Schultz and Wang (2020) is shown in gray.

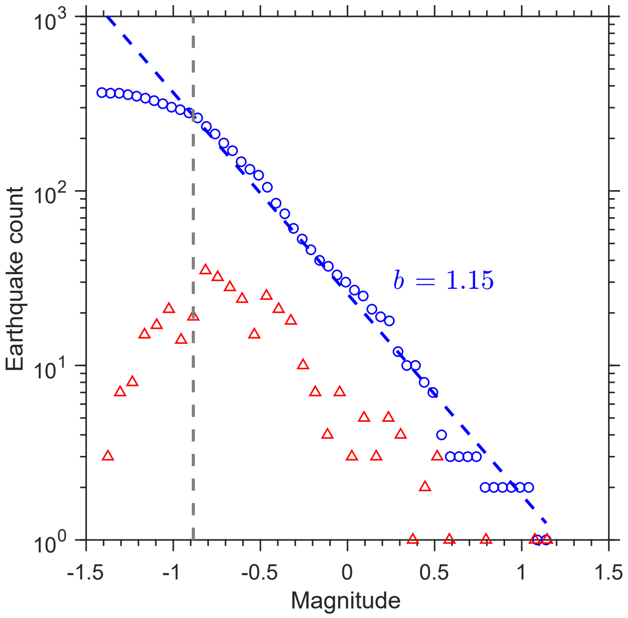

Figure 2.3: Cumulative (blue) and non-cumulative (red) frequency-magnitude distribution of all earthquakes from the nodal group. The magnitude of completeness (shown as the gray vertical dashed line) is calculated using the maximum curvature method (Wiemer & Wyss, 2000), and the b value is estimated using least squares fitting. The blue dashed line represents the best truncated Gutenberg-Richter fit.

Taken together, the spatiotemporal distribution of the earthquake swarm clearly defines a 2-km-long NE trending rupture zone consisting of a principal segment that intersects the well trajectory and a semi-parallel subsidiary strand (Figures 2.2b and 2.6a). The best fit orientations of these two segments are N25°E/89°NW (principal) and N38°E/66°SE (subsidiary). The foreshocks and ML4 are located on the principal segment, and the subsequent aftershocks extended the activity southward along strike. The focal depths of these events mostly fall within the range of 2.5–3.5 km and peak at 2.9 km, consistent with the relocated mainshock depth of 2.7 km (Figure 2.2). After April 2019, earthquakes are mainly located on the subsidiary segment, and most of them occurred at hypocentral depths (less than 2 km; Figure 2.2) shallower than those of other events. It is noteworthy that none of the cataloged events occurred within the basement.

In general, the relocated earthquakes appear to propagate eastward over time. Given that HF treatments would increase the diffusivity near the wells, we estimated the hydraulic diffusivity (D) for the bulk crust near the two HF wells by

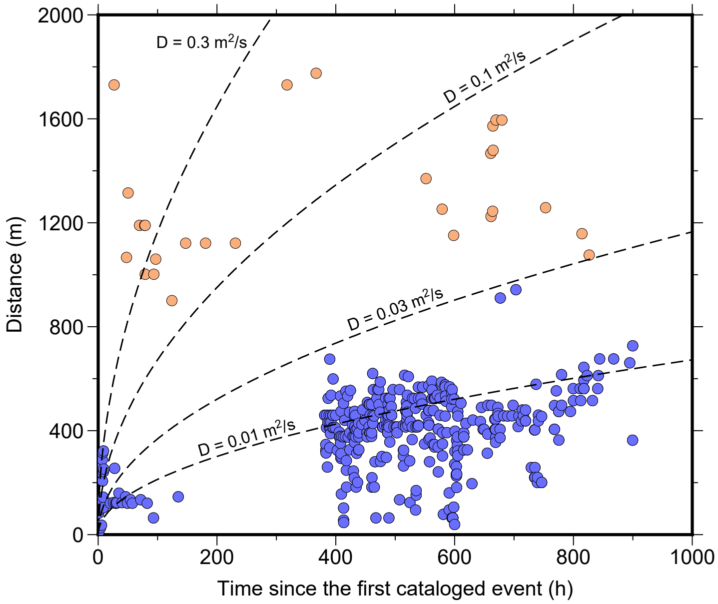

Figure 2.4: The space-time evolution of events relative to the start of seismicity in our relocated catalog. The blue circles are events that occurred within the box area outlined in Figure 2.2a. The orange circles are events that occurred outside the box area. The black dashed curves are pore pressure diffusion curves with different hydraulic diffusivity (*D*) values.

modeling the seismicity migration pattern. Following S. A. Shapiro et al. (1997), the spatiotemporal evolution of the earthquake activity front follows a parabolic rate law

$$r = \sqrt{4\pi D t}, \tag{2.1}$$

where r is the distance of the triggering front from the source, and t is the occurrence time. Here we set the origin time and the hypocenter of the first event in our relocated catalog as $r = 0$ and $t = 0$. A range of diffusivity values between 0.01 m^2/s and 0.3 m^2/s match the migration pattern and the preferred value for events closest to the wells is 0.03 m^2/s (Figure 2.4). The D values are much higher than those estimated for in situ shale formations (10^{-10}–10^{-9} m^2/s; Guglielmi et al., 2015) and are in agreement with the preferred value (0.2 m^2/s) of an HF site in the Montney Basin of western Canada (H. Yu et al., 2019).

Well-constrained hypocenter information enables us to determine the key source parameters (strike, dip, and rake) of a subset of 40 earthquakes (Figure 2.5), which are summarized in Table A.2. The foreshocks show similar source properties, demonstrating N-S right-lateral strike-slip focal mechanisms in the context of the regional stress field. The average strike, dip, and rake values are $183^\circ \pm 3^\circ$, $74^\circ \pm 8^\circ$, $173^\circ \pm 4^\circ$, respectively. In comparison, the mechanisms of ML4 (strike = 12°, dip = 60°, and rake = -165°) and its aftershocks in the next five days (mean strike = $11^\circ \pm 3^\circ$, dip = $76^\circ \pm 7^\circ$, and rake = $-168^\circ \pm 3^\circ$) are generally NNE-SSW right-lateral strike-slip, consistent with an earlier solution from full moment tensor inversion (Schultz & Wang, 2020). The mechanisms of the subsequent events (all from the nodal group) are mainly pure NE-SW strike-slip with average strike, dip, and rake angles of 23°, 78°, and 169°, respectively.

It is worth noting that we identify two aftershock clusters relatively remote from ML4. A cluster of early aftershocks is located west of the wells and follows N-S (slightly toward the east) strike-slip focal mechanisms. The second cluster, which is observed in the northeastern corner of the rupture area with 22 late (approximately one month after shut-in) aftershocks, delineates a steeply dipping (85°NW) fault plane with a similar strike to the subsidiary segment (Figure 2.2b). Compared to the remaining earthquakes, this cluster consistently shows shallow hypocentral depths ($\sim$1 km) and more oblique strike-slip mechanisms (with minor dip-slip components) (Figure 2.5b).

2.5 Discussion

2.5.1 Event Triggering

The deployment of the nodal array has enabled detection of aftershocks of much smaller magnitudes with greatly improved hypocenter locations and source characteristics than previously available, whereas the regional broadband networks were only able to capture most of the $M \geq 2$ earthquakes. Combining these two data sets, we built a high-precision earthquake catalog that contains 19 foreshocks, the mainshock (ML4), and 397 aftershocks. All earthquakes are relocated within 2 km from the HF wells. Except a remote cluster of 22 events, seismic activities mostly occurred close to the target Duvernay Formation (Figures 2.2c and 2.2d). The close spatial proximity to the wells lends compelling evidence that the HF operations

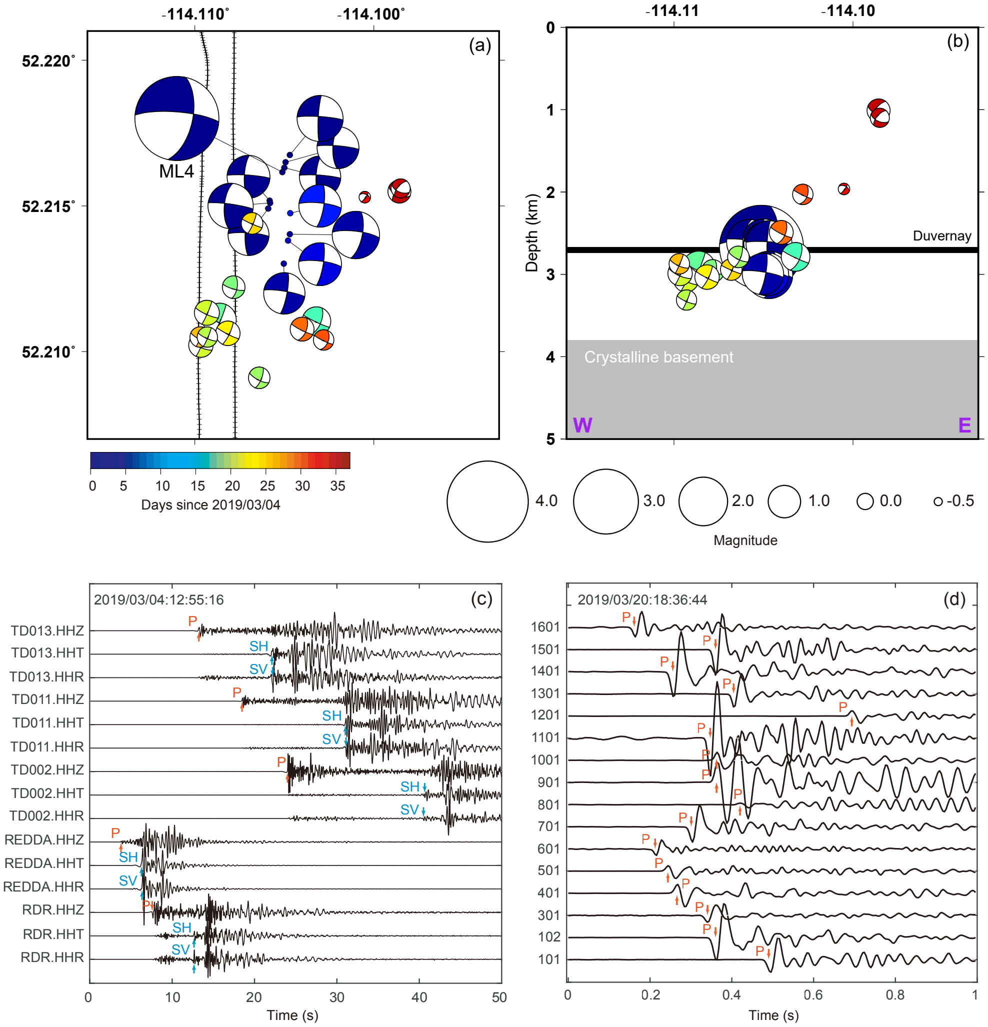

Figure 2.5: (a) Map and (b) cross-sectional views of the resolved double-couple focal mechanisms (scaled by the magnitude and colored by the day of occurrence) of selected earthquakes (Table A.2). (c) The vertical, radial, and transverse components at each broadband station for the focal mechanism solution of ML4. The arrows indicate the polarities of P, SH, and SV waves. (d) The vertical components recorded at each nodal geophone for the focal mechanism determination of a typical event in the nodal group.

were responsible for the recent surge of seismicity near Red Deer. The hypocenter distribution also illuminates a previously unrecognized fault system that spans approximately 2 km along strike (Figure 2.2). We suggest that the occurrences of earthquakes discussed in this study are linked to the reactivation of these preexisting faults by HF since (1) right-lateral strike-slip (wrench) faults in the WCSB are commonly reported (Davies & Smith Jr, 2006; R. Wang et al., 2017) and (2) stimulated microseismicity induced by opening new fractures typically occurs at $M < -2$ (Wolhart et al., 2006).

Three fundamental mechanisms have been proposed for injection-induced seismicity, which include (1) fault slip triggered by increased pore pressure (S. A. Shapiro et al., 1997, 2002), (2) stress alteration through poroelastic stress changes (Segall, 1989; Segall & Lu, 2015), and (3) stress transfer via aseismic creep (Eyre et al., 2019). Event nucleation related to HF in the Red Deer area appears to favor increasing pore pressure as the main trigger of the seismicity since (1) the principal segment of the fault system intersects the HF wells (Figure 2.2b), thus providing a hydraulic connection to the induced events, and (2) seismicity migration patterns follow a fluid diffusion model (Figure 2.4) which suggests that faults act as fluid conduits due to increased pore pressure. The rapid onset of seismicity, which occurred immediately when stage completions reached the seismically delineated fault (Figure 2.2e; Schultz & Wang, 2020), is also consistent with the expected behavior from pore pressure diffusion (Simpson et al., 1988). Alternatively, event-event interaction has been suggested as a potential mechanism for ongoing seismicity after HF completion (Schoenball et al., 2012). We use the Coulomb modeling (Toda et al., 2011), which is a diagnostic tool for earthquake interactions (e.g., Peña Castro et al., 2020; Sumy et al., 2014), to determine whether the coseismic slip of ML4 is partly responsible for the occurrence of aftershocks (see Text A.2). Our results suggest that the aftershock distribution appears unfavorable to the Coulomb stress transfer model (Figure A.3).

The aftershock cluster observed after 7 April 2019 signals remotely triggered fault slip that may be linked to pore pressure diffusion (Figure 2.6a), away from the injection point during the shut-in phase (e.g., Hsieh & Bredehoeft, 1981; Mc-

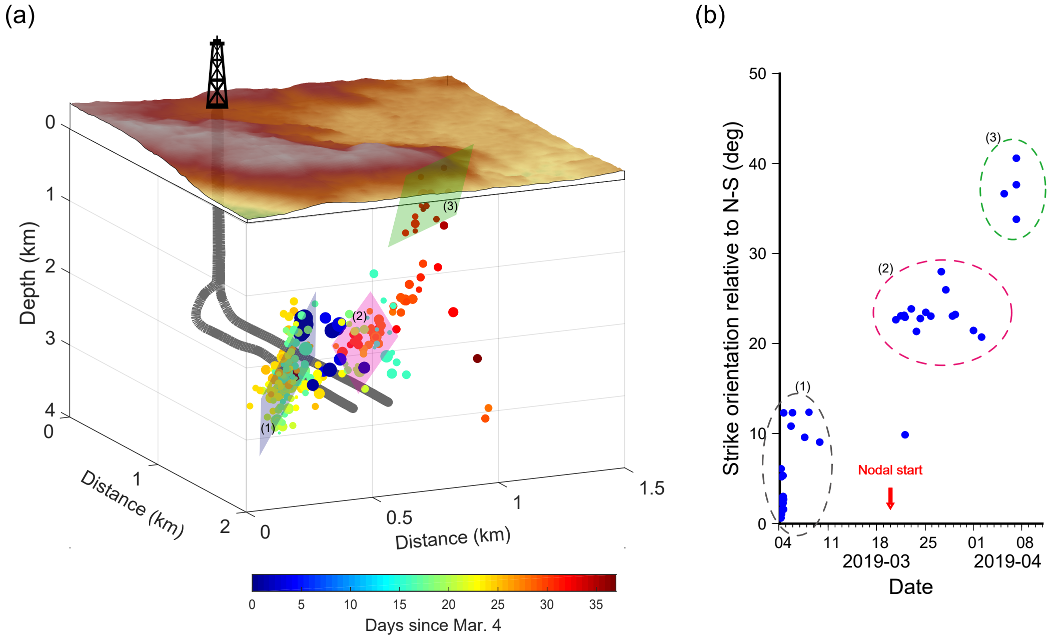

Figure 2.6: (a) A 3-D view of the earthquakes (scaled by the magnitude and colored by the day of occurrence) within the boxed area in Figure 2.2a. The blue, pink, and red shaded areas show the interpreted (1) principal and (2) subsidiary fault planes, and (3) the distant fault that was active one month after ML4, respectively. The two gray lines indicate the two HF well pads. (b) Temporal variations in the strike orientations (relative to the N-S direction) of all 40 earthquakes. The three interpreted fault planes are highlighted by dashed circles.

Clure & Horne, 2011). In other words, delayed fault slip at greater distances can result in post shut-in seismicity. In our case, the delayed focal mechanisms show less favorable fault orientations relative to the direction of S_{Hmax} in central Alberta (Reiter et al., 2014; L. W. Shen et al., 2019). This observation favors a second-order triggering effect that was previously documented near Fox Creek (Schultz et al., 2017). The remote occurrence and diverse orientations are potentially associated with aseismic deformation in the driving process of seismicity (De Barros et al., 2018). Poroelastic redistribution of stresses, either from aseismic slip or the HF operations, may have perturbed the ambient stress field (Martínez-Garzón et al., 2013; Schoenball et al., 2014) and resulted in secondary seismicity.

2.5.2 Geological Implications

From west to east, the dominant focal mechanisms gradually change from N-S and eastward dipping to subvertical N-S to NE trending and westward dipping strike-slip. This spatial variation is consistent with activation within a flower structure that originates from the basement and splays upward (Eaton et al., 2018; R. Wang et al., 2017; H. Zhang et al., 2019). The large hypocentral depth distribution observed in this study implies that the pre-existing faults in untargeted formations are likely reactivated by HF operations. Hence, detailed pre-operational assessment of fault distribution and real-time monitoring of the injection pressure against the regional stress may help mitigate potential hazards.

A key finding of this study is the significant temporal change in strike orientation (Figure 2.6b). The preferred fault orientation is nearly N-S for the foreshocks, whereas the mainshock and aftershocks follow a mean strike of $\sim 20^\circ$ east of the well. This temporal variation is potential evidence for a local change in the stress state following the occurrence of ML4, which cannot be solely explained by ruptures along the same fault. We conjecture that the local stress field was significantly altered by the cessation of injection, similar to the observed reduction in seismic anisotropy after the mainshock near Fox Creek (T. Li et al., 2019). The double- or multi-fault rupture associated with stress changes has been documented in case studies of earthquakes induced by wastewater disposal in Oklahoma (Keranen et al., 2013) and geothermal production in South Korea (K.-H. Kim et al., 2018). In all cases, fluid injection before the mainshock had reactivated pre-existing faults, opening numerous small fractures, but the dissipation of fluid and subsequent closure of the fractures following the mainshock (and the termination of injection) may have a major impact on the state of stress in a relatively short time (e.g., within hours).

Unlike the foreshocks that aligned in the N-S direction, the event locations of the remote cluster were distributed at a 40° angle from the wells. This oblique orientation is parallel to S_{Hmax}. Similar observations have been documented during the HF operations, which are considered to result from the preferential movement of HF stimulation pressures along this axis (T. Li et al., 2019; Schultz & Wang, 2020; H. Zhang et al., 2019). The time sequence of the events from our catalog suggests continued effects of the pre-existing upper-crustal structure on the occurrences of smaller-magnitude induced earthquakes after the initial rupture of ML4. It is worth noting that seismicity persisted even after one month following the shutdown of the wells, showing a maximum magnitude of M_d 0.42 and an average depth of 1 km. This apparent delay necessitates a reconsideration of the duration of shut-in seismicity and trailing-event distribution during the design of operational measures (Atkinson et al., 2020; Schultz, Beroza, et al., 2020; Schultz, Skoumal, et al., 2020). Effective management could benefit from a forecast model of post-injection seismicity (Baisch et al., 2019) and real-time cataloging (Schultz, Beroza, et al., 2020). Our earthquake "chasing" efforts based on near-source recordings highlight the great potential of nodal instruments for (1) unprecedented event detection and monitoring capabilities and (2) improved understanding of the relationship between earthquakes and geological framework in central Alberta.

2.6 Conclusions

This chapter presents a new interpretation of the March 2019 earthquake swarm near Red Deer, Alberta, using continuous data from a near-source nodal array in conjunction with broadband seismic data from regional networks. We constructed a high-precision earthquake catalog that consists of 417 events from 4 March to 10 April 2019. The key conclusions are as follows:

1. All hypocenters are located in close proximity to the HF wells, and the majority of the events occurred at a focal depth of $\sim$3 km at the Duvernay stimulation interval. Aftershocks are more diffuse in space and tend to migrate eastward.
2. The spatiotemporal characteristics of the earthquake swarm suggest the reactivation of two NE striking faults, which could be explained by pore pressure diffusion.
3. The focal mechanisms share similar strike-slip components, and the fault-plane orientations are time-dependent.
4. Shut-in seismicity persisted for over one month, and late aftershocks occurred

along less favorably oriented faults, suggesting a prolonged effect of fault activation.

Finally, the observations shown in this chapter demonstrate that nodal arrays provide a unique opportunity for microseismic event detection and location. Quick-response nodal data after the mainshock could supplement broadband data for improved induced seismicity monitoring and assessment. However, there are significant uncertainties in earthquake location and depth estimation that require further attention. Improved constraints depend on a better understanding of the background geological framework in western Canada, which calls for additional refinements of the background velocity model. Furthermore, the aligned fractures or faults inferred from focal mechanisms can cause seismic anisotropy (Savage, 1999). Chapter 3, therefore, provides a detailed discussion of both isotropic and anisotropic variations of the basement structure from seismic imaging based on several regional arrays.

Chapter 3

Crustal Shear Structure of Southwestern Canada Using Ambient Noise Tomography on Regional Broadband Arrays

3.1 Introduction

Crustal rocks can deform under finite strain caused by a wide range of tectonic processes involving extension, contraction, and shear (e.g., Chapple, 1978; Schulte-Pelkum et al., 2005; Wernicke et al., 1988). Such deformation can be measured directly through laboratory analyses on rock samples (e.g., Godfrey et al., 2000; Johnston & Christensen, 1995) or inferred from seismic anisotropy, a dynamic proxy for deformation that quantifies the direction and polarization dependence of seismic wave speeds (e.g., Courtier et al., 2010; Kaneshima, 1990), at both global (e.g., Dziewonski & Anderson, 1981; Ekström & Dziewonski, 1998) and regional (e.g., Moschetti et al., 2010; N. M. Shapiro et al., 2004) scales. Oriented structures such as large-scale faults or folds (Crampin, 1981, 1984; Kaneshima, 1990) and localized cracks or fractures (Leary et al., 1990), magma emplacement (Bastow et al., 2010) and alignment of crystallographic preferred orientation of anisotropic minerals such as micas (Mainprice & Nicolas, 1989; Meissner et al., 2006) are all capable of producing measurable seismic anisotropy.

Within the continental crust, shear wave anisotropy up to 18% has been reported in western-central Tibet in connection with rock fabrics induced by crustal thinning and channel flow (e.g., Agius & Lebedev, 2014; Guo et al., 2012; N. M. Shapiro et al., 2004). An analog of the Tibetan Plateau is the central Andes, where strong (12–20%) shear wave radial anisotropy is identified at mid-crustal depths through receiver function modeling (Leidig & Zandt, 2003) and inversion of ambient noise data (Lynner et al., 2018). Significant crustal-scale anisotropy belies in many other parts of the world, including the Basin and Range Province of western North America where the amplitudes vary from 2% to 6% (e.g., Moschetti et al., 2010; Xie et al., 2015).

Despite relatively few published studies (Bao et al., 2016; Courtier et al., 2010; Dalton et al., 2011; L. Wu et al., 2019), western Canada offers a natural laboratory for analyzing continental deformation owing to its protracted tectonic history dating back to three billion years ago (Ross et al., 1991). The lithosphere beneath this region has sustained major lithospheric deformation, most notably Paleoproterozoic multi-plate convergence surrounding the Archean Hearne Province and Phanerozoic orogenesis responsible for the Canadian Cordillera (Figure 3.1; Hoffman, 1988; Ross, 2002). Much of the tectonic imprints are currently buried under the thick Phanerozoic sediments in the Western Canada Sedimentary Basin (WCSB) east of the Rocky Mountain Foothills, where direct geological sampling is often untenable. Consequently, the understanding of regional seismic anisotropy relied heavily on occasional reports of shear wave splitting measurements (e.g., Courtier et al., 2010; Currie et al., 2004; L. Wu et al., 2019) and/or frequency-dependent surface waves (e.g., Bao et al., 2016; Yuan & Romanowicz, 2010) from broadband passive seismic data. These studies consistently document a NE-SW fast orientation approximately parallel to the direction of absolute plate motion (see Figure 3.1), suggesting large-scale deformation within a potentially coupled lithosphere-asthenosphere system. At crustal depths, azimuthal anisotropy and the associated stress directions have been inferred from borehole breakouts (Reiter et al., 2014) and time-dependent splitting parameters of direct S waves (T. Li et al., 2019). These crustal and sedimentary observations consistently exhibit a dominant NE-SW trend, approximately aligned with the orientation of the maximum compression axis determined from focal mechanisms of recent induced earthquakes

(R. Wang et al., 2017, 2018). In comparison with the relatively well-constrained azimuthal anisotropy, regional-scale crustal transverse isotropy with a radial symmetry axis (or 'radial anisotropy') is less well-understood with the exception of a 4–5% average amplitude in the middle crust beneath the northern Canadian Cordillera (Dalton & Gaherty, 2013).

This chapter presents a new analysis of radial anisotropy beneath the Cordillera-Craton transition region in western Canada. We focus on the style and strength of radial anisotropy from short-period (8–25 s) ambient seismic noise (e.g., Guo et al., 2012; Moschetti et al., 2010), using more than 10 years of seismic data from five regional networks. Through a joint analysis of fundamental mode Rayleigh and Love wave dispersion measurements, we are able to resolve shear wave velocity and radial anisotropy down to 20 km depth. The key findings offer new clues to the tectonic development of the western margin of the North American craton.

3.2 Tectonic Setting and Previous Geophysical Surveys

Highlighted by strongly deformed crust extending from the orogenic hinterland to the Cordilleran Deformation Front (CDF), our study region comprises mainly of two tectonic units with distinctive ages: the Phanerozoic Canadian Cordillera in the west and Precambrian lithosphere east of the Cordilleran foreland thrust-and-fold belt (Foreland Belt; see Figure 3.1). The former region, which consists of diverse terranes of continental fragments, island arcs and oceanic crust (Monger & Price, 2002), was assembled through multiple collisional and/or accreted events that were initiated at least 200 million years ago (Y. Chen et al., 2019; Dickinson, 2004; Monger & Price, 2002). The latter region, which is largely concealed under the thick sediment sequence of the WCSB, is part of the Canadian Shield that features more than 20 juxtaposed Precambrian crustal domains and over three billion years of tectonic processes involving subduction, continent-continent collision, magmatism, uplift and subsidence at plate boundaries (Hoffman, 1988; Ross et al., 1991). This extensive deformation history is highlighted by the presence of

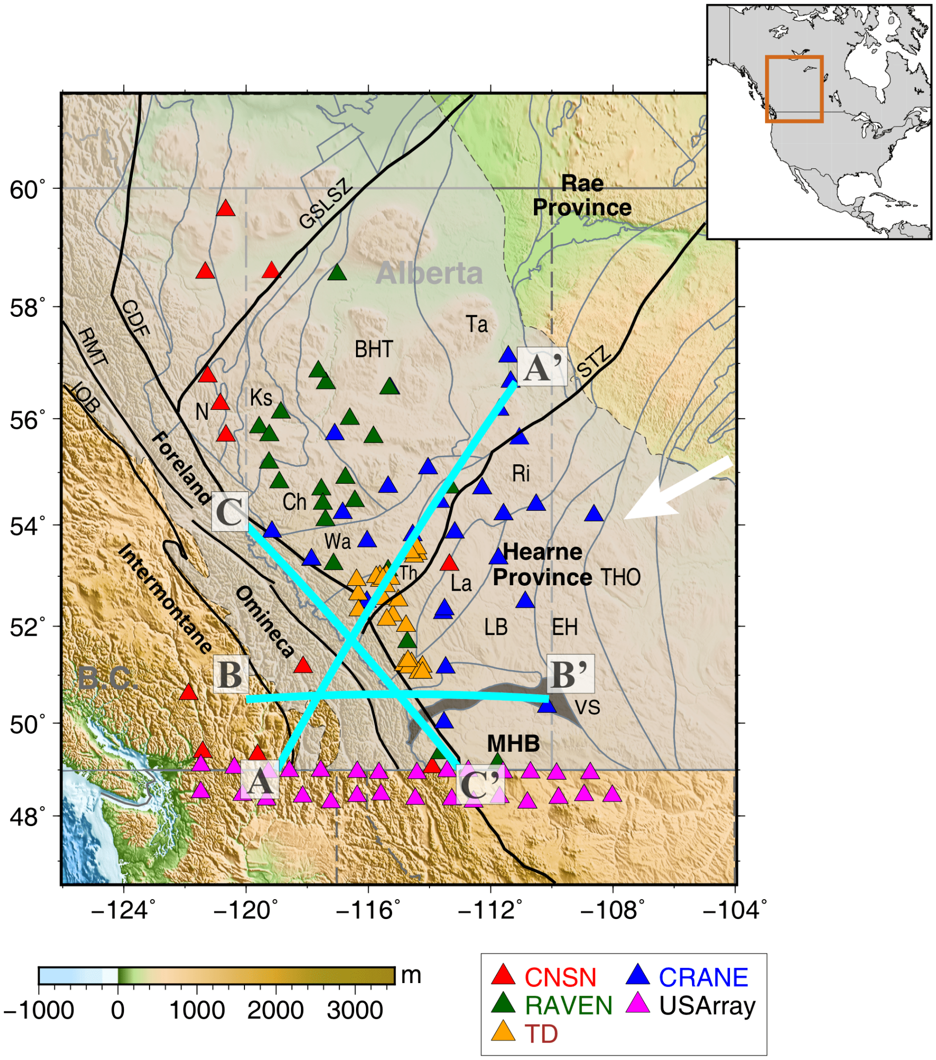

Figure 3.1: Topography of southwestern Canada and the proposed domain boundaries. The background color shows the topography based on ETOPO1 (Amante & Eakins, 2009), and the gray shaded area shows the geographic extent of the WCSB. The purple and blue lines denote the proposed tectonic boundaries within the WCSB (Ross et al., 1991). The crustal domains are labeled with the following abbreviations: BHT, Buffalo Head Terrane; CDF, Cordilleran Deformation Front; Ch, Chinchaga; EH, Eyehill High; GSLSZ: Great Slave Lake Shear Zone; IOB: Intermontane-Omineca Belt Boundary; Ks, Ksituan; La, Lacombe; LB, Loverna Block; MHB, Medicine Hat Block; N, Nova; Ri, Rimbey; RMT, Rocky Mountain Trench; STZ, Snowbird Tectonic Zone; Ta, Taltson; Th, Thorsby; THO, Trans-Hudson Orogen; Wa, Wabamun; VS, Vulcan Structure. The white arrow indicates the current plate motion direction of North America (Gripp & Gordon, 2002). Seismic stations are colored by network, and the three profiles (A-A′, B-B′, and C-C′) are used in Figures 3.4 and 3.8. The brown square in the inset map marks our study region relative to North America.

three proposed tectonic discontinuities known as the Great Slave Lake Shear Zone (GSLSZ), Snowbird Tectonic Zone (STZ), and Vulcan Structure (Figure 3.1), respectively, from north to south. We refer the reader to a more detailed review of the regional tectonics (Y. Chen et al., 2018; Gu et al., 2018).

Existing geophysical studies of the basement structure of the WCSB and surrounding regions have primarily focused on isotropic velocity structures at variable depths and lateral scales. Based largely on potential field observations, Ross et al. (1991, 1993) published the first basement domain boundary map of the WCSB. A subsequent study reinforces these domain definitions through accurate age constraints from geochronological analyses (Villeneuve et al., 1993). The main outcomes of these seminal studies have been supported, and continuously refined, by the active-source component of the LITHOPROBE project (e.g., Clowes et al., 2002; Cook, 1995; Ross, 2000), which largely shaped our current understanding of the basement structure and evolution in western Canada. In parallel, passive broadband seismic analyses from two permanent Canadian National Seismograph Network stations (EDM and WALA) reveal complex receiver-side crustal structures based on P-to-S converted phases (Cassidy, 1995; Eaton & Cassidy, 1996), which provide further evidence for plate convergence along the STZ during the Proterozoic Eon. Much of these findings were corroborated by earlier seismic images of the lithospheric structure from temporary arrays deployed in the WCSB, highlighting a first-order contrast between the Cordillera and the craton (Dalton et al., 2011) and the presence of the deep cratonic roots beneath the Archean crustal domains (Shragge et al., 2002).

During the past 10 years, increased availability of broadband seismic data has enabled a new appraisal of the tectonic history beneath the Cordillera-Craton boundary region. Regional receiver functions presented evidence for a mid-crustal low-velocity zone (LVZ) in central Alberta in connection with Paleoproterozoic plate convergence and syn-/post-collisional partial melting (Y. Chen et al., 2015). This finding is supported by the below-average shear velocities from seismic interferometry (Gu & Shen, 2015). At mantle depths, body wave tomography reveals sharp velocity gradients from stable Precambrian cratons to the tectonically active

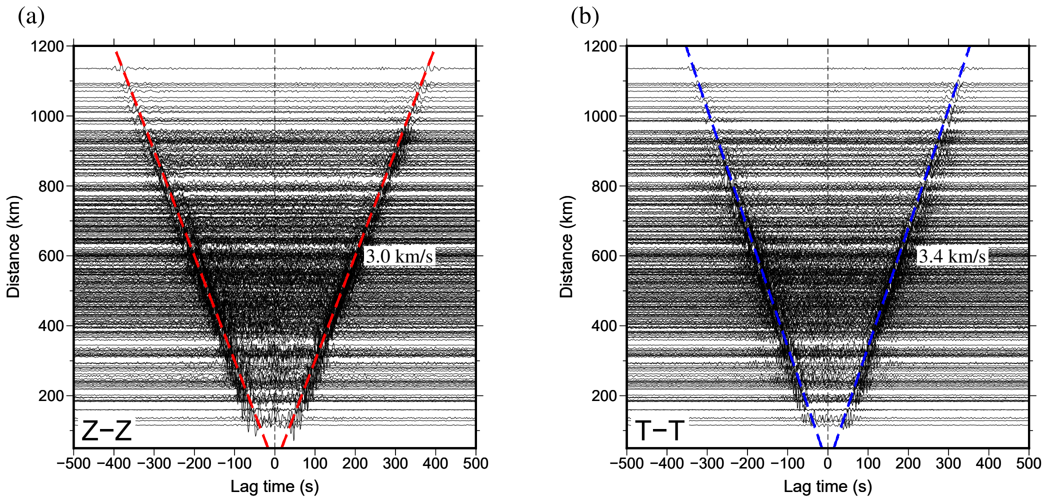

Figure 3.2: Record sections of (a) vertical (Z–Z) and (b) transverse (T–T) component empirical Green's functions between USArray and CRANE stations. The original seismic traces are filtered between the periods of 5 and 150 s. The red and blue dashed lines indicate the respective moveout velocities of 3.0 km/s for the Z-Z component Rayleigh waves and 3.4 km/s for the T-T component Love waves.

Canadian Cordillera (Bao et al., 2014; Bao & Eaton, 2015; Y. Chen et al., 2017, 2018, 2019; Gu & Shen, 2015). These recent findings are generally corroborated by the existing regional geological observations (e.g., Chacko et al., 2000; De et al., 2000; Villeneuve et al., 1993) and geophysical constraints from magnetotellurics (Boerner et al., 1995, 1999, 2000; Nieuwenhuis et al., 2014; Rippe et al., 2013), potential field (Y. Chen et al., 2018; Elissa Lynn et al., 2005; Hope & Eaton, 2002; Lemieux et al., 2000; Pilkington et al., 2000), and heat flow (Bachu, 1993; Majorowicz, 2018; Majorowicz & Grasby, 2010; Majorowicz et al., 2014).

3.3 Data and Methods

3.3.1 Ambient Seismic Noise and Data Processing

In this study, we utilize continuous recordings from 118 broadband seismic stations (Figure 3.1), including 12 stations from the Canadian National Seismograph Network (CNSN; 2006–2008 and 2015–2017), 28 stations from the CRANE network (since September 2006; Gu et al., 2011), 22 stations from the RAVEN network (since November 2013; Schultz & Stern, 2015), and 27 stations from the TD network (since August 2014). To better constrain the structure beneath the southern WCSB, we also incorporate 29 stations from the Transportable Array of USArray operated from 2006 to 2009. The station coverage is particularly dense in the southern Canadian Cordillera and southwestern WCSB (Figure 3.1).

It has been both analytically and experimentally demonstrated that the Green's function between two receivers can be retrieved by cross-correlating the diffuse wavefields embedded within ambient seismic noise (e.g., Lin et al., 2008; Sabra et al., 2005; N. M. Shapiro & Campillo, 2004; Snieder, 2004). In this study we follow the proposed workflows of Bensen et al. (2007) and Lin et al. (2008) to extract Rayleigh and Love wave empirical Green's functions for all available station pairs. After dividing three-component (north, east, and vertical) seismograms into 24-hour-long intervals, we remove the means, trends, and instrument responses from the recorded waveforms. We then (1) apply a fourth-order bandpass Butterworth filter with corner periods at 5 and 150 s, (2) minimize the effects of instrumental irregularities and earthquake/non-ambient signals via running-absolute-mean normalization (Bensen et al., 2007; Goutorbe et al., 2015), and (3) perform spectral whitening to broaden the noise band. Finally, stations with arbitrary horizontal channels (XX1 and XX2) are adjusted based on the station metadata to obtain the north and east components.

To obtain reliable Love wave signals from the processed data, we correct the horizontal misorientations of five CRANE stations by aligning the north component with the geographical north through a rotation angle measured by the polarization of Rayleigh waves (Stachnik et al., 2012). Instead of directly rotating the horizontal components (N and E) to the great circle coordinate system (R and T), we first calculate cross-component (E-E, E-N, N-N, and N-E) noise cross-correlation functions. These four horizontal component cross correlations are then rotated to produce transverse-transverse correlograms based on interstation azimuth and back azimuth (Lin et al., 2008). Finally, all available daily cross-correlation functions for a given station pair are stacked for noise suppression. The resulting $\sim$4,000 vertical-vertical (Z-Z) and transverse-transverse (T-T) cross-correlation stacks (see Figure 3.2 for all USArray-CRANE station pairs) are dominated by the fundamental mode

Rayleigh and Love waves, respectively. Coherent surface waves arrive at both positive (causal) and negative (anticausal) lag times, and a linear trend can be clearly identified on both record sections. Love waves on the T-T component show a significantly higher moveout velocity (3.4 km/s) than the vertical-component Rayleigh waves (3.0 km/s) (Figure 3.2).

3.3.2 Dispersion Measurements and Tomographic Inversion

We adopt the frequency-time analysis with a phase-matched filter (Levshin & Ritzwoller, 2001) to measure Rayleigh and Love wave group velocity dispersion curves between 8 and 25 s from the cross-correlation stacks. To assess data robustness, we define the SNR as the fraction of the maximum absolute amplitude within the signal window (defined by surface wave arrivals between 2.5 and 5.0 km/s) to the standard deviation of a 500-s-long trailing noise window, starting 500 s after the signal window (Goutorbe et al., 2015). Dispersion measurements from station pairs with an interstation distance greater than three wavelengths (Bensen et al., 2007) and an SNR greater than 15 are retained; a lower SNR is accepted only if the dispersion measurements exhibit minimal seasonal variability (Goutorbe et al., 2015; Yang et al., 2007), which is defined as the standard deviation of dispersion curves from three-month segments of the data (e.g., January-March, February-April, etc.). A reasonable level of variation is reached if the measurement error is less than 0.1 km/s. Based on the above selection criteria, we retain approximately 3,100 high-quality dispersion curves for the subsequent velocity inversion, which accounts for 77% of the raw measurements.

It is worth noting that the equipartitioning of seismic wavefield is a prerequisite for precise extraction of empirical Green's functions by correlations (e.g., Sánchez-Sesma & Campillo, 2006). Biased spatial distribution of ambient noise, which is often evidenced by asymmetric correlation peaks relative to the zero lag, may introduce travel time biases into the surface waves and thereby contaminate the dispersion measurements. To ensure the quality of the dispersion data, we examine the variation of high-quality Rayleigh and Love waves as a function of azimuth in the frequency bands of 7–10 s, 10–15 s, and 15–20 s (Figure B.1) by calculating the percentage of raypaths with SNR > 10 in a 20° azimuthal bin (Bensen et al., 2008). The results show well-distributed surface wave energy with fractions greater than 0.8 and 0.7 for Rayleigh and Love waves, respectively (Figure B.1). This observation, in conjunction with symmetric waveform characteristics, suggests relatively minor effects of noise directionality on our surface wave travel times.

In the subsequent step, we calculate Rayleigh and Love group velocity maps at 10 periods between 8 and 25 s on a $0.5^\circ \times 0.5^\circ$ grid following the ray-theoretical tomographic algorithm of Barmin et al. (2001). Surface waves are treated as rays propagating between two stations, and hence the relationship between the data and model parameters can be expressed via a linear equation

$$\mathbf{d} = \mathbf{G}\mathbf{m}, \tag{3.1}$$

where $\mathbf{d}$ is the data vector of measured travel time perturbations at a given period, and $\mathbf{G}$ is the kernel matrix defined as the integration of slowness along the path. The model vector $\mathbf{m}$ contains velocity perturbations of each grid, which are estimated by minimizing the following cost function

$$J(\mathbf{m}) = (\mathbf{G}\mathbf{m} - \mathbf{d})^T \mathbf{C}^{-1} (\mathbf{G}\mathbf{m} - \mathbf{d}) + \alpha^2 \|\mathbf{F}\mathbf{m}\|_2^2 + \beta^2 \|\mathbf{H}\mathbf{m}\|_2^2. \tag{3.2}$$

The first term of $J(\mathbf{m})$ represents the data misfit ($\mathbf{C}$ is the covariance matrix of the observed travel time errors). This tomographic inversion is further subjected to spatial Gaussian smoothness (α) and path-density (β) constraints to ensure a robust model outcome. The spatial smoothing condition $\mathbf{F}$ is defined as

$$F_{ij} = \begin{cases} 1, & i = j, \\ \dfrac{-S(\mathbf{r}_i, \mathbf{r}_j)}{\sum_j S(\mathbf{r}_i, \mathbf{r}_j)}, & i \neq j, \end{cases} \tag{3.3}$$

where S is the smoothing kernel

$$S(\mathbf{r}_i, \mathbf{r}_j) = \exp\left(-\frac{\|\mathbf{r}_i - \mathbf{r}_j\|_2^2}{2\gamma^2}\right), \tag{3.4}$$

$\mathbf{r}_i$ is the location of the i-th grid node, and γ is the correlation length. The weighting function $\mathbf{H}$ penalizes the weighted model norm

$$H_{ij} = \exp\left[-\lambda \rho_c(\mathbf{r}_j)\right] \delta_{ij}, \tag{3.5}$$

where λ is a user-defined constant, ρ_c is the number of paths intersecting the cell centered on the j-th node, and δ_{ij} is the Kronecker delta function. The least squares solution $\mathbf{m}_{\mathrm{LS}}$ that minimizes the objective function $J(\mathbf{m})$ is given by

$$\mathbf{m}_{\mathrm{LS}} = (\mathbf{G}^T\mathbf{C}^{-1}\mathbf{G} + \alpha^2\mathbf{F}^T\mathbf{F} + \beta^2\mathbf{H}^T\mathbf{H})^{-1}\mathbf{G}^T\mathbf{C}^{-1}\mathbf{d}. \tag{3.6}$$

To determine the optimal damping factor α that controls the strength of spatial smoothing, we generate the trade-off curves (Figure B.2) for Love wave group velocities at each period with α ranging from 30 to 350 at a constant increment of 5. The optimal value is determined by a compromise between data variance reduction (VR; Gu & Shen, 2015) and model L^2 norm. We fix the strength of path density damping β to 200 and the weighting factor λ to 0.3 after carefully investigating their dependences on the regional geology while minimizing inversion artifacts. The spatial smoothing width γ is set to 150 km, which is empirically determined from the average spacing of regional stations. After Love group speed maps are obtained, a series of checkerboard tests are performed on Rayleigh group data using the same α range (30 to 350). The optimal α during Rayleigh group velocity inversions at each period are determined by minimizing the differences in the checkerboard recovery amplitudes of velocity perturbations between the recovered Rayleigh and Love wave models (see Section 3.5.1 for a detailed description of the checkerboard test). This approach ensures comparable amplitudes between the inverted Rayleigh and Love wave group velocities, which is critical for mitigating potential biases in the radial anisotropy due to differences in their relative perturbations (see Section 3.3.3).

Following Barmin et al. (2001), we apply a two-step process in the group velocity inversions: (1) create an overdamped map (α = 1000) that rejects the outliers with travel time residuals greater than two standard deviations, and (2) invert the remaining measurements to produce the final group velocity maps using the optimal regularization parameters.

3.3.3 Inversion for Shear Velocity and Radial Anisotropy

During the final step, Rayleigh and Love waves at 8–25 s are inverted and assembled to obtain a 3-D shear velocity model. For a radially anisotropic medium, the material properties are often described by density ρ and five elastic parameters: the velocities of horizontally and vertically polarized P and S waves V_{PH}, V_{SH}, V_{PV}, V_{SV}, and the ellipticity η which is related to velocities at intermediate incidence angles (Dziewonski & Anderson, 1981; Takeuchi & Saito, 1972). Because surface waves are primarily sensitive to shear velocities whereas their sensitivities to η and ρ are significantly smaller (Dalton et al., 2011), we assume that (1) variations in the latter two parameters are minimal, and (2) Rayleigh and Love waves are exclusively sensitive to V_{SV} and V_{SH}, respectively. During the iterative inversions, we update the P wave velocities by scaling their S wave counterparts using a fixed V_P/V_S ratio of 1.82, while density is scaled from P velocities using the Nafe-Drake relation (Brocher, 2005; Ludwig et al., 1970).

In the ensuing step, we extract dispersion curves at 896 equally spaced nodes along the geographical coordinates from the group velocity maps. A 20-point cubic spline interpolation is applied to regularize the dispersion measurements. The group velocities of Rayleigh and Love waves are then inverted independently for the respective V_{SV} and V_{SH} profiles at each node. The best-fitting 1-D shear velocity structure at each grid point is obtained using an iterative linearized inversion algorithm *surf96* from the Computer Programs in Seismology (Herrmann, 2013). We start with a 1-D crust/upper mantle model consisting of 17 layers down to 65 km depth over a half-space. The upper crust (first 10 km) of the initial model is modified from the published model of Welford and Clowes (2006) based on an earlier controlled source experiment. The lower crustal velocities are obtained by a recent regional receiver function analysis (Y. Chen et al., 2015), and the Preliminary Reference Earth Model (PREM; Dziewonski & Anderson, 1981) is used to account for the mantle velocities and crust/mantle attenuation. We apply vertical smoothing (Herrmann, 2013) and vary the weights of different crustal layers. The choice of the depth-weighting parameters is based on group velocity sensitivity, which decreases with depth, especially for Love waves; this depth-weighting scheme aims to ensure comparable depth sensitivities of Rayleigh and Love wave data to shear velocity. We then perturb the shear velocity over 12 iterations at each node and construct the final 3-D V_{SV} and V_{SH} models by integrating 1-D depth-dependent velocity profiles from all 896 nodes; we mainly concentrate on the upper 20 km due to reduced data sensitivities at greater depths.

Once these independent velocities are retrieved, we construct an isotropic V_S model by calculating the Voigt average (Ekström & Dziewonski, 1998)

$$\delta V_S = \frac{2}{3}\delta V_{SV} + \frac{1}{3}\delta V_{SH}, \tag{3.7}$$

where δV_{SH} and δV_{SV} are the lateral variations relative to the regional average V_{SH}^0 and V_{SV}^0, respectively. We follow Gu et al. (2005) [see also Dalton et al. (2011) and Kustowski et al. (2008)] and express radial anisotropy (ξ) as the difference between perturbations of SH and SV speeds,

$$\xi = \delta V_{SH} - \delta V_{SV}. \tag{3.8}$$

This parameterization offers a sensitive measure of crustal and mantle anisotropy with respect to the vertical symmetry axis.

3.4 Results

3.4.1 Group Velocity Maps

Rayleigh and Love wave group velocity maps between 8 and 25 s are well correlated, both showing strong spatial correlations with the sedimentary strata and the underlying basement domains (Figure 3.3). Most of the foreland basin is characterized by low-velocity anomalies surrounded by the high-velocity Rocky Mountains in the southwest and the Precambrian cratons in the northeast. The most notable features are (1) a sharp Cordillera-Craton velocity transition near the CDF in both Rayleigh and Love wave maps, and (2) a NW-SE oriented high (~5%) velocity corridor between the Foreland Belt and the Alberta Basin in Rayleigh wave group velocities. Similar to the basement depth profile from CRUST1.0 (Laske et al., 2013), cross-sections of Rayleigh and Love group speeds over the largest topographic variations in this region (Figure 3.4; profile A-A′) both show minimum

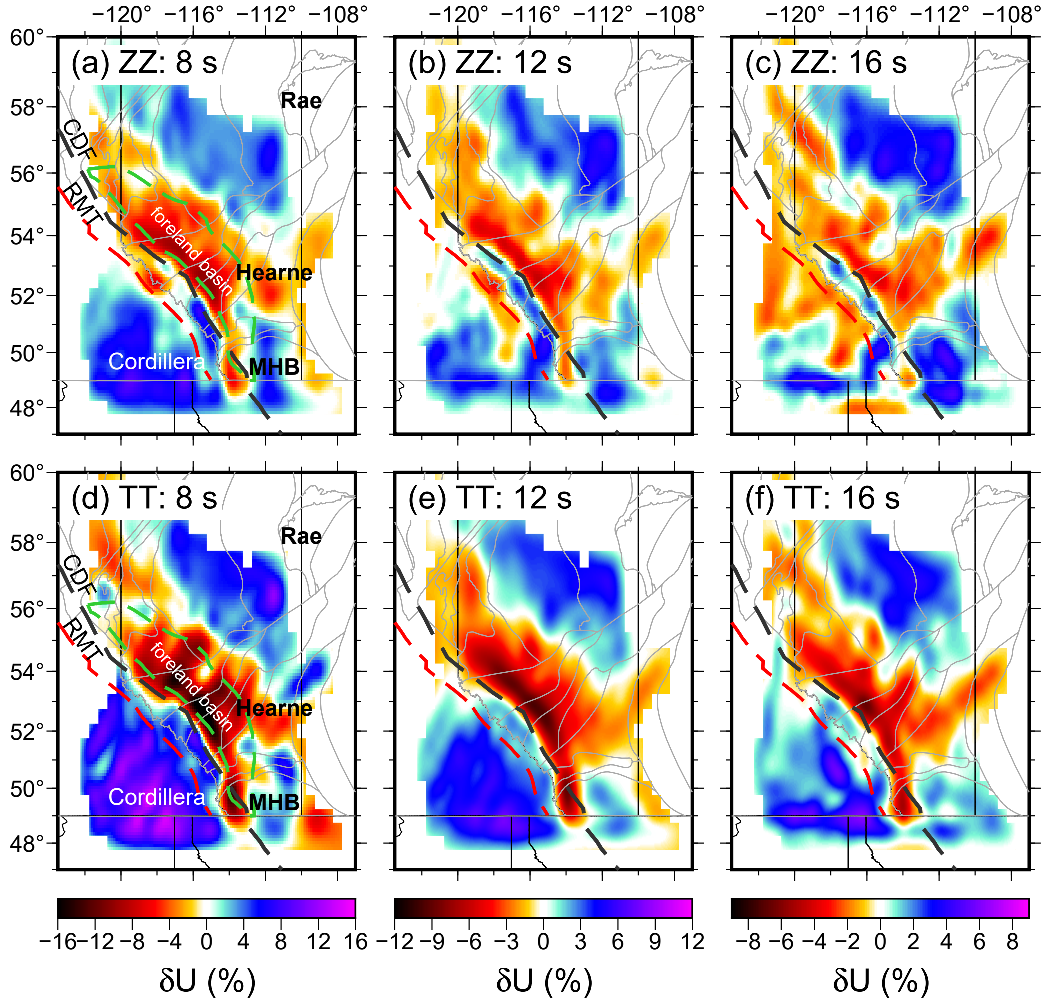

Figure 3.3: Group velocity maps inverted from (a-c) Z-Z and (d-f) T-T component noise cross correlations at 8 s (left column), 12 s (middle column), and 16 s (right column) periods. Group speeds (U) are plotted as perturbations relative to the regional mean values ($\overline{U}$): $\delta U = (U - \overline{U})/\overline{U}$. The dashed black and red lines indicates the Cordilleran Deformation Front (CDF) and Rocky Mountain Trench (RMT), respectively. The dashed green polygons in (a) and (d) delineate the depocenter of the Alberta Basin.

velocities in the Rocky Mountain Foothills. The Rayleigh wave velocity decreases southwestward to a minimum near the basin depocenter but sharply increases by $\sim$12% at the CDF. In comparison, Love waves exhibit more pronounced velocity changes across the CDF, showing a $\sim$30% increase in amplitude. With an average correlation coefficient above 0.9, the Love wave profile shows greater affinity to the basement depth at different periods than the Rayleigh waves. Strong focusing effects from loose sedimentary layers on the short-period Love waves, a key contributor to the enhanced spatial correlation, are especially significant along the CDF (see Figure 3.4).

To estimate group speed uncertainties, we apply a bootstrap resampling method (Efron & Tibshirani, 1991) by repeating the tomographic inversion 50 times using random subsets that retain 95% of the original group velocity measurements. The errors at each grid point are reflected by the standard deviation of the bootstrapped data sets: both Rayleigh and Love group velocities are well constrained at most periods, showing average uncertainties less than 0.02 km/s across the map area (Figure 3.5). Relatively large uncertainties are observed at 8 s, where Love group speed uncertainties are higher than those of Rayleigh waves in the mountainous regions. The large uncertainty of Love waves likely results from lower data quality, reduced number of raypaths, or the presence of large (up to 2.6%) azimuthal anisotropy at 8 s (as discussed in Text B.1).

3.4.2 Shear Velocity Models

Maps of the shear wave velocity structure in the upper ($\sim$8 km) and middle crust ($\sim$17 km) are shown in Figure 3.6. Generally, crustal shear velocities range from 3.4 km/s to 4.0 km/s, which are consistent with the shear velocity estimates from inversions of receiver function data (Y. Chen et al., 2015). Both V_{SV} and V_{SH} models reveal similar velocity variations across the study region: in the shallow crust, predominantly low shear velocities (up to -6%) are present in the two models beneath the foreland basin with extensive sediment deposition, whereas the velocity variations reverse sign in the upper crust and reach a maximum amplitude of 4% beneath the southeastern Canadian Cordillera and the Proterozoic terranes in north-

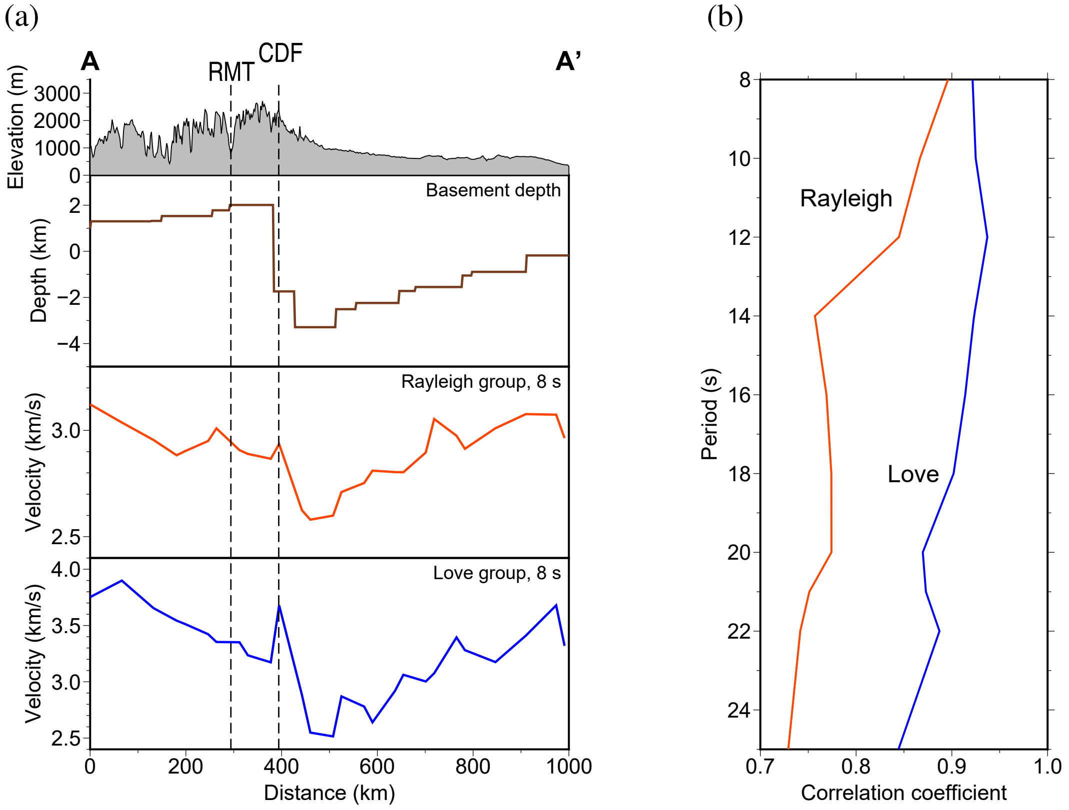

Figure 3.4: (a) Rayleigh and Love group velocities at 8 s and the basement depth along profile A-A′ (see Figure 3.1 for the profile location). The surface topography is shaded in gray in the top panel. (b) Correlation between the basement depth and the group velocities along profile A-A′. Love and Rayleigh profiles are indicated by red and blue colors, respectively.

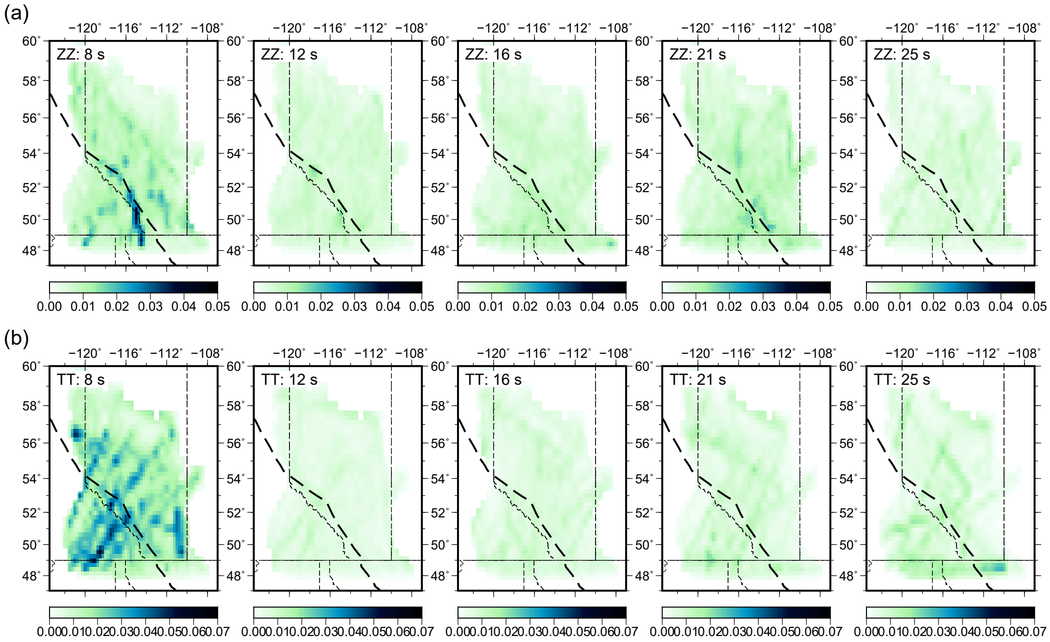

Figure 3.5: Rayleigh (a) and Love (b) group speed uncertainties at periods of 8 s, 12 s, 16 s, 21 s, and 25 s estimated from a bootstrap resampling algorithm. The uncertainties are defined as the standard deviations of 50 bootstrap runs with 5% paths removed at each period.

ern Alberta. The crustal signatures associated with sedimentary layers extend down to mid-crustal depths and diminish at $\sim$12 km. In the Canadian Cordillera, the V_{SH} model shows much higher velocities than its V_{SV} counterpart (especially along the US-Canada border). On the other hand, up to 5% higher SV speeds are observed in a narrow corridor along the Foreland Belt. This anomaly is closely aligned with the CDF and RMT, highlighted by a steep velocity gradient in the Cordillera-Craton transition region.

East of the Rockies, the Archean crust within the Medicine Hat Block (MHB) is characterized by faster-than-average SV and SH velocities. Similar high-velocity patterns are observed beneath most of the Proterozoic terranes in northern Alberta. In general, high-velocities cover most of the Precambrian basement of the WCSB, whereas the young Cordilleran orogenic belt is underlain by relatively low shear velocities (generally $< -3\%$) at similar depths. Both models, particularly V_{SH}, exhibit a linear northeast-trending wedge with a moderate amplitude of -3% velocity variation at 8 km depth. This LVZ is spatially confined in the Loverna Block and

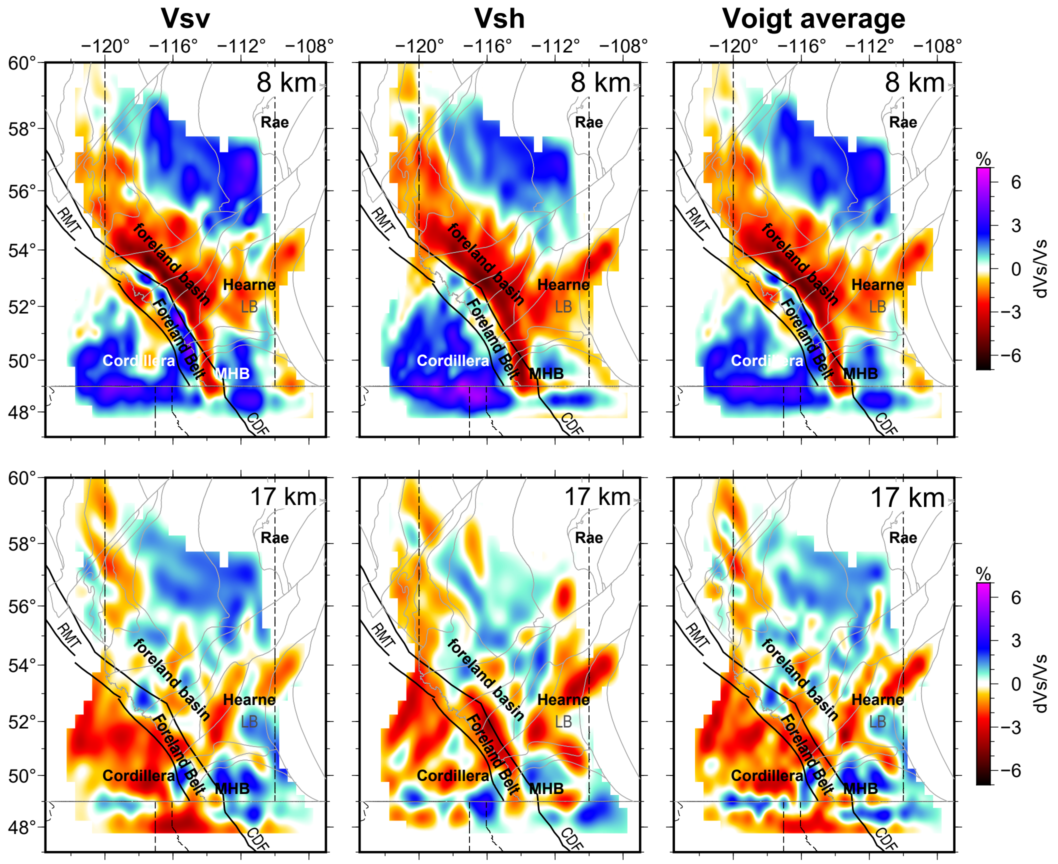

Figure 3.6: The shear velocities determined at 8 km and 17 km depths, plotted as perturbations to the regional average for V_{SV} (left), V_{SH} (middle), and the Voigt-averaged V_S models (right). Key crustal domain are labeled, and their abbreviations are defined in Figure 3.1.

continues to the middle crust. At a depth of 17 km, however, both models show more lateral heterogeneities and less spatial connections with the reported crustal domains (Ross et al., 1991, 1993).

3.4.3 Radial Anisotropy

The striking differences between V_{SH} and V_{SV} in the vast areas west of the CDF offer compelling evidence for radial anisotropy. Radial anisotropy (ξ; see Section 3.3.3 for definition) at the depths of 5, 12, and 17 km (Figure 3.7) is positive ($\xi > 0$; up to 8%) throughout the Omineca Belt and the southernmost WCSB, showing a notable southward migration with increasing depth. In contrast, we observe vertically continuous, negative ($\xi < 0$) anisotropy in the neighboring Foreland Belt in the latitude range of 49–53°, which largely reflects anomalously high V_{SV} at this location, and the boundary between positive and negative anisotropy coincides spatially with the Rocky Mountain Trench (RMT; Figures 3.7b and 3.7c). East of the CDF, the upper crust beneath the sedimentary basin (i.e., in the upper 5 km; Figure 3.7a) shows moderately negative anisotropy. Starting from 12 km depth, the anisotropic anomaly within the bedrocks of the Archean Loverna Block is separated into two distinct clusters (Figure 3.7b), directly north of a -4% anomaly within the cratonic core of the Archean-aged MHB (Figures 3.7b and 3.7c).

Cross-sections of our model further confirm the main observations of radial anisotropy. Along an E-W trending profile B-B′ across the hinterland of the orogenic belts and the MHB (Figure 3.8a), the isotropic velocities are consistent with those from a similar cross-section obtained by Gu and Shen (2015), showing eastward increasing velocities across the CDF. Within the Foreland Belt, however, V_{SH} is much slower than V_{SV} at the corresponding depths (0–20 km) (Figure 3.6). This results in a significant westward dipping anomaly of negative anisotropy at upper crustal depths. Farther west, the Omineca Belt exhibits moderately positive ξ, though the strength decreases with depth and eventually terminates at $\sim$18 km. To the east of the CDF, negative values of ξ dominate the Vulcan Structure, where the largest amplitude is concentrated at shallower (above 10 km) depths. Further evidence of widespread negative ξ is provided by transect C-C′ (Figure 3.8b), a NW-SE trending profile along the Foreland Belt where the observed anomaly spans over 400 km longitudinally.

To assess the robustness of our anisotropic model, we develop an isotropic velocity model by inverting Rayleigh and Love dispersion curves simultaneously. The fit of the predicted dispersion curves to the observations is quantified by the VR as

$$\mathrm{VR} = \left\{ \frac{1}{2}\left[1 - \frac{\sum_{i=1}^{N}(U_{\mathrm{obs}}^{R} - U_{\mathrm{pred}}^{R})^2}{\sum_{i=1}^{N}(U_{\mathrm{obs}}^{R})^2}\right] + \frac{1}{2}\left[1 - \frac{\sum_{i=1}^{N}(U_{\mathrm{obs}}^{L} - U_{\mathrm{pred}}^{L})^2}{\sum_{i=1}^{N}(U_{\mathrm{obs}}^{L})^2}\right]\right\} \times 100\%, \tag{3.9}$$

where N is the number of discrete periods for Rayleigh (“R”) and Love (“L”) dispersion curves, and U_{obs} and U_{pred} are the observed and predicted data, respec-

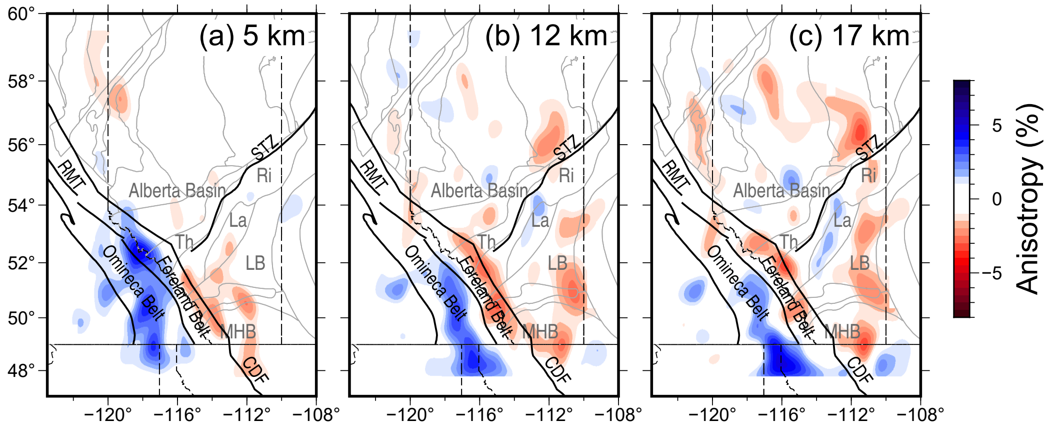

Figure 3.7: Models of radial anisotropy (ξ) at (a) 5 km, (b) 12 km, and (c) 17 km depth. The maps are smoothed using a Gaussian smoothing function with a radius of 2°. Key crustal domain are labeled with their abbreviations defined in Figure 3.1.

tively. The VR of the isotropic model and our preferred (i.e., radially anisotropic) model is presented in Figure 3.9. The foreland basin (to the east of the CDF) remains high VR regardless of whether the model is obtained with/without introducing anisotropy. However, large data misfit in the Canadian Cordillera, the Foreland Belt and Omineca Belt in particular, underscores the limitation of the isotropic V_S model with density and two elastic constants (i.e., bulk and shear moduli) involved in the inversion. This drawback is largely overcome by independent inversions of Rayleigh and Love wave data, which allow for radial anisotropy and utilize twice the number of model parameters than the isotropic model. The VR is increased by over 20% within the orogenic belts and this improvement is statistically significant at the 95% confidence level based on a standard paired t test (using the MATLAB function "ttest").

3.4.4 Model Robustness Test

Due to the non-uniqueness of the inverse problem, it is critical to assess model robustness, especially in view of potential biases associated with the choice of the initial model. To accomplish this, we perform a series of inversions using various initial model structures that consist of (1) an anisotropic basement, (2) perturbed basin structures, and (3) varying V_P/V_S ratios (Figure 3.10). In the first test,

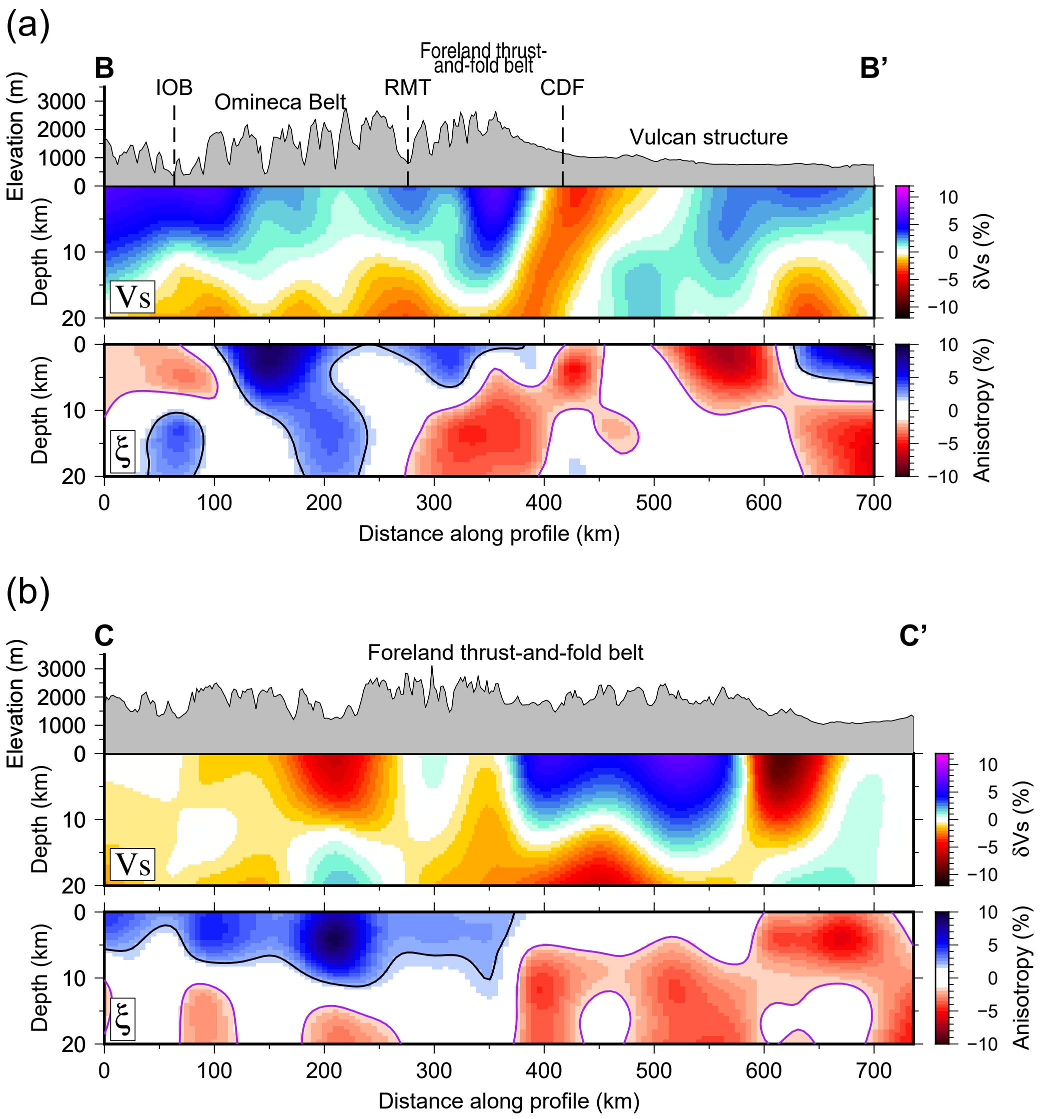

Figure 3.8: Cross-sections of average V_S and radial anisotropy ξ along transect (a) B-B$'$ and (b) C-C$'$ (see Figure 3.1 for the surface projections). The tectonic domains are indicated at the top of the cross-sections. Regions of positive ($\xi > 0$) and negative ($\xi < 0$) anisotropy are highlighted by blue and red colors, respectively. The purple and black lines indicate -1.5% and 2% radial anisotropy contours.

we invert Rayleigh and Love dispersion curves independently with a transversely isotropic initial model that contains isotropic sedimentary layers and a 5% difference in $(V_{SH} - V_{SV})/V_S$ in the crystalline basement (Figure 3.10a). We then quantify the similarity between the output model and our preferred model from Section 3.4.3 by correlating the radially anisotropic structures above 25 km (Figure 3.10b). The inversion results remain largely unchanged with an average correlation coefficient greater than 0.95 and the presence of an anisotropic basement only slightly degrades the correlation (by 0.03) at basement depths. This translates to a maximum of 0.3% perturbation of the apparent anisotropy ξ to our preferred model, which is substantially smaller than the reported anomalies (typically $\sim$8% in magnitude).

In the second test, we perform inversions using ten randomly generated models in which the basement structure is fixed but random velocity perturbations are introduced onto the sedimentary layers (Figure 3.10c). The average correlation coefficients remain high ($>$0.9) among various test models and the most significant differences are observed at mid-crustal depths (7–12 km), where the correlation coefficient varies by as much as 0.1. The slightly lower values (0.9) result from the two end-member models with severe velocity perturbations ($\sim$1 km/s) in the upper and lower sedimentary layers relative to the initial model (see Figure 3.10c), which introduce up to 0.8% bias in the radial anisotropy at mid-crustal depths. Generally, the effect of shallow sedimentary structures on anisotropy is secondary and the key anisotropic structures, which extend down to 20 km depth or greater, are robustly constrained by longer-period surface waves.

In the final test, we scale the P wave velocities of the initial model using a suite of V_P/V_S ratios (ranging from 1.7 to 1.9) from a recent analysis of receiver functions (Gu et al., 2018). The inversion results achieve an overall correlation of 0.9 with a ratio of 1.82 (see Section 3.3.3), suggesting minimal effects of the V_P/V_S ratio on the anisotropic structures (Figure 3.10d).

3.4.5 Uncertainty in Radial Anisotropy

It is worth noting that our separate inversion of Love and Rayleigh waves for anisotropic structures makes implicit simplifying assumptions (e.g., Dziewonski

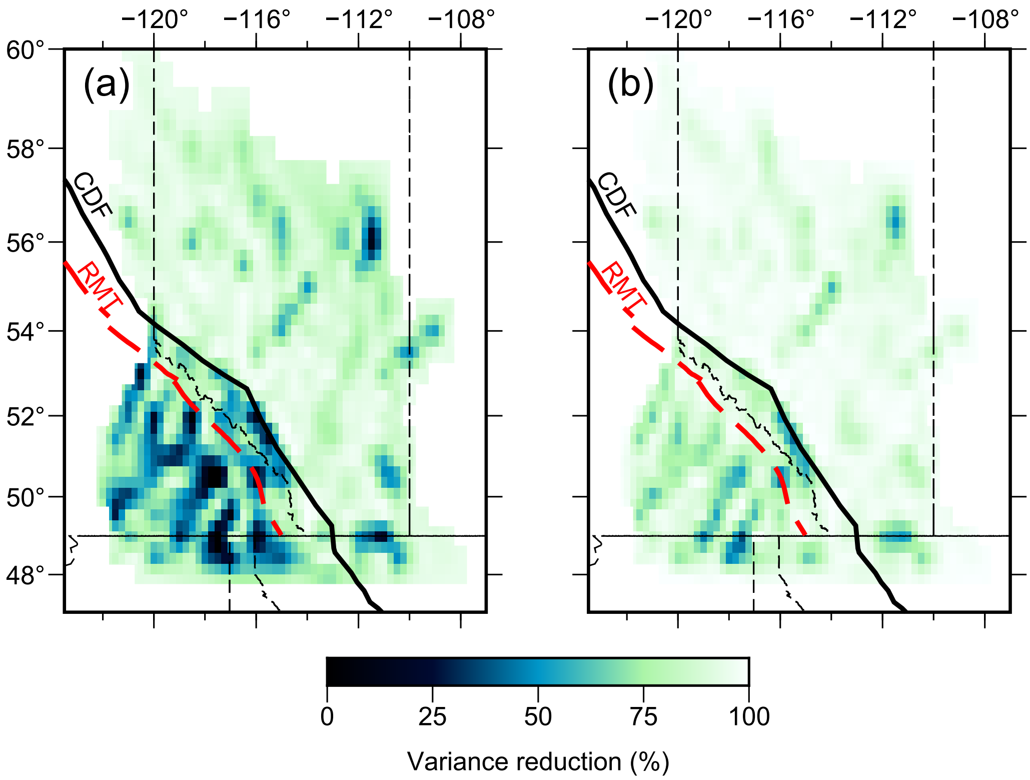

Figure 3.9: Reduction of data variance using the best-fitting (a) isotropic and (b) preferred model in which radial anisotropy is permitted in the crust. The independent inversions of Rayleigh and Love dispersion curves (i.e., introduction of radial anisotropy) greatly reduce the data variance in the Foreland and Omineca Belt.

& Anderson, 1981; Ekström & Dziewonski, 1998; Xie et al., 2013) by ignoring (1) the P wave sensitivity of Rayleigh waves, (2) the V_{SV} sensitivity of Love waves, and (3) the parameter η (Dziewonski & Anderson, 1981) that varies with ray angle. These assumptions are not strictly physical (Anderson, 1965; Anderson & Dziewonski, 1982; Regan & Anderson, 1984) and may result in minor inversion artifacts (Anderson & Dziewonski, 1982) or a slight underestimation of the actual shear wave anisotropy (Xie et al., 2013). To ensure the validity of these assumptions and fully assess model uncertainties, we perform a bootstrapping test of the group speed measurements (see Section 3.4.1) and invert for both shear velocity and anisotropy. All inversion parameters are the same as those used in the actual inversion, and the model uncertainties are calculated as the standard deviation of 50 radial anisotropy models at each node. The resulting anisotropic structures exhibit similar amplitudes (with differences in amplitudes generally less than 1%; Figure 3.11) as those detailed in Section 3.4.3. At 5 km depth, the Foreland Belt shows a maximum uncertainty of 1.3% (Figure 3.11a), which likely results from the large group velocity errors at shorter periods (i.e., 8 s). Although the orogenic belts in the southwestern sector of our study region show higher uncertainties, they are likely robust in view of the large observed amplitudes ($\sim$8%).

3.5 Discussion

3.5.1 General Assessment

Spatial undersampling has traditionally been a major challenge in high-resolution imaging of the crust and mantle beneath the WCSB. Thanks to the vastly improved regional passive array coverage, we are able to provide improved constraints on the large-scale variations in seismic velocities and anisotropy than previously available. To ensure sufficient data resolution, we perform the checkerboard test by constructing an input model with 10% alternating velocity perturbations and checker sizes of 150 and 200 km (Figure 3.12). Synthetic travel times are calculated based on the actual raypath geometry and inverted using the same parameters as those used in the final inversions. We add 10% random noise to the synthetic data prior to inversion

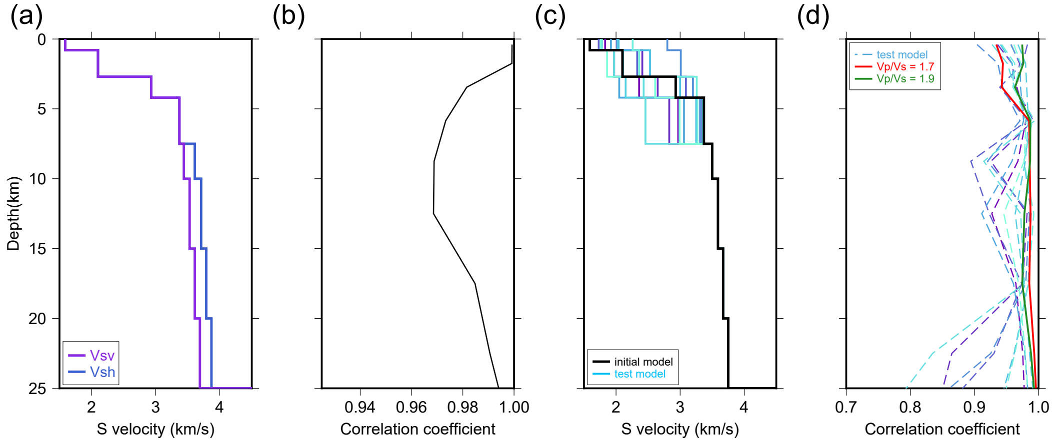

Figure 3.10: (a) A transversely isotropic shear velocity model with isotropic sedimentary layers and an anisotropic basement. (b) The correlation coefficient between our preferred model of radial anisotropy and the model inverted using the transversely isotropic starting model in (a). (c) Shear velocity profiles of ten basin starting models (blue gradient colored lines) relative to the initial model used in the actual inversion (black curve). Note that each of the models has a fixed basement structure but contains different basement boundary depths and velocity gradients. The two models with variable V_P/V_S ratios show the same S wave velocity structures as the actual initial model. (d) The correlation coefficient between our preferred model and the inverted models using different basin starting models (dashed lines) and V_P/V_S ratios (solid lines).

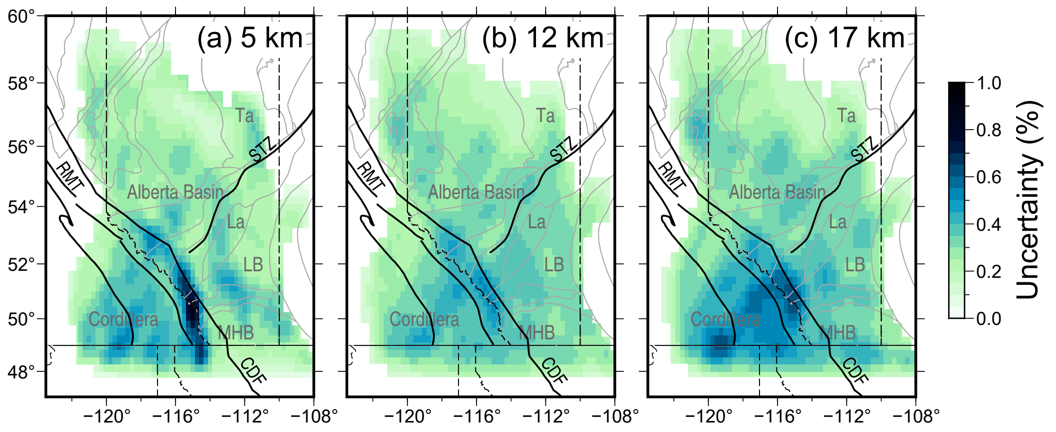

Figure 3.11: Maps of radial anisotropy uncertainties at the depths of (a) 5 km, (b) 12 km, and (c) 17 km. The uncertainties are defined as the standard deviations of the models from 50 bootstrap runs.

to simulate the noise in the actual observations. The output models recover 80–85% of the input amplitude for all the frequencies examined in this study. Despite limited number of stations, the centers and alternating signs of the input patterns in the southern Cordillera are consistently recovered at all frequencies. The highest spatial resolution is achieved in central Alberta, where velocity anomalies with lateral dimensions of 150 km are resolved up to 94% of the input amplitudes. The selected model space in southwestern WCSB and the Cordillera are sufficient for mapping the structure beneath these two tectonic domains as well as their transition region. In contrast, the northeastern sector of the study area (above 57°N) shows severe smearing effects due to reduced raypath coverage. The following discussions will exclusively focus on well resolved areas from the checkerboard test.

Our tomographic models show a reasonable agreement in crustal SV velocities with those determined from a substantially smaller data volume (Gu & Shen, 2015). Our models highlight a sharp velocity contrast between the Cordillera (west) and craton (east) along the Canadian Rocky Mountains. The elongated section of high SV velocities in the middle crust beneath the Foreland Belt is much more pronounced in our model than that of the earlier study using a similar approach (Gu & Shen, 2015), which we attribute to differences in spatial resolution between these two studies. We detect upper crustal LVZs in central Alberta, which were suggested earlier through independent analyses of receiver functions (Y. Chen et al., 2015) and noise correlation tomography (Gu & Shen, 2015). These basin-scale LVZs are rarely observed in stable cratons, and their presence could signify residual imprints of ancient orogenic processes surrounding the STZ and Vulcan Structure (Y. Chen et al., 2015, 2018; Gu et al., 2018). Low isotropic velocities of similar strengths in the mid-to-lower crust beneath the Cordillera are further suggested by ambient noise data (Dalton et al., 2011), which contrasts with the moderately high velocities of the upper crust in the intact Archean and Proterozoic accreted domains.

Typically, positive anisotropy should be expected in sedimentary basins if shape preferred orientation of horizontally bedded strata is solely responsible (Karato, 2008). This assumption is at odds with the radial anisotropy determined from noise correlations, which is generally negative in the shallow crust beneath the Alberta

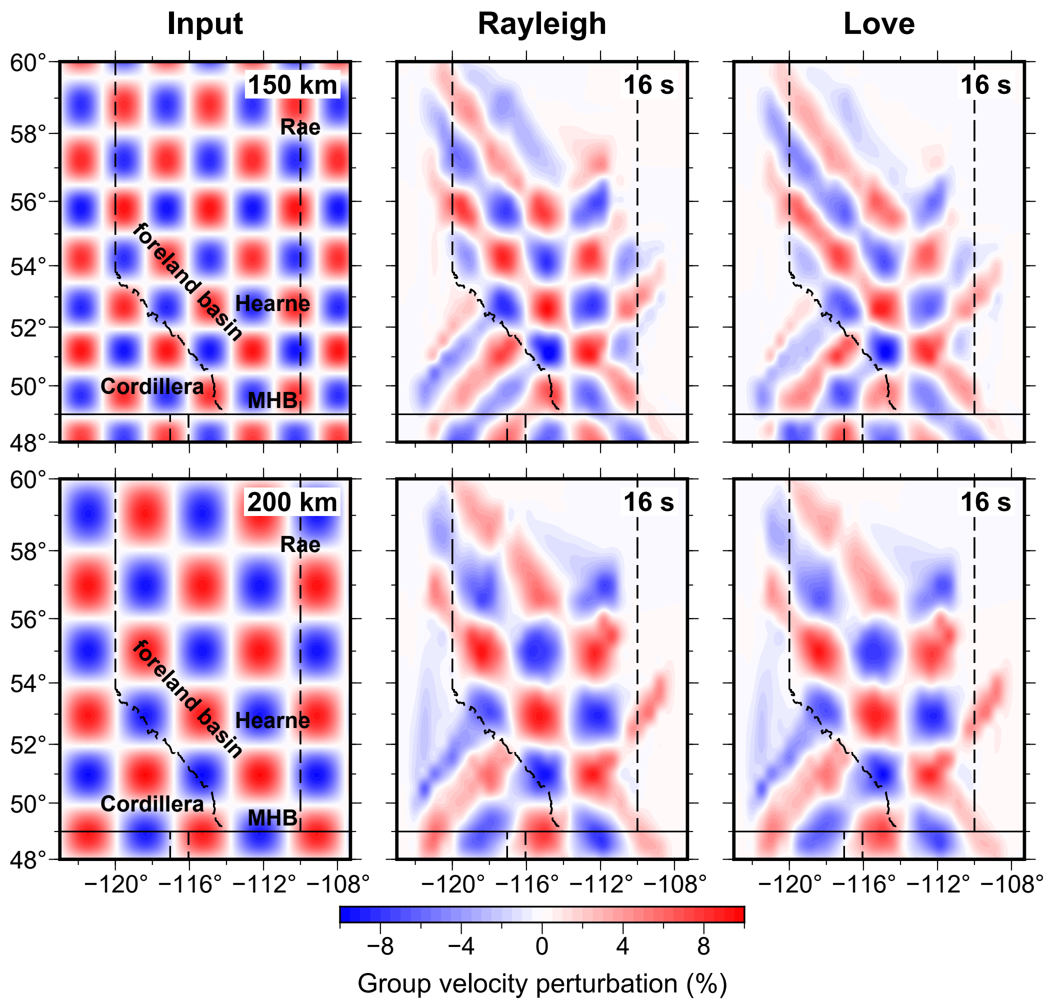

Figure 3.12: Checkerboard resolution tests for Rayleigh (middle column) and Love (right column) waves at 16 s using two different checker sizes. The left panels show the input models with 10% alternating positive and negative velocity perturbations relative to a mean value of 3 km/s.

Basin (Figure 3.7a). Similar observations have been recently reported in the shallow deposits of the Tehran Basin and interpreted as resulting from vertical alignments of cracks (Shirzad & Hossein Shomali, 2014). We will defer a detailed discussion and interpretation of seismic anisotropy east of the CDF to a future study due to (1) the modest amplitude of this anomaly, which is far below the level observed in the Cordillera, and (2) the lack of the need for shear wave anisotropy based on a "squeezing test" (Figure 3.9).

3.5.2 The Foreland Belt

One of the most intriguing observations from our study is a narrow anomaly of high isotropic S wave velocities (>3.8 km/s) and negative ξ from the surface down to the mid-crust beneath the eastern front of the Foreland belt (see Figures 3.6 and 3.7). Based on an empirical scaling relationship (Brocher, 2005), this high-velocity zone is concordant with the existing P velocity results (6.4 km/s) from the LITHOPROBE experiment (Clowes et al., 1995; Cook et al., 2004; Welford et al., 2001) and likely reflects compositional differences in the crust relative to other Cordilleran morphogeological belts. The anomalously high-velocity structure was interpreted as resulting from the upthrust of shallow-water Paleozoic carbonates and clastic sediments over the edge of the North American craton during the orogenesis of the Rocky Mountains (Welford et al., 2001).

We identify higher SV velocities within a continuously negative anisotropic anomaly of $\sim$5% in the east of the Foreland Belt, which dominates the anisotropic structure of this Belt. The presence of this unusual crustal signature has not been previously examined from a broadband seismological perspective and deserves a closer investigation in the context of regional tectonics. As an example of plate convergence between allochthonous Cordilleran terranes and autochthonous continental craton, the origin of the Foreland Belt has been widely associated with a passive margin miogeoclinal sequence (Price, 1981; Welford et al., 2001). The proposed tectonisms involve Proterozoic-Devonian accretion onto the rifted margin of ancestral North America, detachment from the crystalline basement, and upthrusting during the Mesozoic era (Monger & Price, 1979; Price, 1981). The faster SV velocities (hence, negative anisotropy) could result from thrust faults that have a dominant vertical component.

Up to now, the deformation of the Foreland Belt has been explained by the "thin-skinned" tectonic model (e.g., Campbell, 1973; Pfiffner, 2006, 2017; Price, 1981), which assumes that the sedimentary cover is detached from its crystalline basement along a mechanically weak décollement horizon (Pfiffner, 2006). The anisotropic pattern from our study (see Figures 3.8a and 3.14) displays similar dipping structures in geometry to the present-day east-verging imbricate thrust sheets in the Foreland Belt of the southern Canadian Cordillera (Price, 1981). The continuity of this anomaly within the well resolved 12–18 km depth range favors a "thick-skinned" Cordillera-Craton transition. Moreover, earlier exploration seismic studies (e.g., VSP and seismic refraction data) suggested that the Foreland Belt possesses a certain degree of tilted transverse isotropy attributable to clastics, particularly shales (e.g., Grech et al., 2001; Leslie & Lawton, 1999). We speculate that this tilted anisotropy, which is commonly regarded as a practical challenge by exploration seismologists in the imaging and positioning of target structures (e.g., Isaac & Lawton, 1999; Vestrum et al., 1999), could be caused by the alignment of clay minerals (Vernik & Liu, 1997). Anisotropy with a tilted symmetry axis was also revealed by a notable amplitude drop-off of P-to-S conversions from the Moho (Pms; Gu et al., 2018, and references therein). The observed negative sign of ξ further suggests that the shape of this anisotropic anomaly conforms to subvertical foliation plane (subhorizontal symmetry axis; Xie et al., 2013). The steeply dipping foliation plane is likely related to recent crustal deformations, as supracrustal rocks have been folded and foreshortened as a result of the contemporary NE-SW compressional stress across the entire belt (Ristau et al., 2007); this is evidenced by the observed time delays of Pms in the foothills of the Rocky Mountains (Gu et al., 2018). The orientation of thrust sheets would result from horizontal compression. In spite of the apparent resolution difference between the two seismological communities, dipping transversely isotropic strata appear to be ubiquitous beneath the Belt and independent of the data type (active source versus broadband passive source). We conclude that the Foreland Belt is likely to be a tilted transversely isotropic medium with a symmetry axis perpendicular to bedding (Johnston & Christensen, 1995).

On the global scale, negative anisotropy has been previously reported in different orogenic foreland belts. For example, radial anisotropy has been reported at 10 km or shallower depths beneath the Central Andean thrust-and-fold belt in the Eastern Cordillera of Bolivia (Lynner et al., 2018). Y. Chen et al. (2009) and Guo et al. (2012) found $V_{SV} > V_{SH}$ with a magnitude of 8–10% beneath the Himalayan fold-thrust belt. Significant anisotropy with positive $V_{SV} - V_{SH}$ values has also been reported to reside at shallow crustal depths beneath the Apennine fold and thrust belt (Ökeler et al., 2009). Although the origins of anisotropy remain debated, the correlation between crustal radial anisotropy and strong thrusting and folding activities could be, in general, caused by horizontal crustal contraction that creates subvertical faults and/or preferentially aligns crustal minerals in convergent settings.

3.5.3 The Omineca Belt

The Omineca Belt, the hinterland of the Canadian Cordillera, is geologically distinct from the adjacent Rocky Mountains that are underpinned by a negative anisotropic regime. Unlike the Foreland Belt, the Omineca Belt in the Southern Canadian Cordillera is of high metamorphic grade (Monger & Price, 2002) and greater heat flow (Davis & Lewis, 1984). Several metamorphic core complexes have been found in this area, potentially originating from major extensions in the early Tertiary that largely shaped its present-day crustal architecture (Johnson & Brown, 1996; Moschetti et al., 2010; Parrish et al., 1988).

The positive anisotropic anomaly in the Omineca Belt, which terminates at $\sim$18 km on the cross-section at 50.5°N latitude (see Figure 3.8a), is one of the most notable features of our model. This positive mid-crustal anisotropy is similar to that found in extensional provinces of the western United States based on ambient noise tomography (Moschetti et al., 2010). Similar anisotropic signals have been attributed to the lattice preferred orientation of anisotropic crustal minerals, such as micas and amphiboles (Mainprice & Nicolas, 1989; Moschetti et al., 2010). Evidenced by K-Ar mica dates (Archibald et al., 1984), the Eocene crustal extension of the Omineca Belt may have caused rock-forming minerals to align perpendicular to the direction of vertical shortening.

An intriguing feature of the anisotropic anomaly in this study is its southward progression, characterized by a deeper-seated and broader anisotropic body, which suggests that horizontal deformation dominates the upper-to-middle crust in the north (near the RMT at 53°N) and the middle-to-lower crust in the south (northern Montana). This finding is supported by the increased fault slippages from $\sim$12 km to a few kilometers northward near the RMT from seismic reflection data (van der Velden & Cook, 1996). The varying degree of crustal extension (and anisotropy) along the southern Omineca Belt has further implications for the relative motion of the southern Canadian Cordillera to the North American continent. It has been suggested that the allochthonous Omineca Belt rocks (as part of Cordillera) became attached to the North American craton through an oblique plate convergence involving a 60° clockwise rotation during the Late Cretaceous and Paleocene (Cook, 1995; van der Velden & Cook, 1996). This rotation induced extensional stress across the orogen and caused extensive orogen-parallel normal faulting in the southern Canadian Cordillera (Cook, 1995; van der Velden & Cook, 1996). Our anisotropic inversions offers critical kinematic constraints on the proposed relative motion. It is worth noting that highly anisotropic segments coincide spatially with major extensional faults (Figure 3.13a), the midpoints of which are separated from the nearest anisotropic segments by an average distance of $\sim$97 km without considering fault orientations and lengths. The statistical significance between these two observations can be established by a Monte Carlo simulation (Y. Chen et al., 2018); in this quantitative analysis we limit the simulation area to the west of RMT and assume that the geometric centers of the faults follow a uniform distribution. In each simulation, we compute the distance between random fault locations and the averaged anisotropy in the depth range of 10–20 km. After 15,000 simulations, the distribution of anisotropy-fault distance yields the intersection of our observed distance and the cumulative density function at a probability of 0.66% (Figure 3.13b). The statistically significant spatial correlation between the extensional faults and the positive anisotropy in the Cordilleran hinterland argues in favor of widespread crustal extension in this area.

Alternatively, positive ξ may have a thermal origin due to lateral flow of partially molten crust in the southeastern Canadian Cordillera during the Laramide orogeny (Teyssier et al., 2005). A mid-crustal channel flow model was first presented for this area (Brown & Gibson, 2006), and a further study suggests that lower-crustal ductile detachment and flow must have occurred in most of the North American Cordillera (Hyndman, 2017). The horizontal flow can induce anisotropy

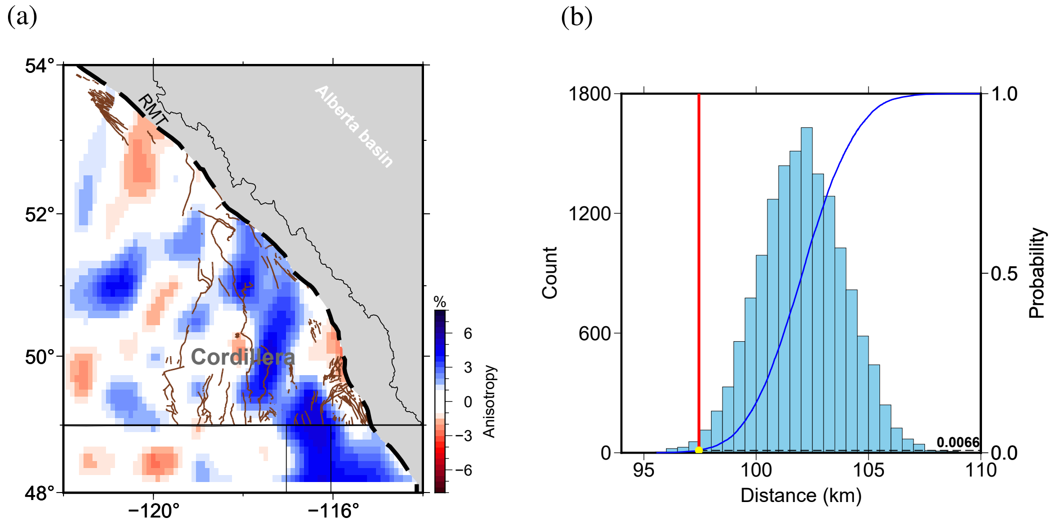

Figure 3.13: (a) Average anisotropy (10–20 km depths) confined in the region west of RMT (black dashed line). The brown lines mark the locations of normal faults. (b) Monte Carlo simulation of fault locations. The histogram shows the simulated anisotropy-fault distances, assuming the midpoints of the faults are randomly distributed. The red line marks the observed average distance between the midpoints of the normal faults and the nearest highly anisotropic segments ($\xi \geq 2\%$). The cumulative probability of the mean anisotropy-fault distance distribution is shown as the blue curve. The intersection of the two lines (the yellow dot) indicates the probability (0.66%) that random faults are distributed at the observed distance (∼97 km) from the anisotropy.

in outcrops exhumed from the lower crust. In other words, the observed anisotropy at shallower depths may have resulted from horizontally sheared fabrics of rocks, while anisotropic signatures at middle to lower crustal depths are largely influenced by the shape preferred orientation of melt lenses or sills. Details of the mechanisms require a future analysis, though both scenarios favor tectonothermal events that were kinematically linked to crustal extension (Kruckenberg et al., 2008).

In short, we attribute the origins of the observed anisotropy to the deformation history of the southern Canadian Cordillera (Figure 3.14). The accretion of supracrustal rocks in the Foreland Belt was preceded by folding and thrust faulting caused by the horizontal compression from plate convergence (Price, 1981). This process facilitated a higher degree of vertical deformation, manifested as vertical thickening and negative anisotropy. Farther west in the Omineca Belt, the post-collisional crustal extension initiated in the Eocene was accompanied by the generation of normal faults. The lateral stretching/deformation was likely responsible for the widespread positive anisotropy from our noise correlation tomography.

3.6 Conclusions

This chapter presents a 3-D model of crustal shear velocity and radial anisotropy beneath southwestern Canada based on ambient noise tomography. In the shallow crust, we identify pronounced low velocities beneath the foreland basin and high velocities beneath the Cordilleran orogenic belt and Proterozoic accreted terranes surrounding the Alberta Basin. The Foreland Belt is characterized by widespread negative anisotropy, which may have resulted from thrust fabrics and horizontal compression during the plate convergence. These deep-seated crustal signatures extend down to 20 km depth, which supports a thick-skinned Cordillera-Craton transition. We also observe positive radial anisotropy beneath the Cordillera, particularly near the Omineca Belt, which reflects strong horizontal crustal deformation or layering associated with episodes of Eocene extension during the Cordilleran orogenesis.

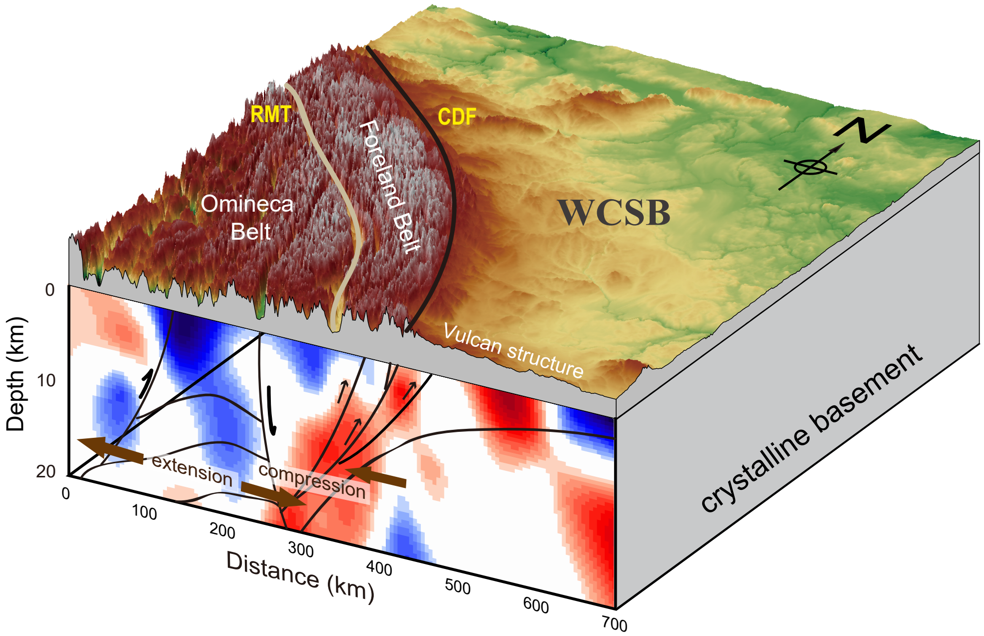

Figure 3.14: A schematic diagram showing our interpretation of the observed ξ anisotropy in the southern Canadian Cordillera along profile B-B′. The surface topography of southwestern Canada is superimposed on the top. The CDF and RMT are marked by black and light yellow colors, respectively. The think black lines and arrows indicate the main geological features (crustal extension in the Omineca Belt and the fold-thrust fabrics within the Foreland Belt).

Chapter 4

Shear Wave Reflectivity Imaging of Upper Mantle Discontinuity Structure Beneath South America

4.1 Introduction

We have demonstrated in Chapters 2 and 3 that significant variations exist in the tectonic stress field. Much of the deformation and change that occurs at the Earth's shallow subsurface is the manifestation of dynamic processes occurring within the mantle (Allen, 2011). Processes from plate tectonics to the generation of mantle heterogeneity are mainly driven by plate subduction wherein downgoing oceanic lithosphere sinks into the deep mantle (Forsyth & Uyeda, 1975). The Nazca-South American subduction zone is an ideal location for interpreting mantle dynamics and circulation. The main objective of this chapter is to investigate the interaction of subducted slab and the overlying mantle at a continental scale from long-period SH reflections recorded by globally distributed seismic stations.

The Nazca-South American plate interaction features a long-lived ocean-continent collisional system dating back to the Mesozoic (Figure 4.1; Pardo-Casas & Molnar, 1987). At a present-day convergence rate of $\sim$7 cm/yr along the margin (DeMets et al., 2010), the ongoing subduction is concurrent with the Andean orogeny, lithospheric shortening and arc magmatism, processes that have been impacted by slab dip angle, break-off, and interactions with the 660-km seismic discontinuity (Y.-W. Chen et al., 2019; Faccenna et al., 2017; Ramos, 2009). Highlighted by deep-focus earthquakes (Cahill & Isacks, 1992) and high velocities in global tomographic models (e.g., Fukao & Obayashi, 2013; C. Li et al., 2008; Lu et al., 2019), the Wadati-Benioff zone (WBZ) along the Nazca-South American convergent margin appears to be relatively flat ($<10^\circ$ dip) in the shallow mantle (Cahill & Isacks, 1992; Gutscher et al., 2000) but the dip increases substantially (to $\sim70^\circ$) at the base of the upper mantle (Scire et al., 2016). This characteristic change of slab morphology has been further investigated through numerical simulations, which disfavors a simple form of slab penetration into the lower mantle (Y.-W. Chen et al., 2019; Faccenna et al., 2017). According to the time delay between the onset of Andean compression and that of slab impingement on the lower mantle (Y.-W. Chen et al., 2019), the Nazca slab flattens near the base of the mantle transition zone (MTZ), analogous to the morphology of the subducting Pacific slab beneath northeast Asia.

A key constraint on slab morphology and slab-MTZ interactions is MTZ thickness. The MTZ is bounded by the 410- and 660-km discontinuities (hereafter referred to as the 410 and 660) associated with mineralogical phase transitions where olivine transforms to wadsleyite at the 410, then to ringwoodite at an intermediate depth ($\sim$520 km), and decomposes to bridgmanite and ferropericlase at the 660 (Ringwood, 1975). Due to the opposite Clausius-Clapeyron slopes of olivine phase transformations at the 410 and 660, a thickened MTZ is expected according to high-pressure mineral physics experiments (Ito & Katsura, 1989) and is widely reported in major subduction zones including, but not limited to, the western Pacific and South America (e.g., Deuss, 2009). Unlike the former region where much progress has been made in capturing the behaviors of the descending Pacific slab (e.g., Gu et al., 2012; X. Li & Yuan, 2003; Zhao & Ohtani, 2009), much of the South American mantle remains undersampled due to sparse data coverage, leaving considerable uncertainties on the fate of subducted oceanic lithosphere. For instance, while locally increased MTZ thickness is compelling evidence for the descending Nazca plate along the convergent margin, unexpected MTZ thickening deduced from regional seismic tomography (Portner et al., 2020; Scire et al., 2016) and secondary reflections/conversions (Deuss, 2009; Gu & Dziewonski, 2002; K. H. Liu et al., 2003; Schmerr & Garnero, 2007) favors at least transient slab stagnation in the MTZ farther inland from the WBZ. Unimpeded slab penetration is further at odds with reports of small-scale MTZ anomalies such as a reflection gap on the 410 (Contenti et al., 2012), upper-MTZ low-velocity anomaly (Portner et al., 2020) and double reflectors (Schmerr & Garnero, 2007). These anomalies, manifested as abrupt changes in velocity and density, generally imply secondary subduction-induced processes that preclude a purely thermal origin.

In this chapter we take advantage of a global data set of SS precursors (termed SdS), which are underside reflections off the d-km discontinuity (Figure 4.2a). By combining travel time measurements sensitive to temperature with reflection amplitudes that are diagnostic of density and velocity jumps across the discontinuities, we propose a self-consistent model of subduction dynamics and provide compelling observations of compositional heterogeneities at MTZ depths beneath South America. An integrated analysis of slab geometry, overriding plate deformation and slab-MTZ interactions suggests remarkable similarities in the fate of subducted slabs between the Nazca-South American and northwestern Pacific subduction systems.

4.2 Seismic Stacking Method

4.2.1 Data Preprocessing

We utilize all available broadband and long-period seismograms recorded between January 1977 and October 2020 (Figure 4.2b), from the Incorporated Research Institutions for Seismology (IRIS) Data Management Center for SS bounce points in the area defined by 40°S–20°N and 105°W–30°W (Figure 4.2c). We retain earthquakes with depths less than 75 km to minimize the interference from depth phases and adopt a cutoff earthquake magnitude of 5.5 to ensure sufficient reflection amplitudes. We further constrain the epicentral distance from 100° to 165°. The seismograms are rotated into transverse components, bandpass filtered at the periods of 15–75 s with a second-order zero-phase Butterworth filter and resampled to 1 Hz. Traces with an SNR less than 3.0 are rejected. The SNR is defined as the ratio between the maximum amplitude of the main phase window (±50 s centered at the

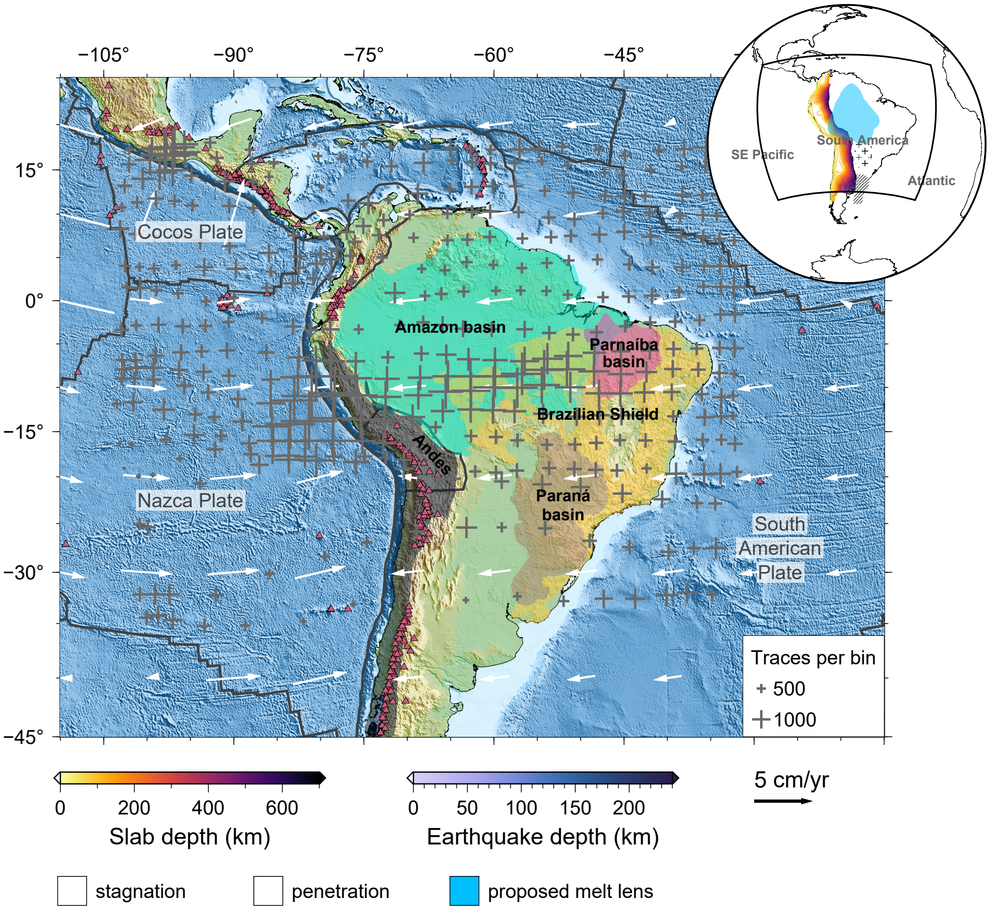

−105°
−90°
−75°
−60°
−45°
15°
0°
−15°
−30°
−45°
Cocos Plate
Nazca Plate
Amazon basin
Parnaíba basin
Brazilian Shield
Andes
Paraná basin
South American Plate
SE Pacific
South America
Atlantic
Traces per bin
500
1000
0
200
400
600
Slab depth (km)
0
50
100
150
200
Earthquake depth (km)
5 cm/yr
stagnation
penetration
proposed melt lens

predicted arrival time of SS) and the precursory window (50 s before the predicted S660S to 50 s after the predicted S410S arrival). Traces are aligned on the first major swing of SS and then normalized to unit amplitude, and a polarity reversal is performed if necessary. The refined data set contains ~52,000 traces from 2,580 events, which is significantly larger than that used in the study of Schmerr and Garnero (2007). The data coverage is relatively dense in central and northern South America (Figures 4.1 and 4.2c).

4.2.2 Common Midpoint Stacking

To study the lateral variations of the 410 and 660 topography, we partition the data into 5–10° radius circular caps (Figure 4.1). North of 20°S, raypaths are binned into caps with 3° spacing and 5° radius, whereas we divide the area south of 20°S into 5° equally spaced caps of 10° radius to maintain sufficient data density. We stack traces in each cap using the common midpoint (CMP) method and obtain two single stacks by summing all traces after moveout correction to a reference distance of 130° for the 410 and 660, respectively. The precursors S410S within distance ranges 100°–110° and 135°–150° and S660S between 100° and 120° are excluded in the CMP stacking to minimize the contamination of interference phases

---

Figure 4.1 *(Figure appears on preceding page)*: Topography and tectonics of South America and its surrounding oceans. The black box in the inset map outlines the study region. The slab geometry (Hayes et al., 2018) is indicated by the colored curves, which reflect slab-depth differences, in the inset map. The areas covered by slashes and crosses have been linked to slab penetration and stagnation, respectively, according to a recent regional tomographic model (Portner et al., 2020). The extent of the proposed melt lens (blue shaded area) is inferred based on the area showing a 50% amplitude reduction from the values predicted by the PREM model (Dziewonski & Anderson, 1981) in an earlier study of SS precursors (Schmerr & Garnero, 2007). In the center plot, the color-shaded areas indicate major tectonic domains according to the United States Geological Survey World Geologic Maps (`https://certmapper.cr.usgs.gov/data/apps/world-maps/`, accessed June 2021). The red triangles show the distribution of Holocene volcanoes. The true bin locations (gray crosses) are scaled by the number of records in each stack. The white arrows indicate the absolute plate motion, and their lengths reflect plate velocities in the spreading-aligned reference frame (Becker et al., 2015). The thick black lines in the center plot denote the plate boundaries (Bird, 2003).

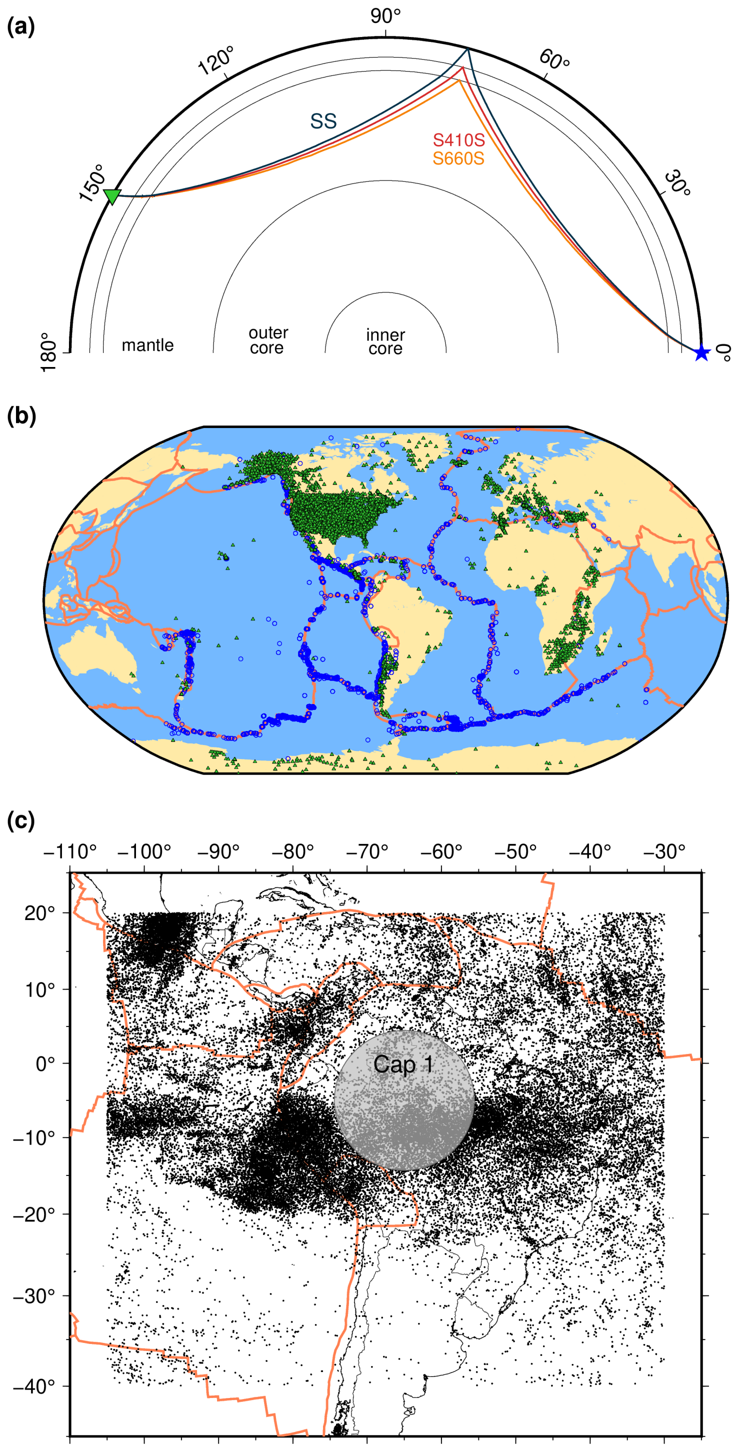

Figure 4.2: (a) Theoretical raypaths of SS (surface reflections) and its precursors SdS (underside reflections off MTZ discontinuities) at a source-receiver distance of 150°. (b) The stations and earthquakes are denoted by green triangles and blue circles, respectively. Major plate boundaries (Bird, 2003) are indicated by orange lines. (c) Distribution of SS bounce points (black dots). The gray shaded circle is the 10°-radius cap used for the amplitude inversion (i.e., Cap 1).

(Schmerr & Garnero, 2006). We apply poststack timing corrections to account for variations in crustal thickness (Laske et al., 2013) and upper mantle velocity structure (Ritsema et al., 2011) for each discontinuity phase. The stacked traces are finally converted from time to depth according to travel times predicted by the PREM model (Dziewonski & Anderson, 1981) after correcting for crustal thickness (Laske et al., 2013) and upper mantle velocity structure (Ritsema et al., 2011). We compare migration results using various tomographic models and the first-order observations are in reasonable agreement (Figure C.1). The resulting stacks are subsequently subjected to a bootstrap resampling test (Efron & Tibshirani, 1991) using 300 random data subsets to gauge the robustness and depth uncertainty of each reflection (Figure C.3).

4.3 Mineral Physics Modeling

The mantle composition can be represented by either an equilibrium assemblage (EA) of pyrolite or an unequilibrated mechanical mixture (MM) of basalt and harzburgite (Xu et al., 2008). The former assumes that the mantle is fully equilibrated, in contrast to the latter model where the mantle has undergone differentiation into the two end-member components. With an identical pyrolitic bulk composition, the EA and MM models result in different elastic properties (Xu et al., 2008). We consider both models and calculate the density and shear wave velocity profiles of EA and MM with basalt fractions (f) varying from 0% to 100% (with a step of 10%) along mantle geotherms with potential temperatures (T_p) ranging from 1200 K to 2000 K (Figure C.4) at intervals of 100 K. Phase equilibria and physical properties are obtained using the Gibbs free energy minimization program Perple_X (Connolly, 2005), and the bulk elastic properties of rock assemblages are computed as the Voigt-Reuss-Hill averages of the individual minerals. We then compute synthetic waveforms of SS precursors for these compositions using the reflectivity method (Fuchs & Müller, 1971), and the synthetics are bandpass filtered in the same frequency range (i.e., 15–75 s) as the real data. The amplitudes of S410S and S660S exhibit greater sensitivity to f than T_p in the MM model (Figures 4.3d and

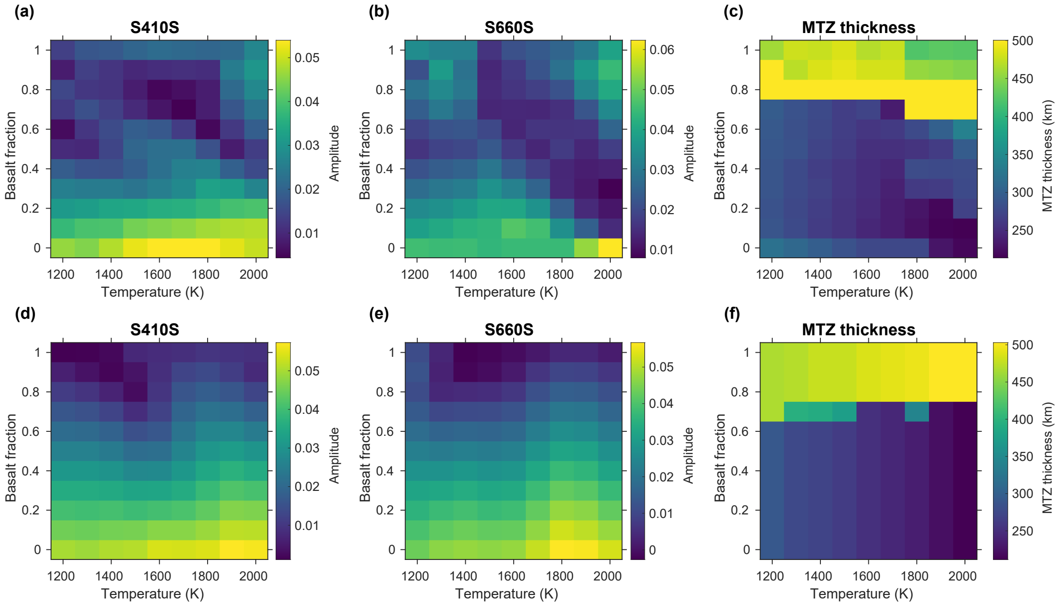

Figure 4.3: (a-c) Predicted (a) S410S amplitudes, (b) S660S amplitudes, and (c) MTZ thickness for different mantle temperatures and basalt fractions in a mantle comprised of an equilibrium assemblage of basalt and harzburgite. (d-f) Same as (a-c) but for a mechanically mixed mantle composition.

4.3e), while the amplitude dependences on EA temperature and composition are less conclusive (Figures 4.3a and 4.3b). The MTZ thickness generally decreases with T_p when $f < 0.7$; beyond the threshold, the MTZ significantly widens due to the dominant post-garnet transition (Figures 4.3c and 4.3f).

According to earlier laboratory experiments, wadsleyite and ringwoodite can contain up to 3.3 weight percent (wt%) water (Inoue et al., 1995; Kohlstedt et al., 1996). This observation is supported by wide-ranging reports based on seismic (Meier et al., 2009), electrical conductivity (Huang et al., 2005), and mineral physics (Fei et al., 2017) data that infer a value of 0.01 to 1 wt% (Karato, 2011). Specific to our study region, a localized water-rich layer has been suggested as the by-product of slab dehydration beneath the overriding South American plate (Schmerr & Garnero, 2007). To further investigate the joint compositional effects of basalt fraction f and water content c_w on amplitudes, we compute full waveforms of SS precursors based on mantle mineral assemblages for a range of f and c_w while keeping temperature fixed ($T_p = 1600$ K) (Figures C.4e and C.4f). We perform non-equilibrium thermodynamic modeling where high-pressure (Mg,

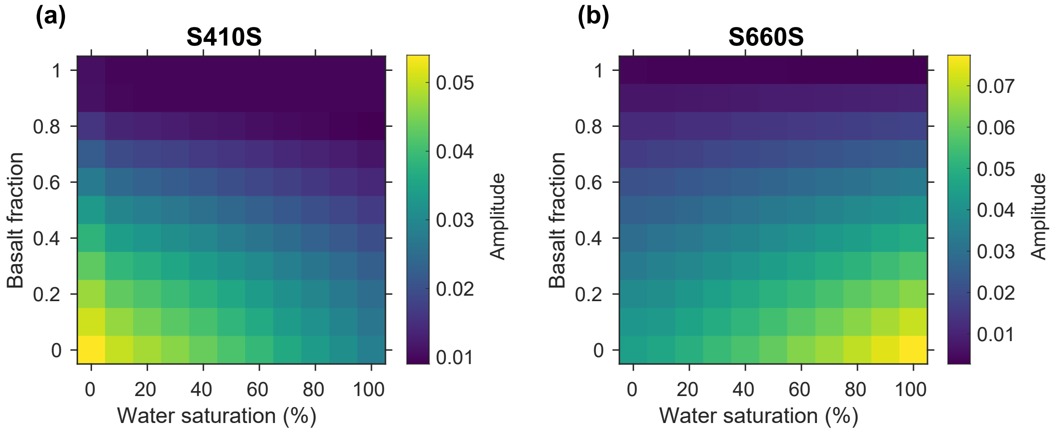

Figure 4.4: Predicted (a) S410S and (b) S660S amplitudes for different water contents (as percentage of maximum MTZ water storage capacity) and basalt fractions in a mechanically mixed mantle. The full water storage capacity is 3.3 wt% in wadsleyite and the water content through the MTZ is partitioned according to Inoue et al. (2010).

Fe)$_2$SiO$_4$ polymorphs are hydrated using HyMaTZ (F. Wang et al., 2018), a Python program that models the effect of hydration on the elastic properties of the MTZ. Since this modeling does not account for the water-content dependence of the discontinuity depths due to the lack of experimental data, only synthetic SS precursor amplitudes are measured. For a fixed water partitioning of olivine, wadsleyite, and ringwoodite at 6:30:15 (Inoue et al., 2010), the amplitudes of both S410S and S660S decrease monotonically when f or c_w increases, especially the former (Figure 4.4).

4.4 Inverse Problem

4.4.1 Inversion for Mantle Temperature and Composition

To determine the best-fitting T_p and f that match our measurements, we follow the approach of Waszek et al. (2021) and perform statistical inversions of the MTZ thickness and amplitudes of S410S and S660S by comparing the data with the predicted models from Section 4.3. We formulate the inversion via the Bayesian inference framework, and the posterior distribution for model parameters (T_p, f) given the data d is given by

$$P(T_p, f|d) \propto P(d|T_p, f)P(T_p, f), \tag{4.1}$$

where $P(T_p, f)$ is the prior probability that is described by a uniform distribution over the model space $\Omega = \left\{T_p, f \in \mathbb{R} | 1,200 \leq T_p \leq 2,000;\ 0 \leq f \leq 1\right\}$. Given this uninformative prior, equation (4.1) simplifies to

$$P(T_p, f|d) \propto P(d|T_p, f). \tag{4.2}$$

The likelihood function of the data $P(d|T_p, f)$ represents a measure of the misfit between the observed data d_{obs} (SS precursor amplitudes or the MTZ thickness) and the respective predictions d_{pred} for a trial model (T_p, f) as follows

$$P(d|T_p, f) = \exp\left[-\frac{\left(d_{\text{obs}} - d_{\text{pred}}\right)^2}{2\sigma^2}\right], \tag{4.3}$$

where σ is the standard deviation for each data type. The joint posterior probability distribution is simply the cumulative product of individual likelihoods for each data type (d_i) including the MTZ thickness and amplitudes of S410S and S660S

$$P(T_p, f|d) = \prod_{i=1}^{3} P(T_p, f|d_i). \tag{4.4}$$

The maximum a posteriori (MAP) solution occurs when the trial model maximizes $P(T_p, f|d)$, and the width of the marginal probability distribution is used to assess the uncertainty of each parameter estimate. Similarly, we also apply the probabilistic inversion to simultaneously constrain basalt fraction and water content in the MTZ of the target region using amplitude data alone.

4.4.2 Amplitude-Versus-Offset Inversion

The amplitudes of SS precursors provide valuable information on the impedance contrasts across the 410 and 660. In general, the reflection amplitudes are affected by (1) reflection coefficients at the discontinuity, (2) intrinsic attenuation, (3) geometric spreading, and (4) source radiation patterns. Among these factors, only the reflection coefficient is sensitive to elastic properties of the discontinuity. In this study we adopt the expression of the 1-D SdS/SS amplitude ratio (C. Yu et al., 2018) to calculate SdS reflection coefficient

$$\frac{R_{SdS}}{R_{SS}} = \frac{\dfrac{A_{SdS}}{A_{SS}}}{\dfrac{G_{SdS}}{G_{SS}}\dfrac{Q_{SdS}}{Q_{SS}}}, \tag{4.5}$$

where for the corresponding phases of SS or SdS, A is the amplitude, R is the reflection coefficient, G denotes the geometric spreading factor, and Q denotes the quality factor. The reflection coefficient at the surface (R_{SS}) is 1. Based on the equation for the energy density on the wavefront in a 1-D spherical Earth (Shearer, 2009), the geometric spreading correction factor (Figures C.5a and C.5b) is

$$\frac{G_{SdS}}{G_{SS}} = \sqrt{\frac{p_{SdS}\cos\theta_1^{SS}\cos\theta_2^{SS}\left|\dfrac{dp_{SdS}}{dr}\right|}{p_{SS}\cos\theta_1^{SdS}\cos\theta_2^{SdS}\left|\dfrac{dp_{SS}}{dr}\right|}}, \tag{4.6}$$

where p is the ray parameter, r is the epicentral distance, and θ_1 and θ_2 are the incidence angles at source and receiver, respectively. Corrections for intrinsic attenuation (Figures C.5c and C.5d) adopt the amplitude decay function $\exp(-\omega t^*/2)$ and assume a center frequency of 30 s

$$\frac{Q_{SdS}}{Q_{SS}} = \exp\left[-\frac{\omega}{2}\,(t^*_{SdS} - t^*_{SS})\right], \tag{4.7}$$

where the t^* operator is defined as the integral of the ratio between SdS or SS travel time t and the quality factor Q along the raypath through the PREM model

$$t^* = \sum_i \frac{\Delta t_i}{Q_i}. \tag{4.8}$$

The effects of source radiation for SS and SdS are canceled out by the amplitude ratio. Incoherent stacking due to topographic variations could also affect measured amplitude ratios. We obtain an amplitude correction factor by empirically estimating the effect of time shifts on the precursor amplitudes, assuming that the uncorrected SS-SdS differential times on stacks for a cap follow a Gaussian distribution with a standard deviation of σ_t (Chambers et al., 2005; Shearer & Flanagan, 1999). At a regional scale, the precursor amplitudes are reduced by 16% ($\sigma_t = 2.7$ s) and 24% ($\sigma_t = 3.2$ s) for S410S and S660S, respectively.

The reflection and transmission coefficients of an incident plane wave for a two-layered isotropic medium change as a function of angle of incidence (equivalent to source-receiver distance), which are formulated by the Zoeppritz equations (Aki & Richards, 2002). Elastic parameters (S wave velocity and density changes) can be inferred based on such amplitude-versus-offset (AVO) analysis. Due to their intrinsic nonlinearity, it is less practical to apply the exact Zoeppritz equations for AVO analysis. Therefore, we adopt the two-term approximation to model the AVO response of the SH-SH reflections (Rüger, 2002).

The linearized two-term approximation parameterizes the reflection coefficient in terms of ray angle, S wave velocity reflectivity, and density reflectivity as

$$R(\theta) = \frac{1}{2}\left[(1-\tan^2\theta)\Delta V_S + \Delta\rho\right], \tag{4.9}$$

where $\Delta\rho$ and ΔV_S are the fractional changes in density and S velocity defined as

$$\Delta V_S = \frac{2(V_{S2}-V_{S1})}{V_{S2}+V_{S1}}, \tag{4.10}$$

$$\Delta\rho = \frac{2(\rho_2-\rho_1)}{\rho_2+\rho_1}. \tag{4.11}$$

The subscripts 1 and 2 refer to the top and bottom layer, respectively. The angle θ is the average of the incident and transmitted angles that are related via Snell's Law. For underside reflections, the incident angle is located below the discontinuity. The approximate reflection coefficients calculated by equation (4.9) provide an accurate estimate of the exact solutions based on a synthetic test using a variety of 1-D seismic reference models (Figure C.6).

We invert for S velocity (ΔV_S) and density ($\Delta\rho$) jumps by measuring reflection coefficients along a sequence of distances (angles). We seek the solution to the overdetermined system of linear equations via a grid search method and quantify the 2σ uncertainties using chi-square statistics

$$\chi^2 = \sum_{i=1}^{N_d} \frac{\left(R_{\mathrm{obs},i}-R_{\mathrm{pred},i}\right)^2}{\sigma_i^2} \tag{4.12}$$

where $R_{\mathrm{obs},i}$ is the observed SdS reflection coefficients with a standard deviation of σ_i, $R_{\mathrm{pred},i}$ is the predicted SdS reflection coefficients calculated by equation (4.9), and N_d is the number of distances. This AVO inversion method, which is typically utilized in hydrocarbon exploration, has the advantage of accentuating amplitude-distance trends in seismic velocity and density without requiring synthetic modeling. By assuming a first-order discontinuity (Rüger, 2002), the inversion directly

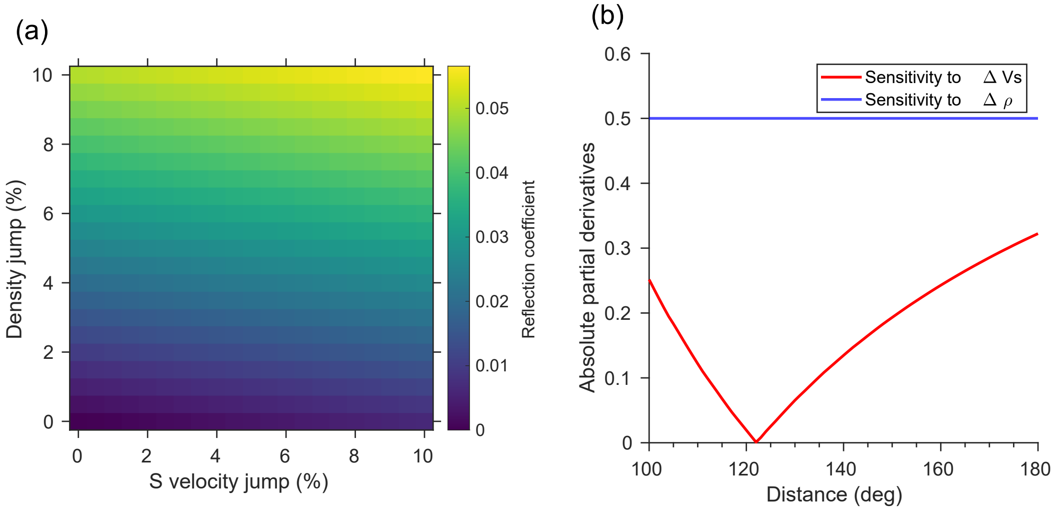

Figure 4.5: (a) Predicted reflection coefficients as a function of S velocity jump and density jump based on the approximate Zoeppritz equation and a reference epicentral distance of 130°. (b) Sensitivity kernels for reflection coefficients to velocity jump (red) and density jump (blue) across a discontinuity.

targets changes in elasticity contrasts over a depth interval across the 410 and 660 (Chambers et al., 2005; Shearer & Flanagan, 1999).

To explore the sensitivity of our inversion method, we perform a preliminary sensitivity analysis which indicates that changes in the reflection coefficients of SS precursors based on equation (4.9) are primarily sensitive to $\Delta\rho$ (Figure 4.5a). Calculations of sensitivity kernels $\partial R/\partial X$ (where X denotes either ΔV_S or $\Delta\rho$) further show that the sensitivity to $\Delta\rho$ is constant throughout the distance range, whereas the sensitivity to ΔV_S is overall lower and diminishes to negligible levels at a distance of $\sim$122° (Figure 4.5b).

We then assess the effectiveness of our AVO inversion algorithm using reflectivity synthetic seismograms with 50% random Gaussian noise (Figure 4.6). The synthetic data are generated for the PREM model and bandpass filtered between 15 and 75 s. A high noise level is used to simulate the noise embedded in the real data. The PREM density and velocity contrasts lie within 2σ limits (95% confidence level) of the inverted results for both 410 and 660, though the results show a strong trade-off between velocity and density for the 410.

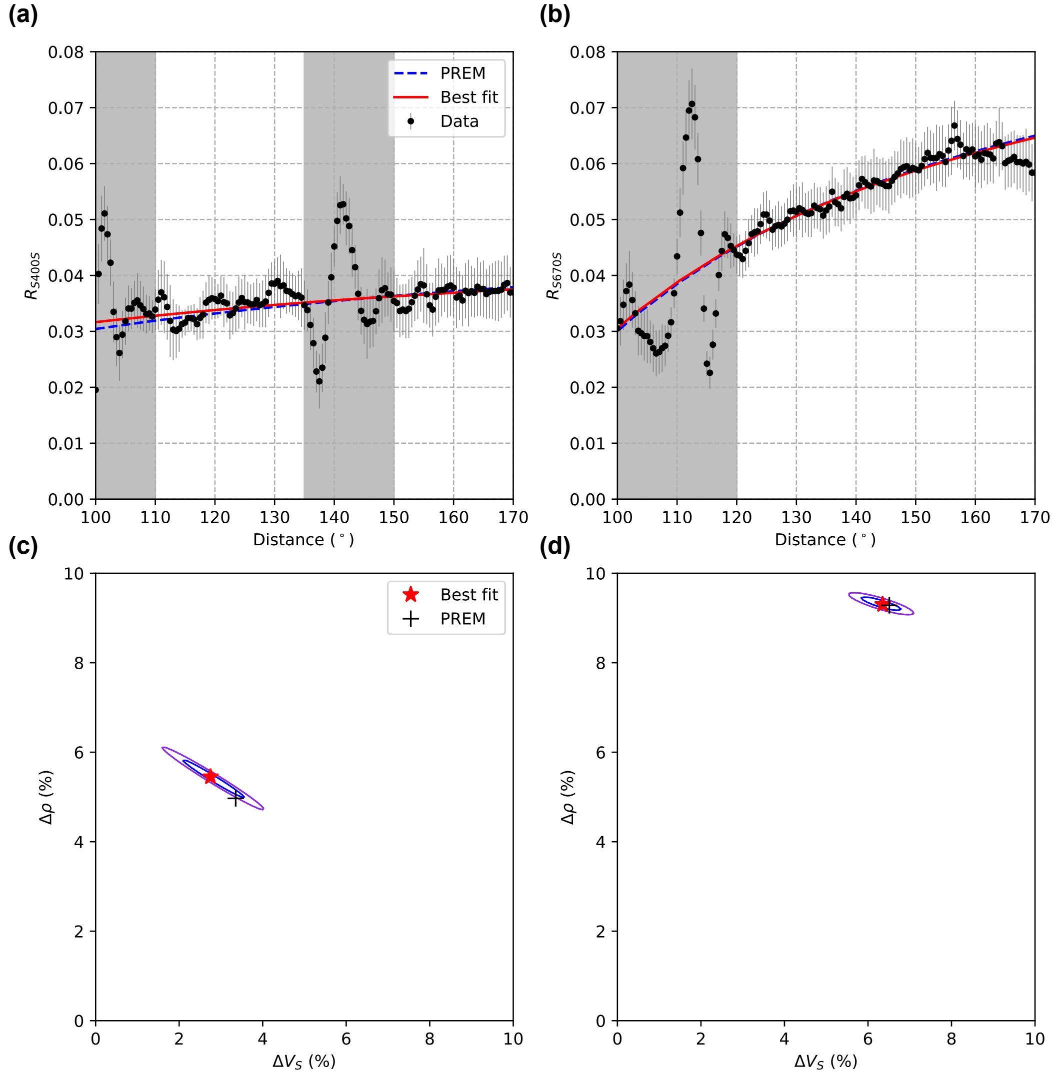

Figure 4.6: Synthetic AVO inversion using reflectivity synthetic seismograms for PREM. The measured S410S and S660S reflection coefficients (black dots) and their corresponding errors are shown in (a) and (b), respectively. The reflection coefficients are corrected for geometric spreading and attenuation. The gray shaded areas denote the distance exclusion windows in the inversion due to interference phases. The synthetic seismograms are contaminated with 50% Gaussian noise and are stacked within 0.5° bins in source-receiver distance. The inverted density and shear velocity contrasts (red stars) across the 410 and 660 are shown in (c) and (d), respectively. The blue and purple ellipses indicate the 1σ and 2σ limits based on chi-square statistics. The PREM values are represented by the black plus symbols, which are within the 2σ limits of the inverted results.

4.5 Results

4.5.1 Overview of Transition Zone Observations

The mean depths of the 410 and 660 are 413 ± 5 km and 656 ± 9 km, respectively (Figures 4.7a and 4.7b), over 412 bins within the study region. The difference between the two discontinuities produces a mean MTZ thickness of 245 ± 9 km (Figure 4.7c), which is $\sim$3 km thicker than earlier reported global averages using similar approaches (Gu & Dziewonski, 2002; Lawrence & Shearer, 2008). The 410 shows minimal depth variations except for a moderate (10–15 km) depression in the northeastern portion of the Amazon basin, which spatially coincides with a reported LVZ at upper-MTZ depths (Contenti et al., 2012). Both the 410 and 660 are depressed from the convergent margin continentward beneath Amazonia. However, depressions of both discontinuities in this region contrast with the expected mineral phase boundary perturbations in the presence of a cold, slab-controlled MTZ, thus raising questions about a temperature-dominated origin. Upon closer examination, a dominant 660 depression north of 15°S ($>$20 km) is primarily responsible for the thickened MTZ that extends to the western edge of the Parnaíba basin and tapers off southward toward central Chile (Figure 4.7d). This MTZ anomaly only exhibits a modest positive spatial correlation ($\leq$0.54) with the S velocity perturbations (Figure C.2). The lack of a stronger correlation likely suggests compositional heterogeneities associated with the accumulation of sub-horizontally deflected slab fragments, a similar case to those observed in the northwestern Pacific (Gu et al., 2012; X. Li & Yuan, 2003).

Systematic changes in MTZ width between the northern (the Peruvian slab) and southern (the Chilean slab) portions of the Nazca slab suggest contrasting styles of slab-MTZ interactions. Unlike the north where significant MTZ thickening is observed, the interaction between the Chilean slab south of 20°S and the 660 appears to cause minimal deformations east of the WBZ. This finding is consistent with earlier reports based on receiver functions (K. H. Liu et al., 2003) and tomographic inversions (Fukao & Obayashi, 2013; Scire et al., 2016), which favor temperature-induced MTZ thickening within the WBZ but exhibit no evidence of stagnation toward the east. The contrasting north-south MTZ topography is corroborated by plate reconstructions, which generally predict an earlier and northward subduction initiation along the northern Andes at 5°S (Y.-W. Chen et al., 2019).

4.5.2 Variations in Seismic Reflectivity and Composition

To improve observational constraints on lateral variations in the MTZ composition, we construct interpolated reflectivity maps using S410S and S660S amplitudes (Figure 4.8). The precursor amplitudes are defined as amplitudes in ± 15 s time windows centered on the PREM-predicted arrival times relative to the onset of SS. In general, both S410S and S660S amplitudes are relatively uniform and high ($>5\%$) beneath the Eastern Pacific Ocean basins. Highly reflective zones are revealed beneath (1) vast oceanic regions, (2) east of the Brazilian Shield, and (3) the central Atlantic. On the other hand, large-scale low reflectivity zones are present beneath Amazonia at both the top and the bottom of the MTZ where the 410 and 660 are $\sim$20 km deeper than the regional average. The below-average amplitudes ($\sim$2%) within this region, which are clearly visible along the transect (Figure 4.7d), are robust in view of the modest uncertainties (with a median of 0.3% for S410S and 0.4% for S660S). The lowest S410S and S660S amplitudes are observed in the southern portion of the Amazon basin and the Bolivian orocline, respectively, showing a 73–83% decrease from the PREM predictions and a 41–72% decrease from the stacks of surrounding areas. The severity of amplitude reduction favors compositional variations, as only a small portion of the reductions (16–24%) can be attributed to incoherent stacking in view of (1) modest mantle heterogeneity corrections and (2) near-constant topographies on the two mineral phase boundaries (Contenti et al., 2012) within each bin. Despite an earlier report of a hydrated zone atop the 410 (that is, a ‘melt lens’) that has previously been suggested to reduce the S410S amplitudes (Schmerr & Garnero, 2007), assessments of the reflection amplitudes have thus far been qualitative in this region.

To provide more quantitative assessments of the amplitudes, we regroup the waveforms into a subset containing midpoint reflections centered in a 1000-km radius cap (Cap 1; see Figures 4.2c and 4.9b for the location) beneath the back-arc

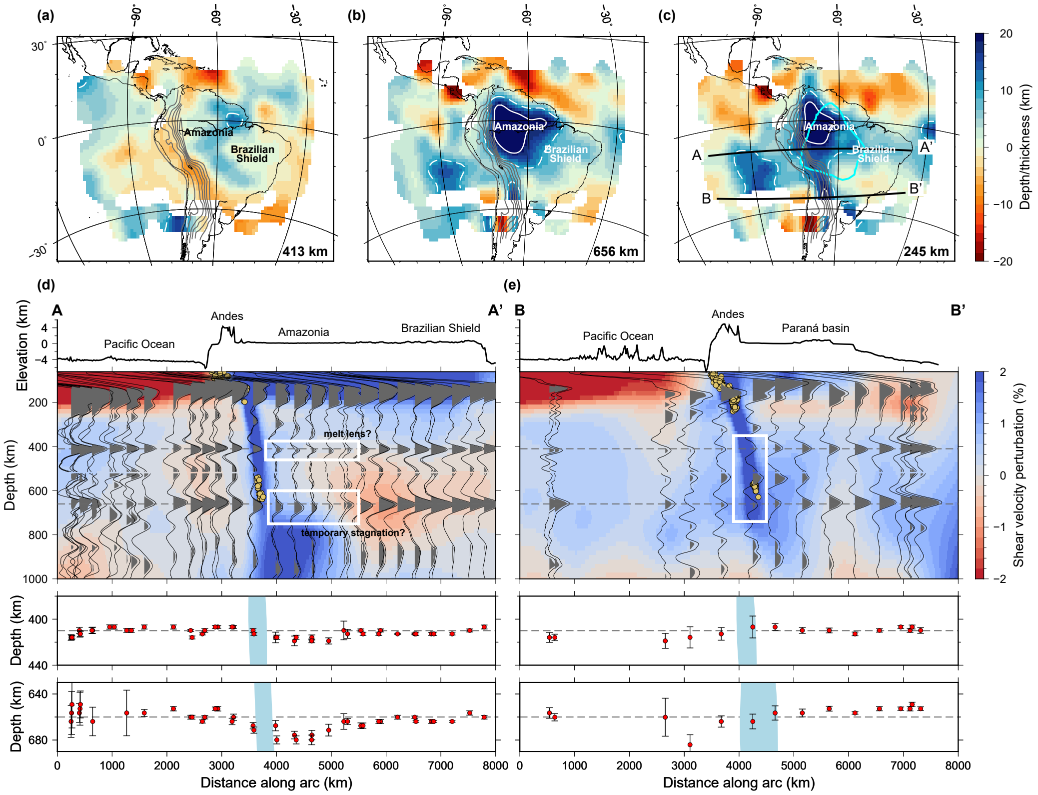

Figure 4.7: Cross-sections of the MTZ velocities and discontinuities. (a-c) Topography of (a) the 410, (b) the 660, and (c) MTZ thickness. The depth estimates are shown relative to the regional average values at the bottom right corner of each panel. The dashed and solid white lines indicate the +10 and +20 km contours, respectively. The cyan curve outlines the boundary of the earlier reported melt lens (Schmerr & Garnero, 2007). The slab contours (thin gray curves) from the Slab2 model (Hayes et al., 2018) are taken at a constant interval of 100 km. The thick black lines indicate the surface projections of cross-sections A-A′ in (d) and B-B′ in (e). The S40RTS tomographic model (Ritsema et al., 2011) is used for upper mantle heterogeneity correction. (d, e) Cross-sections along (d) profile A-A′ and (e) B-B′ superimposed on the S wave velocity perturbations from the TX2019slab model (Lu et al., 2019). The top panel shows the stacked SS waveforms with the 95% confidence intervals from bootstrap resampling (black shaded areas beneath the curves). The bathymetry/topography along the profile is plotted above the cross-sections, and the yellow circles show the Benioff zone seismicity. The dashed lines represent the average depths of the 410 and 660. The lower two panels below the tomographic cross-sections are expanded views of the discontinuity depths (with their respective standard deviations). The light blue shaded areas denote the Benioff zone based on velocity perturbations $\geq 1.2\%$. Key observations are highlighted using white boxes.

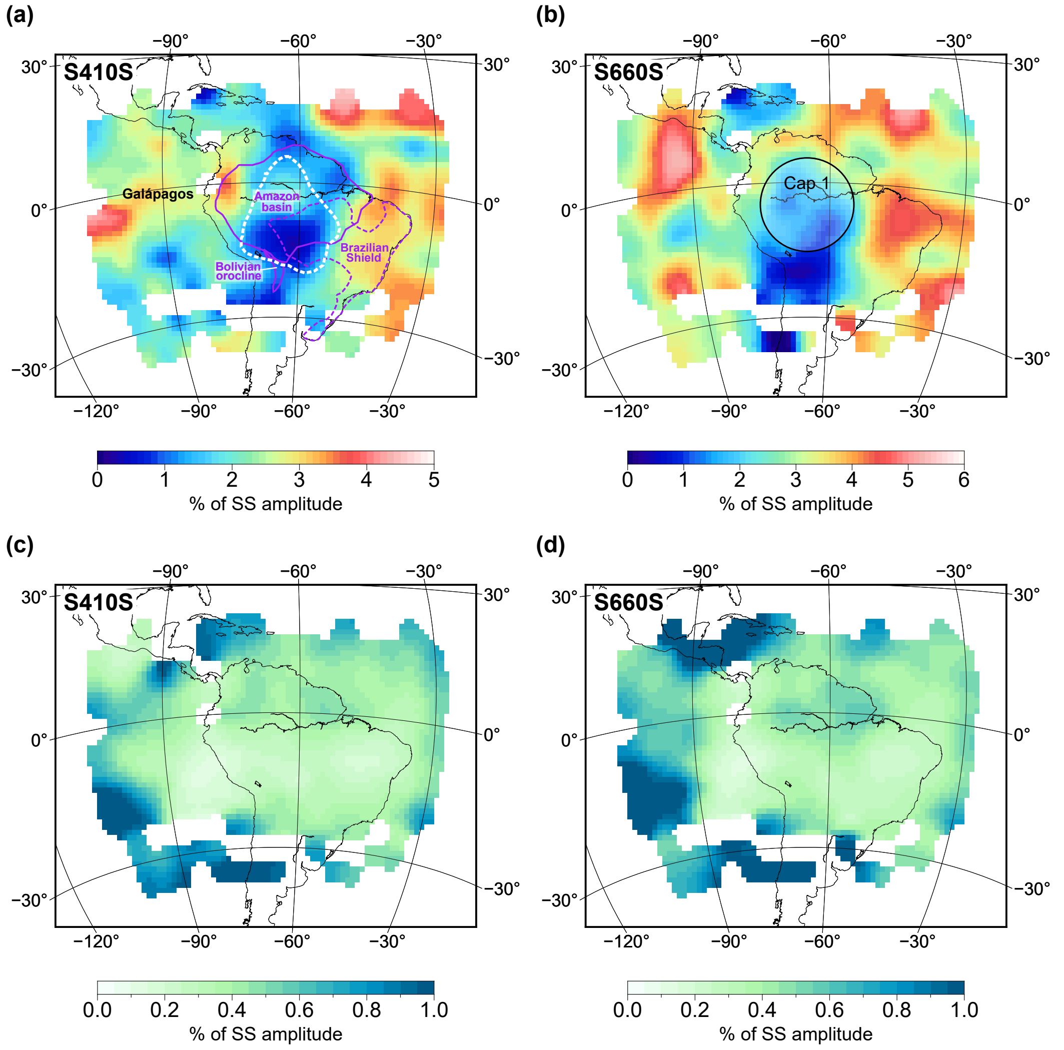

Figure 4.8: Lateral variations in reflection amplitudes of SS precursors. Panels (a) and (b) are interpolated amplitude maps of S410S and S660S, respectively. The precursor amplitudes are normalized to those of SS. The white dashed contour highlights the boundary of the melt lens (Schmerr & Garnero, 2007), and the magenta lines outline major tectonic domains. The black circle marks the location of Cap 1 that is used for amplitude inversions. The uncertainties of (c) S410S and (d) S660S amplitudes are obtained by a bootstrap resampling test.

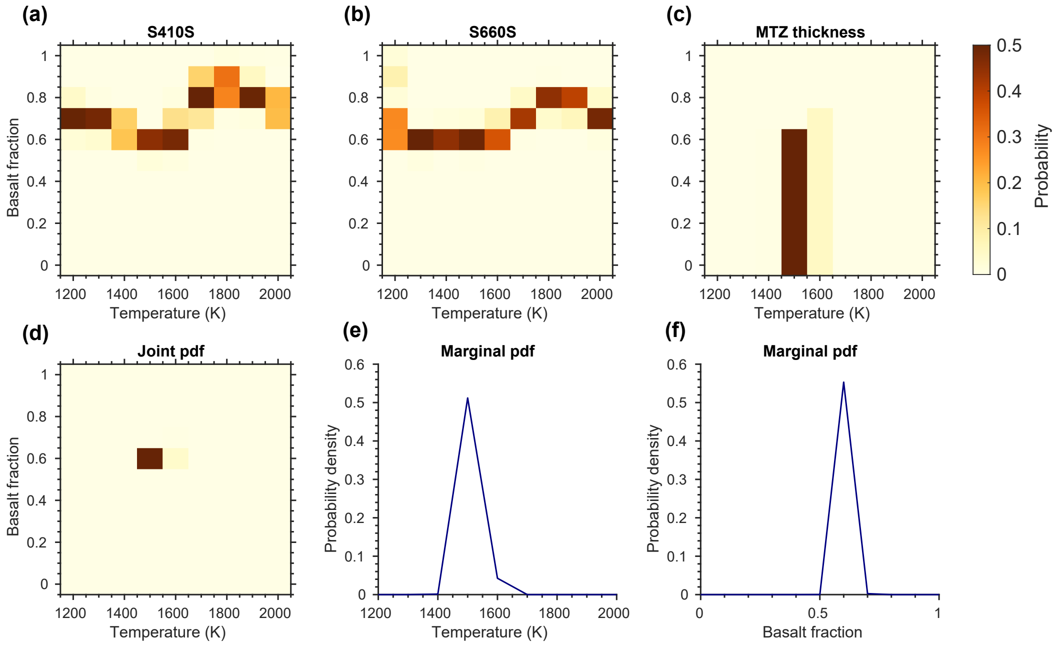

Figure 4.9: Probabilistic inversion for mantle temperature and composition (in terms of the fraction of basalt) for an MM model. (a) The likelihood function (misfit between the observed and predicted measurements) of the S410S amplitudes. (b) Likelihood of the S660S amplitudes. (c) Likelihood of the MTZ thickness. (d) The cumulative posterior probability density function (PDF). Panels (e) and (f) show the marginal posterior probability distributions for potential temperature and basalt fraction, respectively. Dark colors in (a-d) indicate high probabilities.

region of the Nazca-South American subduction zone. The statistical inversion is applied to the CMP stack to infer composition and thermal structure. The MAP solution for the MM model occurs at $T_p = 1500$ K and $f = 0.6$ (Figure 4.9). The T_p estimate is in excellent agreement with the range of 1560 ± 70 K for this region from a recent mantle thermal model based on SS and PP data (Waszek et al., 2021). Though the EA model also supports a basalt-enriched composition ($f = 0.5$), the inferred T_p is 300 K higher than that from the MM model (Figure C.7). A hot MTZ is unlikely due to (1) inconsistency with the earlier reported low temperatures (K. H. Liu et al., 2003; Waszek et al., 2021) and (2) a preference for MM over EA when comparing thermal fields (Ritsema et al., 2009; Waszek et al., 2021).

In a parallel effort, joint inversion of basalt fraction and water content favors a dominant basalt fraction of $f = 0.7$ and hydration to about 20% of the maximum water storage capacity in the MTZ (0.13 wt% water in olivine at 410 km, 0.65

wt% in wadsleyite, and 0.33 wt% in ringwoodite) (Figure C.8). However, in this inversion c_w is characterized by a wide distribution with a standard deviation of 32% (1.1 wt% uncertainty of water contained in wadsleyite). This solution is less certain, however, given the significant uncertainty in the estimated water content and the inherent limitations of the modeling in HyMaTZ.

4.5.3 Validation

We further validate T_p and f estimates from the statistical inversion by comparing the velocity and density jumps at the MTZ discontinuities. Instead of summing all traces into one single stack, we measure the precursor amplitudes along 1° epicentral distance bins across the intervals where precursory arrivals are devoid of interference phases. After correcting for geometric spreading, attenuation, and incoherent stacking, we apply our proposed AVO inversion to measure ΔV_S and $\Delta\rho$ across the 410 and 660. The best-fitting models are determined to be $\Delta V_S = 3.7 \pm 8.5\%$ and $\Delta\rho = 0.9 \pm 0.4\%$ for the 410 (Figures 4.10a and 4.10b) and $\Delta V_S = 3.1 \pm 3.3\%$ and $\Delta\rho = 3.3 \pm 0.5\%$ for the 660 (Figures 4.10c and 4.10d).

To ascertain our inverted elasticity contrasts, we construct a 1-D stack by summing all the time-corrected traces within Cap 1. We then modify PREM with our inverted velocity and density jumps across the 410 and 660 and compute synthetic seismograms using the reflectivity method (Fuchs & Müller, 1971). For both discontinuities, the model predictions based on the AVO-inverted velocity and density contrasts fit the observed amplitudes with 95% confidence level, whereas the PREM synthetics clearly lie outside the error bound (Figure C.9).

The inverted jumps of both discontinuities are significantly lower than the corresponding predicted values from PREM and pyrolite as well as earlier estimates using global stacks (Lawrence & Shearer, 2006; Shearer & Flanagan, 1999). The ΔV_S and $\Delta\rho$ for the MAP model (a mechanically mixed mantle with $T_p = 1500$ K and $f = 0.6$) closely match the results from AVO inversion within the 95% confidence ellipses. Taken together, our model favors a relatively cool MTZ with a higher basaltic concentration in the back-arc of Nazca subduction.

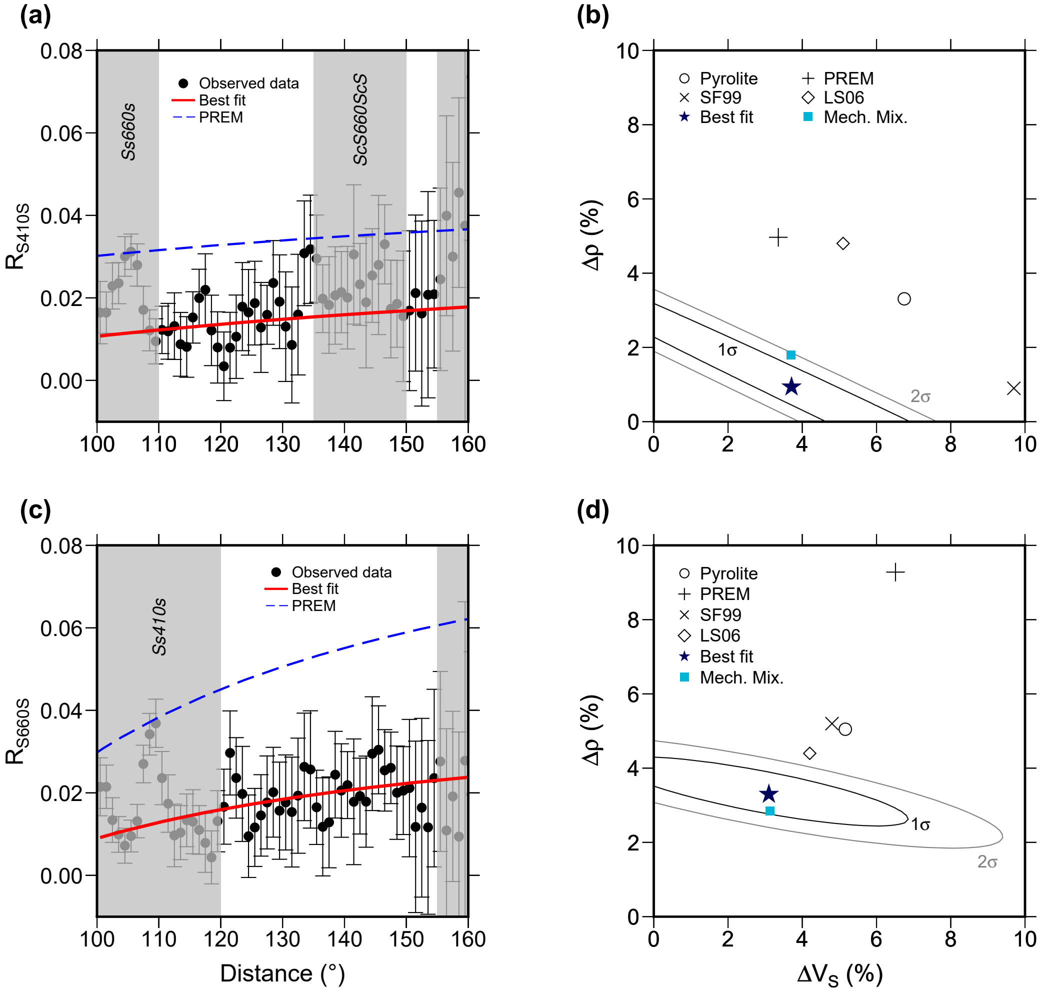

Figure 4.10: AVO inversion of density and shear velocity perturbations across the discontinuities for Cap 1. The cap location is shown in Figure 4.1. (a, c) The resulting reflection coefficients of (a) S410S and (c) S660S are shown as black circles with their corresponding standard deviations (error bars). The best-fitting theoretical curves are shown using red lines. These reflection coefficients have been corrected for geometric spreading, attenuation, and incoherent stacking. The gray shaded areas indicate the distance exclusion windows used in the AVO inversion to minimize the effects of interference phases and unreliable data samples. (b, d) Inverted density and shear velocity perturbations (dark blue stars) across the (b) 410 and (d) 660. The black and gray ellipses indicate the 1σ and 2σ confidence intervals based on chi-square statistics. The best-fitting models are compared with those from the MAP model of the joint inversion (blue squares), PREM (black plus symbols), and pyrolite (black circles). The abbreviation "SF99" represents the global averages (black crosses) reported by Shearer and Flanagan (1999), and "LS06" denotes the global estimates (black diamonds) from Model I of Lawrence and Shearer (2006).

4.6 Discussion

4.6.1 An Integrate Model of MTZ Slab Dynamics

This study benefits from a probabilistic inversion and an inversion-based AVO analysis that accurately determine variations in mantle temperature and composition. Our inversion outcomes, which provide greater constraints on mantle composition than traditional travel-time-based approaches, suggest thermochemical anomalies in the MTZ beneath South America (Figure 4.11). Due to the proximity of this region to the ongoing Nazca subduction, the transport of compositional heterogeneity is likely achieved through entrainment during subduction-induced downwelling. For decades it has been suggested that subducted oceanic crust is separated from its harzburgitic residue and gravitationally segregates at the base of the MTZ, which has been evidenced by both seismological observations (W. Wu et al., 2019) and geodynamic models (Christensen & Hofmann, 1994). The formation of this garnet-rich layering is associated with density profiles where basalt is denser than the surrounding mantle except for the top 100 km below the 660 (Hirose et al., 1999; Irifune & Ringwood, 1993). The segregation of oceanic crust is promoted when local mantle viscosity is sufficiently small (Karato, 1997), and the basalt-enriched reservoir could serve as a chemical filter to sustain mantle stratification (Yan et al., 2020). In combination with the relatively low $\Delta\rho$ across the 660 which favors whole-mantle convection (Shearer & Flanagan, 1999), our finding of local basalt segregation supports a partially stratified mass and heat transfer between the upper and lower mantle.

As a by-product of plate convergence, water can be transported into the MTZ by downward flow along the slab (Iwamori, 2007) as either hydroxyls or molecular fluids in melts and sub-solidus minerals (Karki et al., 2021). In the case of a water-saturated MTZ, the abundance of fluid would trigger dehydration-induced partial melting above the 410, as suggested by the "water filter" hypothesis (Bercovici & Karato, 2003). The presence of such a partial melt layer can hinder the detection of the olivine-wadsleyite transition and thereby limit the effectiveness of our AVO inversion, as this approach is unable to account for the non-linear variation in reflection coefficients with increasing levels of hydration (see Text C.1). Another major source of uncertainty arises from the assumptions made in the hydrous modeling. The thermodynamic database is parameterized without consideration of the effect of water on the phase proportions. This bias will translate to greater velocity changes and eventually to an overestimation of the water content. Despite these caveats, we cannot rule out the alternative interpretation with up to 0.65 wt% of excess water. It is worth noting that the resulting f and c_w are both higher than our preferred model. While this finding appears to be at odds with the expected response of a shift to a lower f when the MTZ is subject to hydration as both decrease amplitudes, it may be related to (1) increased impedance contrast across the 660 in the hydrous model which predicts higher S660S amplitudes (see Fig. C.4c) and (2) the trade-off between temperature and water where the influence of water may be obscured by temperature variations (Thio et al., 2016).

4.6.2 Structural Analogy to Northeast Asia

Several revealing parallels could be drawn between the Nazca-South American and the northwestern Pacific subduction systems. From a geometric perspective, both convergent margins feature curved geometries along the coastal ranges due to increasing trench retreat toward both ends of each slab (Figures 4.12a and 4.12b; Schellart et al., 2007). In addition to similar trench migration velocities (0–2 cm/yr), shallow dip angle ($\sim 30^{\circ}$), and high seismicity, both subducted slabs show maximum resistance responsible for overriding plate shortening and mountain building at the corner where two strands of the slab meet (Schellart, 2008). At MTZ depths, the two subduction systems mirror one another with a depressed 410 overlying a wide 660 depression, observations that favor compositional variations [see this study and Gu et al. (2012)]. Despite the differences in the onset time of subduction initiation, both subducted oceanic lithospheres contain broad (over 1000 km) stagnated segments at the base of the MTZ and possible partial melting atop the 410 (Figures 4.12e and 4.12f; Revenaugh & Sipkin, 1994; Tauzin et al., 2017).

A notable deviation in the correlation between the two systems is the surface observables. While voluminous intraplate volcanism, most notably the Changbai

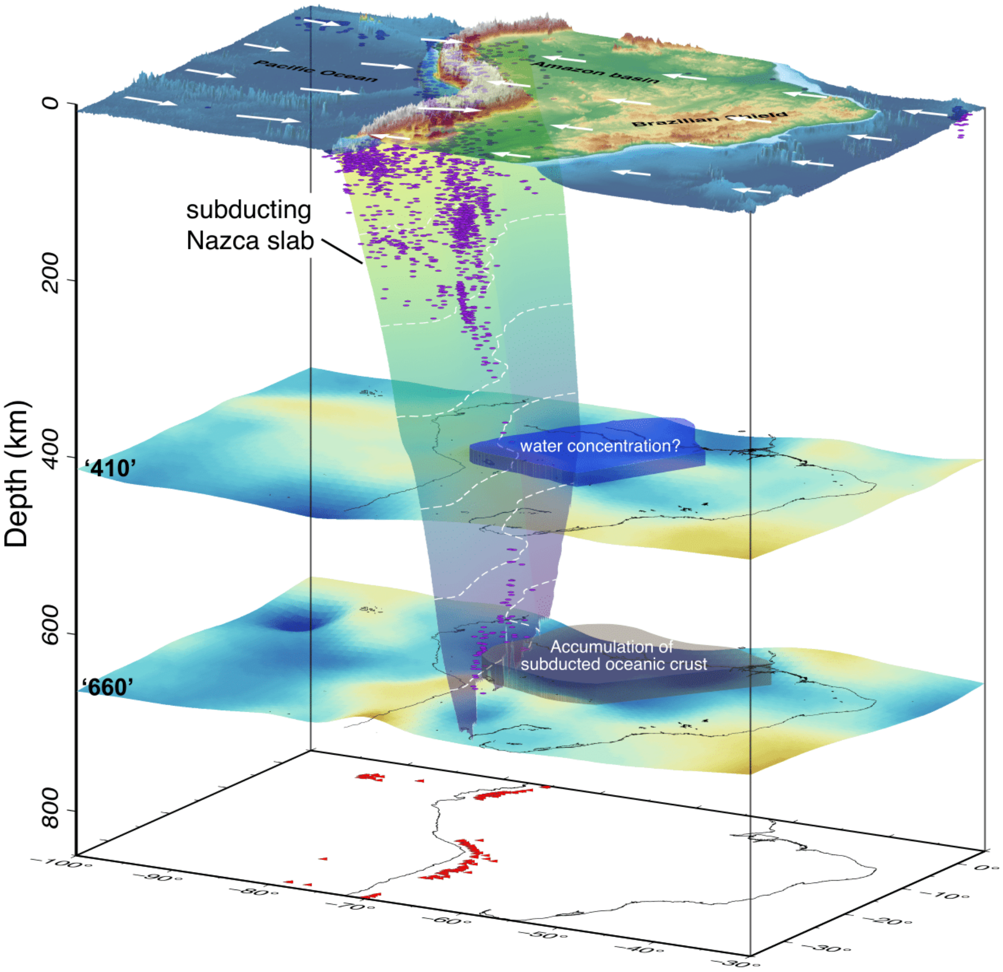

Figure 4.11: A schematic diagram showing compositional enrichment at MTZ depths. The subducted slab then undergoes temporary stagnation above the 660 before plunging into the lower mantle. During this process, the oceanic crust associated with the stagnant slab is likely detached from the lithosphere and causes compositional segregation at the base of the upper mantle beneath the back-arc region. The accumulation of basaltic oceanic crust provides a simple explanation for the observed small impedance contrasts across the 660. The slab subduction might also transport water into the MTZ, resulting in hydrated ($\sim$0.65 wt%) wadsleyite at the top of the MTZ. The white dashed lines show the slab contours, which are taken at 100 km depth intervals starting at 100 km depth (Hayes et al., 2018). The purple circles indicate the locations of the earthquakes, and the red triangles are Holocene volcanoes. Absolute plate velocities in the spreading-aligned reference frame (Becker et al., 2015) are shown as white arrows.

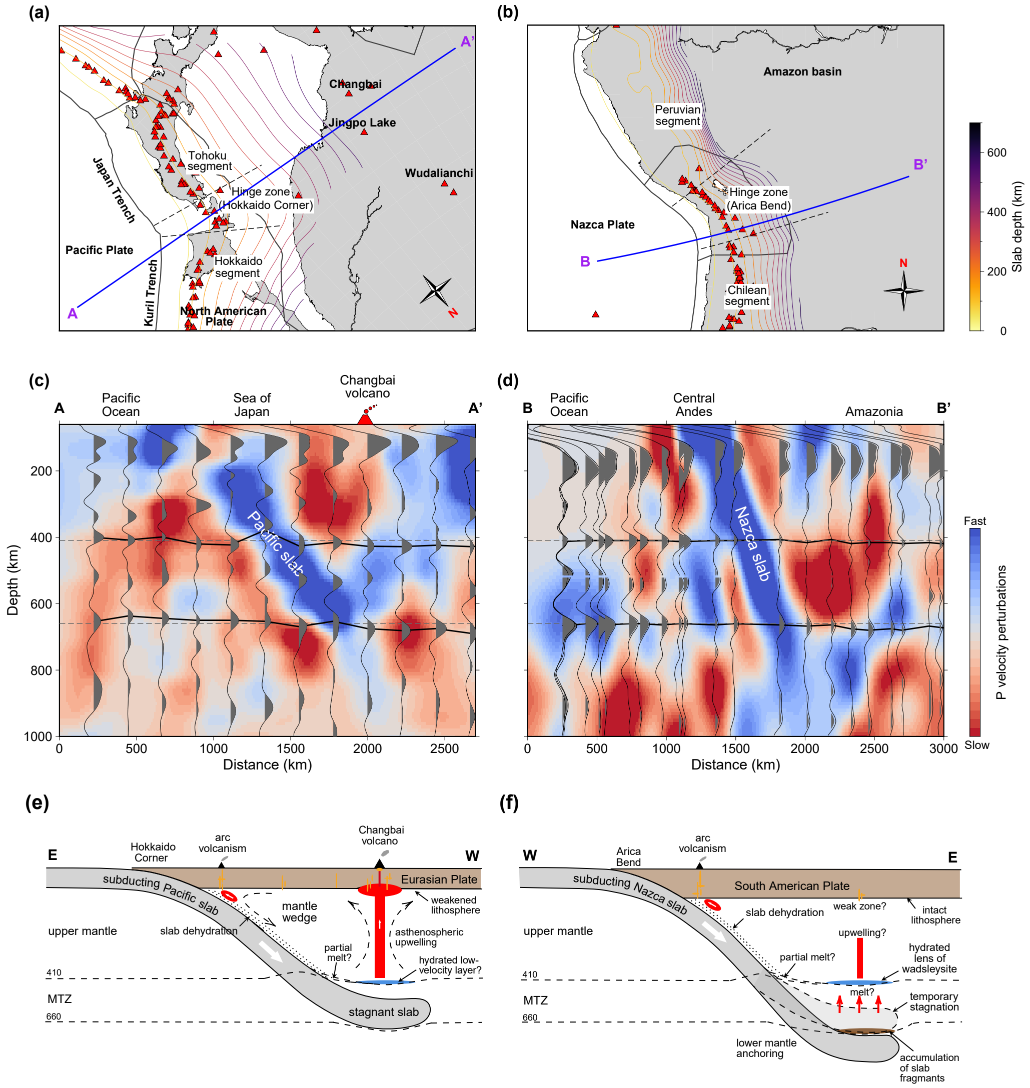
(a)
A
A'
Changbai
Jingpo Lake
Wudalianchi
Tohoku segment
Hinge zone (Hokkaido Corner)
Japan Trench
Pacific Plate
Hokkaido segment
Kuril Trench
North American Plate
N
(b)
Amazon basin
Peruvian segment
Hinge zone (Arica Bend)
Nazca Plate
B
B'
Chilean segment
N
Slab depth (km)
0
200
400
600
(c)
A
A'
Pacific Ocean
Sea of Japan
Changbai volcano
Pacific slab
Depth (km)
200
400
600
800
1000
0
500
1000
1500
2000
2500
Distance (km)
(d)
B
B'
Pacific Ocean
Central Andes
Amazonia
Nazca slab
0
500
1000
1500
2000
2500
3000
Distance (km)
Fast
Slow
P velocity perturbations
(e)
E
W
Hokkaido Corner
arc volcanism
Changbai volcano
Eurasian Plate
subducting Pacific slab
mantle wedge
weakened lithosphere
upper mantle
slab dehydration
asthenospheric upwelling
partial melt?
hydrated low-velocity layer?
410
MTZ
660
stagnant slab
(f)
W
E
Arica Bend
arc volcanism
South American Plate
subducting Nazca slab
slab dehydration
weak zone?
intact lithosphere
upper mantle
upwelling?
hydrated lens of wadsleysite
partial melt?
410
melt?
MTZ
temporary stagnation
660
lower mantle anchoring
accumulation of slab fragments

Mountains and Wudalianchi, could be found thousands of kilometers away from the Japan-Kuril Trench (west of the Hokkaido Corner), back-arc volcanism has been absent along the Nazca-South American convergent zone (east of the Arica Bend). This discrepancy may have resulted from different lithospheric strengths evidenced by a >75 km deficit of effective elastic thickness in northeast Asia (B. Chen et al., 2013) in comparison with the Archean-Neoproterozoic cratonic core beneath Amazonia (Tassara et al., 2007). As recognized in seismic tomography, shear velocity reductions due to hot materials predominantly reside in the upper mantle beneath northeast Asia and its lithospheric roots have experienced extensive Cenozoic modifications due to magmatism (Kang et al., 2016), whereas melt inundation in South America is most likely confined within the MTZ (Figures 4.12c and 4.12d). While slow anomalies potentially extend up to the lithospheric base (Figure 4.12d), the Amazonian craton could remain largely intact due to a thermal boundary layer rich in garnet peridotite in the lowermost lithosphere (Hu et al., 2018).

Figure 4.12 *(Figure appears on preceding page)*: Tectonic maps and mantle tomography of the central South American and northwestern Pacific subduction systems. For a better visual comparison, the map of northeast Asia has been reversed and rotated by 40° counterclockwise. The slab contours (Hayes et al., 2018) are taken at 50 km depth intervals starting at 20 km depth. The thick black lines indicate the plate boundaries (Bird, 2003). The red triangles indicate the locations of Holocene volcanoes. The dashed black lines divide the two regions into three segments. The blue lines indicate the surface projections of cross-sections A-A′ in (c) and B-B′ in (d). (c, d) Cross-sections of P wave velocity perturbations along profiles (c) A-A′ and (d) B-B′ from the tomographic models by C. Li et al. (2008) and Portner et al. (2020), respectively. The discontinuity depths and SS precursor waveforms in (c) are reproduced from Gu et al. (2012). Panels (e) and (f) are schematic cross-sections showing the upper mantle dynamics beneath northeast Asia and South America, respectively. The Pacific plate subduction initiated at 0–30 Myr (X. Liu et al., 2017) and remains stagnant in the MTZ, whereas the Nazca slab may have sunk below the 660 since its subduction period exceeds the maximum stagnation time of 60 Myr (Goes et al., 2017). Partial melting atop the 410 and pockets of subducted oceanic lithosphere above the 660 may be present beneath both regions. However, slab dehydration and convective processes in the mantle wedge above the sinking Pacific slab have resulted in intraplate volcanism beneath the back-arc region of the Japan subduction zone. The cratonic core of the South American plate remains largely intact.

Generally, the interplay between subducted slabs and the MTZ is controlled by various factors such as underlying viscosity structure, slab age, trench mobility, and thermal state of the slab [see Goes et al. (2017) for a review]. Our findings indicate the slab age is not a dominating factor while, instead, both the South American and Japan subduction zones may be experiencing similar ambient mantle conditions (e.g., Clapeyron slope, viscosity jump) that are conducive to a partially stratified convection system hundreds to thousands of kilometers away from the WBZ.

4.7 Conclusions

Our SS precursor analysis has revealed contrasting styles of slab-MTZ interactions beneath northern (i.e., temporary stagnation) and southern South America (i.e., straightforward penetration). Beneath the back-arc of Nazca subduction, we observe depressed 410 and 660 with significantly reduced amplitudes, which cannot be solely explained by thermal anomalies. A joint seismological and mineralogical analysis of the precursor amplitudes and the MTZ thickness suggests basalt accumulation trapped above the 660 with possible water concentrations at the 410 in a non-equilibrated mantle, which is further validated by an AVO inversion approach. The compositional enrichment, in conjunction with slab geometry and overriding plate deformation, suggests the Nazca-South American convergence is analogous to the Pacific plate subduction in northeast Asia as both favor a partially stratified convection system. In short, our study provide a glimpse of the future for imaging the thermal and compositional structure of the mantle based on amplitudes of long-period SS precursors, by improving constraints on density across the MTZ discontinuities. Since the 660 plays a critical role in modulating material flux across the mantle, in Chapter 5 we focus on the 660 and apply the AVO inversion approach to map lateral variations in density jump across the 660.

Chapter 5

Global Variability of Density Jump Across the 660-km Discontinuity From SS Precursors

5.1 Introduction

Density variations within the Earth's mantle, coupled with viscosity, drive mass and heat circulation across internal boundaries to the Earth's surface. Determination of density anomalies has typically relied upon geodynamic observations such as the geoid (Ricard & Bai, 1991; Richards & Hager, 1984), horizontal divergence of plate motions (Ricard et al., 1993), dynamic topography (Forte & Perry, 2000), excess ellipticity of the core-mantle boundary (Forte et al., 1995), and solid Earth tides (Lau et al., 2017). These geophysical and geodetic constraints are complemented by seismic observations, particularly normal mode splitting functions from large earthquakes (e.g., Ishii & Tromp, 1999; Trampert et al., 2004) or a posteriori scaling of tomographically derived velocity variations to those of density (e.g., Karato & Karki, 2001; Koelemeijer et al., 2016; Simmons et al., 2009, 2010). However, due to limited spatial resolution (Kuo & Romanowicz, 2002; Romanowicz, 2001) and non-trivial velocity-to-density scaling relationships (Deschamps et al., 2001; Forte & Perry, 2000), discussions of the resulting density models have been focused on two major high-density provinces, i.e., the "superplumes" under the central Pacific Ocean and Africa (Dziewonski et al., 1993; Su et al., 1994), in the lowermost mantle (e.g., Ishii & Tromp, 1999, 2004; Koelemeijer et al., 2017; Lau et al., 2017; Moulik

& Ekström, 2016). Modest sensitivities of body wave travel times or long-period waveforms, the staples of seismic imaging, to gradients of the physical properties of mantle interfaces remain problematic.

A mantle interface of fundamental importance is the 660 at the base of the MTZ. It directly impacts the mass and heat exchange between the upper and lower mantle (Morgan & Shearer, 1993), a process that plays a pivotal role in the Earth's deep water cycle (Bercovici & Karato, 2003), the fate of subducted slabs (Fukao & Obayashi, 2013), and the mechanisms of deep-focus earthquakes (Frohlich, 1989). Due to the endothermic post-spinel transition, the 660 is expected to deepen and resist further descent of cold subducted oceanic lithospheres and ascent of hot upwelling materials. This pressure-induced phase change also increases seismic velocity and density across the interface (Jeanloz & Thompson, 1983), and both may be further modified through potential compositional variations (Hofmann, 1997; Jeanloz & Knittle, 1989). So far, the topography of the 660 and its association with thermal/compositional variations have been extensively investigated based on arrival times of long-period reflected (e.g., Deuss, 2009; Flanagan & Shearer, 1998; Gu & Dziewonski, 2002; Houser et al., 2008) and converted waves (e.g., Andrews & Deuss, 2008; Chevrot et al., 1999; Tauzin et al., 2008) or surface wave overtone phase velocities (Meier et al., 2009), but amplitude variations (Shearer & Flanagan, 1999) and impedance contrast (Deuss, 2009) across this mineralogical phase boundary are much less certain. Based on the limited information available, the observed jumps across the 660 range from 4.5–10.1% for S wave velocity and 4.2–10.2% for density (e.g., Castle & Creager, 2000; Dziewonski & Anderson, 1981; Estabrook & Kind, 1996; Kato & Kawakatsu, 2001; Lawrence & Shearer, 2006; Matsui, 2001; Montagner & Anderson, 1989; Morelli & Dziewonski, 1993; Shearer & Flanagan, 1999). However, regional-scale estimates (e.g., Castle & Creager, 2000; Kato & Kawakatsu, 2001; Tseng & Chen, 2004; C. Yu et al., 2018) are often at odds with the reported bulk global averages (e.g., Deuss, 2009; Lau & Romanowicz, 2021; Shearer & Flanagan, 1999). Inconsistencies caused by the velocity-density tradeoff, resolution or sensitivity differences among various data types have hampered the efforts to systematically quantify the seismic attributes, particularly density, of the MTZ discontinuities.

Despite the various challenges, amplitude variations of scattered waves from the 660 with the angle of incidence (i.e., source-receiver distance) offer valuable information on the association between the contrasts in elastic parameters and composition. For this reason, this study introduces a processing workflow to constrain the global variations of discontinuity depth, shear velocity and density contrasts across the 660 using SS precursors (S660S; see Figure 4.2a), based largely on the AVO inversion we have derived in Chapter 4. The compilation and investigation of an updated global data set of SS precursors shed new light on the density jumps in connection with subduction and MTZ water content.

5.2 Data Processing

5.2.1 Data Preprocessing

We utilize all available broadband seismograms recorded from 1976 to 2020 at the IRIS Data Management Center for earthquakes with depths less than 45 km and magnitudes of 5.5 or greater (Figure 5.1a). To reduce the effects of interfering phases, we only retain records with epicentral distances between 100° and 170°. After rotating the horizontal components into the radial-transverse coordinate system, we bandpass filter each transverse-component seismogram between 15 and 75 s and resample the trace to 1 Hz. Traces with SNR greater than 3.0 are retained, which are subsequently subjected to visual inspection for duplicate records and overlapping events. Each selected trace is aligned on the first major swing of SS and then normalized to unit amplitude. To further ensure data integrity and accuracy, we generate a reference waveform by stacking handpicked seismograms based on the clarity of SS precursors and only retain records with a correlation coefficient >0.6 relative to the reference waveform (Chambers et al., 2005; Tian et al., 2020). The above procedures result in a refined global data set containing $\sim$110,000 traces, where the coverage is particularly dense in the Pacific Ocean, Northeast Asia, and northern South America (Figure 5.2b).

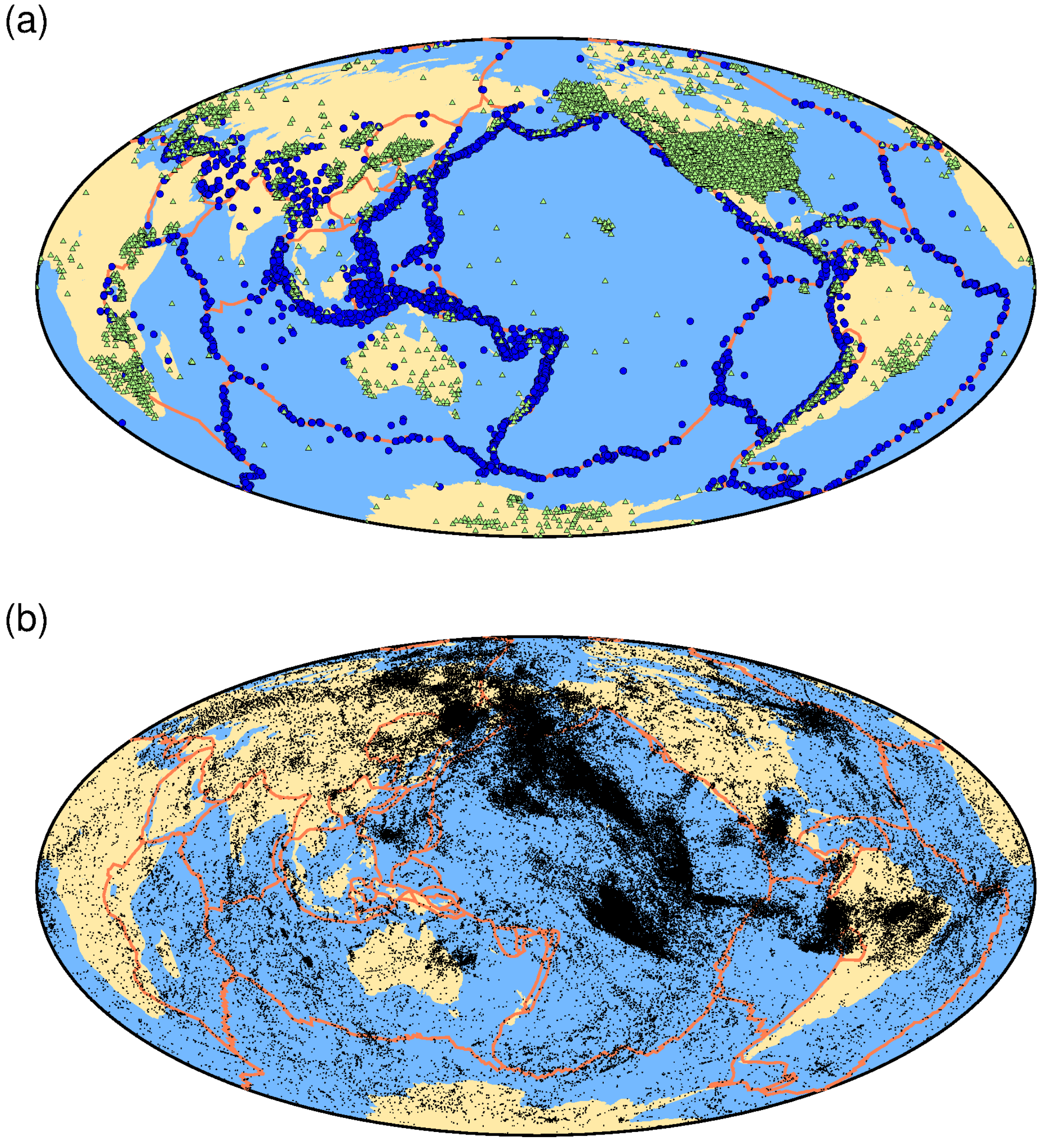

Figure 5.1: (a) Distribution of seismic stations (green triangles) and earthquakes (blue circles) used in this study. (b) Distribution of SS bounce points (black dots). The orange curves denote the plate boundaries (Bird, 2003).

5.2.2 Waveform Stacking

We examine the topography of the 660 and reflection amplitudes by stacking traces within equal-area spherical caps. Based on a global tessellation scheme (Flanagan & Shearer, 1998; Gu & Dziewonski, 2002), we partition the data into 412 caps (10° radius with 5° spacing) and stack all traces with common midpoints after moveout correction to a reference distance of 130°. To reduce the travel time biases and properly retrive the 660 depth, the stacked seismograms are then time-shifted to account for variations in crustal thickness using CRUST1.0 (Laske et al., 2013) and upper mantle velocity structure based on S40RTS (Ritsema et al., 2011). The time-corrected seismograms are then migrated to depth according to travel times predicted by PREM. Our stacking method evaluates the variability of each stack using a bootstrap resampling test (Efron & Tibshirani, 1991) that randomly samples (300 times) the data in each cap, and the depth error estimates are obtained from the standard deviation of the stacks for the bootstrapped data sets.

To maintain a relatively uniform data density, we adopt an alternative cap-averaging scheme consisting of 104 caps of 20° radius (spaced 20° apart) to study global variations of density contrast across the 660. To capture the AVO trends in reflectivity, we pre-condition the data subset within each cap by partially stacking reflections within a 1° distance window. The precursors within the epicentral distance range of 100°–120° are excluded to minimize the contamination of interference phases (Schmerr & Garnero, 2006), which could introduce significant bias in the amplitudes of the stacked waveforms (Figure 5.2).

5.3 Results

5.3.1 Topography of the 660

After stacking the data in 10°-radius caps using the CMP method, we obtain a mean 660 depth of 654.4 ± 7.7 km globally (Figure 5.3a). The 660 is strongly depressed under the western Pacific and South America, overlapping with known regions of ongoing subduction. The robustness of these two large-scale depressions is ascertained by their small depth errors (<3 km; Figure 5.3b). Depressed 660 is

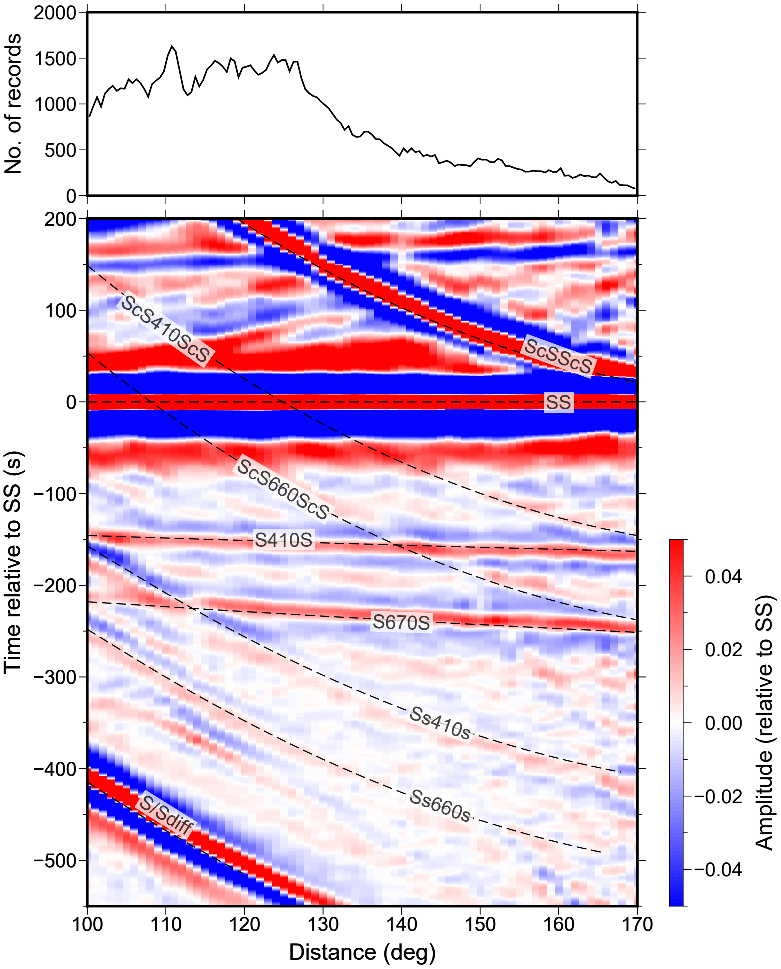

Figure 5.2: Record section of the entire data set stacked in 0.5° distance intervals. Traces are aligned on SS (set to zero time and unit amplitude). Amplitudes are shown relative to SS, with positive amplitudes in red and negative amplitudes in blue. The black dashed curves are theoretical travel times for SS, SS precursors, and other interference phases predicted by PREM. The panel at the top shows the number of records in each distance bin.

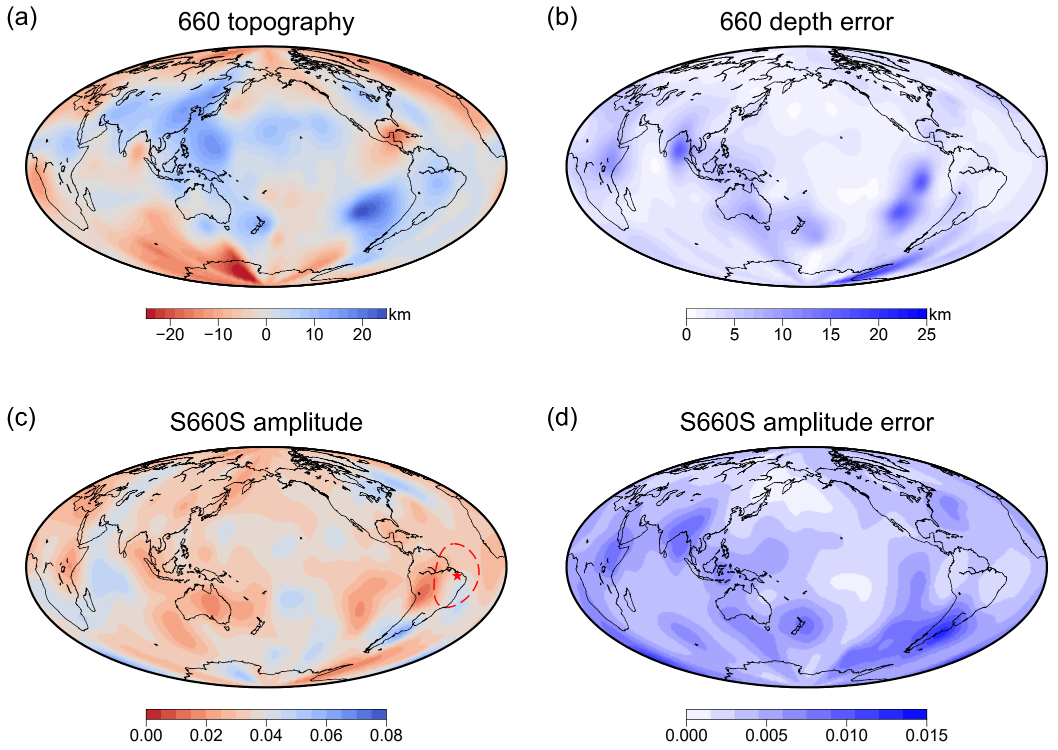

Figure 5.3: (a) Global map of the 660 topography. (b) Standard error of the 660 depth estimates. (c) Lateral variations of S660S/SS amplitude ratios. The red star indicates the geographic location of the cap for the AVO inversion shown in Figures 5.5c and 5.5d. The red dashed circle outlines the actual size of a 20°-radius cap. (d) Standard error of S660S/SS amplitude ratios.

also observed in regions associated with ancient subduction, especially in southern Eurasia associated with the Tethyan subduction during the Cretaceous. On the other hand, the 660 is elevated beneath the Indian Ocean and northern Atlantic by as much as 15 km. Globally, the power spectrum of the depth of the 660 is dominated by the degree 2 spherical harmonics [Figure 5.4a; see also Gu et al. (1998) and Gu et al. (2003)]. The large-scale features of the 660 topography agree well with independent studies using similar data sets (Flanagan & Shearer, 1998; Waszek et al., 2021), though the map of Flanagan and Shearer (1998) shows a stronger degree 1 signature. The positive correlation of >0.7 further confirms the overall agreement among results obtained from SS precursor data (Figure D.1).

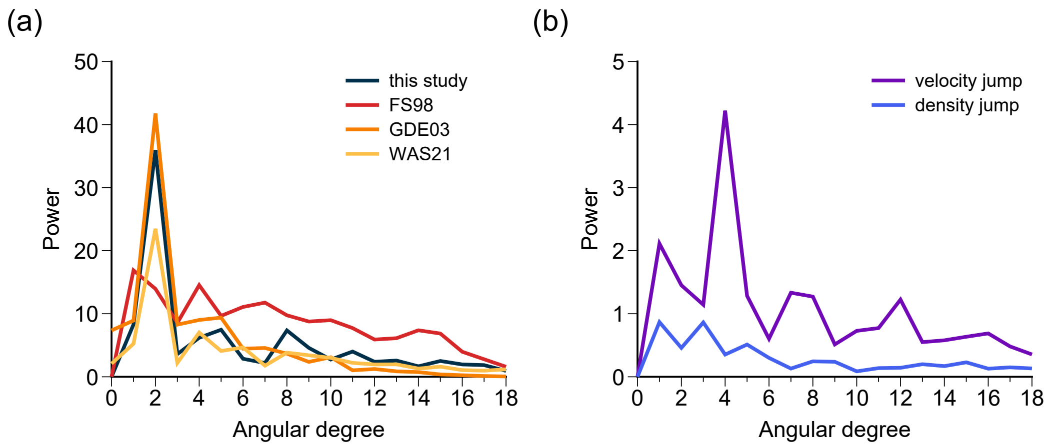

Figure 5.4: (a) Amplitude spectra for the spherical harmonic expansions of the topography of the 660. Our model is compared with those from Flanagan and Shearer (1998) (FS98), Gu et al. (2003) (GDE03), and Waszek et al. (2021) (WAS21). (b) Power spectra of velocity and density jumps across the 660.

5.3.2 Variations of Density Jump

The spatial variations of S660S amplitudes show more scatter compared to those of discontinuity topography (Figure 5.3c). The lack of correlation (~0.07) between S660S amplitudes and the S velocity perturbations at 660 km depth (Figure D.2) suggests minimal thermal effects on precursor amplitudes. This leaves variations in impedance contrast as the primary factor influencing the amplitude variations at the base of the upper mantle.

We determine the global average velocity and density jumps across the 660 from the amplitude-distance trends in reflectivity on the 0.5°-distance stacks of the entire data set. The best fit ΔV_S and $\Delta\rho$ are $4.2 \pm 0.3\%$ and $5.3 \pm 0.2\%$, respectively (Figures 5.5a and 5.5b), which fall outside of the 2σ limits of common 1-D seismic reference models [e.g., PREM and ak135 (Kennett et al., 1995)] but are reasonably consistent with body wave-derived estimates (Lawrence & Shearer, 2006; Shearer & Flanagan, 1999). The pyrolite model fits both parameters better than the piclogite model for the bulk mantle composition. The inverted results are largely independent of the low-pass filter applied to the data set (Figure D.3), as both ΔV_S and $\Delta\rho$ are only marginally increased at the shortest period (5 s) where measurements are more prone to contamination by the high noise level and small-scale mantle

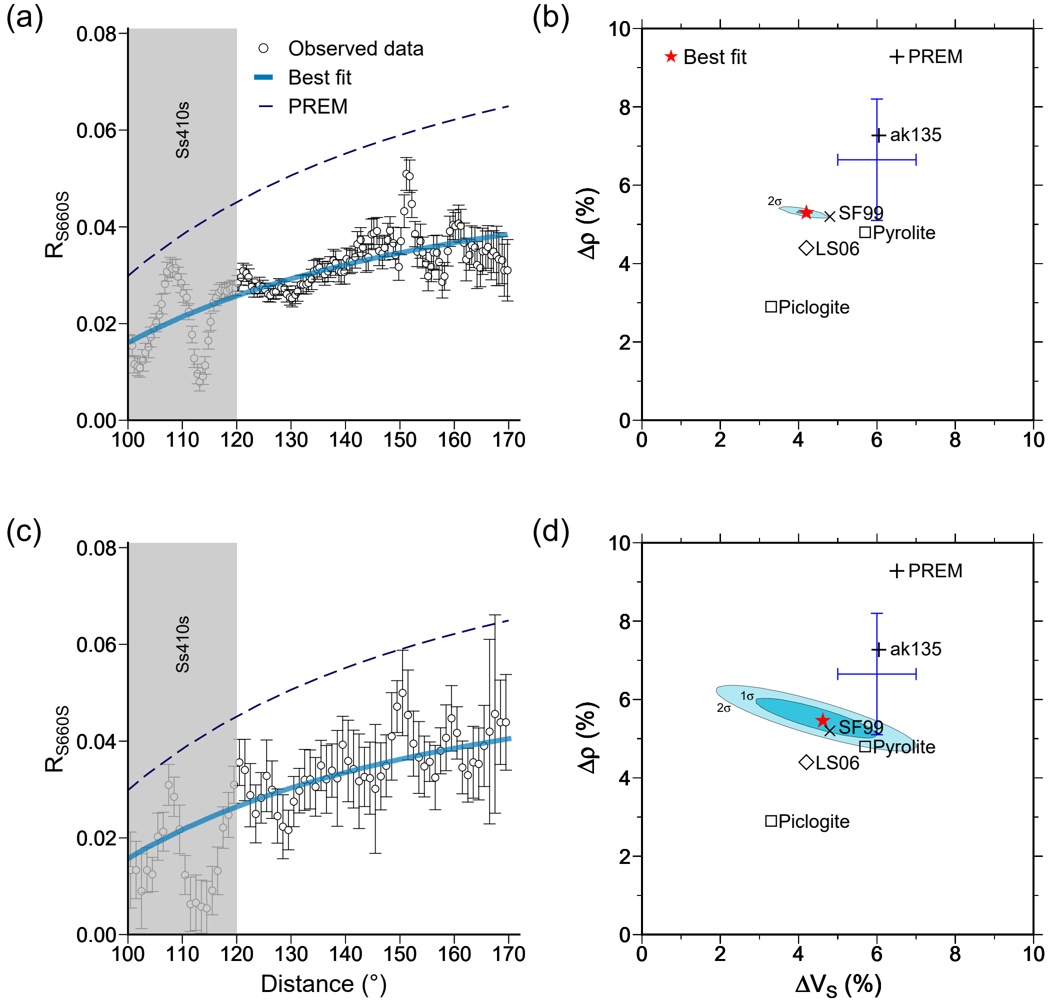

Figure 5.5: AVO inversion of density and shear velocity perturbations across the 660 for (a and b) the entire global data set and (c and d) a data subset in a sample cap. The cap location is shown in Figure 5.3c. (a) The measured S660S reflection coefficients and their standard deviations. These reflection coefficients have been corrected for geometric spreading, attenuation, and incoherent stacking. The best-fitting curve (solid blue line) falls well below the PREM prediction (dashed blue line). The gray shaded area indicates the distance exclusion window to minimize the effect of the interference phase Ss410s. Seismograms are stacked within 0.5° distance bins. (b) Inverted density and shear velocity jumps (red star). The dark and light blue ellipses indicate the respective 1σ and 2σ confidence intervals based on chi-square statistics. The blue error bars indicate the plausible ranges reported by Lau and Romanowicz (2021). Panel (c) is similar to (a) but for the data in the selected cap. Traces are stacked within 1° distance bins. Panel (d) is similar to (b) but for the data in the cap.

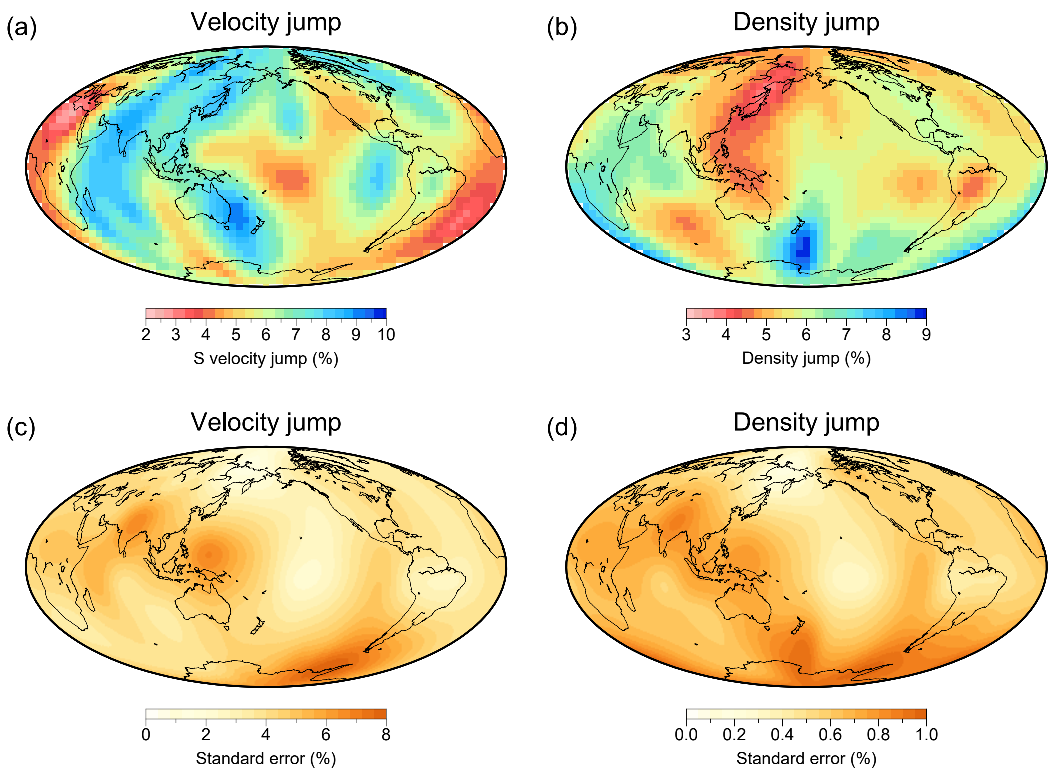

Figure 5.6: Lateral variations of (a) velocity jump and (b) density jump across the 660. Panels (c) and (d) are standard errors of velocity and density jumps, respectively. Note the large (×8) uncertainty scale for velocity jump.

heterogeneity.

We then measure velocity and density jumps in each of the 104 caps (Figures 5.5c and 5.5d) for a complete map of lateral variations in elastis structure. The cap-averaged ΔV_S and $\Delta\rho$ across the 660 are characterized by long-wavelength structures (Figures 5.6). The power of $\Delta\rho$ variations is dominated by low degree (≤ 6) spherical harmonics, while the strongest signals of ΔV_S are concentrated at degree 4 (Figure 5.4b). The uncertainty bounds for 2σ are less than 1% for $\Delta\rho$, whereas ΔV_S is less reliable due to limited sensitivity (see Figure 4.5) and large errors (with a median of 5.6%; Figures 5.6c and 5.6d). The increased uncertainty of $\Delta\rho$ is also evident from individual inversions (Figure 5.5d). For this reason, we will exclusively focus on variations in $\Delta\rho$, the best constrained parameter by AVO inversions. In major subduction zones, e.g., near the western Pacific (Japan, Izu-Bonin, and Sumatra) and South America, we identify decreased $\Delta\rho$ ($\sim$4.5%) except south of

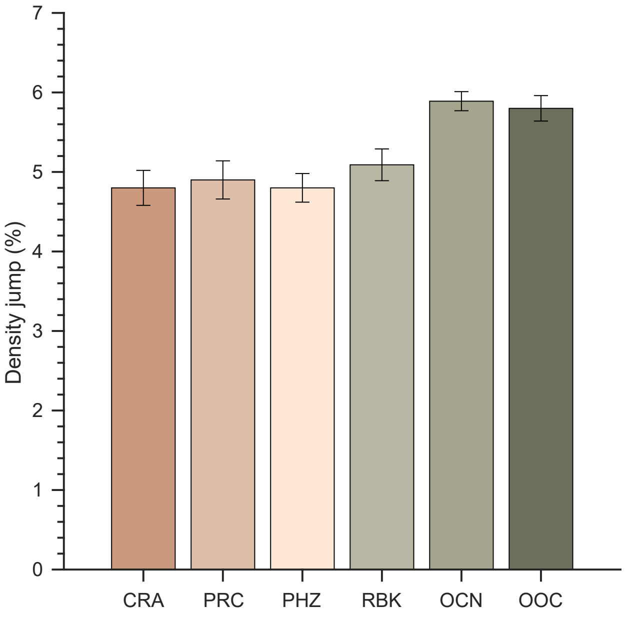

Figure 5.7: The density jumps and standard deviations for six tectonic regimes proposed by the regionalization scheme of Schaeffer and Lebedev (2015). The abbreviated names are defined as follows: CRA, cratons; PRC, Precambrian fold-thrust belts and modified cratons; PHZ, Phanerozoic continents; RBK, ridges and backarcs; OCN, intermediate-aged oceans; OOC, oldest oceans. A notable continent-ocean difference is evident.

New Zealand (up to 8.5%). On the other hand, relatively high $\Delta\rho$ ($\sim$7%) is revealed beneath the Indian Ocean and southern Africa. To further explore the connection between density variations and the tectonic framework, we divide our measurements according to the regionalization scheme of Schaeffer and Lebedev (2015) and find a first-order continent-ocean difference: $\Delta\rho$ is larger under oceanic regions than under continental shields (Figure 5.7).

5.4 Discussion

5.4.1 General Assessment

Taking advantage of vastly improved data coverage (due to a four-decade duration of recordings) and an AVO inversion approach, we are able to impose new constraints on lateral variations of density contrast across the 660. This finding marks a notable improvement over previous studies of density that largely targeted global average measurements. This pilot study directly targets changes in elasticity con-

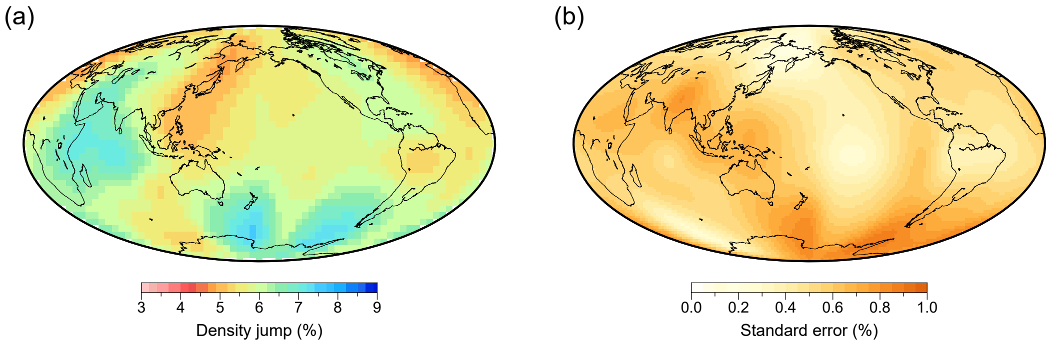

Figure 5.8: Inverted (a) density jump and (b) its standard error, assuming a scaling ratio $\nu = \Delta V_S/\Delta\rho = 0.81$. The correlation coefficient between the results from unconstrained (Figure 5.6b) and constrained inversions is 0.79.

trasts over a depth interval across the boundary (Chambers et al., 2005; Shearer & Flanagan, 1999).

A closer examination of the inversion outcomes reveals a strong trade-off between ΔV_S and $\Delta\rho$, as highlighted by the elongated confidence ellipses (Figures 5.5b and 5.5d). This velocity-density trade-off has been well documented in both body wave (Shearer & Flanagan, 1999) and normal mode analysis (Kuo & Romanowicz, 2002; Resovsky & Trampert, 2003). To test the robustness of our model and mitigate the trade-off, we apply a constrained AVO inversion to the binned data set by assuming a scaling factor to describe ΔV_S variations of $\nu = \Delta V_S/\Delta\rho = 0.81$. This factor is obtained by averaging ν values from several seismic reference models, including PREM, ak135, iasp91 (Kennett & Engdahl, 1991), and STW105 (Kustowski et al., 2008). The consistency between variations in density jump from constrained and unconstrained inversions (Figure 5.8) is supported by an excellent correlation coefficient of 0.79. Overall, the inverted $\Delta\rho$ variations are minimally impacted by the trade-off, though the strengths of $\Delta\rho$ are slightly underestimated owing to the reduced degree of freedom to fit the reflection coefficients in the constrained inversion.

5.4.2 Comparison With Seismic Tomography

To ensure the robustness of the key findings in this study, we compare the map of AVO-inverted density jump and tomography-inferred density variations from a recent mantle tomographic model (ME16; Moulik & Ekström, 2016); using depth-dependent velocity-to-density scaling factors $R_{\rho,S} = \delta \ln \rho / \delta \ln V_S$ and a new collection of dispersion measurements of multi-orbit Rayleigh (R3-R5) and Love (G3-G5) waves, the latter model provides greater constraints on the upper mantle structure than models based solely on mode splitting data. The tomographically derived $\Delta\rho$ is modeled as the contrasts between densities in the lower MTZ (600 km) and in the uppermost lower mantle (700 km) (Figure 5.9b). Since most tomographic models are radially parameterized using low-order B splines, the resulting changes of velocity/density gradients may be projected to greater depth intervals due to depth smoothing. To first order, the tomographic estimates share consistent features with our model, most notably decreased density contrasts in the western Pacific and the anomalously high values south of New Zealand. While regional differences exist under North America and the southern Indian Ocean, a quantitative comparison based on hit count shows an overall correlation of 0.6 between degree 6 variations (Figure 5.9e).

5.4.3 Physical Implications

Due to the negative Clapeyron slope of the ringwoodite dissociation reaction, the 660 would be depressed in response to cold subducted materials that impinge upon the base of the MTZ (Deuss, 2009). Within subduction zones, both global- and regional-scale seismic tomography offer ample evidence that slabs have either penetrated into the lower mantle or sub-horizontally deflected at the base of the upper mantle (Fukao & Obayashi, 2013; van der Hilst et al., 1997). At first glance, regions of decreased density jump correspond to the approximate locations of subducted slabs from the Slab2 model (Hayes et al., 2018), especially beneath the western Pacific and South America. To assess the statistical significance of our observations, we use hit count and perform a correlation analysis between the below-average density jumps and slab contours that are truncated to degree 10. A moderate correlation of 0.50 is obtained (Figure 5.9f), which implicates subducted slabs as a plausible source of the observed reduction in density jump. In particular, the basaltic crust of subduction slabs relative to the underlying peridotite can trigger a density crossover

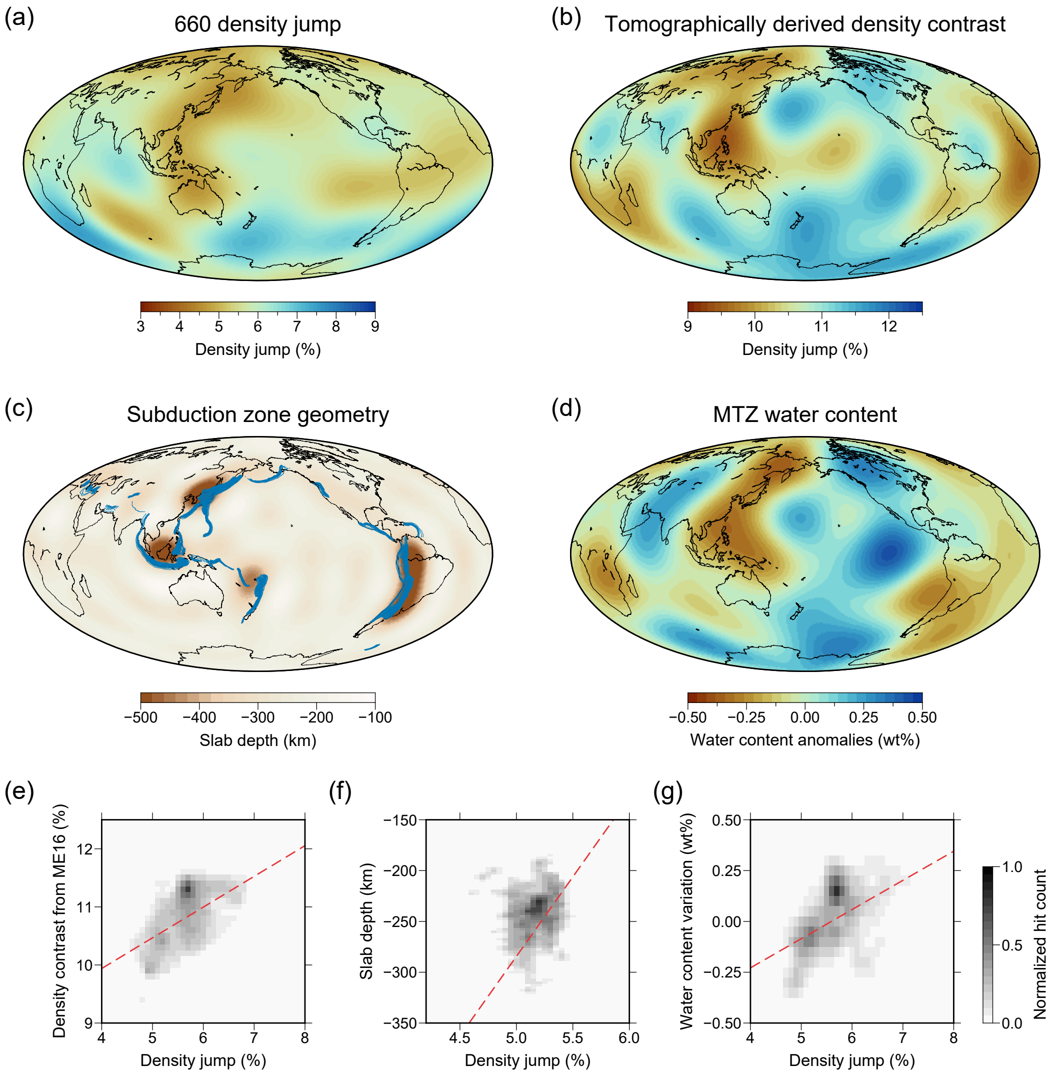

Figure 5.9: (a) A smoothed map of $\Delta\rho$ (Figure 5.6) after a spherical harmonic expansion up to degree 6. (b) Tomographically derived $\Delta\rho$ from the model ME16 after a similar expansion to (a). (c) A low-pass filtration of slab contours from the Slab2 model (Hayes et al., 2018) up to degree 10. (d) MTZ water content anomalies (Meier et al., 2009) expanded to degree 6. (e-g) Correlation between low-pass filtered $\Delta\rho$ and (e) those from the tomographic model ME16, (f) slab depths, and (g) MTZ water content. The color shows the normalized hit counts of grid points. The dashed red lines represent least squares regressions computed using grids after removing outliers (number of hits below threshold values).

at 660 km depth. The crossover conditions of post-spinel and post-garnet transformations could facilitate the segregation of basalt from its harzburgitic residue and gravitational trapping in the MTZ (Anderson, 1979; Ringwood & Irifune, 1988). Alternatively, non-olivine minerals such as ilmenite may also affect $\Delta\rho$, but these phases could be seismically masked by (1) their broad depth range and (2) amplitudes that are comparable to uncertainty levels, resulting in lower values than mineralogical predictions (Vacher et al., 1998).

To further investigate the effect of composition on density jump, we extend the work presented in Chapter 4 on modeling mantle elastic properties [see also Waszek et al. (2021)] and compile a database of density jump across the 660 (Figure 5.10). We assume that the mantle is comprised of a mechanical mixture of basalt and harzburgite that is preferred for subduction zones (Ritsema et al., 2009) where decreased density jumps are found. Globally, the modeling results suggest that the bulk density jump (5.3%) is consistent with a basalt fraction of 18%, which is in excellent agreement with that of pyrolite (Xu et al., 2008). For subduction zones, low density jumps of as much as $4.4 \pm 0.3\%$, which correspond to a basalt fraction of $34 \pm 6\%$, favor a moderately basalt-enriched MTZ.

It has long been suggested that, as a by-product of plate convergence, water is brought into the MTZ by downward flow along the slab (Iwamori, 2007) in the form of either hydroxyls or molecular fluids in melts and sub-solidus minerals (Karki et al., 2021). According to various seismic observations, the MTZ can be grossly characterized as hydrated (van der Meijde et al., 2003), dry (Houser, 2016), or partly hydrated away from subduction zones (Meier et al., 2009). Incorporation of water in nominally anhydrous MTZ minerals that make up 60% of the pyrolite composition would strongly affect their elastic properties, thereby perturbing the elastic structures of the MTZ. Lateral variations of density jump moderately correlate (0.49) with those of water content from the global model of Meier et al. (2009), which could be evidence for the causal association between water content and density jump. This positive correlation is further supported by a quasi-linear relationship between the two variables from thermodynamic modeling, where the addition of one weight percent of water would increase the density jump across the

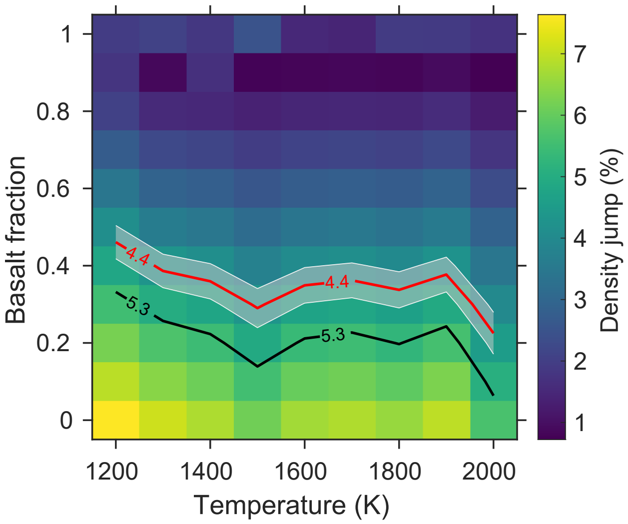

Figure 5.10: Predicted density jump across the 660 for different potential temperature and basalt fractions based on the assumption that the mantle composition is considered as a mechanical mixture of basalt and harzburgite (Xu et al., 2008). The black line is the 5.3% contour, which represents the bulk global average. The red line denotes the contour of the average density jump in subduction zone areas (4.4%) with its uncertainty (white shaded area).

660 by ∼0.7% (see Figure D.4). Despite significant discrepancies among previous studies regarding the distribution of water in the MTZ, density contrast may be more indicative of hydration in the MTZ than other commonly adopted seismic observables such as velocity or discontinuity topography. The apparent link between water and density jump has been corroborated by recent experimental results on high-pressure single-crystal elasticity of wadsleyite (Buchen et al., 2018).

5.5 Conclusions

We present new constraints on density jump across the 660 using AVO inversions. Globally averaged wave speed and density jumps are consistent with those of previous studies and pyrolite. Maps of velocity and density jumps exhibit strong lateral variations and are dominated by long-wavelength patterns. The below-average density jumps and the reported locations of subducted slabs are moderately correlated, implying a potential chemical origin due to basalt enrichment. Contributions from compositional heterogeneities are further supported by a similar level of correlation between density jump and MTZ water distribution from Meier et al. (2009).

From a technical standpoint, the principles used for our AVO inversion could be readily extended to other seismic phases, e.g., P-to-S conversions or PP precursors. Future improvements to our study could be made by (1) incorporating MTZ anisotropy (Huang et al., 2019; Trampert & van Heijst, 2002), which may be significant at shorter epicentral distances but its influences on reflection coefficients remain poorly understood or (2) combining multiple data types with different sensitivities to MTZ discontinuities (Lawrence & Shearer, 2006).

Chapter 6

Conclusions and Outlook

6.1 Conclusions

The increasing availability and fidelity of array data have substantially improved our ability to resolve source properties and map seismic structures across all spatial scales. This thesis applies data-oriented approaches to explore microseismic event detection and location, the structure and evolution of the continental crust, and MTZ discontinuities. The key observations and interpretations of each chapter are briefly summerized below and followed by suggestions on future work.

Chapter 2 characterizes the March 2019 Red Deer induced earthquake swarm using (1) high-precision earthquake relocation to examine the spatial relationship and (2) focal mechanisms to assess source characteristics. We utilize a combined data set from a temporary nodal array and nearby broadband seismic stations and detect a cluster of 417 events using a machine-learning phase picker and an earthquake association and location algorithm. The near-field nodal data enable us to determine the fault-plane solutions for low-magnitude earthquakes based on double-couple components using first-motion polarities and amplitude ratios. The event distribution and the resolved focal mechanisms unveil a NE trending rupture area with two strike-slip fault planes. Reactivation of pre-existing faults by pore pressure diffusion is likely responsible for the occurrence of the earthquake sequence. The temporal sequence of reactivated fault orientations suggests apparent changes in the local stress field after the mainshock. We also observe a remotely triggered cluster one month after the mainshock, which offers further evidence for stress perturbations associated with pressure redistribution due to aseismic slip and/or the HF operation. This secondary triggering process highlights the need to consider trailing seismicity during risk assessment. In summary, quick-response nodal deployment provides an improved understanding of the relationship between HF-induced seismicity and the background geological framework in western Canada.

Chapter 3 examines both the isotropic and anisotropic structures beneath southwestern Canada by jointly analyzing fundamental mode Rayleigh and Love wave dispersion measurements retrieved from ambient noise cross correlation. We take advantage of more than 10 years of continuous recordings from 118 broadband stations from regional networks that became available recently. Love wave group velocity maps at 8–20 s are well correlated with those of Rayleigh waves at similar periods, both showing strong spatial correlations with the sedimentary strata and the underlying basement domains. In the shallow crust, the V_{SV} and V_{SH} maps exhibit predominantly low shear velocities beneath foreland basins with extensive sediment deposition, and the pattern transitions into high-velocity crust underneath the Proterozoic terranes across most of northern Alberta. The widespread negative anisotropy in the Foreland Belt, which may have resulted from thrust faulting due to horizontal compression during plate convergence, supports a thick-skinned Cordillera-Craton transition. We also identify strong, positive radial anisotropy beneath the southern Canadian Cordillera, which is indicative of strong horizontal crustal deformation associated with Eocene extension similar to that observed in the western United States. Overall, the shear velocity and radial anisotropy of the exotic terranes are distinct from those of the Foreland, which provide updated seismic constraints on the location and geometry of the Cordillera-Craton transition.

Motivated by the existing controversy about the fate of subducted oceanic lithosphere, Chapter 4 investigates the mantle reflectivity structure beneath South America and surrounding oceans based on a large data set of SS precursors. The topographic variations of MTZ discontinuities reveal contrasting styles of slab-MTZ interactions along the convergent margin: temporary stagnation in the north and straightforward penetration in the south. We find diminished reflection amplitudes beneath the Amazon basin that disfavor a thermal origin. We then combine the arrival times and amplitudes of SS precursors with mineral physics modeling to constrain the MTZ composition. The presence of the low-amplitude anomaly requires a chemically unequilibrated and basalt-enriched MTZ, which is further verified using a novel AVO inversion approach. Our findings offer direct observational evidence for compositional heterogeneities in the mantle, suggesting a partially stratified material transfer between the upper and lower mantle.

Chapter 5 presents an updated model of the 660 topography and a new model of shear velocity and density contrasts across the 660. Results of our analysis based on AVO inversions show that the average bulk velocity and density jumps across the 660 are consistent with those of pyrolite. Lateral variations of density jump show good agreement with those derived from a recent tomographic model. In major subduction zones near the western Pacific (Japan, Izu-Bonin, and Sumatra) and South America, we identify decreased density jumps in regions with severely depressed 660, which are both associated with the accumulation of cold oceanic lithosphere at the base of the upper mantle. Comparisons with mineral physics predictions indicate basalt enrichment ($\sim$34% in fraction) in the MTZ beneath subduction zones. A moderate correlation between MTZ water content and density jump implies the potential of the latter as a mantle hydration detector. Overall, amplitudes of SS precursors offer a new diagnostic tool for imaging the thermal and compositional structure of the mantle.

6.2 Future Directions

Our study on the characterization of HF-induced seismicity near Red Deer benefits from a well-trained neural network-based phase picker and a sequential earthquake association and location workflow, which are already assembled into an end-to-end location workflow known as LOC-FLOW (M. Zhang et al., 2022). Such methods can be readily applied to other event clusters in the WCSB which remain poorly understood, including but not limited to naturally occurring earthquakes in the Rocky Mountain House Seismogenic Zone (Schultz & Wang, 2020), emerging clusters of wastewater disposal-induced seismicity near Musreau Lake (T. Li et al., 2022), and mining blasts in the Rocky Mountains. It should be noted that our hypoDD relocation only relies on differential travel times of P and S phase picks. A major improvement can be done by combining both catalog differential times and waveform cross-correlation differential times, the latter offering a higher timing precision (M. Zhang et al., 2022). As a natural follow-up, the relocated earthquakes can be used as local sources to image the 3-D velocity structure in the source area of the earthquake sequence for a better understanding of the relationship between seismic activity and the tectonic environment.

Our regional seismic model reveals a sharp Cordillera-Craton transition at crustal depths. One of the key findings is that high velocity and negative anisotropy characterize the Foreland Belt. This anomaly indicates a compositional difference relative to other morphological belts of the Canadian Cordillera and warrants further investigations. Future efforts should be directed toward improving resolution of the basement structure. Our crustal model can be refined by incorporating Rayleigh and Love group and phase velocities from ambient noise or earthquake data (e.g., Moschetti et al., 2010), thereby providing sensitivity to greater depths. Joint inversion of surface wave dispersion curves and receiver functions (e.g., Julia et al., 2000), which combines both sensitivities, can be a natural direction to determine the shear velocity structure. On the other hand, more advanced techniques can be adopted to enhance the quality and robustness of the images. For instance, future work can benefit from adjoint tomography (also known as full waveform inversion) that requires accurate 3-D sensitivity kernels computed by the spectral element method instead of a ray-theoretical approach (e.g., Fichtner et al., 2009, 2010; Tape et al., 2009; K. Wang et al., 2018).

We combine a large data set of SS precursors with thermodynamic modeling to investigate the interaction between the subducted slab and the MTZ beneath the Nazca-South American subduction zone. This joint seismological and mineralogical analysis can be directly applied to other tectonically active regions, for example, the northwestern Pacific which represents an archetypal example of active subduction and central Pacific where the Hawaiian plume is located. In addition, the stability and accuracy of our AVO inversion can be improved by adding P-P constraints and jointly inverting for the elastic properties (P/S velocity and density jumps) of MTZ discontinuities. The combined analysis of arrival times and amplitudes can also be expanded to other reflected phases to study other discontinuities with sudden increases in seismic velocity and density, such as the Lehmann discontinuity at around 220 km depth, the X-discontinuity (250–350 km depth), and the inner core boundary. Two known sources of errors in our analysis include (1) the trade-off between seismic velocity and discontinuity topography and (2) the velocity-density trade-off. Waveform inversion offers a potential solution to both technical issues (Dokht et al., 2016). Expanding the analysis to exploit full waveform information would enable us to simultaneously constrain the velocity and density structure as well as discontinuity topography.

References

Agius, M. R., & Lebedev, S. (2014). Shear-velocity structure, radial anisotropy and dynamics of the Tibetan crust. *Geophysical Journal International*, *199*(3), 1395–1415.

Aki, K., & Richards, P. G. (2002). *Quantitative seismology*. Mill Valley, CA: University Science Books.

Alberta Energy Regulator. (2019). Recommendations around hydraulic fracturing in the Red Deer area. *AER Bulletin 2019-07*. Retrieved from `https://static.aer.ca/prd/documents/bulletins/Bulletin-2019-07.pdf`

Allen, P. A. (2011). Surface impact of mantle processes. *Nature Geoscience*, *4*(8), 498–499.

Amante, C., & Eakins, B. W. (2009). *ETOPO1 1 arc-minute global relief model: Procedures, data sources and analysis* (Tech. Rep.). National Geophysical Data Center, NOAA.

Anderson, D. L. (1965). Recent evidence concerning the structure and composition of the Earth's mantle. *Physics and Chemistry of the Earth*, *6*, 1–131.

Anderson, D. L. (1979). Chemical stratification of the mantle. *Journal of Geophysical Research*, *84*(B11), 6297–6298.

Anderson, D. L., & Dziewonski, A. M. (1982). Upper mantle anisotropy: evidence from free oscillations. *Geophysical Journal International*, *69*(2), 383–404.

Andrews, J., & Deuss, A. (2008). Detailed nature of the 660 km region of the mantle from global receiver function data. *Journal of Geophysical Research: Solid Earth*, *113*(B6).

Archibald, D. A., Krogh, T. E., Armstrong, R. L., & Farrar, E. (1984). Geochronology and tectonic implications of magmatism and metamorphism, southern Kootenay Arc and neighbouring regions, southeastern British Columbia. Part II: Mid-Cretaceous to Eocene. *Canadian Journal of Earth Sciences*, *21*(5), 567-583.

Atkinson, G. M., Eaton, D. W., Ghofrani, H., Walker, D., Cheadle, B., Schultz, R., et al. (2016). Hydraulic fracturing and seismicity in the Western Canada Sedimentary Basin. *Seismological Research Letters*, *87*(3), 631–647.

Atkinson, G. M., Eaton, D. W., & Igonin, N. (2020). Developments in understanding seismicity triggered by hydraulic fracturing. *Nature Reviews Earth & Environment*, *1*(5), 264–277.

Bachu, S. (1993). Basement heat flow in the Western Canada Sedimentary Basin. *Tectonophysics*, *222*(1), 119–133.

Baisch, S., Koch, C., & Muntendam-Bos, A. (2019). Traffic light systems: To what extent can induced seismicity be controlled? *Seismological Research Letters*, *90*(3), 1145–1154.

Bao, X., & Eaton, D. W. (2015). Large variations in lithospheric thickness of western Laurentia: Tectonic inheritance or collisional reworking? *Precambrian Research*, *266*, 579–586.

Bao, X., Eaton, D. W., & Gu, Y. J. (2016). Rayleigh wave azimuthally anisotropic phase velocity maps beneath western Canada. *Journal of Geophysical Research: Solid Earth*, *121*(3), 1821–1834.

Bao, X., Eaton, D. W., & Guest, B. (2014). Plateau uplift in western Canada caused by lithospheric delamination along a craton edge. *Nature Geoscience*, *7*(11), 830–833.

Barmin, M. P., Ritzwoller, M. H., & Levshin, A. L. (2001). A fast and reliable method for surface wave tomography. *Pure and Applied Geophysics*, *158*(8), 1351-1375.

Bastow, I. D., Pilidou, S., Kendall, J.-M., & Stuart, G. W. (2010). Melt-induced seismic anisotropy and magma assisted rifting in Ethiopia: Evidence from surface waves. *Geochemistry, Geophysics, Geosystems*, *11*(6).

Becker, T. W., Schaeffer, A. J., Lebedev, S., & Conrad, C. P. (2015). Toward a generalized plate motion reference frame. *Geophysical Research Letters*, *42*(9), 3188–3196.

Bell, J. S., & Gough, D. I. (1979). Northeast-southwest compressive stress in Alberta evidence from oil wells. *Earth and Planetary Science Letters*, *45*(2), 475–482.

Bell, J. S., & Grasby, S. E. (2012). The stress regime of the Western Canadian Sedimentary Basin. *Geofluids*, *12*(2), 150–165.

Bell, J. S., Price, P. R., McLellan, P. J., Mossop, G. D., & Shetsen, I. (1994). In-situ stress in the Western Canada Sedimentary Basin. In G. D. Mossop & I. Shetsen (Eds.), *Geological Atlas of the Western Canadian Sedimentary Basin* (pp. 439–446). Canadian Society of Petroleum Geologists and Alberta Research Council.

Bensen, G. D., Ritzwoller, M. H., Barmin, M. P., Levshin, A. L., Lin, F., Moschetti, M. P., et al. (2007). Processing seismic ambient noise data to obtain reliable broad-band surface wave dispersion measurements. *Geophysical Journal International*, *169*(3), 1239–1260.

Bensen, G. D., Ritzwoller, M. H., & Shapiro, N. M. (2008). Broadband ambient noise surface wave tomography across the United States. *Journal of Geophysical Research: Solid Earth*, *113*(B5).

Bercovici, D., & Karato, S.-i. (2003). Whole-mantle convection and the transition-zone water filter. *Nature*, *425*(6953), 39–44.

Beyreuther, M., Barsch, R., Krischer, L., Megies, T., Behr, Y., & Wassermann, J. (2010). ObsPy: A Python toolbox for seismology. *Seismological Research Letters*, *81*(3), 530–533.

Bird, P. (2003). An updated digital model of plate boundaries. *Geochemistry, Geophysics, Geosystems*, *4*(3).

Boerner, D. E., Kurtz, R. D., Craven, J. A., Rondenay, S., & Qian, W. (1995). Buried Proterozoic foredeep under the Western Canada Sedimentary Basin? *Geology*, *23*(4), 297–300.

Boerner, D. E., Kurtz, R. D., Craven, J. A., Ross, G. M., & Jones, F. W. (2000). A synthesis of electromagnetic studies in the Lithoprobe Alberta Basement Transect: constraints on Paleoproterozoic indentation tectonics. *Canadian Journal of Earth Sciences*, *37*(11), 1509–1534.

Boerner, D. E., Kurtz, R. D., Craven, J. A., Ross, G. M., Jones, F. W., & Davis, W. J. (1999). Electrical conductivity in the Precambrian lithosphere of western Canada. *Science*, *283*(5402), 668–670.

Brocher, T. M. (2005). Empirical relations between elastic wavespeeds and density in the Earth's crust. *Bulletin of the Seismological Society of America*, *95*(6), 2081–2092.

Brown, R. L., & Gibson, H. D. (2006). An argument for channel flow in the southern Canadian Cordillera and comparison with Himalayan tectonics. In R. D. Law, M. P. Searle, & L. Godin (Eds.), *Channel flow, ductile extrusion and exhumation in continental collision zones, Geological Society of London Special Publications* (Vol. 268, pp. 543–559). Geological Society of London.

Buchen, J., Marquardt, H., Speziale, S., Kawazoe, T., Ballaran, T. B., & Kurnosov, A. (2018). High-pressure single-crystal elasticity of wadsleyite and the seismic signature of water in the shallow transition zone. *Earth and Planetary Science Letters*, *498*, 77–87.

Cahill, T., & Isacks, B. L. (1992). Seismicity and shape of the subducted Nazca plate. *Journal of Geophysical Research: Solid Earth*, *97*(B12), 17503–17529.

Campbell, R. B. (1973). Structural cross-section and tectonic model of the southeastern Canadian Cordillera. *Canadian Journal of Earth Sciences*, *10*(11), 1607–1620.

Cassidy, J. F. (1995). A comparison of the receiver structure beneath stations of the Canadian National Seismograph Network. *Canadian Journal of Earth Sciences*, *32*(7), 938–951.

Castle, J. C., & Creager, K. C. (2000). Local sharpness and shear wave speed jump across the 660-km discontinuity. *Journal of Geophysical Research: Solid Earth*, *105*(B3), 6191–6200.

Chacko, T., De, S. K., Creaser, R. A., & Muehlenbachs, K. (2000). Tectonic setting of the Taltson magmatic zone at 1.9–2.0 Ga: A granitoid-based perspective. *Canadian Journal of Earth Sciences*, *37*(11), 1597–1609.

Chambers, K., Deuss, A., & Woodhouse, J. (2005). Reflectivity of the 410-km discontinuity from PP and SS precursors. *Journal of Geophysical Research: Solid Earth*, *110*(B2).

Chapple, W. M. (1978). Mechanics of thin-skinned fold-and-thrust belts. *Geological Society of America Bulletin*, *89*(8), 1189–1198.

Chen, B., Chen, C., Kaban, M. K., Du, J., Liang, Q., & Thomas, M. (2013). Variations of the effective elastic thickness over China and surroundings and their relation to the lithosphere dynamics. *Earth and Planetary Science Letters*, *363*, 61–72.

Chen, Y., Badal, J., & Zhang, Z. (2009). Radial anisotropy in the crust and upper mantle beneath the Qinghai-Tibet Plateau and surrounding regions. *Journal of Asian Earth Sciences*, *36*(4-5), 289–302.

Chen, Y., Gu, Y. J., Currie, C. A., Johnston, S. T., Hung, S.-H., Schaeffer, A. J., & Audet, P. (2019). Seismic evidence for a mantle suture and implications for the origin of the Canadian Cordillera. *Nature Communications*, *10*(1), 1–10.

Chen, Y., Gu, Y. J., Dokht, R. M. H., & Sacchi, M. D. (2015). Crustal imprints of Precambrian orogenesis in western Laurentia. *Journal of Geophysical Research: Solid Earth*, *120*(10), 6993–7012.

Chen, Y., Gu, Y. J., & Hung, S.-H. (2017). Finite-frequency P-wave tomography of the Western Canada Sedimentary Basin: implications for the lithospheric evolution in Western Laurentia. *Tectonophysics*, *698*, 79–90.

Chen, Y., Gu, Y. J., & Hung, S.-H. (2018). A new appraisal of lithospheric structures of the Cordillera-Craton boundary region in western Canada. *Tectonics*, *37*(9), 3207–3228.

Chen, Y.-W., Wu, J., & Suppe, J. (2019). Southward propagation of Nazca subduction along the Andes. *Nature*, *565*(7740), 441–447.

Chevrot, S., Vinnik, L., & Montagner, J.-P. (1999). Global-scale analysis of the mantle Pds phases. *Journal of Geophysical Research: Solid Earth*, *104*(B9), 20203–20219.

Christensen, U. R., & Hofmann, A. W. (1994). Segregation of subducted oceanic crust in the convecting mantle. *Journal of Geophysical Research: Solid Earth*, *99*(B10), 19867–19884.

Clowes, R. M., Burianyk, M. J. A., Gorman, A. R., & Kanasewich, E. R. (2002). Crustal velocity structure from SAREX, the Southern Alberta Refraction Experiment. *Canadian Journal of Earth Sciences*, *39*(3), 351–373.

Clowes, R. M., Zelt, C. A., Amor, J. R., & Ellis, R. M. (1995). Lithospheric structure in the southern Canadian Cordillera from a network of seismic refraction lines. *Canadian Journal of Earth Sciences*, *32*(10), 1485–1513.

Connolly, J. A. D. (2005). Computation of phase equilibria by linear programming: a tool for geodynamic modeling and its application to subduction zone decarbonation. *Earth and Planetary Science Letters*, *236*(1-2), 524–541.

Contenti, S., Gu, Y. J., Ökeler, A., & Sacchi, M. D. (2012). Shear wave reflectivity imaging of the Nazca-South America subduction zone: Stagnant slab in the mantle transition zone? *Geophysical Research Letters*, *39*(2).

Cook, F. A. (1995). Lithospheric processes and products in the southern Canadian Cordillera: a Lithoprobe perspective. *Canadian Journal of Earth Sciences*, *32*(10), 1803–1824.

Cook, F. A., Clowes, R. M., Snyder, D. B., van der Velden, A. J., Hall, K. W., Erdmer, P., & Evenchick, C. A. (2004). Precambrian crust beneath the Mesozoic northern Canadian Cordillera discovered by Lithoprobe seismic reflection profiling. *Tectonics*, *23*(2).

Courtier, A. M., Gaherty, J. B., Revenaugh, J., Bostock, M. G., & Garnero, E. J. (2010). Seismic anisotropy associated with continental lithosphere accretion beneath the CANOE array, northwestern Canada. *Geology*, *38*(10), 887–890.

Crampin, S. (1981). A review of wave motion in anisotropic and cracked elastic-media. *Wave Motion*, *3*(4), 343–391.

Crampin, S. (1984). Effective anisotropic elastic constants for wave propagation through cracked solids. *Geophysical Journal International*, *76*(1), 135–145.

Crotwell, H. P., Owens, T. J., & Ritsema, J. (1999). The TauP Toolkit: Flexible seismic travel-time and ray-path utilities. *Seismological Research Letters*, *70*, 154–160.

Cui, L., & Atkinson, G. M. (2016). Spatiotemporal variations in the completeness magnitude of the Composite Alberta Seismicity Catalog (CASC). *Seismological Research Letters*, *87*(4), 853–863.

Currie, C. A., Cassidy, J. F., Hyndman, R. D., & Bostock, M. G. (2004). Shear wave anisotropy beneath the Cascadia subduction zone and western North American craton. *Geophysical Journal International*, *157*(1), 341–353.

Dalton, C. A., & Gaherty, J. B. (2013). Seismic anisotropy in the continental crust of northwestern Canada. *Geophysical Journal International*, *193*(1), 338–348.

Dalton, C. A., Gaherty, J. B., & Courtier, A. M. (2011). Crustal V_S structure in northwestern Canada: Imaging the Cordillera-craton transition with ambient noise tomography. *Journal of Geophysical Research: Solid Earth*, *116*(B12).

Davies, G. R., & Smith Jr, L. B. (2006). Structurally controlled hydrothermal dolomite reservoir facies: An overview. *AAPG Bulletin*, *90*(11), 1641–1690.

Davis, E. E., & Lewis, T. J. (1984). Heat flow in a back-arc environment: Intermontane and Omineca Crystalline belts, southern Canadian Cordillera. *Canadian Journal of Earth Sciences*, *21*(6), 715–726.

De, S. K., Chacko, T., Creaser, R. A., & Muehlenbachs, K. (2000). Geochemical and Nd-Pb-O isotope systematics of granites from the Taltson Magmatic Zone, NE Alberta: implications for early Proterozoic tectonics in western Laurentia. *Precambrian Research*, *102*(3-4), 221–249.

De Barros, L., Guglielmi, Y., Rivet, D., Cappa, F., & Duboeuf, L. (2018). Seismicity and fault aseismic deformation caused by fluid injection in decametric in-situ experiments. *Comptes Rendus Geoscience*, *350*(8), 464–475.

DeMets, C., Gordon, R. G., & Argus, D. F. (2010). Geologically current plate motions. *Geophysical Journal International*, *181*(1), 1–80.

Deschamps, F., Snieder, R., & Trampert, J. (2001). The relative density-to-shear velocity scaling in the uppermost mantle. *Physics of the Earth and Planetary Interiors*, *124*(3-4), 193–212.

Deuss, A. (2009). Global observations of mantle discontinuities using SS and PP precursors. *Surveys in Geophysics*, *30*(4), 301–326.

Dickinson, W. R. (2004). Evolution of the North American Cordillera. *Annual Review of Earth and Planetary Sciences*, *32*, 13–45.

Dokht, R. M. H., Gu, Y. J., & Sacchi, M. D. (2016). Waveform inversion of SS precursors: An investigation of the northwestern Pacific subduction zones and intraplate volcanoes in China. *Gondwana Research*, *40*, 77–90.

Dziewonski, A. M., & Anderson, D. L. (1981). Preliminary reference Earth model. *Physics of the Earth and Planetary Interiors*, *25*(4), 297–356.

Dziewonski, A. M., Forte, A. M., Su, W., & Woodward, R. L. (1993). Seismic tomography and geodynamics. In K. Aki & R. Dmowska (Eds.), *Relating Geophysical Structures and Processes: The Jeffreys Volume* (pp. 67–105). American Geophysical Union.

Eaton, D. W., & Cassidy, J. F. (1996). A relic Proterozoic subduction zone in western Canada: New evidence from seismic reflection and receiver function data. *Geophysical Research Letters*, *23*(25), 3791–3794.

Eaton, D. W., Igonin, N., Poulin, A., Weir, R., Zhang, H., Pellegrino, S., & Rodriguez, G. (2018). Induced seismicity characterization during hydraulic-fracture monitoring with a shallow-wellbore geophone array and broadband sensors. *Seismological Research Letters*, *89*(5), 1641–1651.

Efron, B., & Tibshirani, R. (1991). Statistical data analysis in the computer age. *Science*, *253*(5018), 390–395.

Ekström, G., & Dziewonski, A. M. (1998). The unique anisotropy of the Pacific upper mantle. *Nature*, *394*(6689), 168–172.

Elissa Lynn, C., Cook, F. A., & Hall, K. W. (2005). Tectonic significance of potential-field anomalies in western Canada: results from the Lithoprobe SNORCLE transect. *Canadian Journal of Earth Sciences*, *42*(6), 1239–1255.

Estabrook, C. H., & Kind, R. (1996). The nature of the 660-kilometer upper-mantle seismic discontinuity from precursors to the PP phase. *Science*, *274*(5290), 1179–1182.

Eyre, T. S., Eaton, D. W., Garagash, D. I., Zecevic, M., Venieri, M., Weir, R., & Lawton, D. C. (2019). The role of aseismic slip in hydraulic fracturing-induced seismicity. *Science Advances*, *5*(8), eaav7172.

Faccenna, C., Oncken, O., Holt, A. F., & Becker, T. W. (2017). Initiation of the Andean orogeny by lower mantle subduction. *Earth and Planetary Science Letters*, *463*, 189–201.

Fei, H., Yamazaki, D., Sakurai, M., Miyajima, N., Ohfuji, H., Katsura, T., & Yamamoto, T. (2017). A nearly water-saturated mantle transition zone inferred from mineral viscosity. *Science Advances*, *3*(6), e1603024.

Fichtner, A., Kennett, B. L. N., Igel, H., & Bunge, H.-P. (2009). Full seismic waveform tomography for upper-mantle structure in the Australasian region using adjoint methods. *Geophysical Journal International*, *179*(3), 1703–1725.

Fichtner, A., Kennett, B. L. N., Igel, H., & Bunge, H.-P. (2010). Full waveform tomography for radially anisotropic structure: new insights into present and past states of the Australasian upper mantle. *Earth and Planetary Science Letters*, *290*(3-4), 270–280.

Flanagan, M. P., & Shearer, P. M. (1998). Global mapping of topography on transition zone velocity discontinuities by stacking SS precursors. *Journal of Geophysical Research: Solid Earth*, *103*(B2), 2673–2692.

Fordjor, C. K., Bell, J. S., & Gough, D. I. (1983). Breakouts in Alberta and stress in the North American plate. *Canadian Journal of Earth Sciences*, *20*(9), 1445–1455.

Forsyth, D., & Uyeda, S. (1975). On the relative importance of the driving forces of plate motion. *Geophysical Journal International*, *43*(1), 163–200.

Forte, A. M., Mitrovica, J. X., & Woodward, R. L. (1995). Seismic-geodynamic determination of the origin of excess ellipticity of the core-mantle boundary. *Geophysical Research Letters*, *22*(9), 1013–1016.

Forte, A. M., & Perry, H. K. C. (2000). Geodynamic evidence for a chemically depleted continental tectosphere. *Science*, *290*(5498), 1940–1944.

Fox, A. D., & Soltanzadeh, M. (2015). A regional geomechanical study of the Duvernay Formation in Alberta, Canada. In *GeoConvention 2015: New Horizon.* Calgary, AB.

Frohlich, C. (1989). The nature of deep-focus earthquakes. *Annual Review of Earth and Planetary Sciences*, *17*, 227.

Fuchs, K., & Müller, G. (1971). Computation of synthetic seismograms with the reflectivity method and comparison with observations. *Geophysical Journal International*, *23*(4), 417–433.

Fukao, Y., & Obayashi, M. (2013). Subducted slabs stagnant above, penetrating through, and trapped below the 660 km discontinuity. *Journal of Geophysical Research: Solid Earth*, *118*(11), 5920–5938.

Godfrey, N. J., Christensen, N. I., & Okaya, D. A. (2000). Anisotropy of schists: Contribution of crustal anisotropy to active source seismic experiments and shear wave splitting observations. *Journal of Geophysical Research: Solid Earth*, *105*(B12), 27991–28007.

Goes, S., Agrusta, R., van Hunen, J., & Garel, F. (2017). Subduction-transition zone interaction: A review. *Geosphere*, *13*(3), 644–664.

Goldstein, P., & Snoke, A. (2005). SAC availability for the IRIS community. *Incorporated Research Institutions for Seismology Newsletter*, *7*(1).

Goutorbe, B., de Oliveira Coelho, D. L., & Drouet, S. (2015). Rayleigh wave group velocities at periods of 6–23 s across Brazil from ambient noise tomography. *Geophysical Journal International*, *203*(2), 869–882.

Grech, M. G. K., Cheadle, S., & Lawton, D. C. (2001). Integrating borehole information and surface seismic for velocity anisotropy analysis and depth imaging. *The Leading Edge*, *20*(5), 519–523.

Gripp, A. E., & Gordon, R. G. (2002). Young tracks of hotspots and current plate velocities. *Geophysical Journal International*, *150*(2), 321–361.

Gu, Y. J., Chen, Y., Dokht, R. M. H., & Wang, R. (2018). Precambrian tectonic discontinuities in western Laurentia: Broadband seismological perspectives on the Snowbird and Great Falls tectonic zones. *Tectonics*, *37*(5), 1411–1434.

Gu, Y. J., & Dziewonski, A. M. (2002). Global variability of transition zone thickness. *Journal of Geophysical Research: Solid Earth*, *107*(B7), ESE–2.

Gu, Y. J., Dziewonski, A. M., & Agee, C. B. (1998). Global de-correlation of the topography of transition zone discontinuities. *Earth and Planetary Science Letters*, *157*(1-2), 57–67.

Gu, Y. J., Dziewoński, A. M., & Ekström, G. (2003). Simultaneous inversion for mantle shear velocity and topography of transition zone discontinuities. *Geophysical Journal International*, *154*(2), 559–583.

Gu, Y. J., Lerner-Lam, A. L., Dziewonski, A. M., & Ekström, G. (2005). Deep structure and seismic anisotropy beneath the East Pacific Rise. *Earth and Planetary Science Letters*, *232*(3-4), 259–272.

Gu, Y. J., Okeler, A., & Schultz, R. (2012). Tracking slabs beneath northwestern Pacific subduction zones. *Earth and Planetary Science Letters*, *331*, 269–280.

Gu, Y. J., Okeler, A., Shen, L., & Contenti, S. (2011). The Canadian Rockies and Alberta Network (CRANE): New constraints on the Rockies and Western Canada Sedimentary Basin. *Seismological Research Letters*, *82*(4), 575–588.

Gu, Y. J., & Shen, L. (2015). Noise correlation tomography of Southwest Western Canada Sedimentary Basin. *Geophysical Journal International*, *202*(1), 142–162.

Guglielmi, Y., Elsworth, D., Cappa, F., Henry, P., Gout, C., Dick, P., & Durand, J. (2015). In situ observations on the coupling between hydraulic diffusivity and displacements during fault reactivation in shales. *Journal of Geophysical Research: Solid Earth*, *120*(11), 7729–7748.

Guo, Z., Gao, X., Wang, W., & Yao, Z. (2012). Upper- and mid-crustal radial anisotropy beneath the central Himalaya and southern Tibet from seismic ambient noise tomography. *Geophysical Journal International*, *189*(2), 1169–1182.

Gutscher, M.-A., Spakman, W., Bijwaard, H., & Engdahl, E. R. (2000). Geodynamics of flat subduction: Seismicity and tomographic constraints from the Andean margin. *Tectonics*, *19*(5), 814–833.

Hansen, S. M., & Schmandt, B. (2015). Automated detection and location of microseismicity at Mount St. Helens with a large-N geophone array. *Geophysical Research Letters*, *42*(18), 7390–7397.

Hayes, G. P., Moore, G. L., Portner, D. E., Hearne, M., Flamme, H., Furtney, M., & Smoczyk, G. M. (2018). Slab2, a comprehensive subduction zone geometry model. *Science*, *362*(6410), 58–61.

Haynes, M. W., Gorbatov, A., Hejrani, B., Hassan, R., Zhao, J., Zhang, F., & Reading, A. M. (2020). AusArray: imaging the lithospheric mantle using body-wave tomography. In K. Czarnota et al. (Eds.), *Exploring for the future: Extended abstracts* (pp. 1–4). Geoscience Australia.

Heidbach, O., Rajabi, M., Cui, X., Fuchs, K., Müller, B., Reinecker, J., et al. (2018). The World Stress Map database release 2016: Crustal stress pattern across scales. *Tectonophysics*, *744*, 484–498.

Herrmann, R. B. (2013). Computer programs in seismology: An evolving tool for instruction and research. *Seismological Research Letters*, *84*(6), 1081–1088.

Hetényi, G., Molinari, I., Clinton, J., Bokelmann, G., Bondár, I., Crawford, W. C., et al. (2018). The AlpArray seismic network: a large-scale European experiment to image the Alpine orogen. *Surveys in Geophysics*, *39*(5), 1009–1033.

Hirose, K., Fei, Y., Ma, Y., & Mao, H.-K. (1999). The fate of subducted basaltic crust in the Earth's lower mantle. *Nature*, *397*(6714), 53–56.

Hoffman, P. F. (1988). United Plates of America, the birth of a craton-Early Proterozoic assembly and growth of Laurentia. *Annual Review of Earth and Planetary Sciences*, *16*, 543–603.

Hofmann, A. W. (1997). Mantle geochemistry: the message from oceanic volcanism. *Nature*, *385*(6613), 219–229.

Hope, J., & Eaton, D. (2002). Crustal structure beneath the Western Canada Sedimentary Basin: constraints from gravity and magnetic modelling. *Canadian Journal of Earth Sciences*, *39*(3), 291–312.

Houser, C. (2016). Global seismic data reveal little water in the mantle transition zone. *Earth and Planetary Science Letters*, *448*, 94–101.

Houser, C., Masters, G., Flanagan, M., & Shearer, P. (2008). Determination and analysis of long-wavelength transition zone structure using SS precursors. *Geophysical Journal International*, *174*(1), 178–194.

Hsieh, P. A., & Bredehoeft, J. D. (1981). A reservoir analysis of the Denver earthquakes: A case of induced seismicity. *Journal of Geophysical Research: Solid Earth*, *86*(B2), 903–920.

Hu, J., Liu, L., Faccenda, M., Zhou, Q., Fischer, K. M., Marshak, S., & Lundstrom, C. (2018). Modification of the Western Gondwana craton by plume-lithosphere interaction. *Nature Geoscience*, *11*(3), 203–210.

Huang, X., Xu, Y., & Karato, S.-i. (2005). Water content in the transition zone from electrical conductivity of wadsleyite and ringwoodite. *Nature*, *434*(7034), 746–749.

Hyndman, R. D. (2017). Lower-crustal flow and detachment in the North American Cordillera: a consequence of Cordillera-wide high temperatures. *Geophysical Journal International*, *209*(3), 1779–1799.

Inoue, T., Wada, T., Sasaki, R., & Yurimoto, H. (2010). Water partitioning in the Earth's mantle. *Physics of the Earth and Planetary Interiors*, *183*(1-2), 245–251.

Inoue, T., Yurimoto, H., & Kudoh, Y. (1995). Hydrous modified spinel, $Mg_{1.75}SiH_{0.5}O_4$: a new water reservoir in the mantle transition region. *Geophysical Research Letters*, *22*(2), 117–120.

Irifune, T., & Ringwood, A. E. (1993). Phase transformations in subducted oceanic crust and buoyancy relationships at depths of 600–800 km in the mantle. *Earth and Planetary Science Letters*, *117*(1-2), 101–110.

Isaac, J. H., & Lawton, D. C. (1999). Image mispositioning due to dipping TI media: A physical seismic modeling study. *Geophysics*, *64*(4), 1230–1238.

Isacks, B., Oliver, J., & Sykes, L. R. (1968). Seismology and the new global tectonics. *Journal of Geophysical Research*, *73*(18), 5855–5899.

Ishii, M., & Tromp, J. (1999). Normal-mode and free-air gravity constraints on lateral variations in velocity and density of Earth's mantle. *Science*, *285*(5431), 1231–1236.

Ishii, M., & Tromp, J. (2004). Constraining large-scale mantle heterogeneity using mantle and inner-core sensitive normal modes. *Physics of the Earth and*

Planetary Interiors, *146*(1-2), 113–124.

Ito, E., & Katsura, T. (1989). A temperature profile of the mantle transition zone. *Geophysical Research Letters*, *16*(5), 425–428.

Iwamori, H. (2007). Transportation of H_2O beneath the Japan arcs and its implications for global water circulation. *Chemical Geology*, *239*(3-4), 182–198.

Jacobsen, S. D., Smyth, J. R., Spetzler, H., Holl, C. M., & Frost, D. J. (2004). Sound velocities and elastic constants of iron-bearing hydrous ringwoodite. *Physics of the Earth and Planetary Interiors*, *143*, 47–56.

Jeanloz, R., & Knittle, E. (1989). Density and composition of the lower mantle. *Philosophical Transactions of the Royal Society of London. Series A, Mathematical and Physical Sciences*, *328*(1599), 377–389.

Jeanloz, R., & Thompson, A. B. (1983). Phase transitions and mantle discontinuities. *Reviews of Geophysics*, *21*(1), 51–74.

Johnson, B. J., & Brown, R. L. (1996). Crustal structure and early Tertiary extensional tectonics of the Omineca belt at 51°N latitude, southern Canadian Cordillera. *Canadian Journal of Earth Sciences*, *33*(12), 1596–1611.

Johnston, J. E., & Christensen, N. I. (1995). Seismic anisotropy of shales. *Journal of Geophysical Research: Solid Earth*, *100*(B4), 5991–6003.

Julia, J., Ammon, C. J., Herrmann, R. B., & Correig, A. M. (2000). Joint inversion of receiver function and surface wave dispersion observations. *Geophysical Journal International*, *143*(1), 99–112.

Kaneshima, S. (1990). Origin of crustal anisotropy: Shear wave splitting studies in Japan. *Journal of Geophysical Research: Solid Earth*, *95*(B7), 11121–11133.

Kang, D., Shen, W., Ning, J., & Ritzwoller, M. H. (2016). Seismic evidence for lithospheric modification associated with intracontinental volcanism in Northeastern China. *Geophysical Journal International*, *204*(1), 215–235.

Karato, S.-i. (1997). On the separation of crustal component from subducted oceanic lithosphere near the 660 km discontinuity. *Physics of the Earth and Planetary Interiors*, *99*(1-2), 103–111.

Karato, S.-i. (2006). Remote sensing of hydrogen in Earth's mantle. *Reviews in Mineralogy and Geochemistry*, *62*(1), 343–375.

Karato, S.-i. (2008). *Deformation of Earth materials: An introduction to the rheology of solid Earth*. Cambridge, UK: Cambridge University Press.

Karato, S.-i. (2011). Water distribution across the mantle transition zone and its implications for global material circulation. *Earth and Planetary Science Letters*, *301*(3-4), 413–423.

Karato, S.-i., & Karki, B. B. (2001). Origin of lateral variation of seismic wave velocities and density in the deep mantle. *Journal of Geophysical Research: Solid Earth*, *106*(B10), 21771–21783.

Karki, B. B., Ghosh, D. B., & Karato, S.-i. (2021). Behavior and properties of water in silicate melts under deep mantle conditions. *Scientific Reports*, *11*(1).

Karplus, M., & Schmandt, B. (2018). Preface to the focus section on geophone array seismology. *Seismological Research Letters*, *89*(5), 1597–1600.

Kato, M., & Kawakatsu, H. (2001). Seismological in situ estimation of density jumps across the transition zone discontinuities beneath Japan. *Geophysical Research Letters*, *28*(13), 2541–2544.

Kennett, B. L. N., & Engdahl, E. R. (1991). Traveltimes for global earthquake location and phase identification. *Geophysical Journal International*, *105*(2), 429–465.

Kennett, B. L. N., Engdahl, E. R., & Buland, R. (1995). Constraints on seismic velocities in the Earth from traveltimes. *Geophysical Journal International*, *122*(1), 108–124.

Keranen, K. M., Savage, H. M., Abers, G. A., & Cochran, E. S. (2013). Potentially induced earthquakes in Oklahoma, USA: Links between wastewater injection and the 2011 Mw 5.7 earthquake sequence. *Geology*, *41*(6), 699–702.

Kim, D., Lekić, V., Ménard, B., Baron, D., & Taghizadeh-Popp, M. (2020). Sequencing seismograms: A panoptic view of scattering in the core-mantle boundary region. *Science*, *368*(6496), 1223–1228.

Kim, K.-H., Ree, J.-H., Kim, Y., Kim, S., Kang, S. Y., & Seo, W. (2018). Assessing whether the 2017 Mw 5.4 Pohang earthquake in South Korea was an induced event. *Science*, *360*(6392), 1007–1009.

Kissling, E., Ellsworth, W. L., Eberhart-Phillips, D., & Kradolfer, U. (1994). Initial reference models in local earthquake tomography. *Journal of Geophysical Research: Solid Earth*, *99*(B10), 19635–19646.

Knapp, L. J., McMillan, J. M., & Harris, N. B. (2017). A depositional model for organic-rich Duvernay Formation mudstones. *Sedimentary Geology*, *347*, 160–182.

Koelemeijer, P., Deuss, A., & Ritsema, J. (2017). Density structure of Earth's lowermost mantle from Stoneley mode splitting observations. *Nature Communications*, *8*(1), 1–10.

Koelemeijer, P., Ritsema, J., Deuss, A., & van Heijst, H.-J. (2016). SP12RTS: a degree-12 model of shear-and compressional-wave velocity for Earth's mantle. *Geophysical Journal International*, *204*(2), 1024–1039.

Kohlstedt, D., Keppler, H., & Rubie, D. (1996). Solubility of water in the α, β and γ phases of (Mg, Fe)$_2$SiO$_4$. *Contributions to Mineralogy and Petrology*, *123*(4), 345–357.

Kruckenberg, S. C., Whitney, D. L., Teyssier, C., Fanning, C. M., & Dunlap, W. J. (2008). Paleocene-Eocene migmatite crystallization, extension, and exhumation in the hinterland of the northern Cordillera: Okanogan dome, Washington, USA. *Geological Society of America Bulletin*, *120*(7-8), 912–929.

Kuo, C., & Romanowicz, B. (2002). On the resolution of density anomalies in the Earth's mantle using spectral fitting of normal-mode data. *Geophysical Journal International*, *150*(1), 162–179.

Kustowski, B., Ekström, G., & Dziewoński, A. (2008). Anisotropic shear-wave velocity structure of the Earth's mantle: A global model. *Journal of Geophysical Research: Solid Earth*, *113*(B6).

Laske, G., Masters, G., Ma, Z., & Pasyanos, M. (2013). Update on CRUST1.0—- A 1-degree global model of Earth's crust. In *EGU General Assembly 2013*

(Vol. 15, p. 2658). Vienna, Austria.

Lau, H. C. P., Mitrovica, J. X., Davis, J. L., Tromp, J., Yang, H.-Y., & Al-Attar, D. (2017). Tidal tomography constrains Earth's deep-mantle buoyancy. *Nature*, *551*(7680), 321–326.

Lau, H. C. P., & Romanowicz, B. (2021). Constraining jumps in density and elastic properties at the 660 km discontinuity using normal mode data via the Backus-Gilbert method. *Geophysical Research Letters*, *48*(9), e2020GL092217.

Lawrence, J. F., & Shearer, P. M. (2006). Constraining seismic velocity and density for the mantle transition zone with reflected and transmitted waveforms. *Geochemistry, Geophysics, Geosystems*, *7*(10).

Lawrence, J. F., & Shearer, P. M. (2008). Imaging mantle transition zone thickness with SdS-SS finite-frequency sensitivity kernels. *Geophysical Journal International*, *174*(1), 143–158.

Leary, P. C., Crampin, S., & McEvilly, T. V. (1990). Seismic fracture anisotropy in the Earth's crust: An overview. *Journal of Geophysical Research: Solid Earth*, *95*(B7), 11105–11114.

Leidig, M., & Zandt, G. (2003). Modeling of highly anisotropic crust and application to the Altiplano-Puna volcanic complex of the central Andes. *Journal of Geophysical Research: Solid Earth*, *108*(B1), ESE–5.

Lemieux, S., Ross, G. M., & Cook, F. A. (2000). Crustal geometry and tectonic evolution of the Archean crystalline basement beneath the southern Alberta Plains, from new seismic reflection and potential-field studies. *Canadian Journal of Earth Sciences*, *37*(11), 1473–1491.

Leslie, J. M., & Lawton, D. C. (1999). A refraction-seismic field study to determine the anisotropic parameters of shales. *Geophysics*, *64*(4), 1247–1252.

Levshin, A. L., & Ritzwoller, M. H. (2001). Automated detection, extraction, and measurement of regional surface waves. *Pure and Applied Geophysics*, *158*(8), 1531–1545.

Li, C., van der Hilst, R. D., Engdahl, E. R., & Burdick, S. (2008). A new global model for P wave speed variations in Earth's mantle. *Geochemistry, Geophysics, Geosystems*, *9*(5).

Li, T., Gu, Y. J., Wang, J., Wang, R., Yusifbayov, J., Canales, M. R., & Shipman, T. (2022). Earthquakes Induced by Wastewater Disposal near Musreau Lake, Alberta, 2018–2020. *Seismological Research Letters*, *93*(2A), 727–738.

Li, T., Gu, Y. J., Wang, Z., Wang, R., Chen, Y., Song, T.-R. A., & Wang, R. (2019). Spatiotemporal variations in crustal seismic anisotropy surrounding induced earthquakes near Fox Creek, Alberta. *Geophysical Research Letters*, *46*(10), 5180–5189.

Li, X., & Yuan, X. (2003). Receiver functions in northeast China–implications for slab penetration into the lower mantle in northwest Pacific subduction zone. *Earth and Planetary Science Letters*, *216*(4), 679–691.

Lin, F.-C., Li, D., Clayton, R. W., & Hollis, D. (2013). High-resolution 3D shallow crustal structure in Long Beach, California: Application of ambient noise tomography on a dense seismic array. *Geophysics*, *78*(4), Q45–Q56.

Lin, F.-C., Moschetti, M. P., & Ritzwoller, M. H. (2008). Surface wave tomography of the western United States from ambient seismic noise: Rayleigh and Love wave phase velocity maps. *Geophysical Journal International*, *173*(1), 281–298.

Liu, K. H., Gao, S. S., Silver, P. G., & Zhang, Y. (2003). Mantle layering across central South America. *Journal of Geophysical Research: Solid Earth*, *108*(B11).

Liu, M., Zhang, M., Zhu, W., Ellsworth, W. L., & Li, H. (2020). Rapid characterization of the July 2019 Ridgecrest, California, earthquake sequence from raw seismic data using machine-learning phase picker. *Geophysical Research Letters*, *47*(4), e2019GL086189.

Liu, X., Zhao, D., Li, S., & Wei, W. (2017). Age of the subducting Pacific slab beneath East Asia and its geodynamic implications. *Earth and Planetary Science Letters*, *464*, 166–174.

Long, M. D., Levander, A., & Shearer, P. M. (2014). An introduction to the special issue of Earth and Planetary Science Letters on USArray science. *Earth and Planetary Science Letters*, *402*, 1–5.

Lu, C., Grand, S. P., Lai, H., & Garnero, E. J. (2019). TX2019slab: A new P and S tomography model incorporating subducting slabs. *Journal of Geophysical Research: Solid Earth*, *124*(11), 11549–11567.

Ludwig, W. J., Nafe, J. E., & Drake, C. L. (1970). Seismic refraction. In A. E. Maxwell (Ed.), *The sea* (Vol. 4, pp. 53–84). Wiley-Interscience.

Lynner, C., Beck, S. L., Zandt, G., Porritt, R. W., Lin, F.-C., & Eilon, Z. C. (2018). Midcrustal deformation in the Central Andes constrained by radial anisotropy. *Journal of Geophysical Research: Solid Earth*, *123*(6), 4798–4813.

Mainprice, D., & Nicolas, A. (1989). Development of shape and lattice preferred orientations: application to the seismic anisotropy of the lower crust. *Journal of Structural Geology*, *11*(1-2), 175–189.

Majorowicz, J. (2018). Heat flow-heat production relationship not found: what drives heat flow variability of the Western Canadian foreland basin? *International Journal of Earth Sciences*, *107*(1), 5–18.

Majorowicz, J., Chan, J., Crowell, J., Gosnold, W., Heaman, L. M., Kück, et al. (2014). The first deep heat flow determination in crystalline basement rocks beneath the Western Canadian Sedimentary Basin. *Geophysical Journal International*, *197*(2), 731–747.

Majorowicz, J., & Grasby, S. E. (2010). Heat flow, depth-temperature variations and stored thermal energy for enhanced geothermal systems in Canada. *Journal of Geophysics and Engineering*, *7*(3), 232–241.

Mao, Z., Lin, J.-F., Jacobsen, S. D., Duffy, T. S., Chang, Y.-Y., Smyth, J. R., et al. (2012). Sound velocities of hydrous ringwoodite to 16 GPa and 673 K. *Earth and Planetary Science Letters*, *331*, 112–119.

Martínez-Garzón, P., Bohnhoff, M., Kwiatek, G., & Dresen, G. (2013). Stress tensor changes related to fluid injection at The Geysers geothermal field, California. *Geophysical Research Letters*, *40*(11), 2596–2601.

Matsui, M. (2001). Density and bulk sound velocity jumps across the 660 km seismic discontinuity. *Physics of the Earth and Planetary Interiors*, *125*(1-4), 141–146.

McClure, M. W., & Horne, R. N. (2011). Investigation of injection-induced seismicity using a coupled fluid flow and rate/state friction model. *Geophysics*, *76*(6), WC181–WC198.

Meier, U., Trampert, J., & Curtis, A. (2009). Global variations of temperature and water content in the mantle transition zone from higher mode surface waves. *Earth and Planetary Science Letters*, *282*(1-4), 91–101.

Meissner, R., Rabbel, W., & Kern, H. (2006). Seismic lamination and anisotropy of the lower continental crust. *Tectonophysics*, *416*(1-4), 81–99.

Monger, J. W. H., & Price, R. A. (1979). Geodynamic evolution of the Canadian Cordillera–progress and problems. *Canadian Journal of Earth Sciences*, *16*(3), 770–791.

Monger, J. W. H., & Price, R. A. (2002). The Canadian Cordillera: geology and tectonic evolution. *CSEG Recorder*, *27*(2), 17–36.

Montagner, J.-P., & Anderson, D. L. (1989). Constrained reference mantle model. *Physics of the Earth and Planetary Interiors*, *58*(2-3), 205–227.

Montagner, J.-P., & Nataf, H.-C. (1986). A simple method for inverting the azimuthal anisotropy of surface waves. *Journal of Geophysical Research: Solid Earth*, *91*(B1), 511–520.

Morelli, A., & Dziewonski, A. M. (1993). Body wave traveltimes and a spherically symmetric P-and S-wave velocity model. *Geophysical Journal International*, *112*(2), 178–194.

Morgan, J. P., & Shearer, P. M. (1993). Seismic constraints on mantle flow and topography of the 660-km discontinuity: evidence for whole-mantle convection. *Nature*, *365*(6446), 506–511.

Moschetti, M. P., Ritzwoller, M. H., Lin, F.-C., & Yang, Y. (2010). Seismic evidence for widespread western-US deep-crustal deformation caused by extension. *Nature*, *464*(7290), 885–889.

Moulik, P., & Ekström, G. (2016). The relationships between large-scale variations in shear velocity, density, and compressional velocity in the Earth's mantle. *Journal of Geophysical Research: Solid Earth*, *121*(4), 2737–2771.

Nieuwenhuis, G., Unsworth, M. J., Pana, D., Craven, J., & Bertrand, E. (2014). Three-dimensional resistivity structure of Southern Alberta, Canada: implications for Precambrian tectonics. *Geophysical Journal International*, *197*(2), 838–859.

Okada, Y., Kasahara, K., Hori, S., Obara, K., Sekiguchi, S., Fujiwara, H., & Yamamoto, A. (2004). Recent progress of seismic observation networks in Japan——Hi-net, F-net, K-NET and KiK-net——. *Earth, Planets and Space*, *56*(8), xv–xxviii.

Ökeler, A., Gu, Y. J., Lerner-Lam, A., & Steckler, M. S. (2009). Seismic structure of the southern Apennines as revealed by waveform modelling of regional surface waves. *Geophysical Journal International*, *178*(3), 1473–1492.

Oliver, J., & Murphy, L. (1971). WWNSS: seismology's global network of observing stations. *Science*, *174*(4006), 254–261.

Owens, T. J., Crotwell, H. P., Groves, C., & Oliver-Paul, P. (2004). SOD: Standing order for data. *Seismological Research Letters*, *75*(4), 515–520.

Panning, M. P., Lekić, V., & Romanowicz, B. A. (2010). Importance of crustal corrections in the development of a new global model of radial anisotropy. *Journal of Geophysical Research: Solid Earth*, *115*(B12).

Pardo-Casas, F., & Molnar, P. (1987). Relative motion of the Nazca (Farallon) and South American plates since Late Cretaceous time. *Tectonics*, *6*(3), 233–248.

Parrish, R. R., Carr, S. D., & Parkinson, D. L. (1988). Eocene extensional tectonics and geochronology of the southern Omineca Belt, British Columbia and Washington. *Tectonics*, *7*(2), 181–212.

Pawley, S., Schultz, R., Playter, T., Corlett, H., Shipman, T., Lyster, S., & Hauck, T. (2018). The geological susceptibility of induced earthquakes in the Duvernay play. *Geophysical Research Letters*, *45*(4), 1786–1793.

Peña Castro, A. F., Roth, M. P., Verdecchia, A., Onwuemeka, J., Liu, Y., Harrington, R. M., et al. (2020). Stress chatter via fluid flow and fault slip in a hydraulic fracturing-induced earthquake sequence in the Montney Formation, British Columbia. *Geophysical Research Letters*, *47*(14), e2020GL087254.

Pfiffner, O. A. (2006). Thick-skinned and thin-skinned styles of continental contraction. In S. Mazzoli & R. W. H. Butler (Eds.), *Styles of continental contraction, Geological Society of America, Special Paper* (Vol. 414, pp. 153–177). Geological Society of America.

Pfiffner, O. A. (2017). Thick-skinned and thin-skinned tectonics: a global perspective. *Geosciences*, *7*(3), 71.

Pilkington, M., Miles, W. F., Ross, G. M., & Roest, W. R. (2000). Potential-field signatures of buried Precambrian basement in the Western Canada Sedimentary Basin. *Canadian Journal of Earth Sciences*, *37*(11), 1453–1471.

Portner, D. E., Rodríguez, E. E., Beck, S., Zandt, G., Scire, A., Rocha, M. P., et al. (2020). Detailed structure of the subducted Nazca slab into the lower mantle derived from continent-scale teleseismic P wave tomography. *Journal of Geophysical Research: Solid Earth*, *125*(5), e2019JB017884.

Preston, A., Garner, G., Beavis, K., Sadiq, O., & Stricker, S. (2016). *Duvernay reserves and resources report: A comprehensive analysis of Alberta's foremost liquids-rich shale resource*. Calgary, Alberta: Alberta Energy Regulator.

Price, R. A. (1981). The Cordilleran foreland thrust and fold belt in the southern Canadian Rocky Mountains. In K. R. McClay & N. J. Price (Eds.), *Thrust and Nappe Tectonics, Geological Society of London Special Publications* (Vol. 9, pp. 427–448). Geological Society of London.

Ramos, V. A. (2009). Anatomy and global context of the andes: Main geologic features and the andean orogenic cycle. In S. M. Kay, V. A. Ramos, & W. R. Dickinson (Eds.), *Backbone of the Americas: Shallow subduction, plateau uplift, and ridge and terrane collision, Geological Society of America Memoir* (Vol. 204, pp. 31–65). Geological Society of America.

Regan, J., & Anderson, D. L. (1984). Anisotropic models of the upper mantle. *Physics of the Earth and Planetary Interiors*, *35*(4), 227–263.

Reiter, K., Heidbach, O., Schmitt, D., Haug, K., Ziegler, M., & Moeck, I. (2014). A revised crustal stress orientation database for Canada. *Tectonophysics*, *636*, 111–124.

Resovsky, J., & Trampert, J. (2003). Using probabilistic seismic tomography to test mantle velocity-density relationships. *Earth and Planetary Science Letters*, *215*(1-2), 121–134.

Revenaugh, J., & Sipkin, S. A. (1994). Seismic evidence for silicate melt atop the 410-km mantle discontinuity. *Nature*, *369*(6480), 474–476.

Ricard, Y., & Bai, W. (1991). Inferring the viscosity and the 3-D density structure of the mantle from geoid, topography and plate velocities. *Geophysical Journal International*, *105*(3), 561–571.

Ricard, Y., Richards, M., Lithgow-Bertelloni, C., & Le Stunff, Y. (1993). A geodynamic model of mantle density heterogeneity. *Journal of Geophysical Research: Solid Earth*, *98*(B12), 21895–21909.

Richards, M. A., & Hager, B. H. (1984). Geoid anomalies in a dynamic Earth. *Journal of Geophysical Research: Solid Earth*, *89*(B7), 5987–6002.

Ringler, A. T., Anthony, R. E., Karplus, M. S., Holland, A. A., & Wilson, D. C. (2018). Laboratory tests of three Z-Land Fairfield Nodal 5-Hz, three-component sensors. *Seismological Research Letters*, *89*(5), 1601–1608.

Ringwood, A. E. (1975). *Composition and petrology of the Earth's mantle*. New York, NY: McGraw-Hill.

Ringwood, A. E., & Irifune, T. (1988). Nature of the 650-km seismic discontinuity: implications for mantle dynamics and differentiation. *Nature*, *331*(6152), 131–136.

Rippe, D., Unsworth, M. J., & Currie, C. A. (2013). Magnetotelluric constraints on the fluid content in the upper mantle beneath the southern Canadian Cordillera: Implications for rheology. *Journal of Geophysical Research: Solid Earth*, *118*(10), 5601–5624.

Ristau, J., Rogers, G. C., & Cassidy, J. F. (2007). Stress in western Canada from regional moment tensor analysis. *Canadian Journal of Earth Sciences*, *44*(2), 127–148.

Ritsema, J., Deuss, A., van Heijst, H. J., & Woodhouse, J. H. (2011). S40RTS: a degree-40 shear-velocity model for the mantle from new Rayleigh wave dispersion, teleseismic traveltime and normal-mode splitting function measurements. *Geophysical Journal International*, *184*(3), 1223–1236.

Ritsema, J., Xu, W., Stixrude, L., & Lithgow-Bertelloni, C. (2009). Estimates of the transition zone temperature in a mechanically mixed upper mantle. *Earth and Planetary Science Letters*, *277*(1-2), 244–252.

Rodríguez-Pradilla, G., & Eaton, D. W. (2019). The application of coda and energy methods for magnitude estimation of microseismic events. *Seismological Research Letters*, *90*(3), 1296–1307.

Romanowicz, B. (2001). Can we resolve 3D density heterogeneity in the lower mantle? *Geophysical Research Letters*, *28*(6), 1107–1110.

Romanowicz, B., Cara, M., Fel, J. F., & Rouland, D. (1984). GEOSCOPE: A French initiative in long-period three-component global seismic networks. *Eos, Transactions American Geophysical Union*, *65*(42), 753–753.

Ross, G. M. (2000). Introduction to special issue of Canadian Journal of Earth Sciences: The Alberta basement transect of Lithoprobe. *Canadian Journal of Earth Sciences*, *37*(11), 1447–1452.

Ross, G. M. (2002). Evolution of Precambrian continental lithosphere in western Canada: results from Lithoprobe studies in Alberta and beyond. *Canadian Journal of Earth Sciences*, *39*(3), 413–437.

Ross, G. M., McNicoll, V. J., Geldsetzer, H. H. J., Parrish, R. R., Carr, S. D., & Kinsman, A. (1993). Detrital zircon geochronology of Siluro-Devonian sandstones, Rocky Mountains, northeastern British Columbia. *Bulletin of Canadian Petroleum Geology*, *41*(3), 349–357.

Ross, G. M., Parrish, R. R., Villeneuve, M. E., & Bowring, S. A. (1991). Geophysics and geochronology of the crystalline basement of the Alberta Basin, western Canada. *Canadian Journal of Earth Sciences*, *28*(4), 512–522.

Rost, S., & Garnero, E. J. (2004). Array seismology advances research into Earth's interior. *Eos, Transactions American Geophysical Union*, *85*(32), 301–306.

Rost, S., & Thomas, C. (2002). Array seismology: Methods and applications. *Reviews of Geophysics*, *40*(3), 2–1.

Rüger, A. (2002). *Reflection coefficients and azimuthal AVO analysis in anisotropic media*. Tulsa, OK: Society of Exploration Geophysicists.

Sabra, K. G., Gerstoft, P., Roux, P., Kuperman, W. A., & Fehler, M. C. (2005). Extracting time-domain Green's function estimates from ambient seismic noise. *Geophysical Research Letters*, *32*(3).

Sánchez-Sesma, F. J., & Campillo, M. (2006). Retrieval of the Green's function from cross correlation: the canonical elastic problem. *Bulletin of the Seismological Society of America*, *96*(3), 1182–1191.

Savage, M. K. (1999). Seismic anisotropy and mantle deformation: what have we learned from shear wave splitting? *Reviews of Geophysics*, *37*(1), 65–106.

Schaeffer, A. J., & Lebedev, S. (2015). Global heterogeneity of the lithosphere and underlying mantle: A seismological appraisal based on multimode surface-wave dispersion analysis, shear-velocity tomography, and tectonic regionalization. In A. Khan & F. Deschamps (Eds.), *The Earth's heterogeneous mantle* (pp. 3–46). Springer.

Schellart, W. P. (2008). Overriding plate shortening and extension above subduction zones: A parametric study to explain formation of the Andes Mountains. *Geological Society of America Bulletin*, *120*(11-12), 1441–1454.

Schellart, W. P., Freeman, J., Stegman, D. R., Moresi, L., & May, D. (2007). Evolution and diversity of subduction zones controlled by slab width. *Nature*, *446*(7133), 308–311.

Schmerr, N., & Garnero, E. (2006). Investigation of upper mantle discontinuity structure beneath the central Pacific using SS precursors. *Journal of Geophysical Research: Solid Earth*, *111*(B8).

Schmerr, N., & Garnero, E. J. (2007). Upper mantle discontinuity topography from thermal and chemical heterogeneity. *Science*, *318*(5850), 623–626.

Schoenball, M., Baujard, C., Kohl, T., & Dorbath, L. (2012). The role of triggering by static stress transfer during geothermal reservoir stimulation. *Journal of Geophysical Research: Solid Earth*, *117*(B9).

Schoenball, M., Dorbath, L., Gaucher, E., Wellmann, J. F., & Kohl, T. (2014). Change of stress regime during geothermal reservoir stimulation. *Geophysical Research Letters*, *41*(4), 1163–1170.

Schulte-Pelkum, V., Monsalve, G., Sheehan, A., Pandey, M. R., Sapkota, S., Bilham, R., & Wu, F. (2005). Imaging the Indian subcontinent beneath the Himalaya. *Nature*, *435*(7046), 1222–1225.

Schultz, R., Atkinson, G., Eaton, D. W., Gu, Y. J., & Kao, H. (2018). Hydraulic fracturing volume is associated with induced earthquake productivity in the Duvernay play. *Science*, *359*(6373), 304–308.

Schultz, R., Beroza, G., Ellsworth, W., & Baker, J. (2020). Risk-informed recommendations for managing hydraulic fracturing-induced seismicity via traffic light protocols. *Bulletin of the Seismological Society of America*, *110*(5), 2411–2422.

Schultz, R., Corlett, H., Haug, K., Kocon, K., MacCormack, K., Stern, V., et al. (2016). Linking fossil reefs with earthquakes: Geologic insight to where induced seismicity occurs in Alberta. *Geophysical Research Letters*, *43*(6), 2534–2542.

Schultz, R., Pawley, S. M., & Hauck, T. E. (2019). Preliminary overview of the 2018 and 2019 earthquakes near Red Deer, Alberta. *AER/AGS Open File Report 2019-12*. Retrieved from `https://static.ags.aer.ca/files/document/OFR/OFR_2019_12.pdf`

Schultz, R., Skoumal, R. J., Brudzinski, M. R., Eaton, D., Baptie, B., & Ellsworth, W. (2020). Hydraulic fracturing-induced seismicity. *Reviews of Geophysics*, *58*(3), e2019RG000695.

Schultz, R., & Stern, V. (2015). The regional Alberta observatory for earthquake studies network (RAVEN). *CSEG Recorder*, *40*(8), 34–37.

Schultz, R., Stern, V., Gu, Y. J., & Eaton, D. (2015). Detection threshold and location resolution of the Alberta Geological Survey earthquake catalogue. *Seismological Research Letters*, *86*(2A), 385–397.

Schultz, R., & Wang, R. (2020). Newly emerging cases of hydraulic fracturing induced seismicity in the Duvernay East Shale Basin. *Tectonophysics*, *779*, 228393.

Schultz, R., Wang, R., Gu, Y. J., Haug, K., & Atkinson, G. (2017). A seismological overview of the induced earthquakes in the Duvernay play near Fox Creek, Alberta. *Journal of Geophysical Research: Solid Earth*, *122*(1), 492–505.

Scire, A., Zandt, G., Beck, S., Long, M., Wagner, L., Minaya, E., & Tavera, H. (2016). Imaging the transition from flat to normal subduction: Variations in the structure of the Nazca slab and upper mantle under southern Peru and northwestern Bolivia. *Geophysical Journal International*, *204*(1), 457–479.

Segall, P. (1989). Earthquakes triggered by fluid extraction. *Geology*, *17*(10), 942–946.

Segall, P., & Lu, S. (2015). Injection-induced seismicity: Poroelastic and earthquake nucleation effects. *Journal of Geophysical Research: Solid Earth*, *120*(7), 5082–5103.

Shapiro, N. M., & Campillo, M. (2004). Emergence of broadband Rayleigh waves from correlations of the ambient seismic noise. *Geophysical Research Letters*, *31*(7).

Shapiro, N. M., Ritzwoller, M. H., Molnar, P., & Levin, V. (2004). Thinning and flow of Tibetan crust constrained by seismic anisotropy. *Science*, *305*(5681), 233–236.

Shapiro, S. A., Huenges, E., & Borm, G. (1997). Estimating the crust permeability from fluid-injection-induced seismic emission at the KTB site. *Geophysical Journal International*, *131*(2), F15–F18.

Shapiro, S. A., Rothert, E., Rath, V., & Rindschwentner, J. (2002). Characterization of fluid transport properties of reservoirs using induced microseismicity. *Geophysics*, *67*(1), 212–220.

Shearer, P. M. (2009). *Introduction to seismology*. New York, NY: Cambridge University Press.

Shearer, P. M., & Flanagan, M. P. (1999). Seismic velocity and density jumps across the 410-and 660-kilometer discontinuities. *Science*, *285*(5433), 1545–1548.

Shen, L. W., Schmitt, D. R., & Haug, K. (2019). Quantitative constraints to the complete state of stress from the combined borehole and focal mechanism inversions: Fox Creek, Alberta. *Tectonophysics*, *764*, 110–123.

Shen, W., & Ritzwoller, M. H. (2016). Crustal and uppermost mantle structure beneath the United States. *Journal of Geophysical Research: Solid Earth*, *121*(6), 4306–4342.

Shirzad, T., & Hossein Shomali, Z. (2014). Shallow crustal structures of the Tehran basin in Iran resolved by ambient noise tomography. *Geophysical Journal International*, *196*(2), 1162–1176.

Shragge, J., Bostock, M. G., Bank, C. G., & Ellis, R. M. (2002). Integrated teleseismic studies of the southern Alberta upper mantle. *Canadian Journal of Earth Sciences*, *39*(3), 399–411.

Simmons, N. A., Forte, A. M., Boschi, L., & Grand, S. P. (2010). GyPSuM: A joint tomographic model of mantle density and seismic wave speeds. *Journal of Geophysical Research: Solid Earth*, *115*(B12).

Simmons, N. A., Forte, A. M., & Grand, S. P. (2007). Thermochemical structure and dynamics of the African superplume. *Geophysical Research Letters*, *34*(2).

Simmons, N. A., Forte, A. M., & Grand, S. P. (2009). Joint seismic, geodynamic and mineral physical constraints on three-dimensional mantle heterogeneity: Implications for the relative importance of thermal versus compositional heterogeneity. *Geophysical Journal International*, *177*(3), 1284–1304.

Simpson, D. W., Leith, W. S., & Scholz, C. H. (1988). Two types of reservoir-induced seismicity. *Bulletin of the Seismological Society of America*, *78*(6), 2025–2040.

Smith, M. L., & Dahlen, F. A. (1973). The azimuthal dependence of Love and Rayleigh wave propagation in a slightly anisotropic medium. *Journal of Geophysical Research*, *78*(17), 3321–3333.

Snieder, R. (2004). Extracting the Green's function from the correlation of coda waves: A derivation based on stationary phase. *Physical Review E*, *69*(4), 046610.

Snoke, J. A. (1984). A program for focal mechanism determination by combined use of polarity and SV-P amplitude ratio data. *Earthquake Notes*, *55*, 15.

Stachnik, J. C., Sheehan, A. F., Zietlow, D. W., Yang, Z., Collins, J., & Ferris, A. (2012). Determination of New Zealand ocean bottom seismometer orientation via Rayleigh-wave polarization. *Seismological Research Letters*, *83*(4), 704–713.

Stern, V. H., Schultz, R. J., Shen, L., Gu, Y. J., & Eaton, D. W. (2013). Alberta earthquake catalogue, version 1.0: September 2006 through December 2010. *AER/AGS Open File Report 2013-15*. Retrieved from `https://static.ags.aer.ca/files/document/OFR/OFR_2013_15.pdf`

Su, W.-j., Woodward, R. L., & Dziewonski, A. M. (1994). Degree 12 model of shear velocity heterogeneity in the mantle. *Journal of Geophysical Research: Solid Earth*, *99*(B4), 6945–6980.

Sumy, D. F., Cochran, E. S., Keranen, K. M., Wei, M., & Abers, G. A. (2014). Observations of static Coulomb stress triggering of the November 2011 M5.7 Oklahoma earthquake sequence. *Journal of Geophysical Research: Solid Earth*, *119*(3), 1904–1923.

Sweet, J. R., Anderson, K. R., Bilek, S., Brudzinski, M., Chen, X., DeShon, H., et al. (2018). A community experiment to record the full seismic wavefield in Oklahoma. *Seismological Research Letters*, *89*(5), 1923–1930.

Switzer, S. B., Holland, W. G., Christie, D. S., Graf, G. C., Hedinger, A. S., McAuley, R. J., et al. (1994). Devonian Woodbend-Winterburn strata of the Western Canada Sedimentary Basin. In G. D. Mossop & I. Shetsen (Eds.), *Geological Atlas of the Western Canada Sedimentary Basin* (pp. 165–202). Canadian Society of Petroleum Geologists and Alberta Research Council.

Takeuchi, H., & Saito, M. (1972). Seismic surface waves. In B. A. Bolt (Ed.), *Methods in computational physics* (Vol. 11, pp. 217–295). Academic Press.

Tape, C., Liu, Q., Maggi, A., & Tromp, J. (2009). Adjoint tomography of the southern California crust. *Science*, *325*(5943), 988–992.

Tassara, A., Swain, C., Hackney, R., & Kirby, J. (2007). Elastic thickness structure of south america estimated using wavelets and satellite-derived gravity data. *Earth and Planetary Science Letters*, *253*(1-2), 17–36.

Tauzin, B., Debayle, E., & Wittlinger, G. (2008). The mantle transition zone as seen by global Pds phases: No clear evidence for a thin transition zone beneath hotspots. *Journal of Geophysical Research: Solid Earth*, *113*(B8).

Tauzin, B., Kim, S., & Kennett, B. L. N. (2017). Pervasive seismic low-velocity zones within stagnant plates in the mantle transition zone: Thermal or compositional origin? *Earth and Planetary Science Letters*, *477*, 1–13.

Teyssier, C., Ferré, E. C., Whitney, D. L., Norlander, B., Vanderhaeghe, O., & Parkinson, D. (2005). Flow of partially molten crust and origin of detachments during collapse of the Cordilleran Orogen. In D. Bruhn & L. Burlini (Eds.), *High-strain zones: structure and physical properties, Geological Society of London Special Publications* (Vol. 245, pp. 39–64). Geological Society of London.

Thio, V., Cobden, L., & Trampert, J. (2016). Seismic signature of a hydrous mantle transition zone. *Physics of the Earth and Planetary Interiors*, *250*, 46–63.

Tian, D., Lv, M., Wei, S. S., Dorfman, S. M., & Shearer, P. M. (2020). Global variations of Earth's 520-and 560-km discontinuities. *Earth and Planetary Science Letters*, *552*, 116600.

Toda, S., Stein, R. S., Sevilgen, V., & Lin, J. (2011). Coulomb 3.3 Graphic-rich deformation and stress-change software for earthquake, tectonic, and volcano research and teaching-user guide. *US Geological Survey Open-File Report 2011-1060*. Retrieved from `https://pubs.usgs.gov/of/2011/1060/of2011-1060.pdf`

Trampert, J., Deschamps, F., Resovsky, J., & Yuen, D. (2004). Probabilistic tomography maps chemical heterogeneities throughout the lower mantle. *Science*, *306*(5697), 853–856.

Trugman, D. T., & Shearer, P. M. (2017). GrowClust: A hierarchical clustering algorithm for relative earthquake relocation, with application to the Spanish Springs and Sheldon, Nevada, earthquake sequences. *Seismological Research Letters*, *88*(2A), 379–391.

Tseng, T.-L., & Chen, W.-P. (2004). Contrasts in seismic wave speeds and density across the 660-km discontinuity beneath the Philippine and the Japan Seas. *Journal of Geophysical Research: Solid Earth*, *109*(B4).

Vacher, P., Mocquet, A., & Sotin, C. (1998). Computation of seismic profiles from mineral physics: the importance of the non-olivine components for explaining the 660 km depth discontinuity. *Physics of the Earth and Planetary Interiors*, *106*(3-4), 275–298.

van der Hilst, R. D., Widiyantoro, S., & Engdahl, E. R. (1997). Evidence for deep mantle circulation from global tomography. *Nature*, *386*(6625), 578–584.

van der Meijde, M., Marone, F., Giardini, D., & van der Lee, S. (2003). Seismic evidence for water deep in Earth's upper mantle. *Science*, *300*(5625), 1556–1558.

van der Velden, A. J., & Cook, F. A. (1996). Structure and tectonic development of the southern Rocky Mountain trench. *Tectonics*, *15*(3), 517–544.

Vernik, L., & Liu, X. (1997). Velocity anisotropy in shales: A petrophysical study. *Geophysics*, *62*(2), 521–532.

Vestrum, R. W., Lawton, D. C., & Schmid, R. (1999). Imaging structures below dipping TI media. *Geophysics*, *64*(4), 1239–1246.

Villeneuve, M. E., Ross, G. M., Thériault, R. J., Miles, W., Parrish, R. R., & Broome, J. (1993). Tectonic subdivision and U-Pb geochronology of the crystalline basement of the Alberta Basin, western Canada. *Geological Sur-*

vey of Canada Bulletin, *447*.

Waldhauser, F., & Ellsworth, W. L. (2000). A double-difference earthquake location algorithm: Method and application to the northern Hayward fault, California. *Bulletin of the Seismological Society of America*, *90*(6), 1353–1368.

Wang, F., Barklage, M., Lou, X., van der Lee, S., Bina, C. R., & Jacobsen, S. D. (2018). HyMaTZ: A Python program for modeling seismic velocities in hydrous regions of the mantle transition zone. *Geochemistry, Geophysics, Geosystems*, *19*(8), 2308–2324.

Wang, K., Yang, Y., Basini, P., Tong, P., Tape, C., & Liu, Q. (2018). Refined crustal and uppermost mantle structure of southern California by ambient noise adjoint tomography. *Geophysical Journal International*, *215*(2), 844–863.

Wang, R., Gu, Y. J., Schultz, R., & Chen, Y. (2018). Faults and non-double-couple components for induced earthquakes. *Geophysical Research Letters*, *45*(17), 8966–8975.

Wang, R., Gu, Y. J., Schultz, R., Zhang, M., & Kim, A. (2017). Source characteristics and geological implications of the January 2016 induced earthquake swarm near Crooked Lake, Alberta. *Geophysical Journal International*, *210*(2), 979–988.

Wang, Y., Allam, A., & Lin, F.-C. (2019). Imaging the fault damage zone of the San Jacinto fault near Anza with ambient noise tomography using a dense nodal array. *Geophysical Research Letters*, *46*(22), 12938–12948.

Waszek, L., Tauzin, B., Schmerr, N. C., Ballmer, M. D., & Afonso, J. C. (2021). A poorly mixed mantle transition zone and its thermal state inferred from seismic waves. *Nature Geoscience*, *14*(12), 949–955.

Welford, J. K., & Clowes, R. M. (2006). Three-dimensional seismic reflection investigation of the upper crustal Winagami sill complex of northwestern Alberta, Canada. *Geophysical Journal International*, *166*(1), 155–169.

Welford, J. K., Clowes, R. M., Ellis, R. M., Spence, G. D., Asudeh, I., & Hajnal, Z. (2001). Lithospheric structure across the craton-Cordilleran transition of northeastern British Columbia. *Canadian Journal of Earth Sciences*, *38*(8), 1169–1189.

Wernicke, B., Axen, G. J., & Snow, J. K. (1988). Basin and Range extensional tectonics at the latitude of Las Vegas, Nevada. *Geological Society of America Bulletin*, *100*(11), 1738–1757.

Wessel, P., Smith, W. H. F., Scharroo, R., Luis, J., & Wobbe, F. (2013). Generic mapping tools: improved version released. *Eos, Transactions American Geophysical Union*, *94*(45), 409–410.

Wiemer, S., & Wyss, M. (2000). Minimum magnitude of completeness in earthquake catalogs: Examples from Alaska, the western United States, and Japan. *Bulletin of the Seismological Society of America*, *90*(4), 859–869.

Wolhart, S. L., Harting, T. A., Dahlem, J. E., Young, T., Mayerhofer, M. J., & Lolon, E. P. (2006). Hydraulic fracture diagnostics used to optimize development in the Jonah field. In *SPE Annual Technical Conference and Exhibition.* San Antonio, TX.

Woodhouse, J. H., & Dziewonski, A. M. (1984). Mapping the upper mantle: Three-dimensional modeling of Earth structure by inversion of seismic waveforms. *Journal of Geophysical Research: Solid Earth*, *89*(B7), 5953–5986.

Wu, L., Gu, Y. J., Chen, Y., & Liang, H. (2019). Shear wave splitting discloses two episodes of collision-related convergence in western North America. *Journal of Geophysical Research: Solid Earth*, *124*(3), 2990–3010.

Wu, W., Ni, S., & Irving, J. C. E. (2019). Inferring Earth's discontinuous chemical layering from the 660-kilometer boundary topography. *Science*, *363*(6428), 736–740.

Xiao, Z., Fuji, N., Iidaka, T., Gao, Y., Sun, X., & Liu, Q. (2020). Seismic structure beneath the Tibetan plateau from iterative finite-frequency tomography based on ChinArray: New insights into the Indo-Asian collision. *Journal of Geophysical Research: Solid Earth*, *125*(2), e2019JB018344.

Xie, J., Ritzwoller, M. H., Brownlee, S. J., & Hacker, B. R. (2015). Inferring the oriented elastic tensor from surface wave observations: preliminary application across the western United States. *Geophysical Journal International*, *201*(2), 996–1021.

Xie, J., Ritzwoller, M. H., Shen, W., Yang, Y., Zheng, Y., & Zhou, L. (2013). Crustal radial anisotropy across eastern Tibet and the western Yangtze craton. *Journal of Geophysical Research: Solid Earth*, *118*(8), 4226–4252.

Xu, W., Lithgow-Bertelloni, C., Stixrude, L., & Ritsema, J. (2008). The effect of bulk composition and temperature on mantle seismic structure. *Earth and Planetary Science Letters*, *275*(1-2), 70–79.

Yan, J., Ballmer, M. D., & Tackley, P. J. (2020). The evolution and distribution of recycled oceanic crust in the Earth's mantle: Insight from geodynamic models. *Earth and Planetary Science Letters*, *537*, 116171.

Yang, Y., Ritzwoller, M. H., Levshin, A. L., & Shapiro, N. M. (2007). Ambient noise Rayleigh wave tomography across Europe. *Geophysical Journal International*, *168*(1), 259–274.

Yu, C., Day, E. A., de Hoop, M. V., Campillo, M., Goes, S., Blythe, R. A., & van der Hilst, R. D. (2018). Compositional heterogeneity near the base of the mantle transition zone beneath Hawaii. *Nature Communications*, *9*(1), 1–9.

Yu, H., Harrington, R. M., Liu, Y., & Wang, B. (2019). Induced seismicity driven by fluid diffusion revealed by a near-field hydraulic stimulation monitoring array in the Montney Basin, British Columbia. *Journal of Geophysical Research: Solid Earth*, *124*(5), 4694–4709.

Yuan, H., & Romanowicz, B. (2010). Lithospheric layering in the North American craton. *Nature*, *466*(7310), 1063–1068.

Zhang, C., Gu, Y. J., Dokht, R., & Chen, Y. (2019). Recovery of the upper crustal structures from forward modeling and inversions of receiver functions. In *AGU Fall Meeting 2019 Abstracts.* San Francisco, CA.

Zhang, H., Eaton, D. W., Rodriguez, G., & Jia, S. Q. (2019). Source-mechanism analysis and stress inversion for hydraulic-fracturing-induced event sequences near Fox Creek, Alberta. *Bulletin of the Seismological Society of America*, *109*(2), 636-651.

Zhang, M., Ellsworth, W. L., & Beroza, G. C. (2019). Rapid earthquake association and location. *Seismological Research Letters*, *90*(6), 2276–2284.

Zhang, M., Liu, M., Feng, T., Wang, R., & Zhu, W. (2022). LOC-FLOW: An end-to-end machine learning-based high-precision earthquake location workflow. *Seismological Research Letters*.

Zhang, M., & Wen, L. (2015). An effective method for small event detection: Match and locate (M&L). *Geophysical Journal International*, *200*(3), 1523–1537.

Zhao, D., & Ohtani, E. (2009). Deep slab subduction and dehydration and their geodynamic consequences: evidence from seismology and mineral physics. *Gondwana Research*, *16*(3-4), 401–413.

Zhu, W., & Beroza, G. C. (2019). PhaseNet: a deep-neural-network-based seismic arrival-time picking method. *Geophysical Journal International*, *216*(1), 261–273.

Zoback, M. D., & Gorelick, S. M. (2012). Earthquake triggering and large-scale geologic storage of carbon dioxide. *Proceedings of the National Academy of Sciences*, *109*(26), 10164–10168.

Appendix A

Supplementary Materials for Chapter 2

A.1 Modeling Coulomb Stress Changes

We calculated the Coulomb stress changes resulting from the fault slip of ML4 on specified receiver fault planes following (1) the average source parameters of the AGS group (strike = 11°, dip = 76°, and rake = $-168°$; Figures A.3a and A.3b), (2) the average fault-plane parameters of the nodal group (strike = 23°, dip = 78°, and rake = 169°; Figures A.3c and A.3d), and (3) the focal mechanism solution of the largest aftershock of the remote cluster (strike = 218°, dip = 67°, and rake = $-147°$; Figures A.3e and A.3f) (Toda et al., 2011). The calculations of the Coulomb stress changes (ΔCFF), which are independent of the regional stress field and aftershock fault geometry, strictly follow the Coulomb failure criterion

$$\Delta \mathrm{CFF} = \Delta\tau + \mu\Delta\sigma_n, \tag{A.1}$$

where μ is the effective coefficient of friction, and $\Delta\tau$ and $\Delta\sigma_n$ are the changes in shear stress and normal stress, respectively. Using the empirical relationships among the earthquake magnitude, fault size, and fault slip length (Zoback & Gorelick, 2012), we assumed a 1 km (length) × 0.4 km (width) fault plane with a net slip of 0.04 m. The effective friction coefficient was set to the default value of 0.4. Failure is promoted when the Coulomb stress change is positive. Our modeling results show that most of the early aftershocks lie within the region with negative ΔCFF, whereas late aftershocks, especially the remote cluster, are within the positive ΔCFF regime (Figure A.3). We suggest that both mechanisms (i.e., fluid diffusion and poroelastic stress change) may take effect in the triggering of the earthquake sequence, with most of the events dominated by fluid flow and the Coulomb stress transfer responsible for the late aftershocks.

Layer Depth (km)	V_P (km/s)	V_S (km/s)	Density (g/cm^3)	Q_P	Q_S
0.0	1.360	0.770	1.216	1456	600
0.2	1.367	0.773	1.216		
1.1	3.126	1.768	1.793		
1.9	3.569	2.018	1.938		
2.7	4.713	2.665	2.314		
5.0	6.099	3.449	2.768		
9.0	6.230	3.467	2.811		
13.0	6.327	3.486	2.843		
16.9	6.414	3.511	2.872		
20.9	6.448	3.530	2.883		
24.9	6.466	3.656	2.889		
28.9	6.703	3.669	2.967		
32.9	6.794	3.710	2.990		
37.7	6.794	3.710	2.990		
45.7	6.794	3.710	2.990		
46.1	6.900	3.930	3.030		

Table A.1: The 1-D velocity model used in this study. This model is obtained from recent regional receiver function inversions beneath two broadband seismic stations near Red Deer (Y. Chen et al., 2015; C. Zhang et al., 2019).

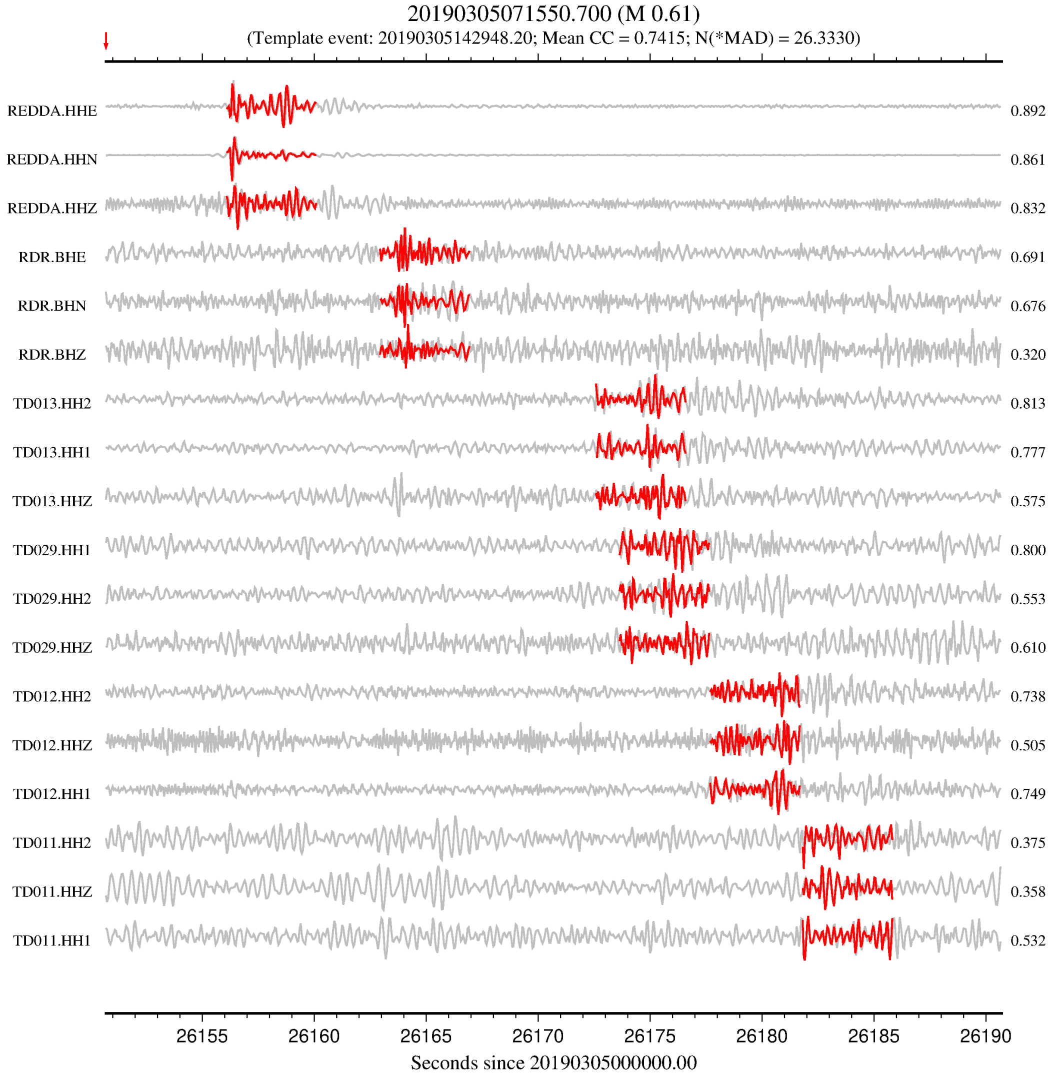

Figure A.1: Waveform comparison between the template event (red) and one of the detected events in the AGS group (gray). Broadband station names (‘NAME.CHANNEL’) and the corresponding CC values are labeled on the left and right sides, respectively. The red arrow marks the determined origin time of the detected earthquake.

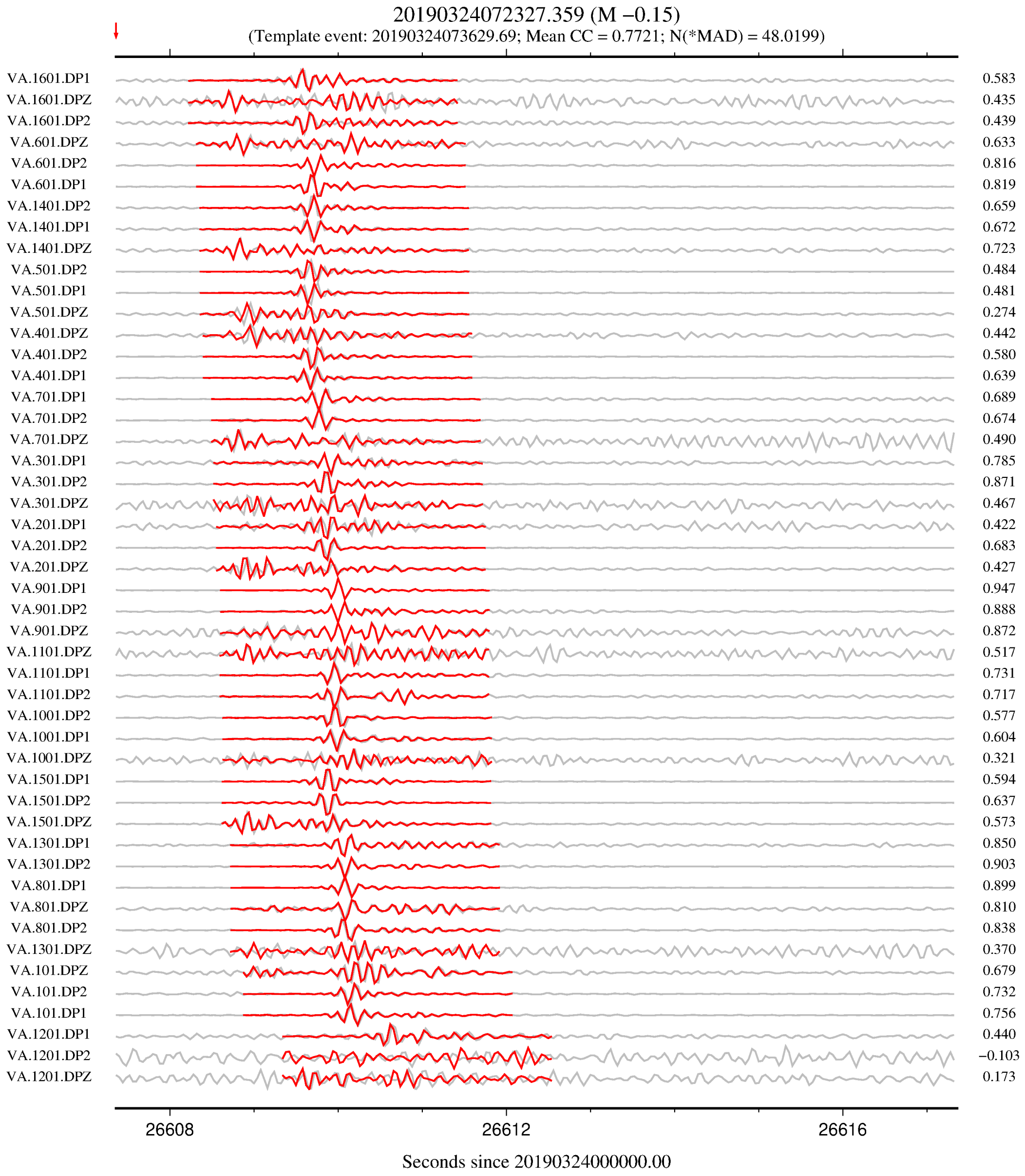

Figure A.2: Waveform comparison between the template event (red) and one of the detected events in the nodal group (gray). Nodal geophone names ('NETWORK.NAME.CHANNEL') and the corresponding CC values are labeled on the left and right sides, respectively. The event origin time is indicated by the red arrow.

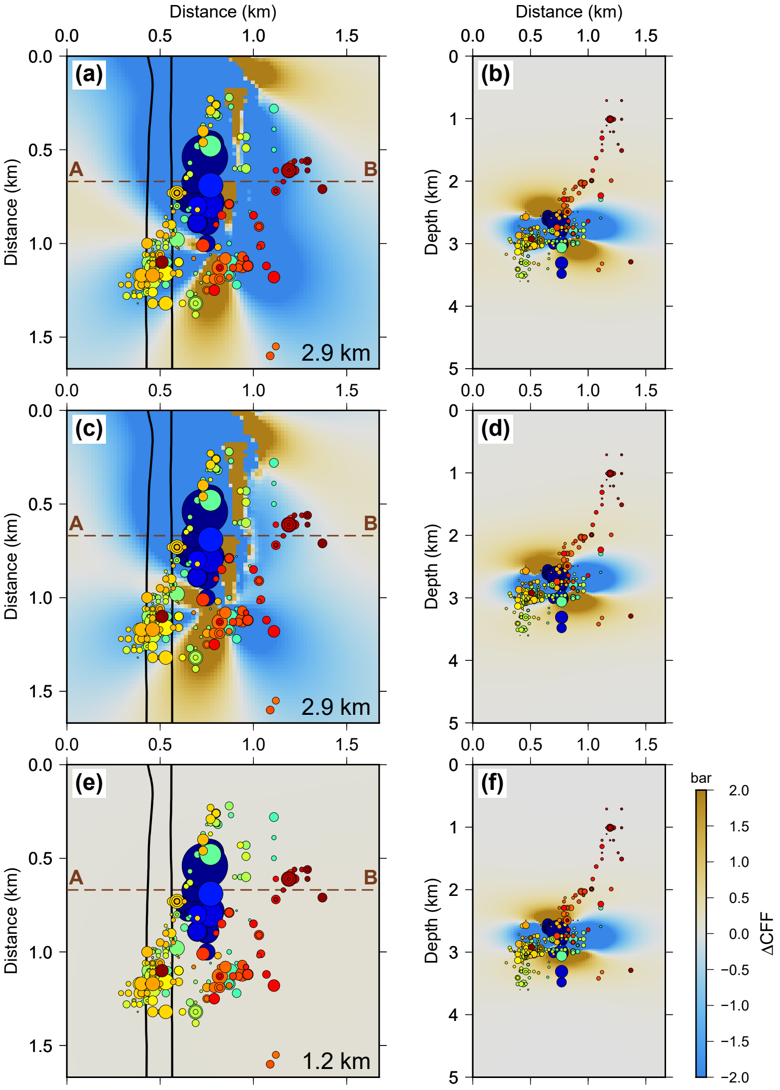

Figure A.3: Coulomb stress changes (ΔCFF) using (1) the average fault-plane parameters of the AGS group (a-b), (2) the average fault-plane parameters of the nodal group (c-d), and (3) the focal mechanism solution of the largest aftershock of the remote cluster (e-f) due to the fault slip of the mainshock (ML4). The Coulomb stress changes are shown in map views at (a, c) 2.9 km depth and (e) 1.2 km depth and (b, d, and f) cross-sectional views along profile A-B. The earthquakes are colored by the day of occurrence. Please refer to Figure 2.2 for the color bar of the event origin time.

Timing	Latitude (°)	Longitude (°)	Depth (km)	Magnitude	Strike (°)	Dip (°)	Rake (°)	Flag
2019/03/04 03:31:40.06	52.2141	-114.1067	2.644	1.47	180.63	83.80	175.53	N
2019/03/04 04:06:44.09	52.2149	-114.1062	2.610	1.31	186.09	72.51	175.22	N
2019/03/04 05:23:40.00	52.2153	-114.1059	2.665	1.40	181.06	76.55	169.01	N
2019/03/04 05:48:07.07	52.2151	-114.1060	2.637	1.79	185.21	67.27	172.90	Y
2019/03/04 07:25:14.10	52.2143	-114.1066	2.624	1.29	182.88	66.34	173.71	N
2019/03/04 07:30:01.01	52.2166	-114.1050	2.656	1.40	182.88	66.34	173.71	N
2019/03/04 07:32:39.09	52.2149	-114.1061	2.646	1.52	181.59	76.27	170.67	Y
2019/03/04 07:53:56.03	52.2163	-114.1052	2.606	1.55	182.28	73.92	173.51	Y
2019/03/04 09:48:31.05	52.2152	-114.1061	2.629	1.64	182.28	73.92	173.51	Y
2019/03/04 10:21:46.07	52.2165	-114.1052	2.650	1.58	182.27	69.77	172.63	Y
2019/03/04 10:51:52.01	52.2158	-114.1056	2.622	1.42	185.34	82.27	177.61	N
2019/03/04 11:25:35.03	52.2167	-114.1049	2.656	1.84	183.02	83.19	173.14	Y
2019/03/04 12:18:44.03	52.2146	-114.1065	2.690	1.51	181.59	76.27	170.67	N
2019/03/04 12:34:58.02	52.2168	-114.1051	2.671	1.47	182.70	69.39	173.65	N
2019/03/04 12:55:16.07	52.2162	-114.1053	2.700	4.17	12.30	59.49	-165.14	⋆
2019/03/05 14:29:48.02	52.2131	-114.1050	2.994	1.55	10.83	79.59	-171.26	Y
2019/03/05 19:41:19.01	52.2136	-114.1048	3.007	1.92	12.32	68.47	-165.72	Y
2019/03/07 14:04:40.00	52.2139	-114.1047	2.997	1.64	9.59	78.22	-167.66	Y
2019/03/08 04:24:22.00	52.2092	-114.1198	3.010	1.75	12.37	69.55	-168.20	N
2019/03/09 18:14:50.00	52.2149	-114.1046	2.980	1.62	9.06	76.20	-168.13	Y
2019/03/20 18:36:44.02	52.2110	-114.1032	2.788	0.77	22.65	64.00	174.23	Y
2019/03/21 11:45:27.10	52.2111	-114.1086	2.921	1.06	23.08	84.72	166.68	Y
2019/03/21 23:36:27.02	52.2108	-114.1091	2.994	0.12	23.14	85.40	165.81	N
2019/03/22 02:34:41.05	52.2122	-114.1078	2.959	0.40	9.87	65.22	165.36	Y
2019/03/22 02:36:06.01	52.2110	-114.1087	2.982	0.11	22.92	84.55	166.94	N
2019/03/23 00:02:50.02	52.2111	-114.1100	3.498	0.29	23.86	87.75	169.55	N

2019/03/23 17:59:00.03	52.2091	-114.1064	2.788	0.33	21.35	72.34	161.50	Y
2019/03/24 07:36:29.07	52.2105	-114.1093	3.312	0.25	22.79	84.50	168.11	Y
2019/03/25 02:38:40.02	52.2113	-114.1093	3.064	0.54	23.47	85.05	169.12	Y
2019/03/25 19:52:31.08	52.2102	-114.1097	2.989	0.51	23.05	84.90	164.14	Y
2019/03/27 08:21:21.04	52.2105	-114.1098	3.134	0.19	27.99	82.76	172.02	N
2019/03/27 23:59:00.01	52.2106	-114.1082	3.033	0.51	25.97	79.01	174.24	Y
2019/03/28 23:09:13.03	52.2144	-114.1068	2.942	0.33	23.06	82.09	175.53	Y
2019/03/29 08:47:09.07	52.2105	-114.1097	2.872	0.26	23.23	85.76	162.78	Y
2019/04/01 00:11:24.10	52.2108	-114.1040	2.491	0.47	21.46	60.24	170.00	Y
2019/04/02 04:14:17.08	52.2104	-114.1028	2.029	0.26	20.73	52.17	171.85	Y
2019/04/05 10:38:35.07	52.2153	-114.1005	1.963	-0.29	36.65	79.49	-134.10	Y
2019/04/07 04:59:17.04	52.2155	-114.0986	1.097	0.42	217.65	66.66	-146.69	Y
2019/04/07 04:59:30.04	52.2156	-114.0985	1.099	0.18	220.60	64.83	-143.51	Y
2019/04/07 04:59:44.01	52.2167	-114.1030	3.073	-0.33	213.81	84.13	142.08	N

Table A.2: Summary of fault-plane solutions for the 40 selected earthquakes. The ML4 is highlighted by the star symbol. The events used for plotting in Figure 2.3 are labeled with a flag “Y” (otherwise with “N”).

Appendix B

Supplementary Materials for Chapter 3

B.1 Azimuthal Anisotropy

To reduce biases in the estimation of radial anisotropy, we (1) carefully determine the inversion parameters to ensure consistent recovery amplitudes of V_{SH} and V_{SV} (see Sections 3.3.2 and 3.3.3) and (2) assess the effect of azimuthal anisotropy. We compute the azimuthal distributions of Rayleigh and Love wave group velocities at 8 s, 16 s, and 25 s by averaging the group velocities within 10° azimuthal bins. Following the theoretical formulation for a weakly anisotropic medium (Smith & Dahlen, 1973), we fit the observed group speed variation with azimuthal angle

$$U(\theta) = U_0 \left[1 + A_2 \cos 2\left(\theta - \phi_2\right) + A_2 \cos 4\left(\theta - \phi_4\right)\right], \tag{B.1}$$

where U_0 is the average group speed, θ is the azimuth, A_2 and A_4 are the peak-to-peak amplitudes of the 2θ and 4θ terms, and ϕ_2 and ϕ_4 define the fast directions of 2θ and 4θ anisotropy. Anisotropy of Rayleigh waves is dominated by 2θ terms, and thus 4θ terms are negligible (Montagner & Nataf, 1986) in our data sets. The optimal data fit reveals relatively small amplitudes (up to 1%) for the Rayleigh-2θ terms, 1% to 2.6% for Love-2θ, and 0.6% to 1.5% for Love-4θ components (Figure B.3). Both Rayleigh and Love wave 2θ fast directions range from 70° to 80° clockwise from the north. Despite being frequency-dependent, the orientations are in good agreement with those from crustal stress estimates (Reiter et al., 2014), shear wave splitting (L. Wu et al., 2019), regional earthquake focal mechanisms

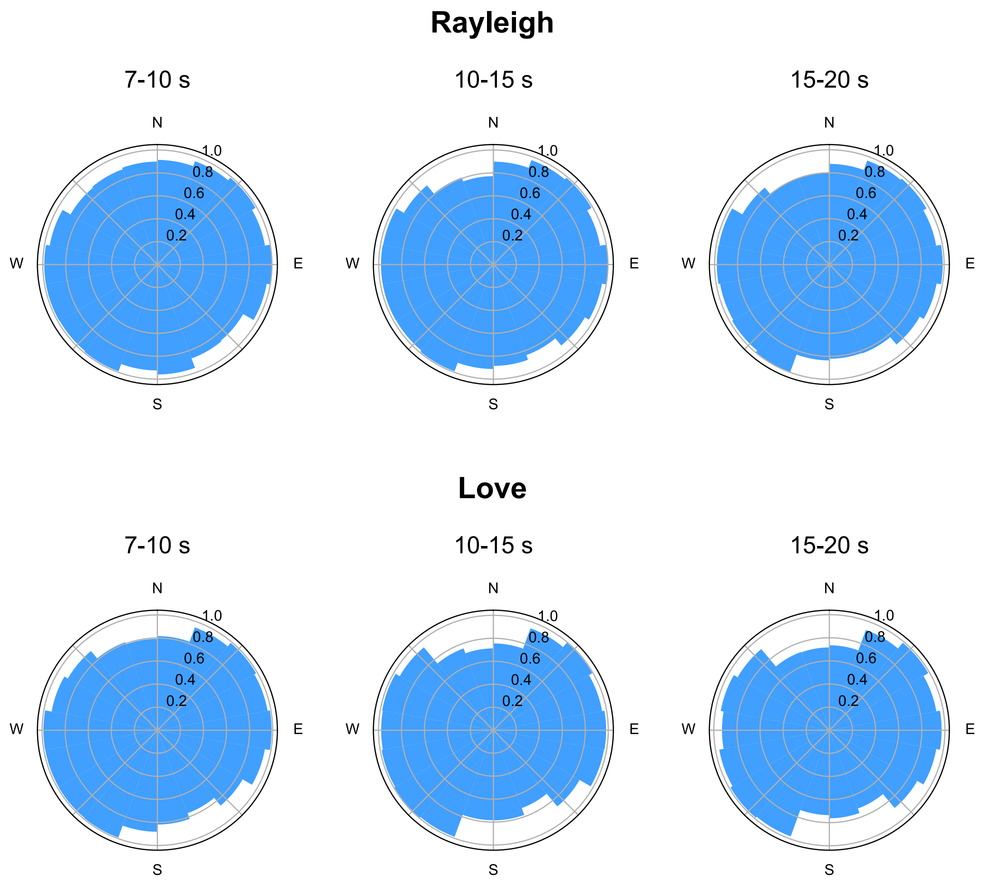

Figure B.1: The azimuthal dependence of high SNR (>10) Rayleigh and Love empirical Green's functions at three frequency bands (7–10 s, 10–15 s, and 15–20 s). Results are presented as fractions defined as the number of paths in a 20° azimuthal bin with SNR $>$ 10 divided by the total number of paths in that bin.

(R. Wang et al., 2017, 2018), and the present-day absolute plate motion (Gripp & Gordon, 2002). The inferred Love-4θ anisotropy, on the other hand, orients around 12°, which possibly reflects the presence of north-south trending basement faults (R. Wang et al., 2017). The consistent orientations from various data sets suggest ordered crustal fabrics/faults that, despite their minimal effects on our solutions for radial anisotropy, warrant a future study for a better overall understanding of crustal deformation history.

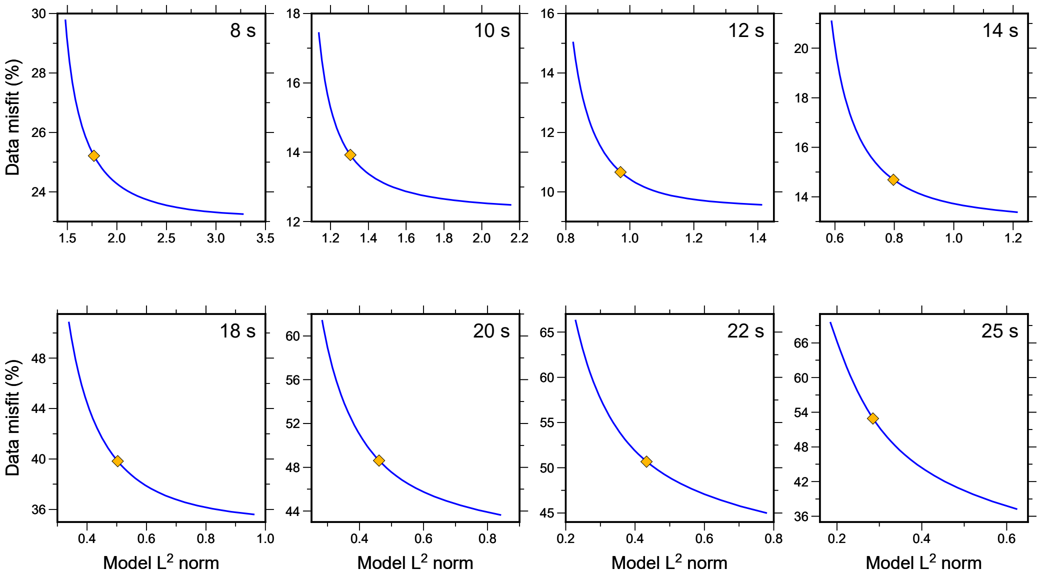

Figure B.2: Trade-off curves for Love wave group velocity tomography at different periods. The optimal damping factors (orange diamonds) are chosen based on a compromise between data misfit (1 – VR) and model smoothness (L^2 norm).

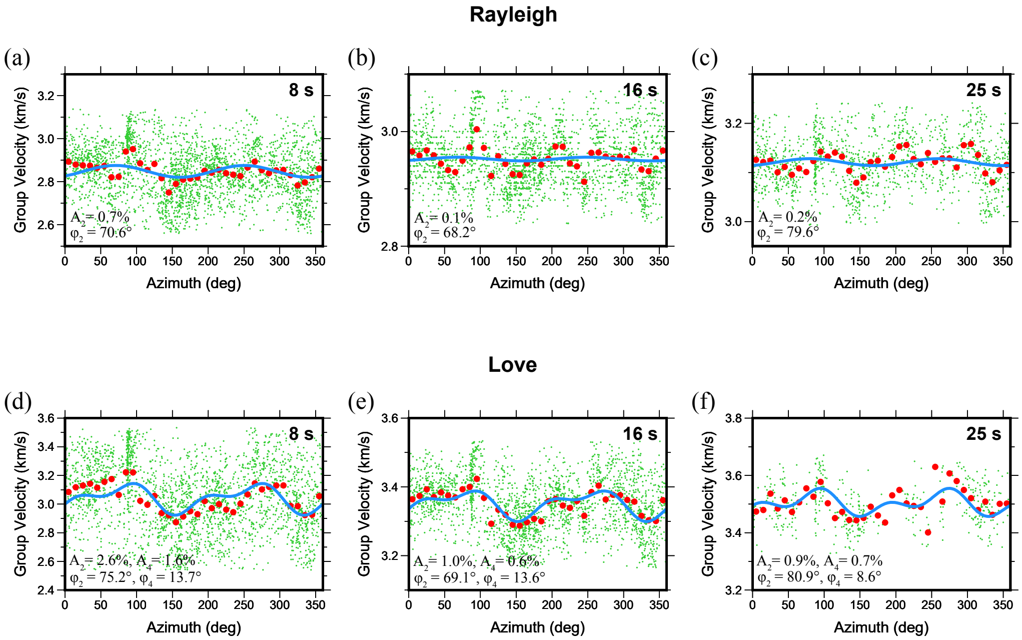

Figure B.3: Rayleigh (a-c) and Love (d-f) group speeds as a function of azimuthal angle and averaged in 10° azimuthal bins (shown as large red circles) at 8 s, 16 s, and 25 s. The small green dots are the individual group velocity measurements. The best fits for the Rayleigh-2θ and Love-2θ+4θ azimuthal anisotropy defined by equation (B.1) are presented as the blue curves in each panel. The estimated peak-to-peak amplitudes A and fast axes ϕ are listed at the bottom left corner of each panel.

Appendix C

Supplementary Materials for Chapter 4

C.1 The Effect of Low-Velocity Layers on S410S Reflectivity

Based on the assumption of a hydrous MTZ due to downgoing flows of the subducted slab, a low-velocity layer (LVL) of partial melt above the 410 could be induced resulting from hydrous materials ascending through the water-bearing MTZ into the nominally anhydrous upper mantle (Bercovici & Karato, 2003). The existence of such LVL beneath the South American continent was previously suggested using a similar technique to this study (Schmerr & Garnero, 2007). Here we follow the method of Schmerr and Garnero (2007) to investigate the effect of an LVL above the 410 on S410S reflection coefficients.

We express the perturbations of the 410 depth, S wave velocity, and density in terms of the water content of the LVL as

$$\begin{aligned} \delta d &= \frac{\partial d}{\partial c_w} c_w, \\ \delta V_S &= \frac{\partial V_S}{\partial c_w} c_w, \\ \delta \rho &= \frac{\partial \rho}{\partial c_w} c_w, \end{aligned} \tag{C.1}$$

where δd is the deviation of the average depth from the 410 (the depth is fixed at 400 km in PREM), δV_S and $\delta \rho$ are the shear velocity and density anomalies from PREM values, and c_w is the water content in weight percent (wt%). Those partial derivatives are obtained from experimentally determined values where $\partial d/\partial c_w = -30$ km/wt% (Karato, 2006), $\partial V_S/\partial c_w = -4.5\%$/wt% (Mao et al., 2012), and $\partial \rho/\partial c_w = -1.4\%$/wt% (Jacobsen et al., 2004). We assume that the changes in model parameters (i.e., d, V_S, and ρ) are controlled by water content by ignoring temperature-dependent terms. The velocity and density profiles near 410 km depth are perturbed relative to PREM for water contents ranging from 0 wt% to 1.25 wt% (Figures C.10a and C.10b). The thickness of the LVL is computed using equation (C.1) while fixing the base of the LVL at 410 km.

Reflectivity synthetic seismograms are then calculated for the shear velocity and density structures (Figure C.10c). We use seismograms at 125° with clean S410S phases and measure their amplitudes relative to those of SS. The measured S410S reflection coefficients are obtained after correcting for geometric spreading and attenuation (as illustrated in Section 4.4.2). In the case of a thin LVL (i.e., $c_w \leq 0.2$ wt%), the reflection coefficient is roughly the sum of both top and bottom reflections (Figure C.10d). With increasing levels of hydration, the reflection coefficients first drop due to reduced velocity and density contrasts across the olivine-wadsleyite transition and then increase above $\sim$0.75 wt% as a result of the dominance of the bottom reflections. The Zoeppritz modeling is an incomplete approximation to the true response by ignoring internal multiples or interference. Our results indicate that the variations in reflectivity are diagnostic of hydration, but a quantitative analysis of the water content in the MTZ based on AVO trends warrants further study. In summary, our AVO inversion based on the linear approximation to the Zoeppritz equation should be applied with caution as it may fail to model the non-linear AVO response with accurate amplitude in the presence of an LVL. An approach based on fitting amplitudes from full waveform modeling (e.g., reflectivity) is preferred.

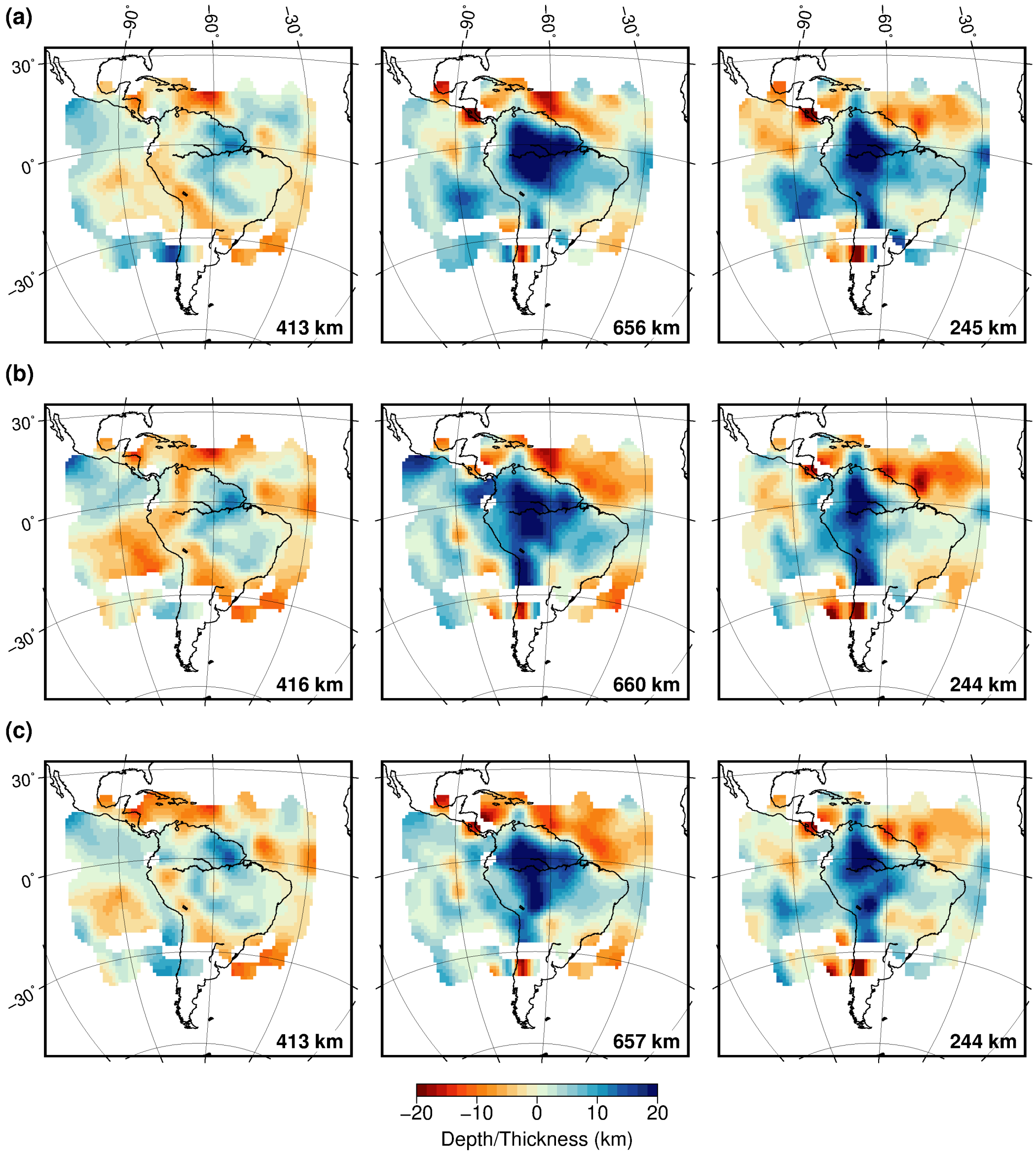

Figure C.1: MTZ topography after corrections for mantle heterogeneity using three different tomographic models. Topographic variations of the 410 (left), the 660 (middle), and the MTZ thickness (right) are shown after upper mantle heterogeneity corrections using three tomographic models (a) S40RTS (Ritsema et al., 2011), (b) SAW642ANb (Panning et al., 2010), and (c) TX2007 (Simmons et al., 2007). The depth/thickness estimates are shown relative to the regional average values at the bottom right corner of each panel.

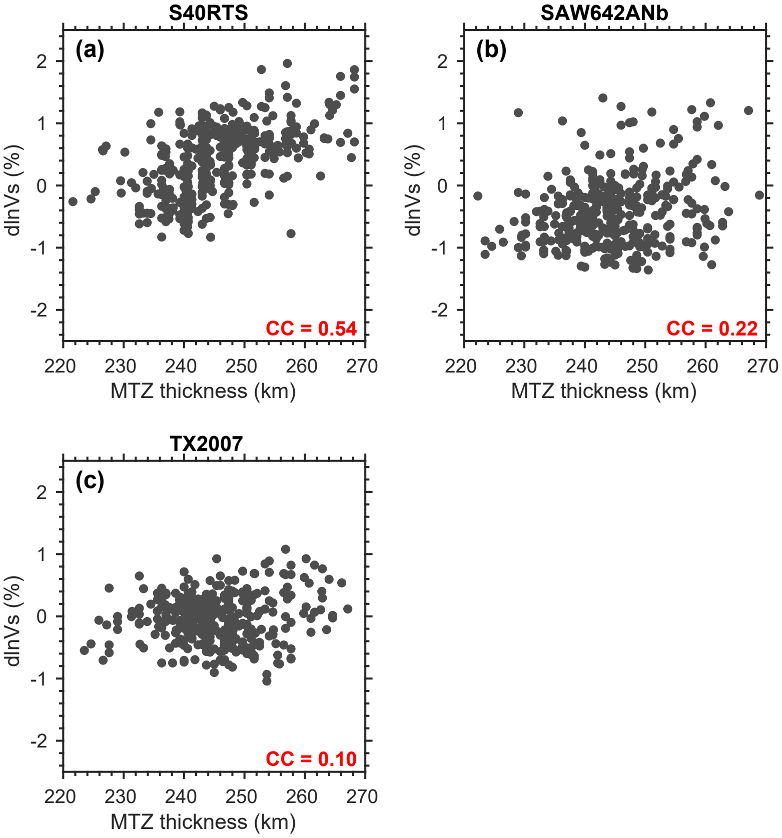

Figure C.2: Correlation between MTZ thickness and average velocity perturbations within the MTZ. The average velocity structure is calculated using tomographic models (a) S40RTS (Ritsema et al., 2011), (b) SAW642ANb (Panning et al., 2010), and (c) TX2007 (Simmons et al., 2007), respectively. The corresponding correlation (CC) coefficients are labeled at the bottom right corner of each panel.

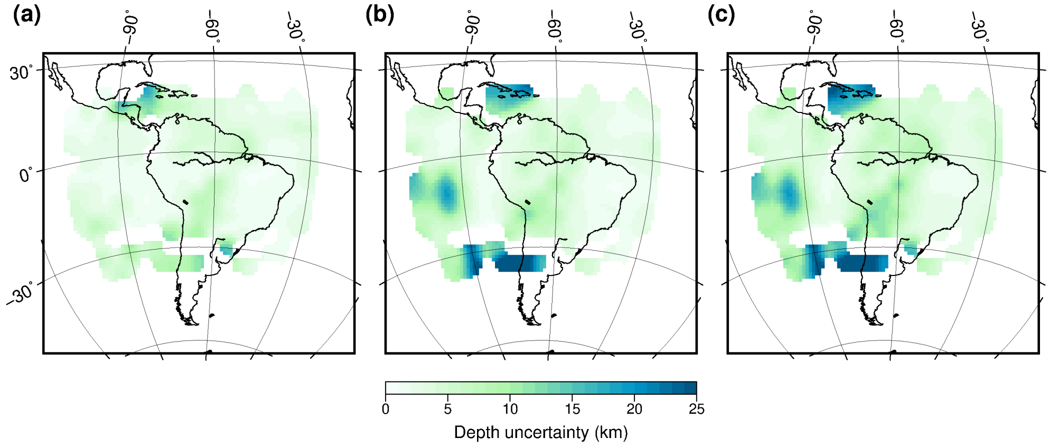

Figure C.3: The standard errors of the MTZ topography. The maps are (a) the 410 depths, (b) the 660 depths, and (c) the MTZ thickness, respectively. The standard errors are calculated by a bootstrap resampling test. Note the large uncertainties in the southernmost part of the study region are due to poor data coverage.

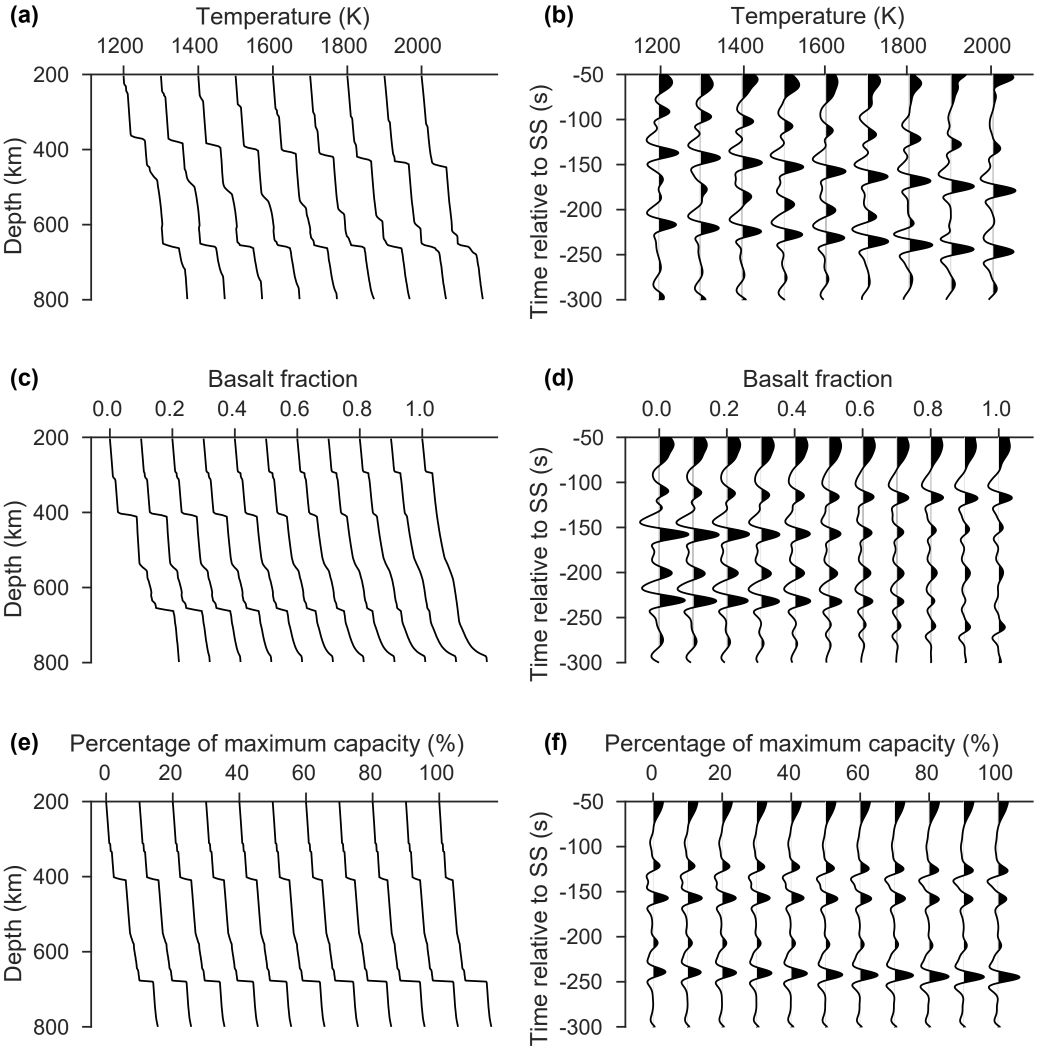

Figure C.4: Example of shear velocity profiles and reflectivity synthetic SS precursor waveforms generated based on the assumption of a mechanically mixed mantle. (a) Velocity profiles as a function of potential temperature for a fixed basalt fraction of 0.2. (b) Predicted SS precursors for models in (a). (c) Velocity profiles as a function of basalt fraction at a mantle adiabat of 1600 K. (d) Predicted SS precursors for models in (c). (e) Velocity profiles as a function of water content (as a percentage of maximum MTZ water storage capacity) for a basalt fraction of 0.2 and a potential temperature of 1600 K. (f) Predicted SS precursors for models in (e).

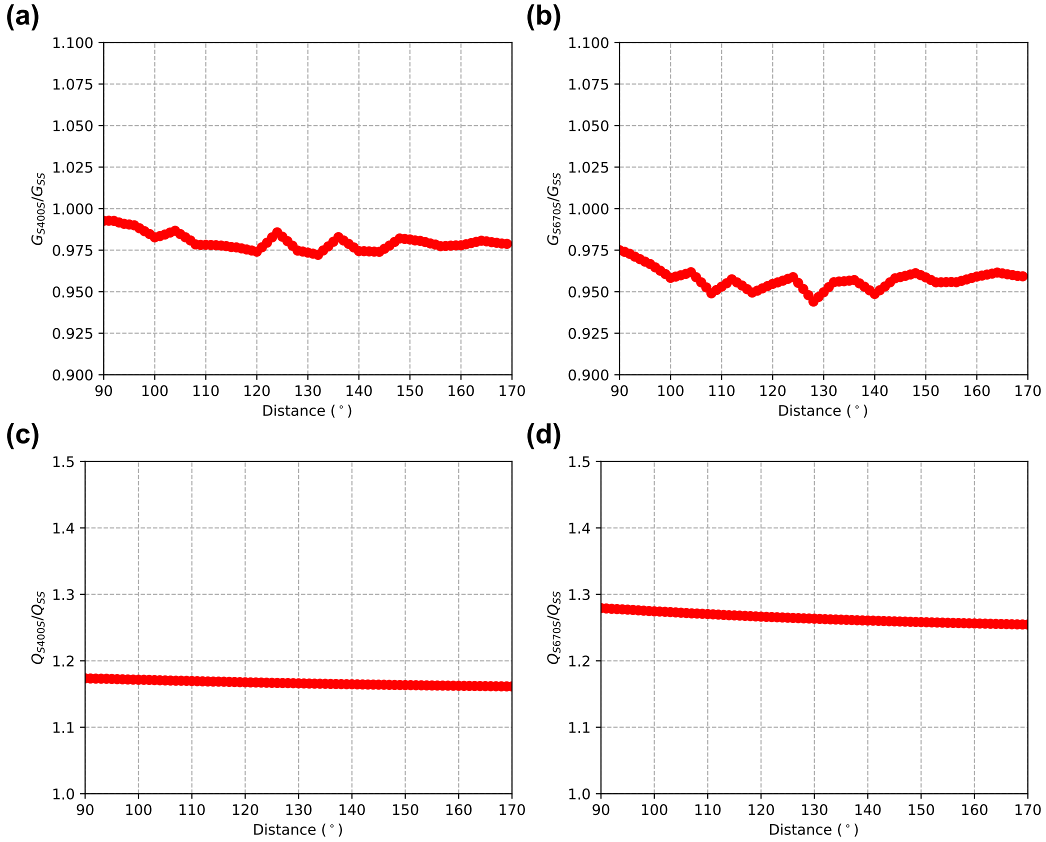

Figure C.5: Relative geometric spreading (G) and quality factor (Q) between SS precursors and the main phase. (a, b) Geometric spreading corrections for S410S and S660S, respectively. The geometric spreading effects are calculated using PREM. (c, d) Intrinsic attenuation corrections for S410S and S660S, respectively. The attenuation correction factors are calculated for PREM, and a center frequency of 30 s is assumed.

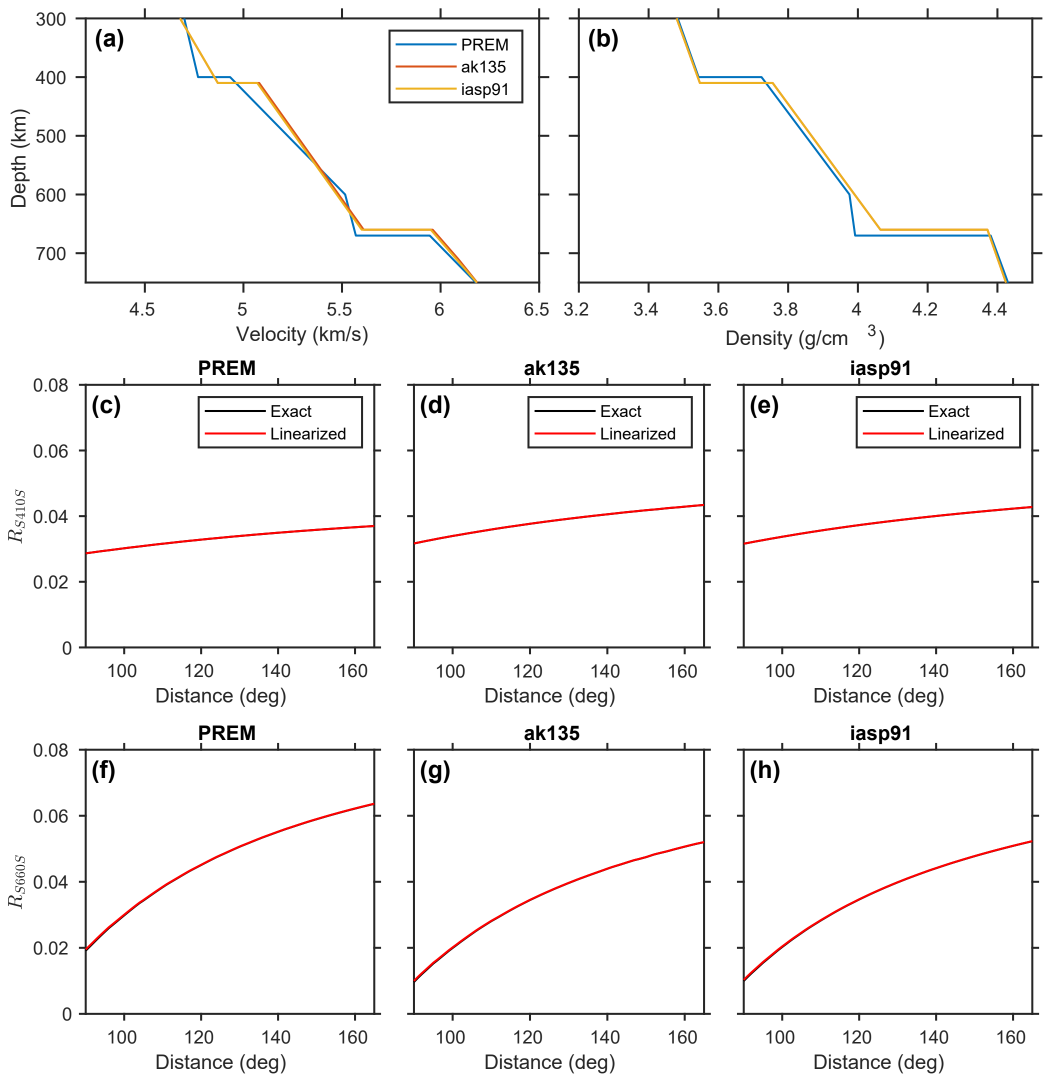

Figure C.6: Comparison of the SdS reflection coefficients of three global 1-D reference models calculated from the exact Zoeppritz equation and the two-term approximate equation. The exact (black lines) and approximate (red lines) solutions are calculated for (c, f) PREM (Dziewonski & Anderson, 1981), (d, g) ak135 (Kennett et al., 1995), and (e, h) iasp91 (Kennett & Engdahl, 1991), respectively. The shear velocity and density profiles of the three models are shown in (a) and (b), respectively. The S410S reflection coefficients are shown in (c-e), and the S660S amplitudes are shown in (f-h). Note that the differences between the exact and approximate solutions are minimal.

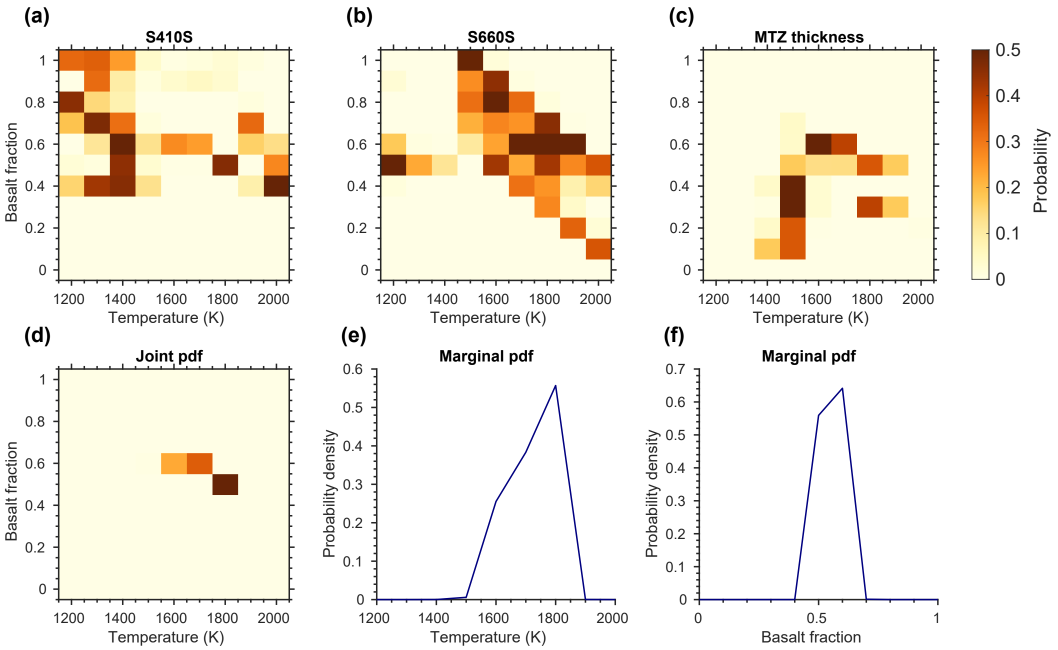

Figure C.7: Probabilistic inversion for mantle temperature and composition (in terms of the fraction of basalt) for an EA model. (a) The likelihood function (misfit between the observed and predicted measurements) of the S410S amplitudes. (b) Likelihood of the S660S amplitudes. (c) Likelihood of the MTZ thickness. (d) The cumulative posterior probability density function (PDF). Panels (e) and (f) are the marginal posterior probability distributions of temperature and basalt fraction, respectively. Dark colors in (a-d) indicate high probabilities.

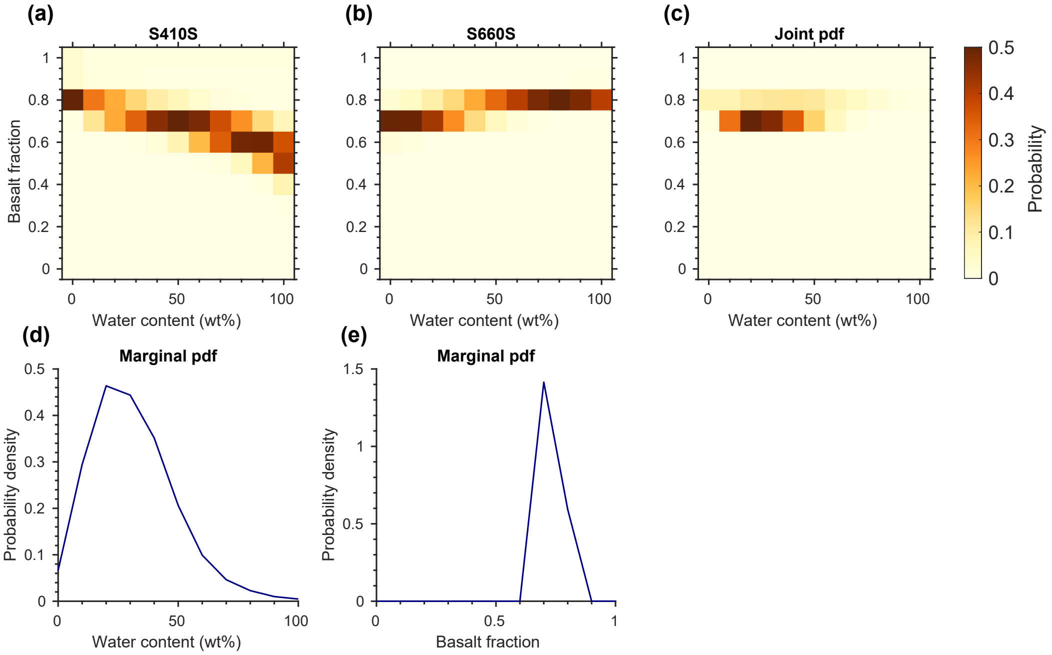

Figure C.8: Probabilistic inversion for water content (as percentage of maximum MTZ water storage capacity) and basalt fraction for an MM model. (a) The likelihood function of the S410S amplitudes. (b) Likelihood of the S660S amplitudes. (c) The cumulative posterior probability distribution. Panels (d) and (e) are the marginal posterior probability distributions of water content and basalt fraction, respectively.

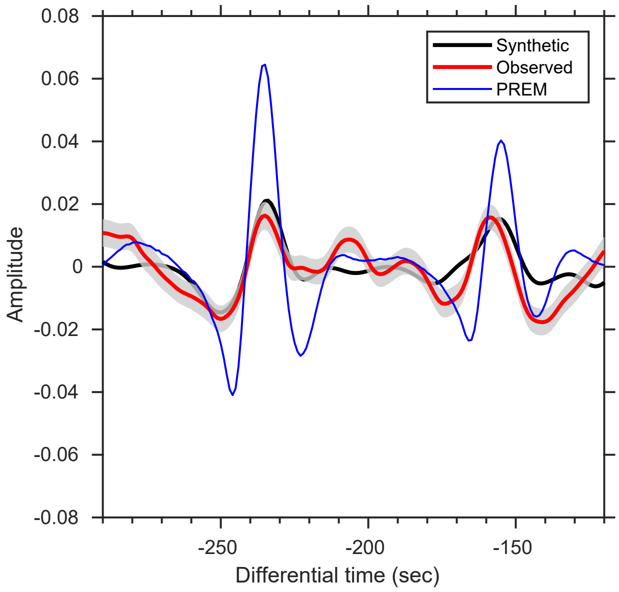

Figure C.9: Comparison between the observed and modeled waveforms for Cap 1. The observed stack (thick red curve) of Cap 1 with its 95% confidence intervals (gray shaded areas). The thick black curve is the synthetic waveform simulated by modifying the PREM model using our inverted density and shear velocity contrasts. The observed and simulated waveforms are close and well below the PREM-predicted waveform (thin blue curve).

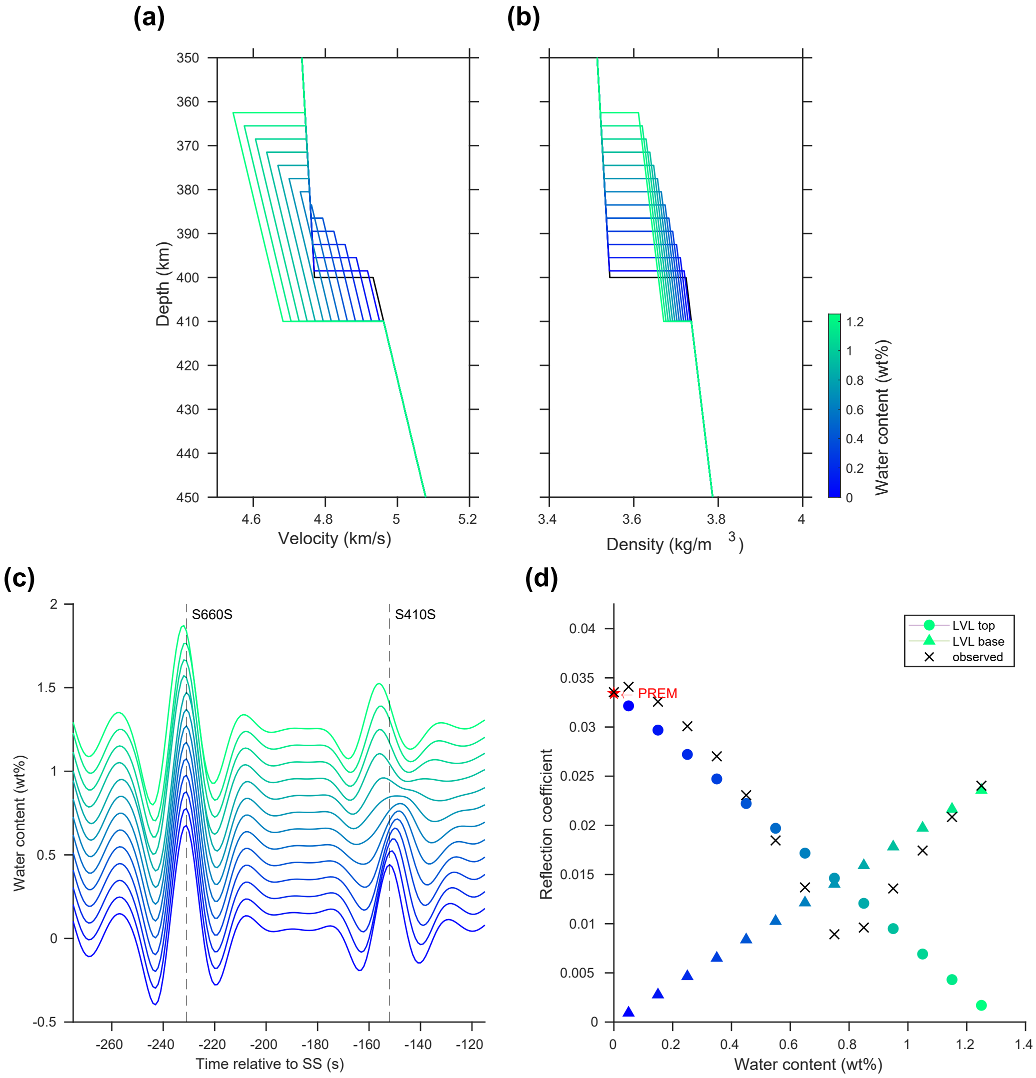

Figure C.10: Synthetic modeling of S410S reflection coefficients in the presence of water in wadsleyite following Schmerr and Garnero (2007). Panels (a) and (b) are the shear velocity and density structures near 410 km depth for increasing water content from 0 wt% to 1.25 wt%. (c) Synthetic S410S and S660S waveforms for varying water contents using the reflectivity method. (d) Zoeppritz-based reflection coefficients of the top (circles) and bottom (triangles) of the LVL compared with S410S reflection coefficients measured from reflectivity synthetic seismograms (cross symbols). We use a reference epicentral distance of 125°.

Appendix D

Supplementary Materials for Chapter 5

The supporting information provides additional details that are complementary to our analysis presented in Chapter 5. Our topography model of the 660 is compared with two other studies. We also explore the frequency dependence of the global average estimates of density jump across the 660. Based on thermodynamic modeling, we show the effect of hydration on density jump.

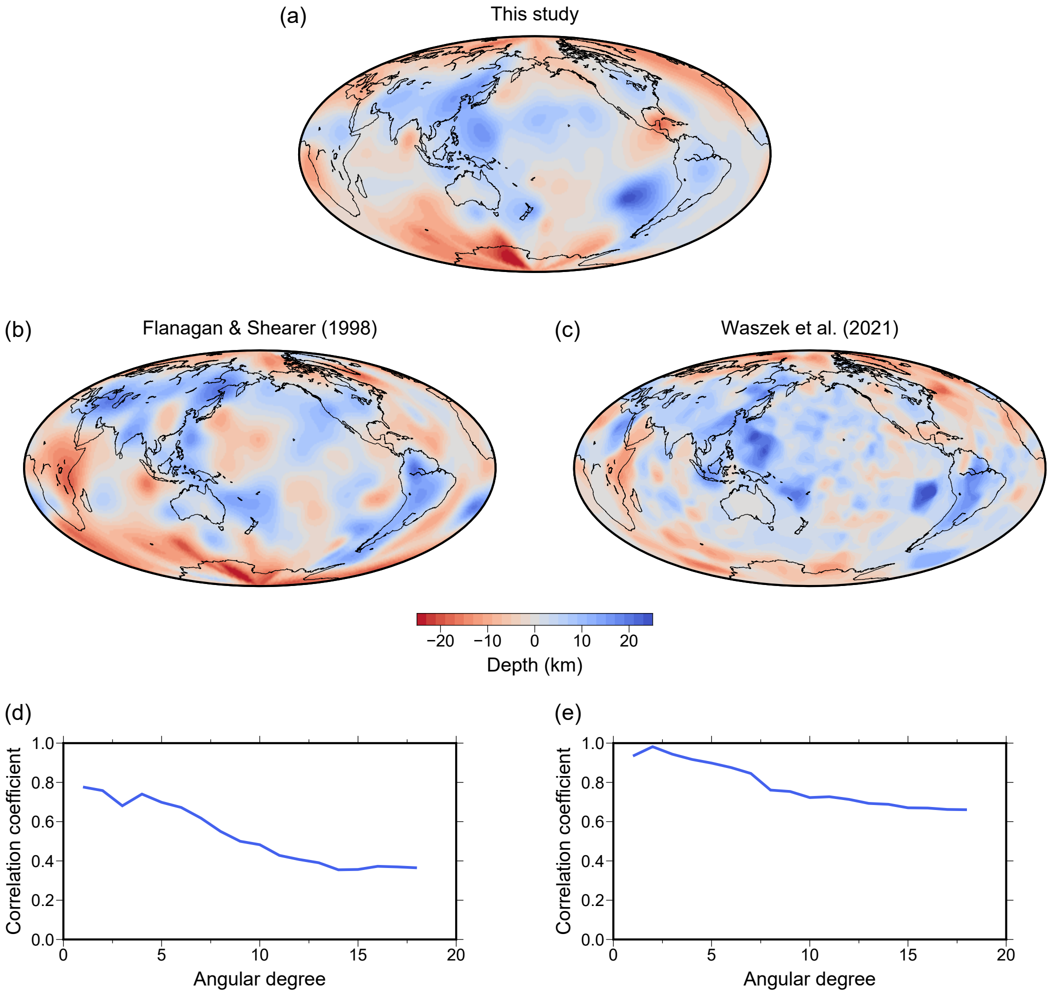

Figure D.1: Comparison of (a) our 660 topography to that from (b) Flanagan and Shearer (1998) and (c) a recently published model (Waszek et al., 2021). Panels (d) and (e) are the correlations as a function of spherical harmonic degree for our topography map versus that of Flanagan and Shearer (1998) and Waszek et al. (2021), respectively.

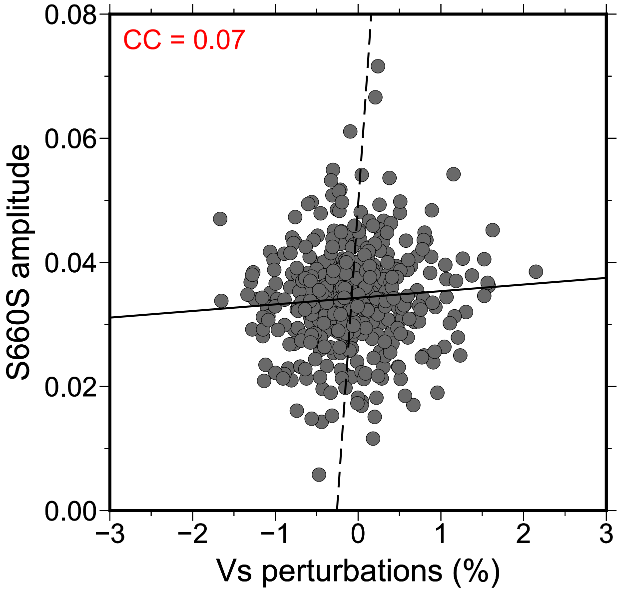

Figure D.2: Correlation between S660S amplitudes with shear velocity anomalies at the 660 km depth from S40RTS. The CC coefficient is shown in the top left corner. The solid and dashed black lines represent the least squares regressions obtained by assuming the S velocity perturbations or the S660S amplitudes to be the independent variables, respectively.

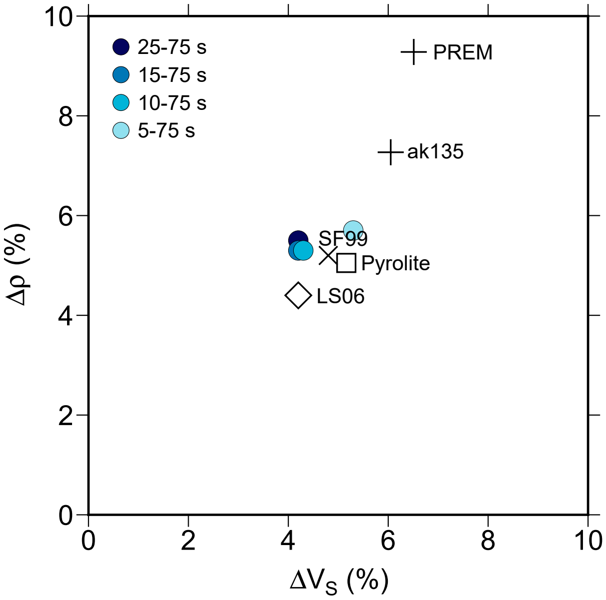

Figure D.3: Frequency dependence of the global average measurements of velocity and density jumps across the 660. The symbols represent values from seismic reference models, previous studies, and the pyrolite model.

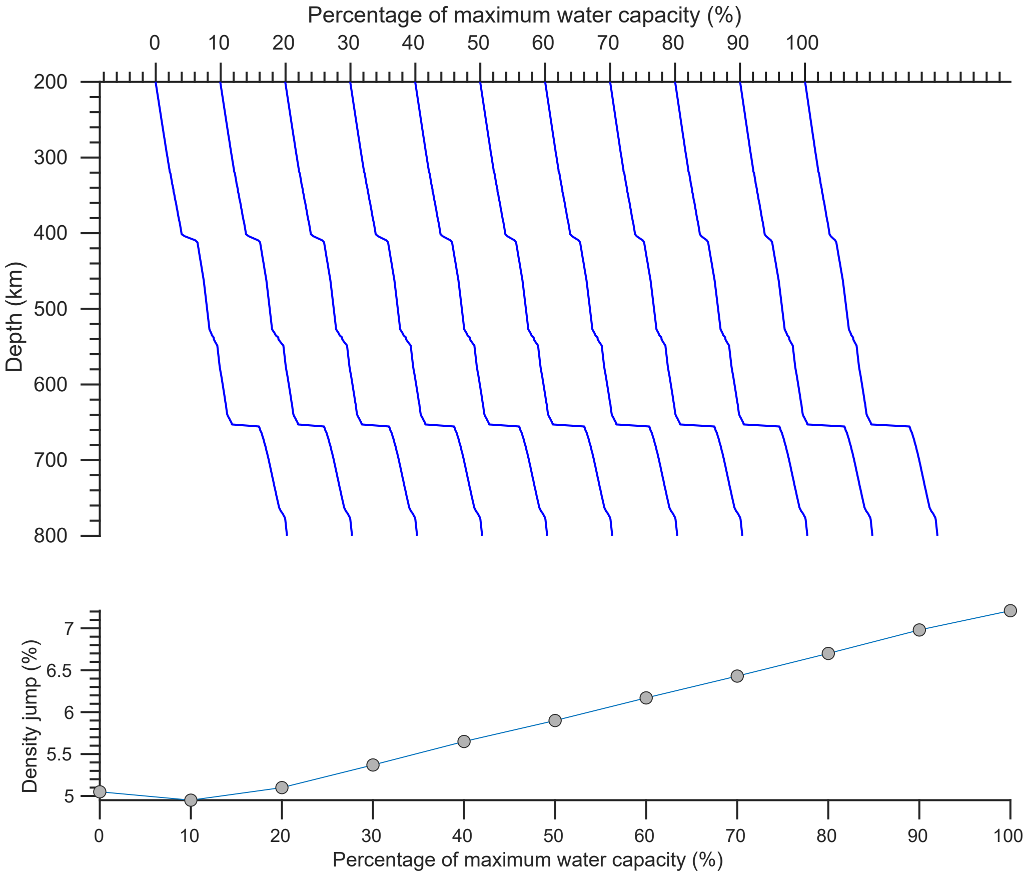

Figure D.4: (a) Shear velocity profiles for a series of water content profiles ranging from 0% to 100% of the maximum storage capacity with an increment of 10%, simulated using HyMaTZ. The thermodynamic modeling assumes a pyrolitic mantle composition along a 1600 K adiabat. Water partitioning in olivine, wadsleyite, and ringwoodite is fixed to be 6:30:15 based on experimental results from Inoue et al. (2010). The presence of hydration perturbs the density structures at both the 410 and 660. (b) Predicted density jumps across the 660. A quasi-linear increase in density jump across the 660 is observed with increasing water content due to reduced density in the MTZ. On average, the addition of 1 wt% of water would increase the density jump by $\sim$0.7%.

Appendix E

List of Software

Software	Description	References
SAC	Seismic data processing	Goldstein and Snoke (2005)
ObsPy	Seismic data processing	Beyreuther et al. (2010)
GMT	Mapping	Wessel et al. (2013)
TauP	Travel time calculation	Crotwell et al. (1999)
SOD	Data request	Owens et al. (2004)
PhaseNet	Arrival time picking	Zhu and Beroza (2019)
REAL	Earthquake association and location	M. Zhang et al. (2019)
M&L	Small event detection and location	M. Zhang and Wen (2015)
GrowClust	Earthquake relocation	Trugman and Shearer (2017)
hypoDD	Earthquake relocation	Waldhauser and Ellsworth (2000)
VELEST	Earthquake location	Kissling et al. (1994)
FOCMEC	Double-couple focal mechanisms	Snoke (1984)
Coulomb 3	Coulomb stress changes	Toda et al. (2011)
CPS330	Surface wave dispersion inversion	Herrmann (2013)
Seismic-noise-tomography	Ambient noise tomography	Goutorbe et al. (2015)
CRFL	Reflectivity synthetic seismogram	Fuchs and Müller (1971)
HyMaTZ	Velocity modeling for hydrous MTZ composition	F. Wang et al. (2018)

Table E.1: A list of seismological software tools used in this thesis.